ISSN 1816-5230

НАНОСИСТЕМИ, НАНОМАТЕРІАЛИ, НАНОТЕХНОЛОГІЇ

Nanosistemi, Nanomateriali, Nanotehnologii

ЗБІРНИК НАУКОВИХ ПРАЦЬ

ТОМ 19, ВИПУСК 4, 2021

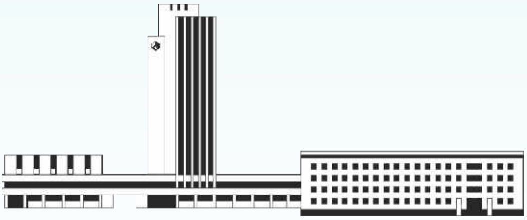

НАЦІОНАЛЬНА АКАДЕМІЯ НАУК УКРАЇНИ

НАНОСИСТЕМИ
НАНОМАТЕРІАЛИ
НАНОТЕХНОЛОГІЇ

NANOSYSTEMS
NANOMATERIALS
NANOTECHNOLOGIES

Засновник: Інститут металофізики ім. Г. В. Курдюмова НАН України
Видавець: Інститут металофізики ім. Г. В. Курдюмова НАН України

«Наносистеми, наноматеріали, нанотехнології» ♦ ‘Nanosistemi, Nanomateriali, Nanotehnologii’

Щоквартальний збірник наукових праць ◊ Quarterly Collected Scientific Transactions

РЕДАКЦІЙНА КОЛЕҐІЯ		EDITORIAL BOARD	
В. А. Татаренко	***головний редактор***, чл.-кор. НАН України, д.ф.-м.н., проф., Ін-т металофізики ім. Г. В. Курдюмова НАН України	***V. A. Tatarenko***	***Editor-in-Chief***, Cor. Mem. of the N.A.S. of Ukraine, Dr. Sci. (Phys.-Math.), Prof., G.V. Kurdyumov Inst. for Metal Physics of the N.A.S. of Ukraine
Б. М. Мордюк	***заступник головного редактора***, д.ф.-м.н., с.н.с., Ін-т металофізики ім. Г. В. Курдюмова НАН України	***B. M. Mordyuk***	***Associate Editor***, Dr. Sci. (Phys.-Math.), Sr. Researcher, G.V. Kurdyumov Inst. for Metal Physics of the N.A.S. of Ukraine
В. В. Лізунов	***відповідальний секретар редколеґії***, д.ф.-м.н., Ін-т металофізики ім. Г. В. Курдюмова НАН України	***V. V. Lizunov***	***Executive Managing Editor***, Dr. Sci. (Phys.-Math.), G.V. Kurdyumov Inst. for Metal Physics of the N.A.S. of Ukraine
М. Я. Валах	чл.-кор. НАН України, д.ф.-м.н., проф., Ін-т фізики напівпровідників ім. В. Є. Лашкарьова НАН України	***M. Ya. Valakh***	Cor. Mem. of the N.A.S. of Ukraine, Dr. Sci. (Phys.-Math.), Prof., V.Ye. Lashkaryov Inst. of Semiconductor Physics of the N.A.S. of Ukraine
П. П. Горбик	д.ф.-м.н., проф., Ін-т хімії поверхні ім. О. О. Чуйка НАН України	***P. P. Gorbyk***	Dr. Sci. (Phys.-Math.), Prof., O.O. Chuiko Inst. of Surface Chemistry of the N.A.S. of Ukraine
В. О. Зажигалов	чл.-кор. НАН України, д.х.н., проф., Ін-т сорбції та проблем ендоекології НАН України	***V. O. Zazhigalov***	Cor. Mem. of the N.A.S. of Ukraine, Dr. Sci. (Chem.), Prof., Inst. of Sorption and Problems of the Endoecology of the N.A.S. of Ukraine
Б. Зайді	кандидат фізичних наук, факультет наук про матерію, Ун-т Батни 1 Хадж Лахдар, Батна, Алжир	***Beddiaf Zaidi***	Docteur en Physique, Faculté des sciences de la matière, Université Batna 1 Hadj Lakhdar, Batna, Algérie
В. Л. Карбівський	д.ф.-м.н., проф., Ін-т металофізики ім. Г. В. Курдюмова НАН України	***V. L. Karbivskyy***	Dr. Sci. (Phys.-Math.), Prof., G.V. Kurdyumov Inst. for Metal Physics of the N.A.S. of Ukraine
В. П. Кладько	чл.-кор. НАН України, д.ф.-м.н., проф., Ін-т фізики напівпровідників ім. В. Є. Лашкарьова НАН України	***V. P. Kladko***	Cor. Mem. of the N.A.S. of Ukraine, Dr. Sci. (Phys.-Math.), Prof., V.Ye. Lashkaryov Inst. of Semiconductor Physics of the N.A.S. of Ukraine
О. А. Кордюк	акад. НАН України, д.ф.-м.н., проф., Київський академічний ун-т	***O. A. Kordyuk***	Mem. of the N.A.S. of Ukraine, Dr. Sci. (Phys.-Math.), Prof., Kyiv Academic Univ.
С. О. Котречко	чл.-кор. НАН України, д.ф.-м.н., проф., Ін-т металофізики ім. Г. В. Курдюмова НАН України	***S. O. Kotrechko***	Cor. Mem. of the N.A.S. of Ukraine, Dr. Sci. (Phys.-Math.), Prof., G.V. Kurdyumov Inst. for Metal Physics of the N.A.S. of Ukraine
М. П. Куліш	чл.-кор. НАН України, д.ф.-м.н., проф., Київський національний ун-т імені Тараса Шевченка МОН України	***M. P. Kulish***	Cor. Mem. of the N.A.S. of Ukraine, Dr. Sci. (Phys.-Math.), Prof., Taras Shevchenko Natl. Univ. of Kyiv of the Ministry of Education and Science of Ukraine
Б. І. Лев	акад. НАН України, д.ф.-м.н., проф., Ін-т теоретичної фізики ім. М. М. Боголюбова НАН України	***B. I. Lev***	Mem. of the N.A.S. of Ukraine, Dr. Sci. (Phys.-Math.), Prof., M.M. Bogolyubov Inst. for Theoretical Physics of the N.A.S. of Ukraine
Є. Г. Лень	д.ф.-м.н., проф., Ін-т металофізики ім. Г. В. Курдюмова НАН України	***E. G. Len***	Dr. Sci. (Phys.-Math.), Prof., G.V. Kurdyumov Inst. for Metal Physics of the N.A.S. of Ukraine
Ю. А. Малєтін	чл.-кор. НАН України, д.х.н., с.н.с., Ін-т сорбції та проблем ендоекології НАН України	***Yu. A. Maletin***	Cor. Mem. of the N.A.S. of Ukraine, Dr. Sci. (Chem.), Sr. Researcher, Inst. of Sorption and Problems of Endoecology of the N.A.S. of Ukraine
В. Б. Молодкін	чл.-кор. НАН України, д.ф.-м.н., проф., Ін-т металофізики ім. Г. В. Курдюмова НАН України	***V. B. Molodkin***	Cor. Mem. of the N.A.S. of Ukraine, Dr. Sci. (Phys.-Math.), Prof., G.V. Kurdyumov Inst. for Metal Physics of the N.A.S. of Ukraine
В. Є. Панарін	д.т.н., с.н.с., Ін-т металофізики ім. Г. В. Курдюмова НАН України	***V. Ye. Panarin***	Dr. Sci. (Tech.), Sr. Researcher, G.V. Kurdyumov Inst. for Metal Physics of the N.A.S. of Ukraine
Р. Р. Панчук	д.б.н., Ін-т біології клітини НАН України	***R. R. Panchuk***	Dr. Sci. (Biol.), Inst. of Cell Biology of the N.A.S. of Ukraine
В. І. Пехньо	акад. НАН України, д.х.н., проф., Ін-т загальної та неорганічної хімії ім. В. І. Вернадського НАН України	***V. I. Pekhnyo***	Mem. of the N.A.S. of Ukraine, Dr. Sci. (Chem.), Prof., V.I. Vernadsky Inst. of General and Inorganic Chemistry of the N.A.S. of Ukraine
О. Д. Погребняк	д.ф.-м.н., проф., Сумський державний ун-т МОН України	***O. D. Pogrebnjak***	Dr. Sci. (Phys.-Math.), Prof., Sumy State Univ. of the Ministry of Education and Science of Ukraine
Ю. І. Прилуцький	д.ф.-м.н., проф., ННЦ «Ін-т біології та медицини» Київського нац. ун-ту імені Тараса Шевченка МОН України	***Yu. I. Prylutskyy***	Dr. Sci. (Phys.-Math.), Prof., NSC ‘Inst. of Biology and Medicine’ of the Taras Shevchenko Natl. Univ. of Kyiv of the Ministry of Education and Science of Ukraine
В. А. Прокопенко	д.т.н., с.н.с., Ін-т біоколоїдної хімії ім. Ф. Д. Овчаренка НАН України	***V. A. Prokopenko***	Dr. Sci. (Tech.), Senior Researcher, F.D. Ovcharenko Inst. of Biocolloidal Chemistry of the N.A.S. of Ukraine
О. А. Пуд	д.х.н., проф., Ін-т біоорганічної хімії та нафтохімії ім. В. П. Кухаря НАН України	***O. A. Pud***	Dr. Sci. (Chem.), Prof., V.P. Kukhar Inst. of Bioorganic Chemistry and Petrochemistry of the N.A.S. of Ukraine
Т. М. Радченко	д.ф.-м.н., с.н.с., Ін-т металофізики ім. Г. В. Курдюмова НАН України	***T. M. Radchenko***	Dr. Sci. (Phys.-Math.), Sr. Researcher, G.V. Kurdyumov Inst. for Metal Physics of the N.A.S. of Ukraine
П. Є. Стрижак	чл.-кор. НАН України, д.х.н., проф., Ін-т фізичної хімії ім. Л. В. Писаржевського НАН України	***P. E. Strizhak***	Cor. Mem. of the N.A.S. of Ukraine, Dr. Sci. (Chem.), Prof., L.V. Pisarzhevsky Inst. of Physical Chemistry of the N.A.S. of Ukraine
В. Й. Сугаков	чл.-кор. НАН України, д.ф.-м.н., проф., Ін-т ядерних досліджень НАН України	***V. J. Sugakov***	Cor. Mem. of the N.A.S. of Ukraine, Dr. Sci. (Phys.-Math.), Prof., Inst. of Nuclear Research of the N.A.S. of Ukraine
Л. Ф. Суходуб	чл.-кор. НАН України, д.ф.-м.н., проф., Сумський держ. ун-т МОН України	***L. F. Sukhodub***	Cor. Mem. of the N.A.S. of Ukraine, Dr. Sci. (Phys.-Math.), Prof., Sumy State Univ. of the Ministry of Education and Science of Ukraine
В. М. Уваров	чл.-кор. НАН України, д.ф.-м.н., проф., Ін-т металофізики ім. Г. В. Курдюмова НАН України	***V. M. Uvarov***	Cor. Mem. of the N.A.S. of Ukraine, Dr. Sci. (Phys.-Math.), Prof., G.V. Kurdyumov Inst. for Metal Physics of the N.A.S. of Ukraine
О. М. Файнлейб	чл.-кор. НАН України, д.х.н., проф., Ін-т хімії високомолекулярних сполук НАН України	***O. M. Fainleib***	Cor. Mem. of the N.A.S. of Ukraine, Dr. Sci. (Chem.), Prof., Inst. of Chemistry of Macromolecular Compounds of the N.A.S. of Ukraine
Д. О. Харченко	д.ф.-м.н., проф., Ін-т прикладної фізики НАН України	***D. O. Kharchenko***	Dr. Sci. (Phys.-Math.), Prof., Inst. of Applied Physics of the N.A.S. of Ukraine
О. В. Хоменко	д.ф.-м.н., проф., Сумський державний ун-т МОН України	***O. V. Khomenko***	Dr. Sci. (Phys.-Math.), Prof., Sumy State Univ. of the Ministry of Education and Science of Ukraine

© Інститут металофізики ім. Г. В. Курдюмова НАН України (Київ), 2021

НАЦІОНАЛЬНА АКАДЕМІЯ НАУК УКРАЇНИ
Інститут металофізики ім. Г. В. Курдюмова

НАНОСИСТЕМИ, НАНОМАТЕРІАЛИ, НАНОТЕХНОЛОГІЇ

ЗБІРНИК НАУКОВИХ ПРАЦЬ

ТОМ 19, ВИПУСК 4

НАНОСИСТЕМИ
НАНОМАТЕРІАЛИ
НАНОТЕХНОЛОГІЇ

NANOSYSTEMS
NANOMATERIALS
NANOTECHNOLOGIES

РВВ ІМФ
КИЇВ — 2021

УДК 536:669

НАНОСИСТЕМИ, НАНОМАТЕРІАЛИ, НАНОТЕХНОЛОГІЇ / Щоквартальний збірник наукових праць / Том 19, вип. 4. — Київ: РВВ ІМФ, 2021. — XVIII с. + 218 с.

У збірнику наведено ориґінальні та оглядові статті за результатами робіт, виконаних у рамках досліджень за напрямом «Перспективні фундаментальні дослідження та інноваційні розробки наноматеріалів і нанотехнологій для потреб промисловості, охорони здоров'я та сільського господарства». Основну увагу приділено розгляду проблемних питань нанофізики, наноелектроніки, особливостей будови наноструктурованих матеріялів, з'ясуванню їхніх електричних, термічних, механічних, реологічних і хемічних властивостей, поверхневих явищ і самоорганізації. Представлено результати фабрикації, оброблення, тестування й аналізування нанорозмірних частинок, наномасштабних структур і багатофункціональних наноматеріялів технічного та біомедичного призначення в умовах впливу зовнішніх чинників. Розглянуто особливості технологій одержання, діягностики та характеризації наносистем.

Статті друкуються мовами ориґіналів.

Збірник розраховано на наукових працівників, інженерів, викладачів ЗВО, аспірантів і студентів відповідних спеціяльностей.

ISSN 1816-5230

НАЦІОНАЛЬНА АКАДЕМІЯ НАУК УКРАЇНИ ● ІНСТИТУТ МЕТАЛОФІЗИКИ ім. Г. В. Курдюмова

НАНОСИСТЕМИ, НАНОМАТЕРІАЛИ, НАНОТЕХНОЛОГІЇ

ЗБІРНИК НАУКОВИХ ПРАЦЬ
ЗАСНОВАНИЙ У ЖОВТНІ 2003 р.

Том 19, вип. 4; 2021 р.

ЗМІСТ

Редакційні об'яви

Науковий редактор випуску — *В. А. Татаренко*
Відповідальний секретар редакційної колеґії — *В. В. Лізунов*
Редактори-коректори: *І. О. Головашич, Д. С. Леонов, Н. А. Леонова*
Технічний редактор — *Д. С. Леонов*
Оригінал-макет для прямого репродукування виготовлено комп'ютеризованою групою РВВ Інституту металофізики ім. Г. В. Курдюмова НАН України
Друкується за постановою редакційної колеґії збірника англійською або українською мовами
Затверджено до друку вченою радою ІМФ ім. Г. В. Курдюмова НАН України
Свідоцтво суб'єкта видавничої справи серії ДК № 5875 від 13.12.2017 р.
Свідоцтво про державну реєстрацію ДЗМІ серії КВ № 23231-13071ПР від 22.03.2018 р.
Підп. до друку 31.12.2021 р. Формат 70×100/16. Гарн. SchoolBookC. Папір офсет. № 1. Друк різограф.
Адреса редакції «ННН»: Інститут металофізики ім. Г. В. Курдюмова НАН України,
бульв. Акад. Вернадського, 36, каб. 210, 1406, 1407; 03142 Київ, Україна
Тел.: +380 44 4229551, +380 44 4249042, +380 44 4241221; факс: +380 44 4242561
Ел. пошта: tatar@imp.kiev.ua, dsleonov@gmail.com
Надруковано в РВВ ІМФ ім. Г. В. Курдюмова НАН України.
бульв. Акад. Вернадського, 36; 03142 Київ, Україна. Тел.: +380 44 4240236
Зав. поліграфічно-розмножувальної групи — *Л. І. Малініна*

NATIONAL ACADEMY OF SCIENCES OF UKRAINE ● G. V. KURDYUMOV INSTITUTE FOR METAL PHYSICS

COLLECTED SCIENTIFIC TRANSACTIONS

NANOSISTEMI, NANOMATERIALI, NANOTEHNOLOGII

FOUNDED IN OCTOBER, 2003

Volume 19, Issue 4 (2021)

CONTENTS

Editorial Announcements

Scientific Editor of the Issue—*V. A. Tatarenko*
Executive Managing Editor—*V. V. Lizunov*
Technical Editor—*D. S. Leonov*
Editorial-Publishing Department, G. V. Kurdyumov Institute for Metal Physics, N.A.S. of Ukraine
Editorial Office: 36 Academician Vernadsky Boulevard, UA-03142 Kyyiv, Ukraine
Telephone: +380 44 4229551, +380 44 4249042, +380 44 4241221. Fax: +380 44 4242561
E-mail: tatar@imp.kiev.ua, dsleonov@gmail.com

ИНФОРМАЦИЯ ДЛЯ ПОДПИСЧИКОВ

Редакция ежеквартального сборника научных трудов
«НАНОСИСТЕМИ, НАНОМАТЕРІАЛИ, НАНОТЕХНОЛОГІЇ»
(CODEN: NNNAAT; ISSN (Print): 1816-5230, ISSN (Online): 2617-3794;
в «Каталоге изданий Украины» подписной индекс: **94919)**
извещает о подписке (начиная с текущего квартала выпуска).
Рекомендуем оформить подписку непосредственным перечислением оплаты

в гривнах:
«Получателю»: Институт металлофизики им. Г. В. Курдюмова НАН Украины
на расчётный счёт № UA058201720313291001201001901 в банке ГУГКСУ в г. Киеве
код банка 820172
код ЗКПО: 05417331
для «Поставщика» — Института металлофизики им. Г. В. Курдюмова НАН Украины
Свидетельство плательщика налога № 36283185
ИНН 054173326066
Код назначения платежа: 25010100
Назначение платежа: за сборник «Наносистеми, наноматеріали, нанотехнології» для РИО ИМФ НАНУ
Основание: предоплата 100%

в иностранной валюте (долларах США, евро) через соответствующие банки-корреспонденты АО «Государственный экспортно-импортный банк Украины»:
«Получателю»: Филиал АО «Государственный экспортно-импортный банк Украины»
в г. Киеве (Украина, 04053 Киев, ул. Бульварно-Кудрявская, 11$^{\text{б}}$)
на расчётный счёт № UA603223130000025308000000067
МФО 322313
для «Поставщика» — Института металлофизики им. Г. В. Курдюмова НАН Украины
Назначение платежа: за сборник «Наносистеми, наноматеріали, нанотехнології» для РИО ИМФ НАНУ
Основание: предоплата 100%

При этом способе подписки необходимо сообщить редакции сборника по почтовому адресу:
РИО (№ 83) ИМФ НАНУ,
бульв. Акад. Вернадского, 36,
03142 Киев, Украина

e-mail: tatar@imp.kiev.ua; факс: +380 44 4242561; телефон: +380 44 4229551, +380 44 4249042

дату оплаты, название учреждения или имя подписчика, адрес для почтовой доставки, а при необходимости — свои реквизиты для налоговой накладной.

Периодичность — том из 4 выпусков в год.

С учётом почтовой пересылки
для подписчиков в Украину подписная стоимость: одного экземпляра выпуска — 312 грн., тома — 1248 грн.;
для подписчиков в страны СНГ подписная стоимость: одного экземпляра выпуска — 36 US$, тома — 144 US$;
для иностранных подписчиков вовне СНГ подписная стоимость: одного экземпляра выпуска — 40 US$ (36 EUR), тома — 160 US$ (144 EUR).

✂ *Образец для оплаты годовой подписки*

Счёт-фактура

«Поставщик»: Институт металлофизики им. Г. В. Курдюмова НАН Украины
«Получатель»: Филиал АО «Государственный экспортно-импортный банк Украины» в г. Киеве
(Украина, 04053 Киев, ул. Бульварно-Кудрявская, 11$^{\text{б}}$)
на расчётный счёт № UA603223130000025308000000067, МФО 322313
Назначение платежа: за сборник «Наносистеми, наноматеріали, нанотехнології» для ИМФ НАНУ
«Плательщик»: ______________________________
Основание: предоплата 100%

№	Наименование	Ед. изм.	Кол-во	Цена	Сумма
1	сборник «Наносистеми, наноматеріали, нанотехнології» (включая доставку почтой)	экз.	4	36 US$	144 US$
	Сумма к оплате				144 US$

INFORMATION FOR SUBSCRIBERS

Editorial Board of Quarterly Collected Scientific Transactions
‘NANOSISTEMI, NANOMATERIALI, NANOTEHNOLOGII’
(*i.e.* ‘NANOSYSTEMS, NANOMATERIALS, NANOTECHNOLOGIES’)
(CODEN: NNNAAT; ISSN (Print): 1816-5230, ISSN (Online): 2617-3794)
advertises the subscription on an annual basis for this year. Orders should be placed through one of the methods described below.

Besides the subscription *via* the centralized service by State Enterprise ‘PRESA’ (2a Georgiy Kyrpa Str., UA-03999 Kyiv, Ukraine; faxes: +380 44 2890774 / 2480377 / 2480384 / 2487802 / 2480406; e-mail: pod_ukr@presa.ua, rozn@presa.ua, info@presa.ua) or *via* Internet:

http://presa.ua/nanosistemi-nanomateriali-nanotehnologii.html?___SID=U

the Editorial Board will take orders sent directly to the Editorial Board. To obtain our edition, the persons and institutions, interested in this title, should made the definite payment sent, according to the order, to the account of the Publisher—Institute for Metal Physics of the N.A.S. of Ukraine.

This edition frequency is 4 issues per year. The annual subscription rate for ‘Nanosistemi, Nanomateriali, Nanotehnologii’ is 160 US$ (or 144 EUR), including airmail postage, packing and handling charges. All other currency payments should be made using the current conversion rate set by the Publisher (subscribers should contact the Editorial Board).

Subscription is valid after obtaining by the Editorial Board of banker’s order. Banker’s order should be sent to the address:

G. V. Kurdyumov Institute for Metal Physics, N.A.S. of Ukraine,
currency account No. UA603223130000025308000000067, MFO 322313
in the Kyiv’s Branch of JSC ‘The State Export-Import Bank of Ukraine’
(Joint Stock Company ‘Ukreximbank’)
(11^b Bulvarno-Kudriavska Str., UA-04053 Kyiv, Ukraine)

simultaneously with written notice providing the Editorial Board with a copy of banker’s order for subscription and detailed address for mailing.

Address of the Editorial Board Office:

G. V. Kurdyumov Institute for Metal Physics, N.A.S. of Ukraine,
36 Academician Vernadsky Blvd.,
UA-03142 Kyiv, Ukraine.

E-mail: tatar@imp.kiev.ua (with subject beginning by word ‘nano’).
Fax: +380 44 4242561.

After receiving of banker’s order, the Editorial Board will send the guarantee letter to the subscriber’s address for mailing the collected scientific transactions for a corresponding term.

Editorial Board of this edition hopes for effective co-operation with its present and future readers and asks to promote the maximum information about its contents to persons, institutions and organizations concerned.

ИНФОРМАЦИЯ ДЛЯ АВТОРОВ

Сборник научных трудов «Наносистеми, наноматеріали, нанотехнології» (ННН) публикует ещё неопубликованные и не находящиеся на рассмотрении для опубликования в иных изданиях научные обзоры и оригинальные статьи, содержащие и характеризующие результаты экспериментальных и теоретических исследований в области физики, химии, техники, методов синтеза, обработки и диагностики наноразмерных систем и наномасштабных материалов: кластеров, наночастиц, нанотрубок, нанокристаллов и наноструктур (апатитоподобных и др. биосистем, аморфных и коллоидных наноразмерных систем, наноструктурных плёнок и покрытий, нанопорошков и т.д.).

Статьи публикуются на одном из двух языков: **английском** или **украинском**.

Статьи, в оформлении которых не соблюдены следующие правила для публикации в ННН, возвращаются авторам без рассмотрения по существу. (Датой поступления считается день повторного представления статьи после соблюдения указанных ниже правил.)

1. Статья должна быть подписана всеми авторами (с указанием их адресов электронной почты); **следует указать** фамилию, имя и отчество автора, с которым редакция будет вести переписку, его почтовый адрес, номер телефона (факса), адрес электронной почты.

2. Изложение должно быть ясным, **структурированным** (разделами «1. Введение», «2. Экспериментальная/Теоретическая методика», «3. Результаты и их обсуждение», «4. Выводы», «Цитированная литература»), сжатым, без длинных введений, отступлений и повторов, дублирования в тексте данных таблиц, рисунков и подписей к ним. Аннотация и раздел «Выводы» должны не дублировать друг друга. Числовые данные следует приводить в общепринятых единицах.

3. Объём статьи должен быть не более 5000 слов (с учётом основного текста, таблиц, подписей к рисункам, списка литературы) и 10 рисунков. Вопросы, связанные с публикацией научных обзоров (не более 22000 слов и 60 рисунков), решаются редколлегией ННН на основании предварительно предоставленной авторами расширенной аннотации работы.

4. В редакцию предоставляется 1 экземпляр рукописи с иллюстративным материалом, напечатанный на бумаге формата А4 через двойной интервал в один столбец с одной стороны листа.

5. В редакцию обязательно предоставляется (по **e-mail** или на компакт-диске) файл рукописи статьи, набранный в текстовом редакторе Microsoft Word 2003, 2007 или 2010 с названием, состоящим из фамилии первого автора (латиницей), например, Smirnov.doc.

6. Печатный вариант рукописи и её электронная версия должны быть идентичными и содержать **5–7 индексов PACS** (в последней редакции ‘Physics and Astronomy Classification Scheme 2010’— http://publishing.aip.org/publishing/pacs/pacs-2010-regular-edition) и **аннотацию** (200–250 слов) статьи (вместе с **5–6 ключевыми словами**). Тексты украиноязычных статей должны также содержать заглавие статьи (вместе со списком авторов и адресами соответствующих учреждений), расширенную аннотацию (300–350 слов), ключевые слова, заголовки таблиц и подписи к рисункам на **английском языке**. Кроме того, содержания аннотаций на украинском и английском языках должны быть идентичными по смыслу.

7. Рисунки (только черно-белые или полутоновые с градацией серого) предоставляются на отдельных листах с указанием номера рисунка и фамилии первого автора. Все рисунки должны быть дополнительно представлены в виде отдельных файлов (предпочтительно в **графических форматах TIFF, EPS или JPEG**) с названиями, состоящими из фамилии первого автора (латиницей) и номера рисунка, например, Smirnov_fig2a.tiff. Качество **иллюстраций** (в том числе полутоновых) должно обеспечивать их воспроизведение с разрешением 300–600 точек на дюйм. Дополнительно рисунки предоставляются в формате программы, в которой они создавались.

8. Надписи на рисунках (особенно на полутоновых) надо по возможности заменить буквенными обозначениями (набранными на контрастном фоне), а кривые обозначить цифрами или различного типа линиями/маркерами, разъясняемыми в подписях к рисункам или в тексте. На графиках все линии/маркёры должны быть чёрного цвета и достаточных толщин/размеров для качественного воспроизведения в уменьшенном в 2–3 раза виде (рекомендуемая ширина рисунка — 12,7 см). Снимки должны быть чёткими и контрастными, а надписи и обозначения должны не закрывать существенные детали (для чего можно использовать стрелки). Вместо указания в подтекстовке увеличения при съёмке желательно проставить масштаб (на контрастном фоне) на одном из идентичных снимков. На графиках подписи к осям, **выполненные на языке статьи**, должны содержать обозначения (или наименования) откладываемых величин и через запятую их единицы измерения.

9. Формулы в текст необходимо вставлять с помощью редактора формул MathType, полностью совместимого с MS Office 2003, 2007, 2010.

10. Рисунки, а также **таблицы** и подстрочные **примечания (сноски)** должны иметь сплошную нумерацию по всей статье.

11. Ссылки на литературные источники следует давать в виде порядкового номера, напечатанного в строку в квадратных скобках. Список литературы составляется в порядке первого упоминания источника. Примеры оформления ссылок приведены ниже; просим обратить внимание на порядок следования инициалов и фамилий авторов, библиографических сведений и на разделительные знаки, а также на необходимость указания **всех** соавторов цитированной работы и (в конце каждой ссылки) её **цифрового идентификатора DOI**, если таковой имеется у соответствующей публикации (и указан на её интернет-странице издательства):

1. T. M. Radchenko and V. A. Tatarenko, *Usp. Fiz. Met.*, **9**, No. 1: 1 (2008) (in Ukrainian); https://doi.org/10.15407/ufm.09.01.001
2. T. M. Radchenko, A. A. Shylau, and I. V. Zozoulenko, *Phys. Rev. B*, **86**: 035418 (2012); https://doi.org/10.1103/PhysRevB.86.035418
3. A. Meisel, G. Leonhardt, and R. Szargan, *Röntgenspektren und Chemische Bindung* [X-Ray Spectra and Chemical Bond] (Leipzig: Akademische Verlagsgesellschaft Geest & Portig K.-G.: 1977) (in German).
4. J. M. Ziman, *Printsipy Teorii Tvyordogo Tela* [Principles of the Theory of Solids] (Moscow: Mir: 1974) (Russian translation).
5. M. A. Stucke, D. M. Dimiduk, and D. M. Hazzledine, *High Temperature Ordered Intermetallic Alloys. V* (Eds. I. Baker and R. Darolia) (Pittsburgh, PA, USA: MRS: 1993), p. 471.
6. *Handbook of Mathematical Functions with Formulas, Graphs and Mathematical Tables* (Eds. M. Abramowitz and I. A. Stegun), Nat'l Bureau of Standards. Appl. Math. Ser. Vol. **55** (Washington, D.C.: U.S. Govt. Printing Office: 1964).
7. B. B. Karpovych and O. B. Borovkoff, *Proc. of Symp. 'Micromaterials Engineering' (Dec. 25–31, 1999)* (Kiev: RVV IMF: 2000), vol. **2**, p. 113 (in Russian).
8. T. M. Radchenko, *Vplyv Uporiadkuvannya Defektnoyi Struktury на Transportni Vlastyvosti Zmishanykh Krystaliv* [Influence of Ordering of the Defect Structure on Transport Properties of the Mixed Crystals] (Thesis of Disser. for Dr. Phys.-Math. Sci.) (Kyiv: G. V. Kurdyumov Institute for Metal Physics, N.A.S.U.: 2015) (in Ukrainian).
9. E. M. Gololobov, V. B. Shipilo, N. I. Sedrenok, and A. I. Dudyak, *Sposob Polucheniya Karbonitridov Metallov* [Production Method of Metal Carbonitrides], Authors' Certificate 722341 SSSR (Published November 21, 1979) (in Russian).
10. V. G. Trubachev, K. V. Chuistov, V. N. Gorshkov, and A. E. Perekos, *Sposob Polucheniya Metallicheskikh Poroshkov* [The Technology of Metallic Powder Production]: Patent 1639892 SU. MKI, B22 F9/02, 9/14 (Otkrytiya i Izobreteniya, **34**, No. 13: 11) (1991) (in Russian).
11. Yu. M. Koval' and V. V. Nemoshkalenko, *O Prirode Martensitnykh Prevrashchenij* [On the Nature of Martensitic Transformations] (Kyiv: 1998) (Prepr./N.A.S. of Ukraine. Inst. for Metal Physics. No. 1, 1998) (in Russian).

Следует применять общепринятые сокращения названий журналов и сборников трудов:
http://www.cas.org/content/references/corejournals; http://rmp.aps.org/files/rmpguapb.pdf; http://images.webofknowledge.com/WOK46P9/help/WOS/A_abrvjt.html; http://www.ams.org/msnhtml/serials.pdf

Обязательным требованием является предоставление дополнительного списка цитированной литературы (References) в **латинской транслитерации** (система **BGN/PCGN**; рекомендуемые транслитераторы: http://www.slovnyk.ua/services/translit.php; http://ru.translit.net/?account=bgn). После транслитерированных названий книг, диссертаций, патентов и пр. надо приводить в квадратных скобках их англоязычный перевод. При транслитерации статей из ННН надо использовать написание Ф.И.О. авторов, приведённое **только** в англоязычном оглавлении соответствующего выпуска, и **официальное** транслитерированное название сборника (см. также сайт).

12. Корректура авторам может быть выслана электронной почтой в виде pdf-файла. На проверку корректуры авторам отводятся 5 рабочих дней, начиная со дня, следующего за датой отправки корректуры. По истечении указанного срока статья автоматически направляется в печать. Исправления следует отметить и прокомментировать в самом pdf-файле либо оформить в виде перечня исправлений и переслать (от имени уполномоченного представителя коллектива авторов) по электронной почте в адрес редакции.

Печатные версии рукописи направляются непосредственно в редакцию ННН по почтовому адресу: **бульвар Акад. Вернадского, 36, каб. 210; 03142 Киев, Украина** либо члену редакционной коллегии (состав редколлегии указан на 2-й странице обложки). Электронный вариант статьи направляется по e-mail: tatar@imp.kiev.ua (с темой, начинающейся словом 'nano').

В соответствии с договорённостью между редакцией ННН и учредителями сборника, редакция считает, что авторы, посылая ей рукопись статьи, передают учредителям и редколлегии право опубликовать эту рукопись на английском (украинском) языке, и просит авторов сразу прикладывать к рукописи

Соглашение о передаче авторского права

Мы, нижеподписавшиеся авторы рукописи «________________», передаём учредителям и редколлегии сборника научных трудов «Наносистеми, наноматеріали, нанотехнології» право опубликовать эту рукопись на английском (украинском) языке. Мы подтверждаем, что эта публикация **не** нарушает авторского права других лиц, учреждений или организаций.

Подписи авторов: ____ (Ф.И.О., дата, адрес, тел., e-mail)

При этом за авторами сохраняются все остальные права как собственников этой рукописи. Авторы могут получить опубликованный выпуск со своей статьёй в редакции сборника по вышеуказанному адресу (тел. №№: **+380 44 4229551, +380 44 4249042**), а также загрузить pdf-файл статьи с сайта сборника: http://www.imp.kiev.ua/nanosys/ru/articles/index.html.

INFORMATION FOR CONTRIBUTORS

Submission of Manuscripts: Papers should be sent to the Executive Managing Editor, Editorial Office, Institute for Metal Physics, N.A.S.U., 36 Academician Vernadsky Boulevard, UA-03142 Kyiv, Ukraine. Manuscripts may also be submitted to a member of the Editorial Advisory Board or to the appropriate Editorial Board Member who is familiar with the research presented.

Submission of a paper to '*Nanosistemi, Nanomateriali, Nanotehnologii*' (i.e., 'Nanosystems, Nanomaterials, Nanotechnologies') will be taken to imply that it represents original work not previously published, it is not being considered for publication elsewhere, and if accepted for publication, it will not be published in the same language without the consent of the Editors and Publisher. It is a condition of acceptance by the Editor of a typescript for publication that the Publishers acquire automatically the copyright in the typescript throughout the world.

Scope of the Collected Scientific Transactions: '*Nanosistemi, Nanomateriali, Nanotehnologii*' (i.e., 'Nanosystems, Nanomaterials, Nanotechnologies'—NNN) is the quarterly multidisciplinary peer-reviewed collected scientific transactions, which publish high-quality work on all aspects of nanoscience and nanotechnology. Currently, transactions stand alone in serving the 'nano' community in providing up-to-date information on all developments and progresses being made in nanoscience and nanotechnology and the future predictions for this extraordinary technology. The topics covered by the transactions relate to all 'nano' related areas of the latest research and recent development works including nanomaterials, characterization tools, fabrication methods, numerical simulation, and theory as well as discussions in the field of nanoscience and technology ranging from basic aspects of the science of nanoscale systems and materials to practical applications of such systems and materials ranging from civil engineering to advanced molecular electronics so promising to transform our everyday technology as well as basic economics. The subjects covered include the following: 1. physical sciences; 2. chemical sciences; 3. life sciences; 4. theoretical and computational science and engineering.

Language: The language of publication may be English or Ukrainian.

Abstract: Each paper requires an English abstract of 200–250 words summarizing the significant coverage and findings.

Keywords and PACS numbers: Up to six keywords and PACS numbers reflecting the content of the contribution should be supplied (see 'Physics and Astronomy Classification Scheme 2010' at http://publishing.aip.org/publishing/pacs/pacs-2010-regular-edition).

Manuscript Preparation: Papers should be typed (in duplicate) with double spacing and wide margins on good quality paper (A4 size). The length of original contributions should not in general exceed 5000 words and 10 figures, and subject review articles should not exceed 22000 words and 60 figures, including tables and diagrams. Authors are urged to arrange the subject matter clearly under headings such as: 1. Introduction, 2. Experimental/Theoretical Details, 3. Results, 4. Discussion, 5. Conclusion, References. Subsections should be identified with section and subsection numbers (such as 6.1. Second-Value Subheading).

References and Notes: Notes are indicated in the text by consecutive superior Arabic numbers (without parentheses). References should be numbered consecutively (in square brackets) throughout the text. The full list should be collected and typed at the end of the paper in numerical order. Listed references should be completed in all details including **DOI** (if available) but excluding article titles in journals. All authors' initials should precede their surnames. Examples of references preparation:

1. T. M. Radchenko and V. A. Tatarenko, *Usp. Fiz. Met.*, **9**, No. 1: 1 (2008) (in Ukrainian); https://doi.org/10.15407/ufm.09.01.001
2. T. M. Radchenko, A. A. Shylau, and I. V. Zozoulenko, *Phys. Rev. B*, **86**: 035418 (2012); https://doi.org/10.1103/PhysRevB.86.035418
3. A. Meisel, G. Leonhardt, and R. Szargan, *Röntgenspektren und Chemische Bindung* [X-Ray Spectra and Chemical Bond] (Leipzig: Akademische Verlagsgesellschaft Geest & Portig K.-G.: 1977) (in German).
4. J. M. Ziman, *Printsipy Teorii Tvyordogo Tela* [Principles of the Theory of Solids] (Moscow: Mir: 1974) (Russian translation).
5. M. A. Stucke, D. M. Dimiduk, and D. M. Hazzledine, *High Temperature Ordered Intermetallic Alloys. V* (Eds. I. Baker and R. Darolia) (Pittsburgh, PA, USA: MRS: 1993), p. 471.
6. *Handbook of Mathematical Functions with Formulas, Graphs and Mathematical Tables* (Eds. M. Abramowitz and I. A. Stegun), Nat'l Bureau of Standards. Appl. Math. Ser. Vol. **55** (Washington, D.C.: U.S. Govt. Printing Office: 1964).
7. B. B. Karpovych and O. B. Borovkoff, *Proc. of Symp. 'Micromaterials Engineering' (Dec. 25–31, 1999)* (Kiev: RVV IMF: 2000), vol. **2**, p. 113 (in Russian).
8. T. M. Radchenko, *Vplyv Uporyadkuvannya Defektnoyi Struktury на Transportni Vlastyvosti*

Zmishanykh Krystaliv [Influence of Ordering of the Defect Structure on Transport Properties of the Mixed Crystals] (Thesis of Disser. for Dr. Phys.-Math. Sci.) (Kyiv: G. V. Kurdyumov Institute for Metal Physics, N.A.S.U.: 2015) (in Ukrainian).
9. E. M. Gololobov, V. B. Shipilo, N. I. Sedrenok, and A. I. Dudyak, *Sposob Polucheniya Karbonitridov Metallov* [Production Method of Metal Carbonitrides], Authors' Certificate 722341 SSSR (Published November 21, 1979) (in Russian).
10. V. G. Trubachev, K. V. Chuistov, V. N. Gorshkov, and A. E. Perekos, *Sposob Polucheniya Metallicheskikh Poroshkov* [The Technology of Metallic Powder Production]: Patent 1639892 SU. MKI, B22 F9/02, 9/14 (Otkrytiya i Izobreteniya, **34**, No. 13: 11) (1991) (in Russian).
11. Yu. M. Koval' and V. V. Nemoshkalenko, *O Prirode Martensitnykh Prevrashchenij* [On the Nature of Martensitic Transformations] (Kyiv: 1998) (Prepr./N.A.S. of Ukraine. Inst. for Metal Physics. No. 1, 1998) (in Russian).

Journal title abbreviations should conform to generally accepted styles:
http://www.cas.org/content/references/corejournals; http://rmp.aps.org/files/rmpguapb.pdf;
http://images.webofknowledge.com/WOK46P9/help/WOS/A_abrvjt.html;
http://www.ams.org/msnhtml/serials.pdf

Equations and Formulae: Formulas in the text should be inserted by MathType, which is fully compatible with MS Office 2003, 2007, 2010.

Tables: Number tables consecutively with arabic numerals and give a clear descriptive caption at the top.

Figures: All figures should be numbered with consecutive arabic numerals, have descriptive captions and be mentioned in the text. Keep figures separate at the end of the text and clearly label each figure with author's name and figure number. The labels at axis should contain the designation (or notation) of quantities and their units.

Preparation: Figures submitted (black-and-white or greyscale strongly recommended) must be of a high enough standard for reproduction with 300–600 dpi resolution (including half-tone illustrations). Redrawing or retouching of unusable figures will be charged to the authors.

Colour Plates: Whenever the use of colour is an integral part of the research, or where the work is generated in colour, the Transactions will publish the colour illustrations with charge to the author. Reprints in colour will carry a surcharge. Please write to the Publisher for details.

Submission of Electronic Text: Authors should also submit papers by e-mail or on a CD (in addition to hard copy with figures). The file should be saved in the native formats of the Microsoft Word 2003, 2007 or 2010 with a name consisting the name of the first author, for example, Smirnov.doc. The electronic form of figures (graphics files in TIFF, EPS or JPEG formats preferably and with name consisting the name of the first author also, for example, Smirnov_fig2a.tiff) should be planned so that they reduce to 12.7 cm column width (or less), and keep them separate from the text file. It is necessary to submit additionally all the **figures** within the format of the program, in which they were created.

Proofs: In a special emergency, contributors may receive page proofs for correction by e-mail as a PDF document. In that case, these must be returned to Kyyiv office (tatar@imp.kiev.ua) with subject beginning by word 'nano' within 120 hours of receipt.

Page Charges: There are no page charges to individuals or institutions.

Reprints: Hard-copy reprints provided to the first-named author of each paper may be ordered by completing the appropriate form sent with proofs. Authors can de-archive a PDF version of their published article from Editorial Office site: http://www.imp.kiev.ua/nanosys/ru/articles/index.html.

Further Information: All questions arising after the acceptance of manuscripts, especially those relating to reprints, should be directed to Executive Managing Editor, Editorial Office, G. V. Kurdyumov Institute for Metal Physics, N.A.S.U., 36 Academician Vernadsky Blvd., UA-03142 Kyiv, Ukraine. Fax: +380 44 4242561, e-mail: tatar@imp.kiev.ua (with subject beginning by word 'nano').

We ask the authors to apply with their manuscript

Copyright Transfer Agreement

We, the undersigned authors of the manuscript '____', transfer to the founders and the Editorial Board of the collected scientific transactions 'Nanosistemi, Nanomateriali, Nanotehnologii' the right to publish this manuscript in English language (or in the Ukrainian translation). We confirm that publication of this manuscript will not infringe a copyright of other persons, institutions or organizations.

Author(s):____
(Last Name, First Name, Affiliation)

Correspondence Address:____
Phone and e-mail: ____

____________________ ________________
(Signature) *(Date)*

ИЗДАТЕЛЬСКАЯ ЭТИКА

И ПРЕДОТВРАЩЕНИЕ НЕДОБРОСОВЕСТНОЙ ПРАКТИКИ ПУБЛИКАЦИЙ

Редакционная коллегия сборника научных трудов «*Наносистеми, наноматеріали, нанотехнології*» следует этическим нормам, принятым международным научным сообществом, и делает всё для предотвращения любых нарушений их. В своей деятельности редакция опирается на рекомендации Комитета по этике научных публикаций (http://publicationethics.org).

Обязанности редакции

- Все представленные статьи рецензируются экспертами в данной области.
- При рассмотрении статьи учитываются её соответствие предметной области, обоснованность, значимость, оригинальность, читабельность и язык (правописание).
- По результатам рецензирования статья может быть принята к опубликованию без доработки, принята с доработкой или отклонена.
- Отклонённые статьи повторно не рецензируются.
- Статьи могут быть отклонены без рецензии, если они очевидным образом не подходят для публикации.
- Редакция принимает решение о публикации, руководствуясь политикой журнала, с учётом действующего законодательства в области авторского права.
- Не допускается к публикации информация, если имеется достаточно оснований полагать, что она является плагиатом.

При наличии каких-либо конфликтов интересов (финансовых, академических, личных) все участники процесса рецензирования должны сообщить об этом редколлегии. Все спорные вопросы рассматриваются на заседании редколлегии.

Принятые к опубликованию статьи размещаются в открытом доступе на сайте сборника; авторские права сохраняются за авторами.

Этические принципы в деятельности рецензентов

- Рецензенты оценивают статьи по их содержанию, безотносительно к национальности, полу, сексуальной ориентации, религиозным убеждениям, этнической принадлежности или политическим убеждениям авторов.
- Сотрудники редакции не должны сообщать какую-либо информацию о поступивших статьях лицам, не являющимся рецензентами, авторами, сотрудниками редакции и издательства.
- Рецензии должны быть проведены объективно. Персональная критика автора неприемлема. Рецензенты обязаны обосновывать свою точку зрения чётко и объективно.
- Рецензирование помогает издателю принимать решение и посредством сотрудничества с рецензентами и авторами улучшить статью.
- Материалы, полученные для рецензии, являются конфиденциальными документами и рецензируются анонимно.
- Рецензент также обязан обращать внимание редактора на существенное или частичное сходство представленной статьи с какой-либо иной работой, с которой рецензент непосредственно знаком.

Принципы, которыми должны руководствоваться авторы научных публикаций

- Авторы статей должны предоставлять точный отчёт о выполненной работе и объективное обсуждение её значимости.
- Авторы статьи должны предоставлять достоверные результаты проведённого обзора и анализа исследований. Заведомо ошибочные или сфальсифицированные утверждения неприемлемы.
- Статья должна содержать достаточное количество информации для проверки и повторения экспериментов или расчётов другими исследователями. Мошеннические или заведомо неправдивые заявления приравниваются к неэтичному поведению и являются неприемлемыми.
- Авторы могут предоставлять оригинальные регулярные и обзорные работы. При использовании текстовой или графической информации, полученной из работ других лиц, обязательно необходимы ссылки на соответствующие публикации или письменное разрешение их авторов.
- Подача статьи более чем в один журнал расценивается как неэтичное поведение и является неприемлемой.
- Авторство должно быть ограничено теми, кто внёс значительный вклад в концепцию, разработку, исполнение или интерпретацию заявленного исследования.
- Источники финансовой поддержки публикуемого исследования могут быть указаны.

PUBLICATION ETHICS

AND MALPRACTICE STATEMENT

The Editorial Board of the Collected Scientific Transactions ‘*Nanosistemi, Nanomateriali, Nanotehnologii*’ (i.e., ‘Nanosystems, Nanomaterials, Nanotechnologies’) follows ethics norms accepted by international scientific community and makes every endeavour to prevent any infringements of the norms. The Editorial Board follows the guidelines of the Committee on Publication Ethics (http://publicationethics.org).

Duties of Editors

- All submitted papers are subject to strict peer-review process by reviewers that are experts in the area of the particular paper.
- The factors, which are taken into account in reviewing process, are relevance, soundness, significance, originality, readability, and quality of language.
- The possible decisions include acceptance, acceptance with revisions, or rejection.
- If authors are encouraged to revise and resubmit a submission, there is no guarantee that the revised submission will be accepted.
- Rejected articles will not be re-reviewed.
- Articles may be rejected without review, if they are obviously not suitable for publication.
- The paper acceptance is constrained by such legal requirements as shall then be in force regarding libel, copyright infringement, and plagiarism.

When a conflict of interests arising, all the participants of reviewing process should inform the Editorial Board. All the contentions questions are considered in the Board meeting.

The accepted papers are allocated in open access on the journal site; copyrights reserved.

Duties of Reviewers

- The reviewers evaluate manuscripts for their intellectual content without regard to race, gender, sexual orientation, religious belief, ethnic origin, citizenship, or political philosophy of the authors.
- The staff must not disclose any information about a submitted manuscript to anyone other than the corresponding author, reviewers, other editorial advisers, and the Publisher, as appropriate.
- Reviews should be conducted objectively. Personal criticism of the author is inappropriate. Referees should express their views clearly with supporting arguments.
- Peer review assists the Publisher in making editorial decisions and through the editorial communications with the experts from the scientific board and the author may assist the author in improving the paper.
- Manuscripts received for review are treated as confidential documents and are reviewed by anonymous staff.
- A reviewer should also call to the Publisher's attention any substantial similarity or overlap between the manuscript under consideration and any other published paper of which they have personal knowledge.

Duties of Authors

- Authors of contributions and studies research should present an accurate account of the work performed as well as an objective discussion of its significance.
- A paper should contain sufficient details and references to permit others to replicate the work. Fraudulent or knowingly inaccurate statements constitute unethical behaviour and are unacceptable.
- The authors should ensure that they have written original regular or entirely review works, if the authors have used the work and/or words of others that this has been obligatory and appropriately cited or quoted.
- Submitting the same manuscript to more than one publication concurrently constitutes unethical publishing behaviour and is unacceptable.
- Authorship should be limited to those who have made a significant contribution to the conception, design, execution, or interpretation of the reported study.
- Sources of financial support for the reported results can be specified.

Наносистеми, наноматеріали, нанотехнології
Nanosistemi, Nanomateriali, Nanotehnologii
2021, т. 19, № 4, сс. 779–798

PACS numbers: 61.43.Gt, 68.37.-d, 68.55.J-, 81.05.Rm, 81.16.Pr, 81.20.Ev, 81.20.Wk

Development of Technologies for Obtaining Metal Powders (Iron) from Production Waste and Studying Their Properties

Kh. M. Mamarakhimov and Kh. Kh. Sirojev

Academy of the Armed Forces of the Republic of Uzbekistan,
2, Parkent Str.,
UZ-100023 Tashkent, Uzbekistan

The article discusses the modern methods of fabrication of iron powders, carries out their classification, analyses the analytical data about powders made from various types of raw materials. The kinetic regularities of the reduction of iron oxides are analysed from the point of view of the adsorption–autocatalytic theory. The structure and mechanical properties of iron powders are considered. The morphology, structure, phase and elemental compositions of the mill scale of the Uzbek Metallurgical Plant are analysed. Technology for the recovery of scale is developed, including the following stages: drying at 250–340°C, grinding in a ball mill for 2 hours, magnetic separation, sieving through a 40-mesh sieve, mixing the charge, recovery for 2 hours in H_2 at the temperatures: 650–700°C (I zone), 950–1000°C (II zone).

У статті розглядаються сучасні методи виготовлення залізних порошків, проводиться їх класифікація, аналізуються аналітичні дані про порошки, виготовлені з різних видів сировини. Кінетичні закономірності відновлення оксидів Феруму аналізуються з точки зору адсорбційно-автокаталітичної теорії. Розглянуто структуру та механічні властивості порошків заліза. Проаналізовано морфологію, структуру, фазовий і елементний склади вторинної жужелиці Узбецького металурґійного заводу. Розроблено технологію відновлення жужелиці, що включає наступні етапи: сушка при 250–340°C, шліфування в кульовому млині протягом 2 годин, магнетне збагачення (відокремлення), просіювання через 40-коміркове сито, змішування шихти, відновлення протягом 2 годин у H_2 за температур у 650–700°C (I зона) і 950–1000°C (II зона).

Key words: iron powder, kinetics, reduction, iron oxide, adsorption, structure, mechanical properties.

Ключові слова: залізний порошок, кінетика, виділення металу з руди, оксид Феруму, адсорбція, структура, механічні властивості.

(Received 30 December, 2020; in revised form, 8 January, 2021)

1. INTRODUCTION

The most important task of the economic and social development of the Republic of Uzbekistan is the acceleration of scientific and technological progress in all branches of industrial production through the use of new materials, progressive technologies, and processes that ensure the predominant output of products with a decrease in material consumption per unit of consumer properties of machinery and equipment.

Powder metallurgy, which is one of the promising technologies of metallurgical and machine-building production, is of great importance in solving the problems posed, the methods of which make it possible not only to create materials with new quality and strength characteristics, but also to introduce waste-free or low-waste technologies for the production of powder metal materials and products of various appointments based on them.

If in the manufacture of parts by traditional methods (casting, forging, stamping followed by mechanical processing) the metal utilization factor is 0.4–0.6, then powder metallurgy allows increasing it to 0.95–0.97 [1, 2].

Powder metallurgy processes, as a rule, proceed at temperatures lower than in large metallurgy (0.7–0.8 from the melting point), thereby providing energy savings. The energy consumption of powder metallurgy is 29 MJ/kg and is significantly lower than the energy consumption of foundry (34–38 MJ/kg), cold stamping (41 MJ/kg), hot stamping (46–49 MJ/kg), cutting (66–82 MJ/kg) [4, 5].

Powder metallurgy has one more advantage—environmental one, because it is not associated with the release of harmful products that pollute the environment.

A feature of powder metallurgy—the possibility of creating compact materials from mixtures of powders, bypassing the stages of melting and casting, opens up broad prospects for the development of new powder metal materials with a variety of properties inherent both in components of a metallic and non-metallic nature, and arising from the interaction of heterogeneous nanodispersed systems.

Using the methods of powder metallurgy, it is possible to obtain composite products from so-called ‘pseudo-alloys’, the components of which either sharply differ in melting temperature, or do not fuse at all (tungsten–copper, tungsten–silver, copper–molybdenum, *etc.*), but are widely used in electrical and radio engineering, electronics.

Powder metallurgy methods have created a large group of new composite materials, which include dispersion-hardened, antifriction and frictional, cermets, fibre-reinforced materials, *etc.* Structurally, this group of materials is a plastic metal matrix that cements the inclusions of the hardening phase.

The development of fundamental and theoretical foundations and new technologies created the prerequisites for expanding the range and scope of powder products. If 20–25 years ago the bulk of powder products was represented by parts of friction units (antifriction and frictional), now more than 60% of manufactured parts are structural, operating under conditions of complex stress and shock exposure, elevated temperatures, corrosive environments, *etc.*, when high strength, density, impact strength, special properties are required from parts [6, 7].

2. THE RELEVANCE OF THE PROBLEM

At present, powder metallurgy is a rapidly developing industry, including the production of powders, metals, and alloys with particles of different dispersion, granules, threads, and other shapes; production of various machine parts and devices, tools, and special-purpose items; development and creation of metallic powder materials and non-metallic substrates; strengthening and restoration of machine parts and devices, as well as imparting increased mechanical or special physicochemical properties to the surface of products by methods of coating with powder composite materials.

In this regard, new promising processes for obtaining powder products are being introduced into practice, as well as new types of high-performance equipment; great attention is paid to scientific developments in the field of powder metallurgy and materials based on them [8].

Among the technological methods for the production of structural products, the method of cold pressing in closed moulds with subsequent sintering has the greatest application [9, 10].

The advantage of obtaining parts in this way is, first of all, high productivity and the possibility of their mass production without using or with the use of minor mechanical processing, which reduces waste and metal losses by 10–15 times in the manufacture of even products with complex shapes [11, 12].

This technology retains inexhaustible possibilities for the creation of new materials based on iron powders with the additional use of alloying and heat treatment methods [13, 14].

In recent years, hot pressing technology has been rapidly developing, which consists of the simultaneous pressing and sintering of powders, which makes it possible to obtain a dense product with a certain level of mechanical properties. With hot pressing, it is possible to significantly reduce the temperature process and thereby slow down the recrystallization process that ultimately leads to the formation of a fine-grained structure and an increase in mechanical properties in the low-temperature region [15, 16].

In contrast to conventional sintering, the methods of hot moulding of blanks and products are carried out on equipment that is more complex, require special preparation of the tooling, and are inferior to it in performance. However, the effect in terms of strength properties and wear resistance is fully justified from both the technical and economic points of view. Methods of hot working with pressure are especially effective in the manufacture of large products, using difficult to sinter or substandard powders when it is necessary to obtain high density and strength of products, which are unattainable under the conditions of conventional sintering.

Large losses of metal occur from corrosion and wear of structures and machine parts. In this regard, a new direction of powder metallurgy is acquiring great importance in increasing wear resistance and corrosion resistance by applying powder materials to the surface of products [17, 18].

Various methods of applying layers (surfacing, plasma spraying, electrophoresis, vapour deposition, detonation spraying, *etc.*), as practice shows, due to the small thickness of the coating, cannot always be effectively used to protect the working surfaces of equipment parts, tools and technological equipment operating in hydroabrasive and aggressive environments, at high pressures and elevated temperatures. Therefore, there is a need for a broad development of work on the creation and implementation of technologies for applying layers of more than 2 mm to ensure reliably a long service life of equipment units.

In this respect, powder metallurgy methods are promising (centrifugal, sintering, pressing with subsequent sintering, electrical contact sintering, hot pressing, *etc.*), which make it possible to obtain layers with high physical, mechanical and operational properties, and a given structure.

Among these methods, preference should be given to the hot pressing method, since the application of pressure accelerates the compaction process and the formation of strong contacts of the powder coating with the substrate.

However, to solve the problem of strengthening the working surfaces of machine parts and mechanisms by applying layers by hot pressing, it is necessary to study the physical and mechanical properties of powder layers on a compact basis, to identify the mechanisms of compaction and formation of a joint depending on the parameters of hot pressing (temperature, pressure, isothermal holding).

Thus, based on the analysis of literature data, it can be concluded that the development of new technological solutions for the processing of iron powders obtained from production of waste is possible only after a wide range of studies of their morphology, structure, physicochemical and technological properties, since, ultimately, they determine the conditions for forming and sintering, as well as the mechanical and operational characteristics of materials based on iron powders.

To develop technology for producing layers from powder materials, it is necessary to study the kinetics of changes in the density of the layer and the strength of its connection with the substrate, depending on the type of starting materials and the main parameters of hot pressing: temperature, pressure, isothermal holding.

3. RESEARCH METHODS

Metallographic, x-ray phase, and electron-microscopy analyses; test for mechanical properties.

4. STUDY RESULTS

Methods for Obtaining Metal Powder Materials. To obtain iron powders, a wide variety of methods are used that is explained not only by the need for powders for various purposes but also by the search for technologies, which would ensure the production of the cheap and high-quality powders [19, 20]. The classification of methods for producing iron powders is shown in Fig. 1.

In terms of composition, all iron powders can be classified into two groups: low-carbon (iron powders proper) and alloyed iron powders [21–23].

The first group should include iron powders containing permanent, hidden, and accidental impurities. Permanent impurities include sulphur, phosphorus, manganese, and silicon, which are present in any steel, scale, or ore that can be the starting material for producing iron powder. The content of these elements in powders is usually in the range, wt.%: sulphur 0.01–0.04, phosphorus 0.01–0.05, manganese 0.3–0.7, silicon 0.2–0.4.

Latent impurities (oxygen, hydrogen, nitrogen) present in the feedstock for the production of iron powder in various quantities, ranging from fractions of a percent in steels, and ending in percent in scale and ores and remaining in small amounts in iron powders.

Accidental impurities are entering the starting materials for the production of iron powders from steels, ores, scrap, and scrap metal.

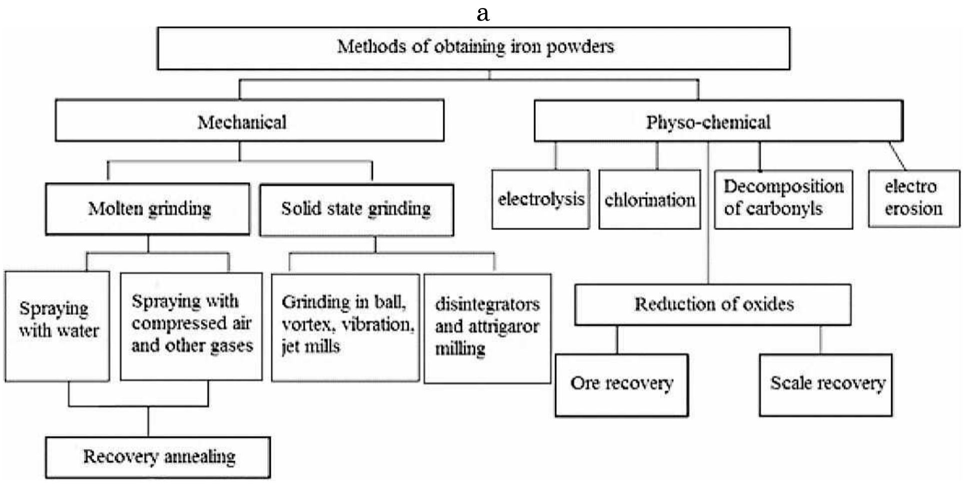

Fig. 1. Classification of methods for producing iron powders.

The presence of the listed impurities is an inevitable consequence of the technological process of producing iron powder from carbon steels, scales, and ores.

The second group should include iron powders containing alloying elements in quantities exceeding impurity and introduced into the powder particles by one of the following methods:

1. alloyed iron powders obtained by grinding or spraying alloy steels, as well as their waste, followed by reduction annealing of raw materials.
2. alloyed iron powders obtained by surface alloying of powder particles.
3. naturally alloyed iron powders obtained by reduction of naturally alloyed ores, pulverized raw materials, or mill scale of alloyed steels, or from shavings formed during the mechanical processing of these steels.

Powders of this group obtained by various methods have the following composition, mass.%: iron 98.0–99.0, oxygen 0.02–1.0, carbon 0.005–0.12, silicon 0.006–0.64, phosphorus 0.001–0.5, manganese 0.002–0.03, and sulphur 0.005–0.003.

For comparison, we note that the average content of impurity elements in iron powders and cast steels (hot-rolled, carbon engineering) is approximately the same, except for the manganese content, which in steels is brought to 0.9 mass.%.

Production of Iron Powders by the Reduction Method. A comparison of methods for the production of the iron powder allows us to conclude that the oxide reduction process is the most promising method for the production of cheap universal-purpose powder. Given the high productivity of the recovery process, the use of cheap raw materials and high-quality reductants, ensuring the completeness of recovery, correct engineering design, and full automation of technological cycles, it can be argued that the recovery process is the most profitable from a technical and economic point of view for obtaining cheap iron powders [24, 25].

The development of the industrial production of iron powders by the reduction method was preceded by the development of the theoretical foundations of this process.

The kinetics of the reduction of iron oxides were studied, the equilibrium constants of the ongoing reactions were determined, and kinetic equations were derived, taking into account the influence of factors such as the rate of diffusion and chemical reactions on the process rate [26, 27].

The existing methods for the reduction of iron oxides are classified according to the reductant used, the type of charge and the method of feeding it into the reduction zone, the pressure of the reducing gases, and the process temperature.

The reduction can be both an independent technological process for obtaining iron powders (the raw material is scale, ore), and the final part of the technological process in the production of powders by crushing steel melts with water or compressed air, in which iron particles are oxidized.

The process of reduction of iron oxides with hydrogen can be described by the following chemical reactions:

$$3Fe_2O_3 + H_2 = 2Fe_3O_4 + H_2O + 5.2\ \text{kcal},$$

$$Fe_3O_4 + H_2 = 3FeO + H_2O - 15.2\ \text{kcal},$$

$$FeO + H_2 = Fe + H_2O - 6.7\ \text{kcal},$$

$$Fe_3O_4 + 4H_2 = 3Fe + 4H_2O - 43.4\ \text{kcal}.$$

According to the adsorption–autocatalytic theory, the reduction process consists of the adsorption of a reducing gas on the oxide surface, the destruction of the oxide crystal lattice, the formation of intermediate oxide phases, and, at the last stage, the metal phase, desorption of gaseous reaction products from the surface of particles [28].

The detachment of oxygen atoms from oxides during their reduction is thermodynamically easier than dissociation because, in the course of the reaction, the energy of binding of oxygen with a reducing agent is released. As a result, either the activation energy of the reaction decreases, and the process is accelerated at a given temperature, or the reaction becomes possible at lower temperatures.

The acceleration of the chemical interaction of oxides with a reducing agent is also stimulated because the boundary between the oxide and the metal reduced from it in most cases is a catalyst for the process, as a result of which, it becomes autocatalytic one. For this reason, the dependence of the free energy of the formation of oxides on temperature makes it possible to estimate the relative thermodynamic strength of these oxides upon reduction [29].

General Principles for the Recovery of Mill Scale. One of the urgent problems of ferrous metallurgy is the use of secondary raw materials and production wastes in the national economy, which are not used in the smelting of high-quality metal in open-hearth and electric arc furnaces.

Such production wastes include scale, which is formed during the rolling of boiling carbon steels, containing 70–75% iron in the form of oxides. In the rolling shops of metallurgical plants, tens of thousands of tons of scale are accumulated, the chemical composition of which depends on the operation of the rolling technological process, at which it was formed. The purest scale is formed during the cooling of rolled products in cold spans; it is not clogged with oxides difficult to recover, does not require magnetic separation, and is cheap and enough clean raw material source for obtaining iron powders.

Usually, mill scale is heavily contaminated with mechanical impurities, unstable in particle size distribution and bulk density, which greatly complicates its use. Therefore, the scale is first subjected to screening to separate large mechanical inclusions (14 mm^3) from it, then dried at a temperature of 350–500°C. In this case, the scale is freed from oils and other combustible impurities [30]. A dried scale with a moisture content of no more than 0.5% is subjected to magnetic separation to remove non-metallic inclusions, mainly, silica. Then, the scale is milled in mills to a particle size of < 1.0 mm.

For the reduction of scale with hydrogen, continuous muffle or tube furnaces with external heating are used. The dross is placed in trays or boats that move continuously through the hot zone of the oven. Hydrogen is supplied from the side of the refrigerator and the counter-flow principle ensures the most complete recovery. The time required for complete-scale recovery depends on its type, particle size, layer thickness, temperature, pressure, and humidity of hydrogen, and other factors.

According to one of the options [31], the reduction is carried out in a tubular two-zone furnace at 650–700°C (I zone) and 700–800°C (II zone).

In another embodiment [32], the reduction is carried out in a continuously operating conveyor furnace at 980°C. The recovery time is of about 5 hours, and furnace productivity is 90 kg/h. There is a known method of reducing iron oxides by converted natural gas at 1100–1150°C [33].

It is proposed to make briquettes from scale and carry out reduction with natural gas conversion products at 900–950°C (stage 1). Then, the obtained sponge iron (the degree of recovery is 90–96%) is ground and additional reduction is carried out in hydrogen at 950–1000°C (stage 2) [34].

The work [35] presents the results of experimental studies of the reduction of iron oxides with wet hydrogen at normal pressure and isothermal conditions in the range 390–500°C. As a result of experiments, it was found that the rate of reduction in the kinetic region of reaction at normal pressure linearly depends on the concentration of water vapour in the gas mixture at their low content, which can be explained by a simple blocking of the active surface of the solid phase by water molecules.

Complete reduction of fine fractions of iron oxides with moist hydrogen is practically impossible due to the adsorption of water vapour on their surface. Therefore, the reduction of iron oxides is advisable to be carried out at moderate temperatures with completely dried hydrogen in installations operating on the counter-flow principle.

Experiments have shown that under these conditions, fine oxide particles with a large specific surface area also have a high reduction rate at low temperatures.

At the same time, an increase in the specific surface area of particles by several times does not entail the same increase in the reduction rate, which indicates a large influence of the internal porosity of oxides on the reduction process.

Besides, an increase in the reduction temperature to 600–800°C leads to a sharp decrease in the rate of the process due to recrystallization of the metal powder, and the time required for the complete reduction of fine oxides (< 0.05 mm) with hydrogen is longer than the time required for the recovery of larger particles of 0.3–0.4 mm.

Study of the Morphology, Structure, Phase and Elemental Compositions of Mill Scale of the Uzbek Metallurgical Plant. Considering that steel at the plant is smelted from scrap metal, one should expect the presence of a wide range of impurity elements in various concentrations. Therefore, comparative studies of the morphology and chemical composition of mill scale and iron oxide grade pure for analysis (P.F.A.) were presented.

It has been shown that iron oxide particles have a generally spherical shape, which is typical for α-Fe_2O_3 [16]. The scale understudy is granules of various sizes (up to 10 mm) of arbitrary shape

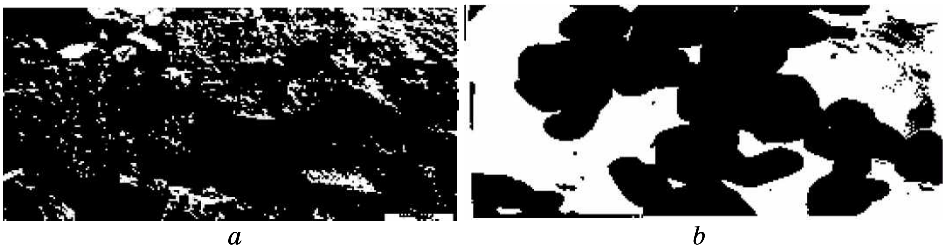

Fig. 2. Microstructure of the initial scale (*a*, ×150) and electron-microscopy structure of milled scale (*b*, ×17.500).

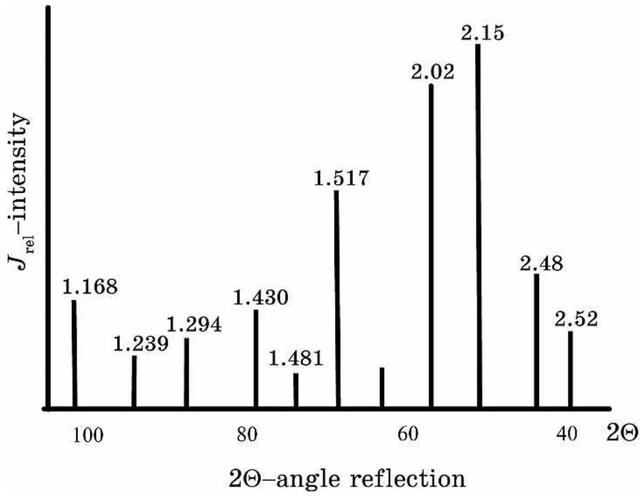

Fig. 3. Section of the x-ray diffraction pattern of mill scale.

with a porous structure (Fig. 2) [16].

As can be seen from the x-ray diffraction pattern (Fig. 3), the scale contains wüstite (FeO) [0.248, 0.215, 0.151, 0.129, 0.123 nm^3], magnetite (Fe_3O_4) [0.248, 0.148 nm^3], and there are traces of hematite (α-Fe_2O_3) [0.252, 0.148, 0.110 nm^3] (Fig. 3).

A comparison of the chemical composition of the scale of the Uzmetkombinat with the results of the analysis of the scale of the Orsk-Khalilovsk metallurgical plant (Table 1) indicates a significant difference in their chemical composition.

The scale of Uzmetkombinat is a powder of low-alloy steels.

Before the investigation, the scale was dried at 300–400°C, grinding in a ball mill at a ratio of the mass of raw materials and steel balls of 1:1 for 1.3 and 6 hours.

After grinding, magnetic separation of the powder was carried out on a belt transport shown in Fig. 4.

TABLE 1. The average chemical composition of the scale of JPA 'Uzmetkombinat' and Orsk-Khalilovskiy metallurgical plant.

Elements	Fe total	Si	Al	$x\cdot10^{-3}$								
				Ca	Mg	Ba	Sr	Mn	Ti	S	Nb	Ga
Scale of Uzmetkombinat content, wt.%	72.0–5.0	1.5	1.0	80	60	20	70	300	10	80	4	0.4
Elements	$x\cdot10^{-3}$											
	Cr	Ag	Cu	Pb	Zb	Ni	Co	Mo	Sn	Ge	La	Zr
Scale of Uzmetkombinat content, wt.%	30	20	400	6	8	100	10	10	3	10	10	5
Elements	Fe total	Si	Al	$x\cdot10^{-3}$								
				Ca	Mg	Ba	Sr	Mn	Ti	S	Nb	Ga
Scale of Orsk-Khalilovsky Metallurgical Combine content, wt.%	96.01	0.85	—	20	—	—	—	67		0.7	—	20
Elements	$x\cdot10^{-3}$											
	Cr	Ag	Cu	Pb	Zb	Ni	Co	Mo	Sn	Ge	La	Zr
Scale of Orsk-Khalilovsky Metallurgical Combine content, wt.%	25	—	—	—	—	25	—	—	—	—	—	—

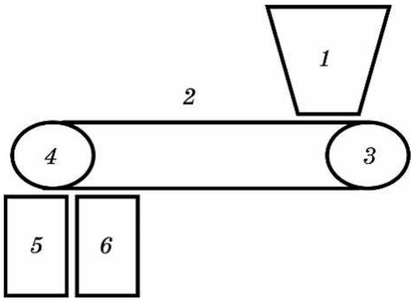

Fig. 4. Installation of magnetic separation.

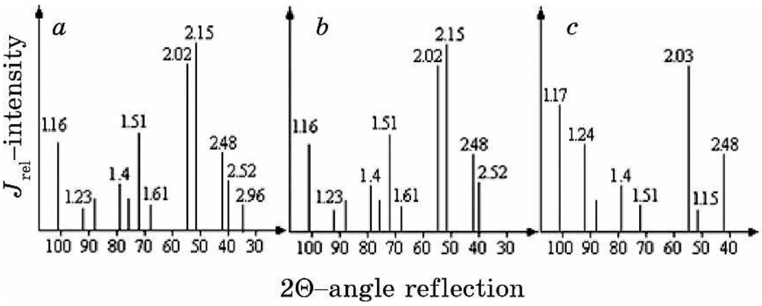

Fig. 5. X-ray diffraction pattern of reduced iron powder at different temperatures: *a*—600°C; *b*—700°C; *c*—800°C.

The scale powder is loaded in portions into the receiving hopper (1), from which it is poured out by gravity in a layer of 0.5–1.0 cm onto a conveyor belt (2) made of thin vacuum rubber. The conveyor belt is driven by two rollers (3) and (4), one of which (4) is a permanent magnet. The rolls are driven by an electric motor with a drive. The powder, moving along the conveyor, reaches the opposite end, and its non-magnetic fraction is dumped down into the hopper (5), and the magnetic fraction, as the effect of the magnetic field weakened, is dumped into the hopper (6). Together with the particles of the magnetic fraction, 0.05–0.1 mass.% of non-magnetic particles are entrained by mechanical adhesion, but their concentration does not significantly affect the quality of the final product.

The average chemical composition of the scale is given in the Table 1.

After magnetic separation, the powder is poured into steel and graphite boats in weights of 0.5, 1.0, 1.5 kg. In this case, the height of the powder layer was of 10–30 mm.

The reduction was carried out in a stream of hydrogen in a single-zone industrial furnace at 600, 700, and 800°C for 1 hour.

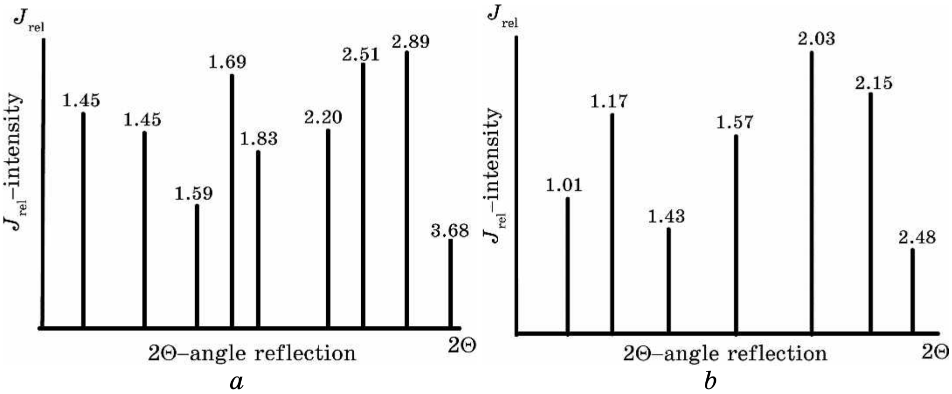

Fig. 6. X-ray diffraction pattern of initial iron oxide (*a*) and reduced iron at 800°C (*b*) for 1 hour.

The reduction of scale at 600°C leads to the formation of α-Fe (≅ 40%), FeO (≅ 38%), [0.248, 0.153 nm^3] FeO* (≅ 11%), Fe_3O_4 [0.297, 0.161 nm^3] (≅ 11%). The total iron content in the samples is ≅ 80 wt.% (Fig. 5, *a*). The reduction of scale at 700°C forms the system α-Fe (≅ 55%), Fe_2O_3 [0.250, 0.116 nm^3], FeO [0.151, 0.123 nm^3] (≅ 23%), FeO* (≅ 15%), Fe_3O_4 [0.161 nm^3] (≅ 7%). The total iron content in the samples is ≅ 87 wt.% (Fig. 5, *b*). The reduction of scale at 800°C leads to the formation of the α-Fe (≅ 70%), FeO [0.151, 0.124 nm^3] (≅ 30%), FeO* (≅ 30%). The total iron content in the samples is ≅ 94 wt.% (Fig. 5, *c*).

The FeO* phase present in all samples contains 48.5% Fe and corresponds to the formula $Fe_{0.35}O$ and corresponds to the preparation obtained by the decomposition of FeC_2O_4 at 800°C (ASTM, 6-0711) [37]. FeO* in terms of *d*(*hkl*) values differs from FeO present in the initial scale and is, apparently, a solid solution FeO–Fe_3O_4 [0.368, 0.251, 0.220, 0.183, 0.163, 0.153 nm^3] (based on FeO), which is usually written as Fe_xO ($x > 0$). To compare the results obtained, we also analysed samples of iron oxide (P.F.A.) reduced at 800°C (Fig. 6, *a*).

However, due to the high chemical activity of the obtained ultragranular iron powders, the presented diffractogram (Fig. 6, *b*) determines the phase composition of the already oxidized product. It includes α-Fe, FeO [0.248, 0.215 nm^3] and Fe_3O_4.

The spectral analysis of the samples obtained by reducing the scale at 700°C is presented in Table 2.

A comparison of the results obtained with the results of the analysis of the content of impurities in the initial scale (Table 1) shows that its reduction at 700°C leads to an increase in the concentration of practically all the elements present. However, in reality, this is

TABLE 2. Average chemical composition (wt.%) of the iron powder obtained by reduction of scale at 700°C.

Element	Si	Al	Ca	Mg	Ba	Sr	Mn	Ti	Cr	Ag	Pb
Mass.%	2.0	2.0	0.06	0.2	0.02	0.02	0.50	0.03	0.08	0.0001	0.006
Element	Zb	Ni	Co	Mo	Sn	Nb	La	Zr	Ga	Cu	other
Mass.%	0.008	0.20	0.01	0.01	0.003	0.007	0.007	0.004	0.0004	0.15	—

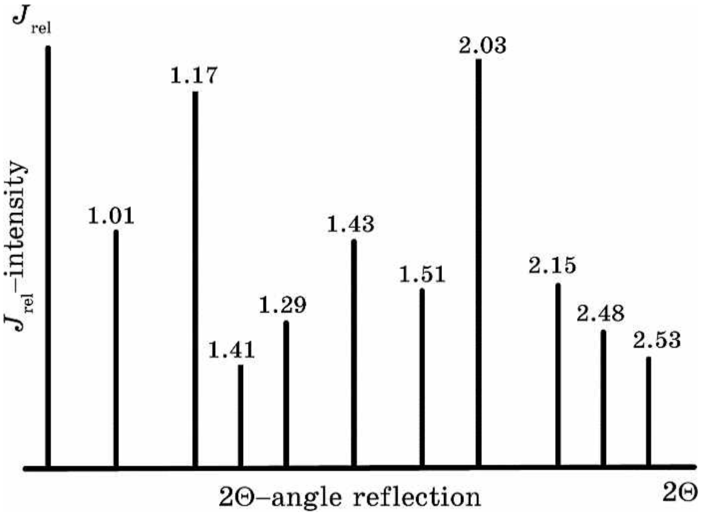

Fig. 7. X-ray diffraction pattern of iron samples obtained by reducing scale in two stages: *1*—650°C (1 hour); *2*—800°C (1 hour).

due to the analysis methodology, which does not take into account the reduction in the volume of dross after its recovery. Nevertheless, it can be argued that under the selected reduction conditions, no significant refining of the product occurs [38].

As can be seen in Fig. 2, the results of electron-microscopy studies of the reduction products of scale, milled to different degrees of fineness (10–500 μm), showed that finer iron powders are obtained from more dispersed scale, the pyrophoricity of which increases with a decrease in the reduction temperature that is manifested in terms of the thickness of the oxide film on the surface of particles.

Under the accepted experimental conditions, the lower layers of the scale powder are not completely restored due to insufficient recovery time (600 and 700°C) or the difficulty of hydrogen penetration due to the formation of a dense surface crust by sintered iron particles (at 800°C).

Based on the data obtained, it was concluded that the reduction process must be carried out in two stages at 600–700°C and 800°C. It is necessary to add a baking powder to the scale composition—soot or iron powder.

Based on these prerequisites, a series of experiments were carried out to restore scale, ground in a ball mill for 1 hour, in a two-phase furnace at temperatures: I zone—650°C; II zone—800°C.

For the study, steel and graphite boats were used, and the scale powder was mixed with 5% graphite or 5–10% iron powder. The charge was poured both into clean boats and onto a thin layer of iron powder.

The results obtained allowed us to conclude that under the selected reduction conditions, soot practically does not contribute to the reduction process and remains in the charge in a free state.

The best option is to recover the charge, which consists of a mixture of scale (90%) and iron (10%) powders. However, the iron powder sticks to the steel boat. Therefore, in terms of technology, preference should be given to graphite boats. The results of x-ray phase analysis of the product obtained by reducing a mixture of scale (90%) and iron (10%) in graphite boats in two stages (1 hour–650°C, 1 hour–800°C) showed that the resulting powder is 98% from α-Fe [0.253, 0.248, 0.215, 0.129 nm^3] (Fig. 7).

However, during storage, there is the slow oxidation of iron powder, [0.244, 0.212, 0.150, 0.128 nm^3]; therefore, experiments proved the need to increase the temperature of the II stage of reduction to 950–1000°C (Fig. 8).

Technological Scheme of Obtaining Iron Powders by Reducing Scale. Preparation of raw materials. If the scale is taken from perennial dumps located in an open area, then it is preliminarily subjected to screening and flotation with running water to remove pieces of silica and alumina. The scale in the spans of rolling mills is not subjected to such an operation.

The scale is dried at 250–340°C to remove moisture, oil, *etc.* Milling of scale is carried out in a ball mill at a ratio of the mass of raw materials and steel balls 1:1 for 2 hours.

After grinding, the powder is magnetically separated on a belt conveyor equipped with an electromagnetic system to remove particles of impurities. The yield of the non-magnetic fraction is 3–10%, depending on the scale contamination.

The powders are sieved through a 40-mesh sieve to remove coarse fractions, which are resent for grinding. The amount of the coarse fraction usually does not exceed 3–5%.

Batch Preparation. To accelerate the reduction process and facilitate the circulation of hydrogen, 8–10 wt.% iron powder is added to the scale powder. The batch is mixed in a mixer or ball mill for 1

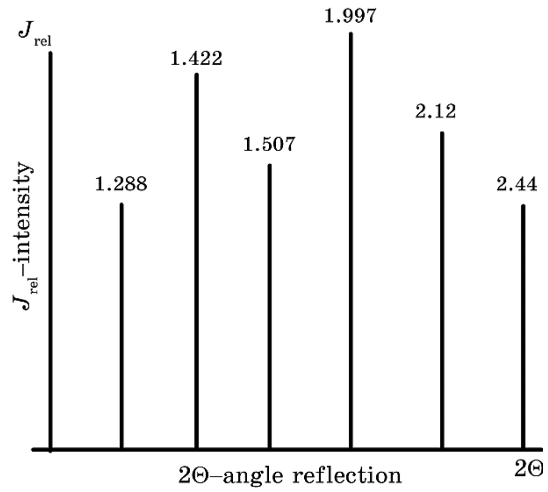

Fig. 8. X-ray diffraction pattern of iron samples obtained by reducing scale in two stages: *1*—650°C (1 h); *2*—1000°C (1 h).

Fig. 9. The microstructure of an iron sponge was obtained by reducing the mill scale, ×1000. *1*—α-Fe.

hour.

Scale Recovery. The charge is poured into standard graphite boats with a layer thickness of 25–30 mm, which are placed in the muffles of an industrial furnace consisting of two zones, and a refrigerator, and are continuously advanced using a pusher.

The temperature of zone I of the furnace is 650–700°C, zone II is 950–1000°C. Hydrogen is supplied from the side of the refrigerator and the counter-flow principle ensures the most complete recovery. The residence time of boats with a charge in each temperature zone is 1 hour, *i.e.*, the restoration process is carried out in 2 hours.

Grinding of the Sponge Iron. The resulting iron sponge (Fig. 9) is subjected to grinding in a ball mill for 2 hours.

After grinding, the powder is sieved through a 60-mesh sieve. Coarse fractions of the powder are returned to the initial cycle for

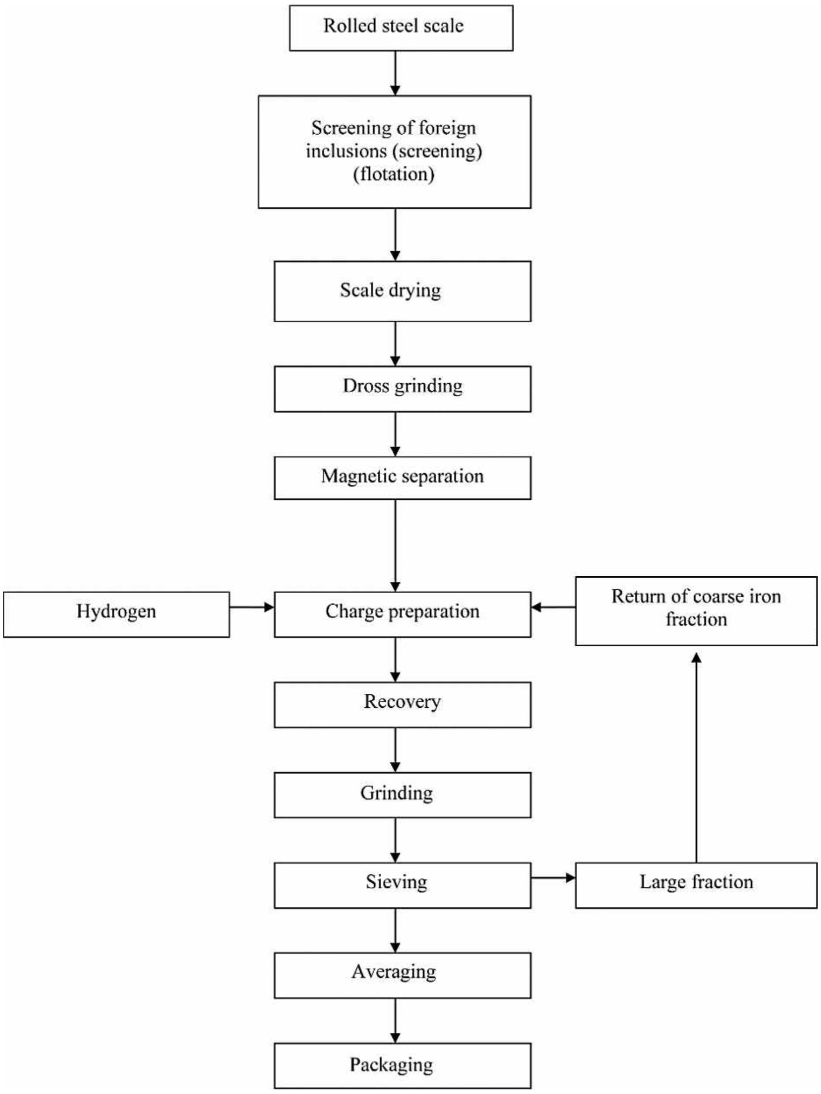

Fig. 10. Technological scheme for obtaining iron powders from the scale of the Uzmetkombinat.

batching the scale.

The technological scheme for obtaining iron powders from the scale of the APO Uzmetkombinat is shown in Fig. 10.

Composition and properties of iron powders. The iron powder obtained by this technology is α-Fe and has the chemical composition shown in Table 3. The results of studying the technological properties of iron powders are presented in Table 4.

TABLE 3. Iron powder chemical composition.

Element	Fe	Si	Al	Mg	Mn	Ba	Ti	Cr
Content, mass.%	98.9	0.3	0.1	0.01	0.2	0.009	0.001	0.05
Element	Zr	S	C	O_2	Ca	Ni	Co	other
Content, mass.%	0.001	0.03	0.05	0.2	0.008	0.1	0.04	0.15

TABLE 4. Technological properties of iron powders.

Particle size, mm	0.16–0.20	0.10–0.16	0.063–0.10	0.05–0.063	not less than 0.05
Grading, %	1.5	10–30	20–35	20–30	15–30
Bulk density, g/sm^3	2.2–3.0				
Fluidity, s/50 g	40				
Compressibility at $P = 700$ MPa, g/sm^3	6.5–7.0				

5. CONCLUSION

The modern methods of obtaining iron powders are considered, their classification is carried out, and analytical data of powders made from various types of raw materials are given.

The kinetic regularities of the reduction of iron oxides are analysed from the point of view of the adsorption–autocatalytic theory. The principles of reduction of mill scale with hydrogen are generalized, the influence of external factors on the reduction process is considered.

The structure and mechanical properties of iron powders are considered.

As concluded, regardless of the production method and raw materials, iron powders have different properties with the same chemical composition.

The morphology, structure, phase and elemental compositions of the mill scale of the Uzbek Metallurgical Combine are analysed. It is concluded that it is a powder of low alloy steels.

The dependence of the change in the phase composition of iron on the temperature and time of scale reduction is investigated. As a result, an optimal mode of obtaining iron powder was developed, the characteristics of which meet the GOST 9849-86 requirements.

The scale recovery technology has been developed, which includes the following stages: drying at 250–340°C, grinding in a ball mill for 2 hours, magnetic separation, sieving through a 40-mesh sieve, mixing the charge, recovery for 2 hours in H_2 at a temperature: I zone—650–700°C, II zone—950–1000°C.

REFERENCES

1. E. T. Denisenko, O. P. Kulik, and T. V. Yeremina, *Poroshkovaya Metallurgiya*, No. 4: 4 (1983) (in Russian).
2. S. S. Kiparisov and G. D. Libenson, *Poroshkovaya Metallurgiya* [Powder Metallurgy] (Moscow: Metallurgiya: 1980) (in Russian).
3. *Poroshkovaya Metallurgiya. Spechennyye Kompozitsionnyye Materialy* [Powder Metallurgy. Sintered Composite Materials] (Ed. V. Shatt) (Moscow: Metallurgiya: 1983) (Russian translation).
4. I. M. Fedorchenko and I. N. Frantsevich, *Poroshkovaya Metallurgiya. Materialy, Tekhnologiya, Svoistva, Oblasti Primeneniya: Spravochnik* [Powder Metallurgy. Materials, Technology, Properties, Applications: Handbook] (Kiev: Naukova Dumka: 1985) (in Russian).
5. F. Eizenkolb, *Uspekhi Poroshkovoi Metallurgii* [Advances in Powder Metallurgy] (Moscow: Metallurgiya: 1989) (Russian translation).
6. D. M. Karpinos, L. I. Tuchinskiy, and L. R. Vishnyakov, *Novyye Kompozitsionnyye Materialy* [New Composite Materials] (Kiev: Vishcha Shkola: 1977) (in Russian).
7. J. N. Dzneladze, R. P. Shchegoleva, L. G. Golubeva, E. M. Rabinovich, and B. A. Borok, *Poroshkovaya Metallurgiya Staley i Splavov* [Powder Metallurgy of Steels and Alloys] (Moscow: Metallurgiya: 1978) (in Russian).
8. V. V. Skorokhod, *Poroshkovaya Metallurgiya*, No. 10: 20 (1985) (in Russian).
9. P. G. Kurilov and V. M. Ribaulin, *Proizvodstva Konstruktsionnykh Izdeliy iz Poroshkov na Osnove Zheleza* [Manufacture of Structural Products from Iron-Based Powders] (Moscow: Metallurgiya: 1972) (in Russian).
10. *Novyye Protsessy i Materialy Poroshkovoy Metallurgii* [Technology of Metal Powders] (Ed. L. H. Yaverbaum) (Moscow: Metallurgiya: 1983) (Russian translation).
11. V. E. Perelman, *Formovanie Poroshkovykh Materialov* [Powder Materials' Forming] (Moscow: Metallurgiya: 1979) (in Russian).
12. V. B. Akimenko, V. Ya. Bulanov, V. E. Rukin et al., *Zheleznyye Poroshki* [Iron Powders] (Moscow: Nauka: 1982) (in Russian).
13. V. N. Antsiferov and V. V. Akimenko, *Spechennyye Legirovannyye Stali* [Sintered Alloyed Steels] (Moscow: Metallurgiya: 1988) (in Russian).
14. S. S. Yermakov and N. F. Vyaznikov, *Poroshkovyye Stali i Izdeliya* [Powder Steels and Products] (Leningrad: Mashinostroenie: 1990) (in Russian).
15. M. S. Kovalchenko, *Teoreticheskie Osnovy Goryachey Obrabotki Poristykh Materialov Davleniem* [Theoretical Foundations of Hot Pressure Treatment of Porous Materials] (Kiev: Naukova dumka: 1980) (in Russian).
16. V. A. Ivensen, *Kinetika Uplotneniya Metallicheskikh Poroshkov pri Spekanii* [Kinetics of Metal Powder Compaction during Sintering] (Moscow: Metallurgiya: 1971) (in Russian).
17. M. N. Fokin and Yu. V. Yemelyanov, *Zashchitnyye Pokritiya v Khimicheskoy Promyshlennosti* [Protective Coatings in the Chemical Industry] (Moscow: Khimiya: 1981) (in Russian).
18. N. N. Dorozhkin, T. M. Abramovich, and V. I. Zhornik, *Poluchenie Pokrytiy Metodom Pripekaniya* [Production of Coatings by Baking Method] (Minsk: Nauka i Tekhnika: 1980) (in Russian).
19. V. Yu. Bulanov and V. F. Ukhov, *Poluchenie Zheleznykh Poroshkov iz Prirodno-*

Legirovannogo Syr'ya [Production of Iron Powders from Natural Alloyed Raw Materials] (Moscow: Nauka: 1978) (in Russian).

20. I. D. Rodomyselskiy, *Poroshkovaya Metallurgiya*, No. 2: 32 (1979) (in Russian).
21. E. Ya. Popichenko and A. G. Bolshechenko, *Poroshkovaya Metallurgiya*, No. 2: 81 (1978) (in Russian).
22. A. M. Polyak and E. K. Sivaeva, *Izvestiya VUZov. Chernaya Metallurgiya*, **7**: 142 (1986) (in Russian).
23. Yu. S. Karabasov, *Fiziko-Khimiya Vosstanovleniya Zheleza iz Oksidov* [Chemistry of Iron Reduction from Oxides] (Moscow: Metallurgiya: 1986) (in Russian).
24. M. Peterdlik, V. Rubesh, I. D. Rodomyselskiy et al., *Poroshkovaya Metallurgiya*, No. **7**: 6 (1971) (in Russian).
25. V. V. Skorokhod, Yu. M. Solonin, and I. V. Uvarova, *Kineticheskie, Diffuzionnyye i Reologicheskie Protsessy v Tekhnologii Poroshkovykh Materialov* [Kinetic, Diffusion and Rheological Processes in Powder Technology] (Kiev: Naukova Dumka: 1990) (in Russian).
26. I. N. Frantsevich and V. I. Trefilov, *Poroshkovaya Metallurgiya v SSSR: Istoriya, Sovremennoye Sostoyanie, Perspektivy* [Powder Metallurgy in the USSR: History, Current State, Prospects] (Moscow: Nauka: 1986) (in Russian).
27. P. N. Ostrik, S. A. Artemenko, A. N. Popov et al., *Poroshkovaya Metallurgiya*, No. 12: 1 (1969) (in Russian).
28. R. A. Andrievskiy, *Poroshkovoye Materialovedenie* [Powder Materials Science] (Moscow: Nauka: 1991) (in Russian).
29. N. Z. Pozdnyak, *Apparaty i Tekhnologicheskoe Oborudovanie Poroshkovoi Metallurgii. Konstruktsionnyye Materialy i Oborudovanie* [Apparatuses and Technological Equipment of Powder Metallurgy. Structural Materials and Equipment] (Kiev: IPM AN UkrSSR: 1976), p. 124 (in Russian).
30. V. Gretchenko, A. F. Chumakov, and N. A. Roslavtsev, *Poroshkovaya Metallurgiya*, No. 2: 101 (1992) (in Russian).
31. G. M. Zhidomirov, A. G. Pelmennikov, N. K. Zhanpeisov, and A. G. Grebenyuk, *Kinetika i Kataliz*, **28**, No. 1: 86 (1987) (in Russian).
32. G. M. Zhidomirov and I. D. Mikheykin, *Itogi Nauki i Tekhniki. Ser. Stroenie Molekul i Khimicheskaya Svyaz* [Results of Science and Technology. Ser. Molecular Structure and Chemical Bond] (Moscow: VINITI: 1984), vol. **9** (in Russian).
33. *Sovremennyye Problemy Poroshkovoy Metallurgii* [Modern Problems of Powder Metallurgy] (Kiev: Naukova Dumka: 1970), p. 21 (in Russian).
34. H. Remy, *Kurs Neorganicheskoy Khimii* [Treatise on Inorganic Chemistry] (Moscow: Mir: 1971) (Russian translation).
35. Kh. M. Mamarakhimov and Sh. M. Shakirov, *Kompozitsionnyye Materiali*, **2**: 55 (2007) (in Russian).
36. R. U. Kalamazov, Kh. M. Mamarakhimov, Sh. M. Shakirov, and F. R. Turaev, *Vestnik. Tashkent GTU*, **3**: 94 (2004) (in Russian).
37. H. Youssef and M. Eudier, *Production and Properties of a New Porous Bearing. Friction and Antifriction Materials* (NewYork–London: Plenum Press: 1970), p. 291.
38. Kh. M. Mamarakhimov, *Vestnik. Tashkent GTU*, **4**: 56 (2007) (in Russian).
39. Kh. M. Mamarakhimov, *Tekhnika i Tekhnologiya*, **5**: 66 (2007) (in Russian).
40. C. Herring, *J. Appl. Phys.*, **2**, No. 5: 437 (1970).
41. Kh. M. Mamarakhimov and A. K. Dzhuraev, *Vestnik. Tashkent GTU*, **2**: 66 (2009) (in Russian).

Наносистеми, наноматеріали, нанотехнології
Nanosistemi, Nanomateriali, Nanotehnologii
2021, т. 19, № 4, сс. 799–806

PACS numbers: 61.05.cp, 61.43.Gt, 62.20.Qp, 68.37.Hk, 81.07.Wx, 81.20.Ev, 81.65.Ps

Effect of Production Methods on the Microstructure, Phase Composition, and Properties of Hard Alloy VK8 with Submicron Grain

A. V. Minitskyi[1], P. I. Loboda[1], Ie. G. Byba[1], I. Yu. Trosnikova[1], and O. I. Khovavko[2]

[1]*National Technical University of Ukraine*
'Igor Sikorsky Kyiv Polytechnic Institute',
37, Prospekt Pobedy,
UA-03056 Kyiv, Ukraine
[2]*Gas Institute, N.A.S. of Ukraine,*
39, Dehtiarivska Str.,
UA-03113 Kyiv, Ukraine

The effect of manufacturing process on the microstructure, phase composition, and properties of hard alloy VK8 that can be used for the cores of small armour-piercing ammunitions is revealed. According to the results obtained by scanning electron microscopy, x-ray phase analysis, and durometry, the sintering kinetics of the hard alloy VK8 allows forming a fine-grained microstructure with different levels of microstresses, depending on the production technique, which affects the mechanical properties of the material.

Встановлено вплив методів одержання на мікроструктуру, фазовий склад і властивості твердого сплаву ВК8, що може використовуватися в якості матеріялу для бронебійних сердечників стрілецької зброї. Методами растрової електронної мікроскопії, рентґенофазової та дюрометричної аналіз встановлено, що кінетика процесу спікання твердого сплаву ВК8, залежно від методу одержання, уможливлює сформувати дрібнозернисту структуру з різним рівнем мікронапружень, що формує механічні властивості матеріялу.

Key words: hard alloy, tungsten carbide, spark plasma-enhanced sintering, electron beam-assisted sintering, radiation sintering, hardness, microstresses.

Ключові слова: твердий сплав, карбід Вольфраму, іскроплазмове спікання, електронно-променеве спікання, радіяційне спікання, твердість, мікронапруження.

(Received 29 October, 2021; in revised form, 5 November, 2021)

1. INTRODUCTION

The use of materials in the arms industry requires the development of high performance alloys with a given level of properties. The cores of small armour-piercing ammunitions are the parts to which high requirements are set; they should have a high penetrating ability, which is provided by high kinetic energy and intactness of the core after piercing. This problem is possible to solve by using for the core a material with high strength, hardness, and specific weight. The combination of these characteristics can be achieved by using hard tungsten carbide alloys. However, the use of standard hard alloy manufacturing technologies does not provide maximum hardness and strength due to the growth of tungsten carbide grains during sintering [1–3].

Currently, a mixture of WC–Co fine powders with a particle size of about 1 μm is used in order to provide high mechanical performance of the hard alloys. One of the ways to create a fine-grained microstructure consists in the use of nanosize and submicron hard alloy powders [4–6]. However, the production of nanosize powders is accomplished by their difficult stabilization and requires energy-consuming grinding in planetary mills or attritors that results in contamination of the mixture, as well as intense deformation that increases absorbed energy and ultimately leads to particle growth. A partial solution to this problem consists in manufacturing carbide nanoparticles by synthesis in gas phase chemical reactions, or plasma chemical synthesis, which ensures a narrower particle size distribution and reduces excess energy [7]. However, another problem of nanostructure formation in carbide materials is the process of particle consolidation during sintering. The sintering in the presence of a liquid phase leads to fast grain growth caused by intensive mass transfer [8]. The diffusion processes can be retarded in solid-phase sintering; however, this makes impossible to get rid of residual porosity.

Traditional vacuum technologies of free sintering are not effective for producing hard alloy materials with nanostructures or fine structures. One way to inhibit grain growth in hard-alloy mixtures consists in applying pressure during sintering, which allows reducing the consolidation temperature. Such methods include hot static (HP) and hot isostatic pressing (HIP) technologies [9–11]. However, the disadvantage of these methods is the high probability of formation of residual porosity in the material, because the consolidation is performed mainly in the conditions of solid-phase sintering. A promising method of forming non-porous hard alloys with fine microstructure is spark plasma sintering (SPS), which implements rapid heating with a rate of about 400–500 degrees per minute [11–13]. Heating with high rate, as well as applied pressure, allow to reduce the sintering temperature to 1200–1300°C. Thus, it is necessary to study in more detail the features of consolidation of the WC-based hard alloys under the conditions of rapid sintering techniques, including those with electron beam application.

The goal of the work is to establish the effect of sintering conditions on the microstructure, phase composition, and properties of a hard WC-based alloy with 8% Co (VK8).

2. EXPERIMENTAL TECHNIQUES

As the object of research, a mixture of VK8 consisting of tungsten carbide (92%) and cobalt bond (8%) with an initial average particle size of 5.5–6.0 μm (determined at laser diffraction analyser Malvern Mastersizer 2000, UK) was selected (Fig. 1, *a*). Since the particle size of the hard-alloy mixture should be less than 1 μm, that is necessary to activate sintering, the mixture was ground in a drum ball mill with ethyl alcohol in a ratio of 1:4 for 120 hours. The average particle size after grinding was 0.80–085 μm (see particle size distribution in Fig. 1, *b*).

After grinding, a part of the mixture was mixed with a plasticizer (solution of rubber in gasoline) in order to provide formability. After mixing with the plasticizer, the mixture was dried in a drying cabinet at 80°C for 3 hours to remove moisture. Then, granulation was performed by rubbing the mixture through a sieve to ensure formability. The formation of the mixture was carried out by static pressing in a hydraulic press under a pressure of 50–100 MPa, using the scheme of bilateral pressing, which is necessary for producing parts with a ratio $H/D > 2$. After forming, the samples were dried in a drying cabinet at 80°C for 3 hours to remove residual moisture.

The compacts were sintered in different ways: sintering in a vacuum

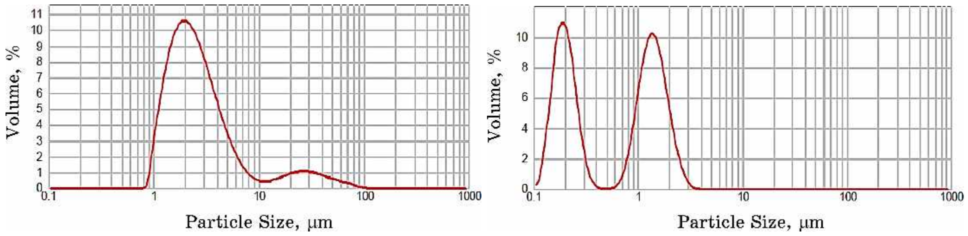

a *b*

Fig. 1. Particle size distribution of VK8 particles: initial mixture (*a*); after grinding for 120 h (*b*).

furnace, electron beam sintering, and spark plasma sintering. Vacuum furnace sintering was performed in a vacuum electric resistance furnace in graphite backfill (fraction −1 + 063) at 1450 ± 10°C with isothermal annealing for 60 min; the samples were heated with a rate of 200°C/h up to 400°C in order to remove gradually the plasticizer; then, the heating rate was increased to 400°C/h.

Electron beam sintering was performed at ELA-6 unit, which allows implementing sintering of cylindrical samples in both manual and fully automatic mode with rotation around vertical and horizontal axis. The advantage of electron beam heating is the ability to change gradually and in a wide range the quantity of applied heat, as well as the configuration of the heating zone. The unit is equipped with vacuum equipment of Pfeiffer Vacuum GmbH (Germany). Electron beam sintering was performed for 60 seconds in different regimes, depending on the current (4–6 mA).

Spark plasma sintering was carried out in graphite moulds using the unit of KSE®-FCT HP D 25-SD type (Germany) equipped with a 25-ton press and a vacuum chamber (with the possibility of using inert gas). The mixture in a graphite mould was heated with a rate of 300°C/min at a pressure of 25 MPa up to 1380°C and annealed at this temperature for 3 min.

The microstructure of the samples was studied using a scanning electron microscope REM-106I SELMI (Ukraine). X-ray studies of phase composition were performed at a RIGAKU ULTIMA IV diffractometer (Japan) using the Rietveld and Reference Intensity Ratio (RIR) methods with $\mathrm{Cu}K_{\alpha_{1,2}}$ ($\lambda_{\mathrm{Cu}K\alpha1} = 0.1541$ nm). The microstresses were determined by the Stokes–Wilson method using the software of RIGAKU ULTIMA IV diffractometer [14]. The HRA (Rockwell) hardness was measured at TK-2 unit by indenting the sample surface by a diamond cone according to the standard ISO 4498. The microhardness was measured by the Vickers method on a microhardness tester LHVS-1000Z (China) with a diamond indenter at a load of 1000 g.

3. RESULTS

The studies of the microstructure of the samples produced by different methods showed that the porosity was below 0.5% (Figs. 2, 3) that was confirmed by the results of density measurements by means of hydrostatic weighing; the density of sintered samples was of 14.6 g/cm^3 that corresponds to the theoretical density of the VK8 alloy.

The studies of microstructure also showed that the samples produced by furnace sintering contained small amount of η-phase (Co_3W_3C) inclusions, which was confirmed by the results of local EDS and x-ray phase analyses (Fig. 3).

The hardness of the samples was in the range of 88–94 HRA. The

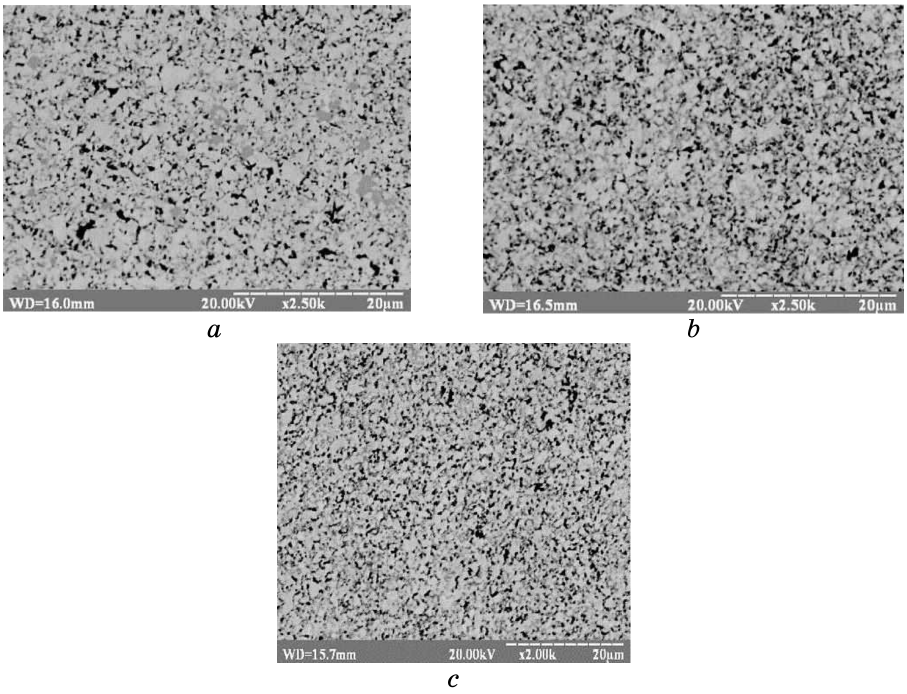

a *b* *c*

Fig. 2. Microstructure of VK8 alloy produced by different methods: vacuum furnace sintering (*a*); electron beam sintering (*b*); spark plasma sintering (*c*).

lowest values corresponded to the samples produced by radiation sintering (88–89 HRA); the samples sintered by electron beam and spark plasma methods had the hardness not less than 93–94 HRA.

The studies of microhardness showed that after furnace sintering the microhardness was about 15.0–15.5 GPa, whereas rapid methods led to its increase up to 17.5–18.0 GPa (Fig. 4).

The microstresses in different phases of the samples produced by different techniques were also determined (Table).

4. DISCUSSION

The results of metallographic studies revealed that the sintering conditions, namely the kinetics of the process, has a significant impact on the formation of the structure of the hard alloy. For example, furnace sintering leads to the formation of a structure with an average grain size of 2–4 µm (Fig. 2, *a*), *i.e.*, grain growth occurs due to recrystallization processes activated by long exposure at high temperatures. Another feature of the microstructure formed upon furnace sintering is the precipitation of a certain amount of the η-

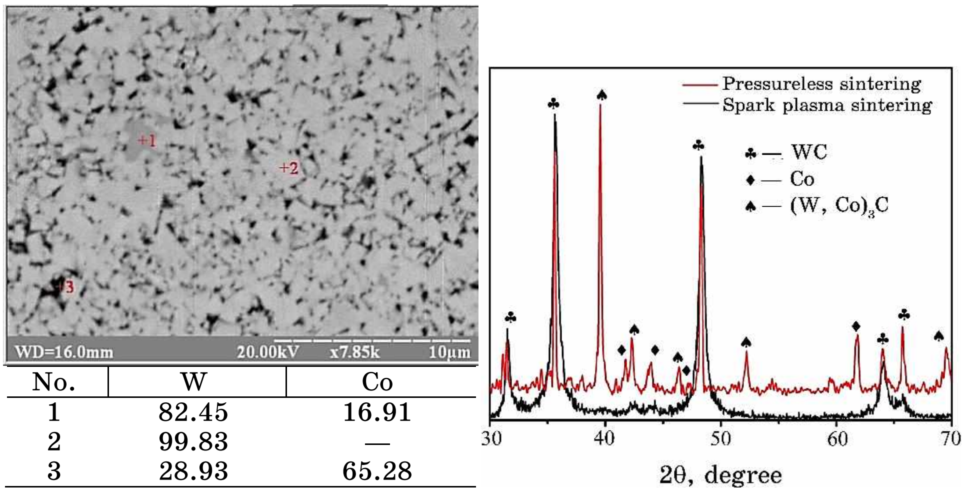

No.	W	Co
1	82.45	16.91
2	99.83	—
3	28.93	65.28

a *b*

Fig. 3. Results of EDS and x-ray phase analyses of VK8 alloy: microstructure and local chemical composition after vacuum furnace sintering (*a*); diffractograms after vacuum furnace and spark plasma sintering (*b*).

phase that is caused by the processes of partial decarburization of the samples. The microstructures of the VK8 alloy after spark plasma and electron beam sintering are somewhat similar to each other (see Figs. 2, *b*, *c*): the grain size is about 1 µm, *i.e.*, almost the same as the size of the particles in the initial powder mixture. It should be also noted that the increase of exposure time during electron beam sintering up to 2 minutes can also lead to the formation of a small amount of the η-phase.

The absence of the η-phase after spark plasma sintering (confirmed by the results of x-ray phase analysis; see Fig. 3, *b*) is explained by the fact that the process was performed in a graphite mould, that prevented decarburization.

The results of durometry confirmed the dependence of the properties on the sintering kinetics: the values of hardness and microhardness fully correlated with the grain size, so the highest hardness and microhardness (93–94 HRA and 17.5–18.0 GPa, respectively) were measured on fine-grained samples after electron beam and spark plasma sintering. At the same time, furnace sintering caused grain growth that resulted in lower hardness and microhardness (88–89 HRA and 15.2–15.5 GPa, respectively).

The level of microstresses is one of the characteristics, which determines the physical and mechanical properties of a material. The measurements of microstresses in the produced samples showed that the highest compressive stresses were observed after spark plasma and

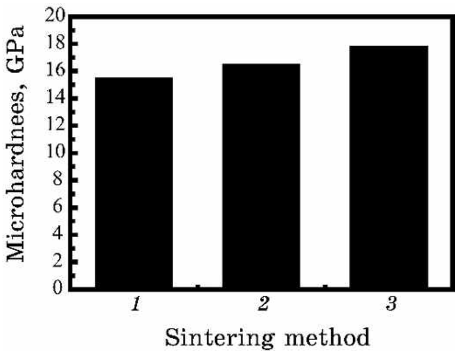

Fig. 4. Microhardness (at load of 1000 g) of VK8 alloy produced by different techniques: vacuum furnace sintering (*1*); electron beam sintering (*2*); spark plasma sintering (*3*).

TABLE. Microstresses in the phase constituents of VK8 alloy produced by different techniques.

No.	Sintering method	Phase composition, %		CSR* size, Å		Microstresses in phases, GPa	
		WC	Co	WC	Co	WC	Co
1	Furnace sintering, exposure time 60 min	94	6	150	235	–4.002	–0.164
2	Electron beam sintering, exposure time 1 min	89	11	365	248	–10.23	–0.69
3	Spark plasma sintering, exposure time 3 min	92	8	101	89	–6.22	–2.66

Note: *Coherent scattering region.

electron beam sintering (see Table). Higher microstresses appeared due to higher sintering rates, which were accompanied by nonequilibrium processes; after electron beam sintering, compressive microstresses in the WC phase reached –10.23 GPa. The lowest microstresses of –4.002 GPa were predictably observed after vacuum furnace sintering with a long isothermal exposure, which is explained by the fullness and completeness of the processes of grain consolidation and partial relaxation of microstresses during slow cooling.

5. CONCLUSIONS

The effect of sintering regimes on the microstructure, phase composition, and properties of the hard alloy VK8 has been studied. It is shown that the conditions of rapid sintering methods, such as spark plasma and electron beam sintering, provide the formation of fine-grained microstructure, high hardness and microhardness in the hard alloy VK8. The features of the microstructure formation, namely the precipitation of small amount of the η-phase with increasing exposure time during electron beam sintering, are revealed for rapid methods. The correlation between the sintering kinetics and the microstresses in the phase constituents of the hard alloy VK8 is shown.

The studies have shown the prospects of rapid sintering techniques for hard alloys and their advantage over traditional furnace sintering. The results can be used in the development of the cores of small armour-piercing ammunitions.

REFERENCES

1. V. S. Panov and A. M. Chuvilin, *Tekhnologiya i Svoistva Spechennykh Tverdykh Splavov i Izdeliy iz Nikh* (Moscow: Izd-vo MISiS: 2001) (in Russian).
2. R. Kieffer and F. Benezovskij, *Tverdyye Splavy* [Hard Alloys] (Moscow: Metallurgiya: 1971) (Russian translation).
3. P. Schwarzkopf and R. Kieffer, *Cemented Carbides* (New York: Macmillan: 1960).
4. A. F. Lisovskij, *Sverkhtverdyye Materialy*, **6**: 31 (2010) (in Russian).
5. Yu. I. Gordeev, A. K. Abkaryan, A. S. Binchurov, V. B. Yasinskiy, I. V. Karpov, A. A. Lepeshev, O. L. Khasanov, and E. S. Dvilis, *Journal of Siberian Federal University. Engineering & Technologies*, **3**: No. 7: 270 (2014) (in Russian).
6. I. Yu. Trosnikova and P. I. Loboda, *Journal of Superhard Materials*, **41**, No. 1: 49 (2019); https://doi.org/10.3103/S1063457619010076
7. E. A. Levashov, V. S. Panov, and I. Yu. Konyashin, *Izvestiya VUZov. Poroshkovaya Metallurgiya i Funktsional'nyye Pokrytiya*, **3**: 14 (2017) (in Russian).
8. H. Kramar, L. Bodrova, Ya. Kovalchuk, S. Marynenko, and I. Koval, *Scientific Journal of the TNTU*, **3**, No. 91: 25 (2018); https://doi.org/10.33108/visnyk_tntu2018.03.063
9. Xingxing Lyu, Xiaosong Jiang, Hongliang Sun, and Zhenyi Shao, *Nanotechnology Reviews*, **9**: 543 (2020); https://doi.org/10.1515/ntrev-2020-0044.
10. I. Azcona, A. Ordonez, J. M. Sanchez, and F. Castro, *Journal of Materials Science*, **37**, No. 19: 4189 (2002); https://doi.org/10.1023/A:1020048105585
11. Chengchang Jia, Lan Sun, Hua Tang, and Xuanhui Qu, *International Journal of Refractory Metals and Hard Materials*, **25**, No. 1: 53 (2007); https://doi.org/10.1016/j.ijrmhm.2005.11.003
12. E. A. Lantsev, V. N. Chuvil'deev, A. V. Nokhrin, M. S. Boldin, N. V. Malekhonova, Y. V. Blagoveshchenskii, N. V. Isaeva, Y. V. Tsvetkov, P. V. Andreev, and K. E. Smetanina, *IOP Conf. Series: Materials Science and Engineering*, **1014**: 012020; https://doi.org/10.1088/1757-899X/1014/1/012020
13. V. N. Chuvil'deev, A. V. Moskvicheva, M. S. Boldin, N. V. Sakharov et al., *Vestnik Nizhegorodskogo Universiteta im. N. I. Lobachevskogo*, **2**, No. 2: 115 (2013) (in Russian).
14. O. P. Karasevs'ka, I. Yu. Trosnikova, and P. I. Loboda,, *Rentgenostrukturnyy Analiz Materialiv u Dyspersnomu Stani* (Kyiv: Politekhnika: 2017) (in Ukrainian).

Наносистеми, наноматеріали, нанотехнології
Nanosistemi, Nanomateriali, Nanotehnologii
2021, т. 19, № 4, сс. 807–821

PACS numbers: 65.40.gd, 75.30.Sg, 75.40.Cx, 75.60.Ch, 75.60.Ej, 75.75.Fk, 81.07.Gf

Вплив теплового руху доменної стінки на термодинамічні властивості залізного циліндричного нанодроту

А. Б. Шевченко, О. В. Олійник

Інститут металофізики ім. Г. В. Курдюмова НАН України,
бульв. Академіка Вернадського, 36,
03142 Київ, Україна

Досліджено вплив теплового руху доменної стінки (ДС) на ентропію та тепломісткість електронної, магнонної та фононної (Дебайової компоненти) підсистем залізного циліндричного нанодроту. З'ясовано, що ентропія та тепломісткість, спричинені динамікою ДС, можуть бути одного порядку з відповідними термодинамічними характеристиками вказаних вище підсистем. Визначено критичні параметри (діяметер нанодроту, температуру), за яких має місце таке становище. Запропоновано механізм збільшення критичного діяметра нанодроту шляхом зменшення його намагнетованости. Встановлено, що величина діяметра залізного нанодроту, за якого поздовжня ДС трансформується у ДС у вигляді Блохової точки, складає 38 нм.

The effect of the thermal motion of a domain wall (DW) on both the entropy and the heat capacity of the electron, magnon and phonon (Debye component) subsystems of cylindrical iron nanowire is investigated. As found out, the entropy and the heat capacity caused by the DW dynamics can be of the same order of magnitude with the corresponding thermodynamic characteristics of above-mentioned subsystems. The critical parameters (nanowire diameter, temperature) for such a circumstance are determined. The method of the critical nanowire diameter increase by means of the decrease of nanowire magnetization is proposed. As ascertained, the iron-nanowire diameter value, at which the transition from the longitudinal DW to the domain wall in the form of a Bloch point occurs, is equal to 38 nm.

Ключові слова: залізний нанодріт, намагнетованість, доменна стінка, тепломісткість, ентропія.

Key words: iron nanowire, magnetization, domain wall, heat capacity, entropy.

(Отримано 14 грудня 2020 р.)

1. ВСТУП

Однією з актуальних задач фізики нанорозмірних систем є вивчення властивостей феромагнетних нанодротів (ФН), застосування яких має відіграти важливу роль у перспективних нано-, біо- та медичних технологіях. Так, наприклад, ФН розглядають як багатообіцяючі матеріяли для доставки лікарських препаратів, лікування онкологічних захворювань, розігріву кріоконсервованих органів і біологічних тканин [1–5]. Приваблює застосування ФН у пристроях зберігання даних і наносенсориці [6–8].

Важливою проблемою, вирішення якої істотно розширює потенціял впровадження ФН, є пошук механізмів керування їхніми фізичними властивостями. Однією з відповідей на поставлену задачу може стати контрольована динаміка магнетних домішок. В якості означених об'єктів перспективним виглядає використання доменних стінок (ДС), що формуються в нанодротах. Такі системи являють собою стійкі наноутворення, які поділяють магнетну структуру ФН на області з протилежними напрямками вектора намагнетованости. Оскільки всередині ФН практично немає дефектів (відволікаємося від неоднорідностей їхніх поверхонь, вважаючи останні досконалими), то адекватним видається модель ДС, що перебувають у стані теплового руху, середня швидкість якого визначається температурою ФН.

Виходячи із даного моделю, в роботах [9, 10] досліджувався вплив поздовжньої ДС (магнетна структура якої визначається конкуренцією обмінної та магнетостатичної енергій ФН) у ферит-ґранатовому та ніклевому циліндричних нанодротах на їхні термодинамічні властивості. Було показано, що ентропія та тепломісткість, зумовлені динамікою ДС, можуть бути одного порядку з аналогічними характеристиками фононної (Дебайової компоненти), магнонної й електронної (для ніклевого нанодроту) підсистем ФН. Більш того, в статтях [9, 10] передбачено, що в слабких магнетних полях (значно менших за $2\pi M$, M — намагнетованість нанодроту) в розглянутих системах має місце неґативний магнетокалоричний ефект, тобто відбувається зменшення температури нанодроту зі збільшенням зовнішнього магнетного поля. Даний результат узгоджується із фундаментальним принципом самореґульовних термодинамічних систем — принципом Ле Шательє–Брауна [11]. Наведені факти свідчать про можливість використання чинника ДС для впливу на термодинамічні стани ФН.

Слід зазначити, що проведені в наведених вище роботах дослідження показали зменшення впливу ДС на ентропію та тепломісткість ФН із збільшенням їхніх діяметрів. Було також встановлено залежність відповідних критичних діяметрів d_{cr} (максимальний діяметер нанодроту, за якого є актуальним чинник ДС) не тільки від температури нанодроту T, але й від величини його намагнетованости M. У зв'язку із цим становить інтерес розгляд аналогічної задачі для залізного нанодроту, намагнетованість якого помітно перевищує намагнетованість ферит-ґранатового та ніклевого дротів. У даному випадку слід очікувати більш характерні температурні залежності $d_{cr}(M)$, особливо в Дебайовій області температур. Крім того, важливість розгляду зазначеної проблеми визначається також і тим фактом, що залізні нанодроти є менш токсичним матеріялом, аніж ніклеві [12], що робить їх більш привабливими для застосування в таких областях медицини, як магнетна терапія, адресна доставка ліків, протезування, нанонагрівання.

Запропонована робота стосується дослідження актуальности впливу теплового руху поздовжньої ДС на ентропію та тепломісткість складових підсистем (електронної, магнетної, фононної) залізного циліндричного нанодроту, а також знаходження відповідних умов реалізації даного явища.

2. ВИРІШЕННЯ ПОСТАВЛЕНОЇ ЗАДАЧІ

Виходячи із результатів [9], ентропію S_{DW} і тепломісткість c_{DW}, зумовлену рухом ДС вздовж довгої осі циліндричного нанодроту, можна записати у вигляді:

$$S_{DW} = Nk_B \frac{c}{2\delta} e^{-a} \left((1+a)(1+\ln D - 0,5\ln a) + 0,5\right),$$

$$c_{DW} = -a\frac{\partial S_{DW}}{\partial a} = Nk_B \frac{c}{2\delta} e^{-a} \left(0,5 + a + a^2(1+\ln D - 0,5\ln a)\right), \tag{1}$$

де $N = \pi d^2 L/(4c^3)$ — кількість фононів нанодроту, c — стала ґратниці заліза, L — довжина нанодроту, d — діяметер нанодроту, k_B — Больцманнова стала, $a = E_{DW}/(k_B T)$, $E_{DW} = \pi A d^2/\delta$ — поверхнева енергія ДС, A — стала обміну, $\delta = (A/\pi M^2)^{1/2}$ — ефективна ширина ДС, $D = d^2 A^{1/2}/(2\sqrt{2}\,\gamma\hbar)$, $\gamma = 2\cdot 10^7\ \text{Е}^{-1}/\text{с}^{-1}$ — гіромагнетне відношення, $\hbar$ — Планкова стала.

Зазначимо, що вектор намагнетованости циліндричного нанодроту, через його аксіяльну симетрію, визначається особливостями магнетної структури ДС, самоорганізації якої відповідає ряд фононів у поздовжньому напрямку нанодроту. В цьому випадку його середня намагнетованість $\bar{M} = -V^{-1}\partial F_{DW}/\partial H$ (F_{DW} — вільна енергія, обумовлена тепловим рухом ДС, $V = \pi d^2 L/4$ — об'єм нанодроту) має бути нормована на $\pi d^2/(4c^2)$ — кількість фононів у поперечному напрямку. У той же час, термодинамічні потенціяли F_{DW}, S_{DW} та тепломісткість c_{DW} залежать від загального числа фононів ФН, що й відображено у формулах (1).

Наша аналіза внеску ДС у термодинамічні властивості залізного нанодроту полягатиме в порівнянні значень, які визначаються з виразів (1), з відповідними співвідношеннями для його електронної, магнонної та фононної підсистем.

Спочатку врахуємо електронну провідність нанодроту. Для нього тепломісткість електронів має вигляд [13]: $c_e = Nk_B \dfrac{\pi k_B T}{2E_F}$, де E_F — енергія Фермі. Виражаючи в даному співвідношенні температуру T через змінну a, останню формулу перепишемо таким чином:

$$c_e = Nk_B \frac{\pi B}{2E_F}, \qquad (2)$$

де $B = \pi^{3/2} A^{1/2} M d^2 / a$.

Аналіза виразу (2) показує, що вираз для ентропії S_e електронної підсистеми ФН має вигляд:

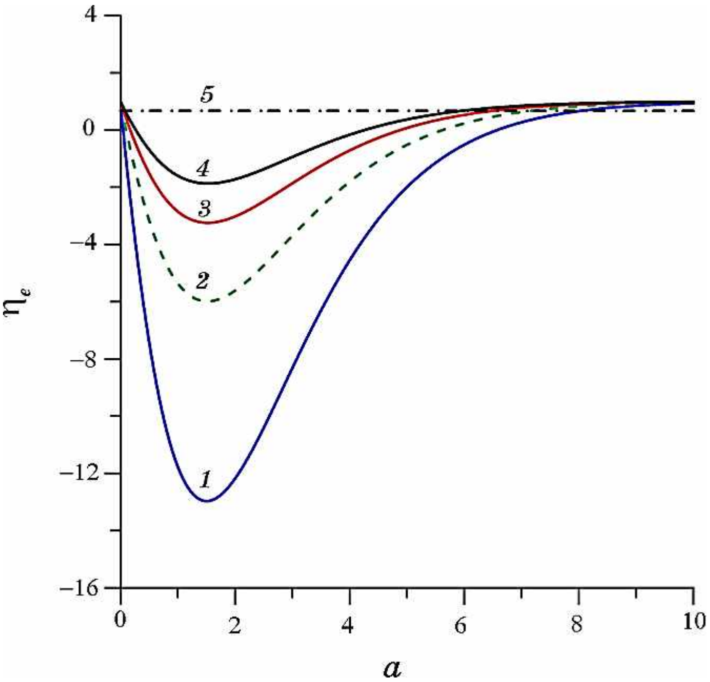

Рис. 1. Температурні залежності відносної ентропії $\eta_e = (S_e - S_{DW})/S_e$ електронної підсистеми для різних значень діяметра залізного циліндричного нанодроту: *1* — $d_e = 1$ нм, *2* — $d_e = 1{,}5$ нм, *3* — $d_e = 2$ нм, *4* — $d_e = 2{,}5$ нм, *5* — $\eta_e = 0{,}667$.[1]

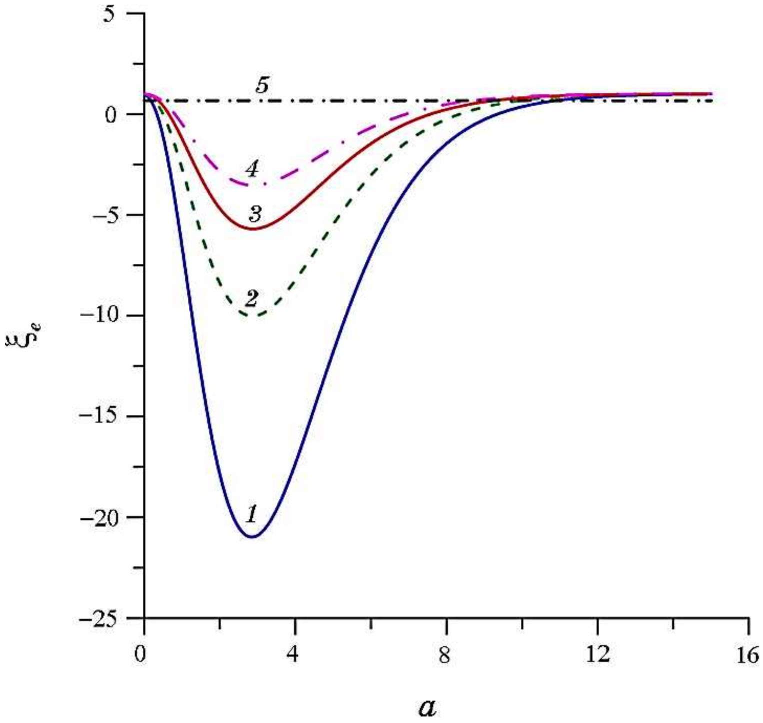

Рис. 2. Температурні залежності відносної тепломіісткости $\xi_e = (c_e - c_{DW})/c_e$ електронної підсистеми для різних значень діяметра залізного циліндричного нанодроту: *1* — $d_e = 1$ нм, *2* — $d_e = 1{,}5$ нм, *3* — $d_e = 2$ нм, *4* — $d_e = 2{,}5$ нм, *5* — $\xi_e = 0{,}667$.[2]

$$S_e = Nk_B \frac{\pi B}{2E_F}. \qquad (3)$$

Результати обчислень за формулами (1)–(3) залежностей $\eta_e = (S_e - S_{DW})/S_e$ і $\xi_e = (c_e - c_{DW})/c_e$ від змінної a для параметрів заліза: $M = 1{,}7 \cdot 10^3$ Гс, $c = 2{,}866 \cdot 10^{-8}$ см, $E_F = 17{,}784 \cdot 10^{-12}$ ерг, $A = 2 \cdot 10^{-6}$ ерг/см наведено на рис. 1 і 2. Будемо надалі вважати, що термодинамічний внесок ДС є актуальним при S_e/S_{DW}, $c_e/c_{DW} \leq 3$ (див. прямі η_e, $\xi_e = 0{,}667$ на рисунках). Тоді для відповідних температурних інтервалів ентропії $\Delta T_{e,S}$ і тепломіісткости $\Delta T_{e,c}$ маємо: $d_e = 1$ нм, $1{,}043 \cdot 10^3$ К $\geq \Delta T_{e,S} \geq 120{,}68$ К, $1{,}043 \cdot 10^3$ К $\geq \Delta T_{e,c} \geq 89$ К; $d_e = 1{,}5$ нм, $1{,}043 \cdot 10^3$ К $\geq \Delta T_{e,S} \geq 305{,}015$ К, $1{,}043 \cdot 10^3$ К $\geq \Delta T_{e,c} \geq 218{,}94$ К; $d_e = 2$ нм, $1{,}043 \cdot 10^4$ К $\geq \Delta T_{e,S} \geq 597{,}654$ К, $1{,}043 \cdot 10^3$ К $\geq \Delta T_{e,c} \geq 418{,}57$ К; $d_e = 2{,}5$ нм, $1{,}043 \cdot 10^3$ К $\geq \Delta T_{e,S} \geq 1018{,}48$ К, $1{,}043 \cdot 10^3$ К $\geq \Delta T_{e,c} \geq 696{,}7$ К.

Зважаючи на те, що температура Кюрі заліза $T_C = 1043$ К, верхні границі температурних інтервалів $\Delta T_{e,S}$ та $\Delta T_{e,c}$ обмежені T_C.

З наведених співвідношень видно, що зі збільшенням діяметра нанодроту зростають значення нижніх границь інтервалів $\Delta T_{e,S}$ і $\Delta T_{e,c}$, тобто має місце зменшення внеску теплового руху ДС в його ентропію та тепломісткість.

Зауважимо, що наведені вище значення $\Delta T_{e,S}$ і $\Delta T_{e,c}$ істотно менші за температуру виродження електронної підсистеми ($E_F/k_B \cong 10^5$ К), що узгоджується з вимогою застосовности формул (2), (3).

Враховуючи [14], вирази для магнонного внеску ентропії S_m і тепломісткости c_m можна записати у вигляді:

$$S_m = \frac{5Nk_B\zeta(5/2)(B/k_BT_c)^{3/2}}{16\pi^{3/2}}, \quad c_m = \frac{15Nk_B\zeta(5/2)(B/k_BT_c)^{3/2}}{32\pi^{3/2}}, \tag{4}$$

де $\xi(x)$ — Ріманова дзета-функція.

Результати проведених у відповідності до формул (1), (4) розрахунків функцій $\eta_m = (S_m - S_{DW})/S_m$ і $\xi_m = (c_m - c_{DW})/c_m$ наведено на рис. 3 та 4. Як і у випадку електронної підсистеми, спостерігається зменшення діяпазонів актуальних температурних інтер-

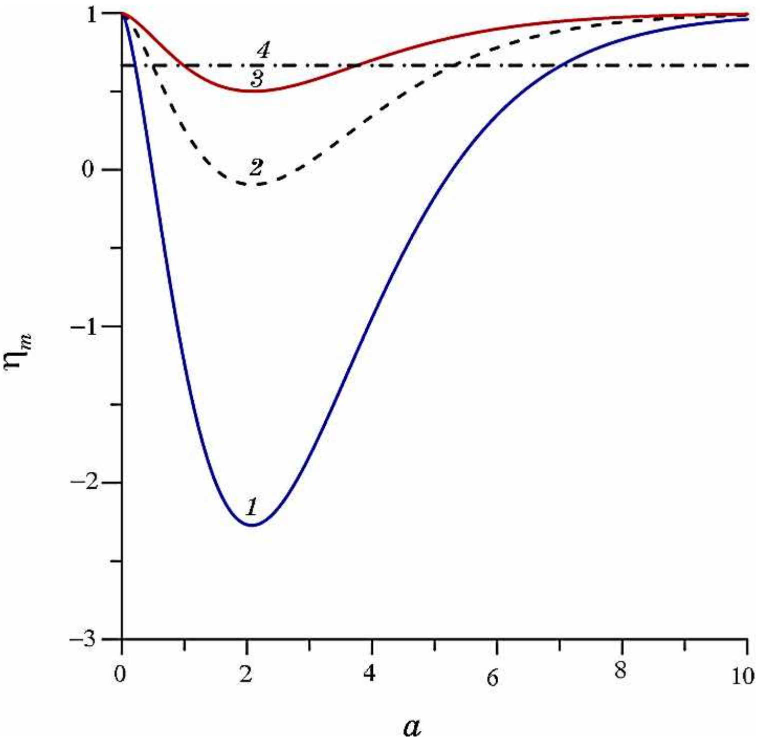

Рис. 3. Температурні залежності відносної ентропії $\eta_m = (S_m - S_{DW})/S_m$ магнонної підсистеми для різних значень діяметра залізного циліндричного нанодроту: *1* — $d_m = 1$ нм, *2* — $d_m = 1{,}5$ нм, *3* — $d_m = 2$ нм, *4* — $\eta_m = 0{,}667$.[3]

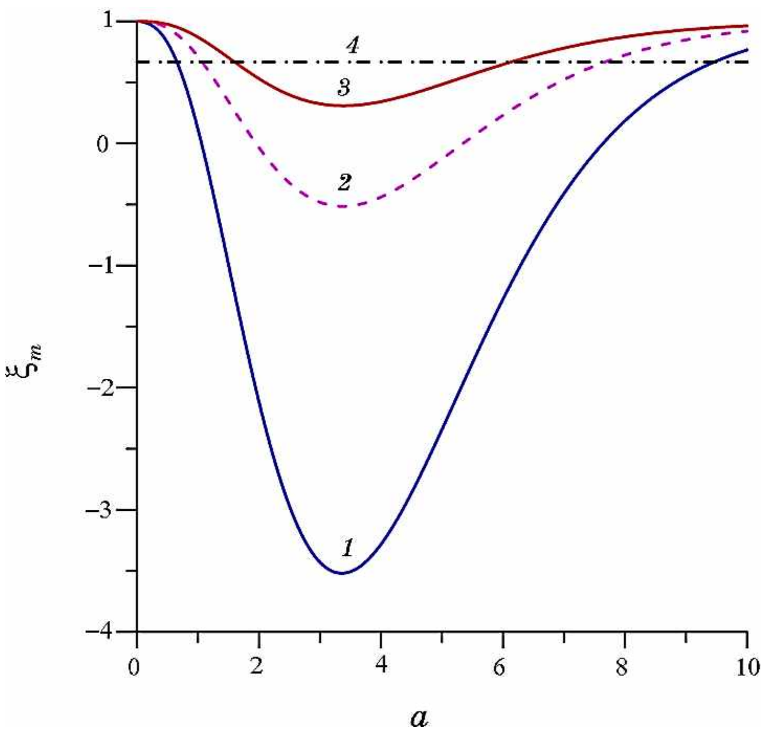

Рис. 4. Температурні залежності відносної тепломісткости $\xi_m = (c_m - c_{DW})/c_m$ магнонної підсистеми для різних значень діяметра залізного циліндричного нанодроту: *1* — $d_m = 1$ нм, *2* — $d_m = 1{,}5$ нм, *3* — $d_m = 2$ нм, *4* — $\xi_m = 0{,}667$.[4]

валів ентропії $\Delta T_{m,S}$ і тепломісткости $\Delta T_{m,c}$ зі збільшенням діяметра нанодроту. Дійсно, для $d_m = 1$ нм $1{,}043 \cdot 10^3$ К $\geq \Delta T_{m,S} \geq 137{,}94$ К, $1{,}043 \cdot 10^3$ К $\geq \Delta T_{m,c} \geq 102{,}46$ К; для $d_m = 1{,}5$ нм, $1{,}043 \cdot 10^3$ К $\geq \Delta T_{m,S} \geq$ $\geq 410{,}6$ К, $1{,}043 \cdot 10^3$ К $\geq \Delta T_{m,c} \geq 284{,}34$ К; для $d_m = 2$ нм, $1{,}043 \cdot 10^3$ К $\geq$ $\geq \Delta T_{m,S} \geq 1030{,}54$ К, $1{,}043 \cdot 10^3$ К $\geq \Delta T_{m,c} \geq 632{,}4$ К.

Зазначимо, що застосовність формул (4) визначається умовою $T >> 1$ К (див. [9]), яка, як легко бачити, добре виконується. В той же час, в області температур $T \leq 1$ К слід враховувати квантовий характер динаміки поздовжньої ДС, яка являє собою магнетний солітон типу ‘kink’ (див. роботи [15–18]). Позаяк для магнетних наноструктур слушним є квазикласичне наближення [19], то в цьому випадку для знаходження статистичної суми та відповідних термодинамічних потенціялів (вільної енергії, ентропії, Ґіббсова потенціялу), зумовлених тепловим рухом ДС, є слушним застосування формалізму, викладеного в [9]. При цьому сам рух ДС має бути «проквантованим» у циліндрі довжиною L.

У відповідності до [13], вирази для ентропії S_{ph} і тепломісткости c_{ph} фононної підсистеми (Дебайової компоненти) залізного дроту запишемо наступним чином:

$$S_{ph} = Nk_B \frac{4\pi^4 (B/k_B T_D)^3}{5}, \quad c_{ph} = Nk_B \frac{12\pi^4 (B/k_B T_D)^3}{5}, \tag{5}$$

де $T_D = 464$ К — Дебайова температура заліза.

Зазначимо, що в області температур $T_D \gg T \gg 1$ К ентропія та тепломісткість фононної підсистеми істотно перевищують відповідні характеристики електронної та магнонної компонент. Дійсно, виходячи з формул (2)–(5), знаходимо, що: S_e/S_{ph} та й $\frac{c_e}{c_{ph}} \simeq 10^{-2}\left(\frac{T_D}{T}\right)^2 \frac{k_B T}{E_F} \cong 10^{-1}$; $\frac{S_m}{S_{ph}}$ і $\frac{c_m}{c_{ph}} \simeq 10^{-1}\left(\frac{T}{T_D}\right)^{3/2}\left(\frac{T_D}{T}\right)^3 \cong 10^{-1}$. В такому випадку можна передбачити, що значення діяметрів залізних нанодротів, які забезпечують актуальні температурні інтервали, є на порядок меншими за відповідні величини його електронної та магнонної підсистем.

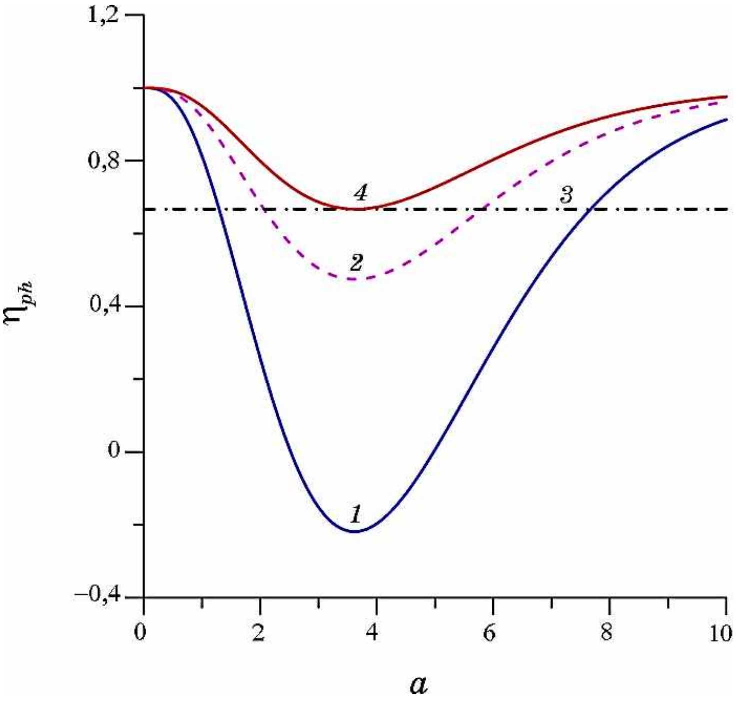

Рис. 5. Температурні залежності відносної ентропії $\eta_{ph} = (S_{ph} - S_{DW})/S_{ph}$ фононної підсистеми для різних значень діяметра залізного циліндричного нанодроту: *1* — $d_{ph} = 0{,}3$ нм; *2* — $d_{ph} = 0{,}35$ нм; *3* — $\eta_{ph} = 0{,}667$; *4* — $d_{ph,crs} = 0{,}3803$ нм.[5]

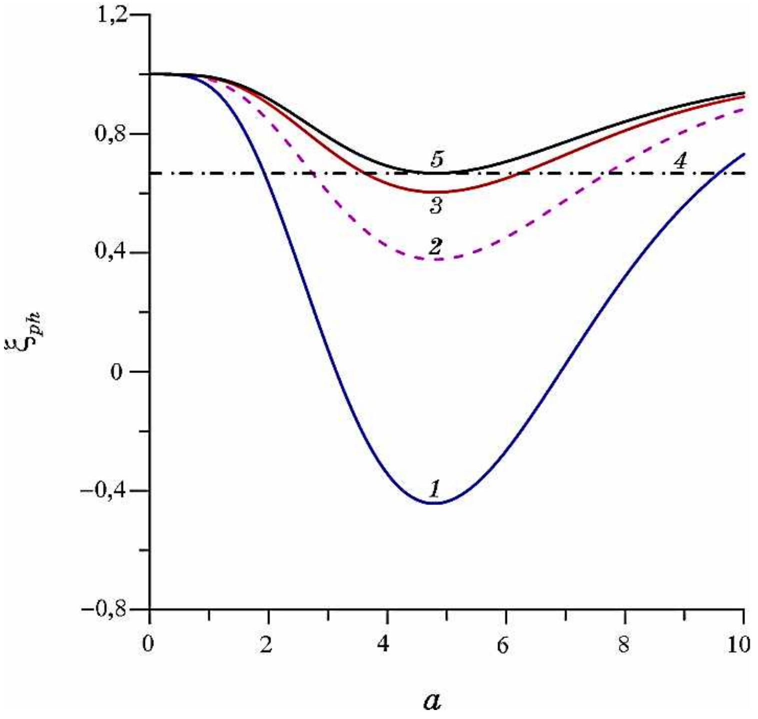

Рис. 6. Температурні залежності відносної тепломісткости $\xi_{ph}=(c_{ph}-c_{DW})/c_{ph}$ фононної підсистеми для різних значень діяметра залізного циліндричного нанодроту: *1* — $d_{ph}=0,3$ нм; *2* — $d_{ph}=0,35$ нм; *3* — $d_{ph}=0,38$ нм; *4* — $\xi_{ph}=0,667$; *5* — $d_{ph,cr_S}=0,39$ нм.[6]

Обчислення, проведені у відповідності до формул (1), (5) (див. також рис. 5, 6), узгоджуються із зазначеним вище припущенням: $d_{ph}=0,3$ нм, $67,44\text{ К}\geq\Delta T_{ph,S}\geq 11,38$ К, $45,29\text{ К}\geq\Delta T_{ph,c}\geq 9,11$ К; $d_{ph}=0,35$ нм, $57,55\text{ К}\geq\Delta T_{ph,S}\geq 20,44$ К, $43,38\text{ К}\geq\Delta T_{ph,c}\geq 15,43$ К; $d_{ph}=0,38$ нм, $40,62\text{ К}\geq\Delta T_{ph,S}\geq 36,50$ К, $38,65\text{ К}\geq\Delta T_{ph,c}\geq 22,47$ К.

Вочевидь, що наведені величини діяметрів, в силу їхньої порівнянности з постійною ґратниці заліза, треба розглядати виключно як оціночні, проте, такими, що вказують на тенденцію зміни інтервалів $\Delta T_{ph,S}$ і $\Delta T_{ph,c}$ із збільшенням d_{ph}. Слід зазначити, що граничні значення $\Delta T_{ph,S}$ і $\Delta T_{ph,c}$ є істотно меншими за Дебайову температуру заліза, що узгоджується з наближенням, закладеним у формулах (5), (6).

В заключній частині цього розділу зауважимо, що оцінки, проведені для области температур $T\geq T_D$ $(a\geq 1)$, вказують на слабкий вплив теплового руху ДС на ентропію та тепломісткість залізного нанодроту в даному температурному діяпазоні — S_{DW}/S_{ph}

і $c_{DW}/c_{ph} \le 10^{-2}$, де $S_{ph} = 3Nk_B(1 + \ln T/T_D)$, $c_{ph} = 3Nk_B$.

2. ОБГОВОРЕННЯ РЕЗУЛЬТАТІВ

Вище було встановлено зменшення діяпазонів актуальних температурних інтервалів зі збільшенням діяметра нанодроту. Максимально можливе значення цього параметра будемо розглядати в якості критичного діяметра d_{cr}. Оскільки верхньою границею $\Delta T_{e,m,S}$ і $\Delta T_{e,m,c}$ є температура Кюрі T_C заліза, то буде природньо для електронної та магнонної підсистем нанодроту визначати d_{cr} з умови рівности нижніх границь зазначених інтервалів тій же температурі T_C. В такому разі обчислення показують, що $d_{e,cr_S} = 2,52$ нм, $d_{e,cr_c} = 3$ нм і $d_{m,cr_S} = 2,01$ нм, $d_{m,cr_c} = 2,33$ нм відповідно. Вочевидь, що критичною температурою розглянутих явищ (максимально можливою температурою, за якої чинник ДС є актуальним) виступає $T_C = 1043$ К.

В той же час, у випадку фононної підсистеми, значення обох границь інтервалів $\Delta T_{ph,S}$ і $\Delta T_{ph,c}$ менші за T_D. Тому коректним буде визначати критичний діяметер із наступних умов: $\eta_{ph,S}(d_{ph,cr_S})_{\min} = 0,667$ і $\xi_{ph,c}(d_{ph,cr_c})_{\min} = 0,667$. Виходячи з наведеного, знаходимо $d_{ph,cr_S} = 0,3803$ нм ($T_{ph,cr_S} = 38,55$ К) (див. рис. 5, криву *4*) і $d_{ph,cr_c} = 0,39$ нм ($T_{ph,cr_c} = 31$ К) (див. рис. 6, криву *5*).

Порівняння одержаних даних з аналогічними характеристиками ніклевого нанодроту [10] показує зменшення значень критичних діяметрів підсистем, що складають залізний нанодріт. Такий результат є наслідком більшої величини M останнього. Справді, збільшення намагнетованости приводить до зростання поля знемагнетування ФН (на одиницю площини), яке, в свою чергу, має відповідати нанодроту з меншим діяметром, що й виявляється в одержаних нами критичних значеннях цього параметра.

Важливо зазначити, що змінна величина a являє собою відношення енергії поздовжньої ДС, яка дорівнює $\pi A d^2/\delta$ (див. формулу (1)), до енергії теплових коливань системи k_BT. Згідно з розрахунками, критичні значення a знаходяться в інтервалі $\cong 3,64$–8,24, що вище за 1. Даний результат вказує на можливість впливу чинника ДС на термодинамічні властивості нанодроту.

Встановлена вище особливість поведінки $d_{cr}(M)$ уможливлює запропонувати простий механізм збільшення критичних діяметрів підсистем залізного нанодроту шляхом зменшення його намагнетованости. Так, зменшення M до 10^3 Ґс приводить до: $d_{e,cr_S} = 3,13$ нм ($T_{e,cr_S} = 1043$ К), $d_{e,cr_c} = 3,73$ нм ($T_{e,cr_c} = 1043$ К), $d_{m,cr_S} = 2,4$ нм ($T_{m,cr_S} = 1043$ К), $d_{m,cr_c} = 2,78$ нм ($T_{m,cr_c} = 1043$ К) і $d_{ph,cr_S} = 0,46$ нм ($T_{ph,cr_S} = 33,2$ К), $d_{ph,cr_c} = 0,48$ нм ($T_{ph,cr_c} = 26,67$ К).

При $M = 10$ Ґс $d_{e,cr_S} = 8,34$ нм ($T_{e,cr_S} = 256$ К), $d_{e,cr_c} = 10,74$ нм ($T_{e,cr_c} = 226$ К), $d_{m,cr_S} = 5,85$ нм ($T_{m,cr_S} = 92,3$ К), $d_{m,cr_c} = 6,58$ нм

($T_{m,cr_c} = 72,34$ К), $d_{ph,cr_S} = 2,35$ нм ($T_{ph,cr_S} = 8,5$ К), $d_{ph,cr_c} = 2,4$ нм ($T_{ph,cr_c} = 6,8$ К).

Легко бачити, що зменшення намагнетованости залізного нанодроту до $M = 10$ Ґс приводить до істотного збільшення критичних діяметрів його складових підсистем.

Слід також зазначити, що значення критичних температур для електронної та магнонної підсистем для $M = 10^3$ Ґс, які дорівнюють 1043 К, є наближеними (до цілих). Вони обумовлені близькістю ентропії та тепломісткости ДС (за даних параметрів) до аналогічних характеристик для $M = 1,7 \cdot 10^3$ Ґс. Як показують обчислення, подальше зменшення намагнетованости приводить до значень ентропії та тепломісткости, значно менших за початкові. В свою чергу, таким термодинамічним станам відповідають більш низькі температури. Цей факт і відображується у значеннях критичних температур для $M = 10$ Ґс, істотно менших за відповідні величини залізного нанодроту з намагнетованістю $M = 1,7 \cdot 10^3$ Ґс.

Зазначимо, що поздовжня ДС утворюється в достатньо тонких нанодротах. Збільшення діяметра нанодроту приводить до трансформації даної ДС у Блохову точку, яка являє собою магнетну синґулярність («магнетний їжак»). Її намагнетованість можна представити у вигляді $\mathbf{M}(\mathbf{r}) = M\dfrac{\mathbf{r}}{r}$ ($\mathbf{r}$ — радіюс-вектор, проведений з центру Блохової точки у довільну точку ефективної сфери, що обмежує її магнетну структуру) [20]. Відповідно, енергія Блохової точки визначається обмінною взаємодією та становить $W_{mB} = AM^{-2}\int\limits_{r \le d} d\mathbf{r}\left(\vec{\nabla}\mathbf{M}(\mathbf{r})\right)^2 = 8\pi A d$. Порівняння цього виразу з енергією E_{DW} показує, що у ФН, діяметер яких $d \ge 8\delta$ (для заліза $d \ge 38$ нм), реалізується ДС у вигляді Блохової точки.

Наприкінці зазначимо, що наявність у магнетних солітонів ефективної маси [21–23] уможливлює розглядати поздовжню ДС і Блохову точку як квазичастинки. Тоді, враховуючи, що симетрія магнетної структури Блохової точки «вище» симетрії поздовжньої ДС, за аналогією з результатами роботи [24], слід очікувати більш слабкий вплив теплового руху ДС у вигляді Блохової точки на термодинамічні та магнетокалоричні властивості ФН.

3. ВИСНОВКИ

Встановлено, що ентропія та тепломісткість, спричинені тепловим рухом поздовжньої ДС, можуть бути одного порядку з ентропією та тепломісткістю електронної, магнонної та фононної (Дебайової компоненти) підсистем залізного циліндричного нанодроту.

Визначено критичні значення діяметрів і температур нанодроту, які відповідають зазначеному становищу.

Показано, що зменшення намагнетованости нанодроту посилює чинник впливу ДС на ентропію та тепломісткість його складових підсистем.

Передбачено більш слабкий вплив теплового руху ДС у вигляді Блохової точки на термодинамічні та магнетокалоричні властивості феромагнетних нанодротів.

Розглянуті в роботі явища можуть знайти практичне застосування в технологіях, що ґрунтуються на термодинамічних властивостях феромагнетних нанодротів, які містять ДС.

ЦИТОВАНА ЛІТЕРАТУРА

1. W. Hong, S. Lee, H. J. Chang, E. S. Lee, Y. Cho, *Biomaterials*, **106**: 78 (2016); 10.1016/j.biomaterials.2016.08.020
2. M. F. Contreras, R. Sougrat, A. Zaher, T. Ravasi, and J. Cosel, *Int. Journ. Nanomed.*, **10**: 2141 (2015); https://doi.org/10.2147/IJN.S77081
3. W. Zhou, J. Um, Ya. Zhang, A. Nelson, Z. Nemati, J. Modiano, B. Stalder, and R. Franklin, *IEEE Journal of Electromagnetics, RF and Microwaves in Medicine and Biology*, **3**, No. 2: 134 (2018); doi:10.1109/JERM.2018.2889049
4. A. B. A. Nana, T. Marimuthu, P. P. D. Kondiah, Y. E. Choonara, L. C. DuToit, and V. Pillay, *Cancers*, **11**, No. 12: 1 (2019); https://doi.org/10.3390/cancers11121956
5. D. Shore, A. Ghemes, O. Dragos-Pinzaru, Z. Gao, Qi Shao, A. Sharma, J. Um, I. Tabakovic, J. C. Bischof, and B. J. H. Stadler, *Nanoscale*, **11**, No. 31: 14607 (2019); https://doi.org/10.1039/C9NR01182J
6. P. D. McGary, L. Tan, J. Zou, B. Stadler, P. R. Downey, and A. B. Flatau, *Journ. Appl. Phys.*, **99**, No. 8: 08B310-1 (2006); https://doi.org/10.1063/1.2167332
7. S. Lepadatu, H. Saarikoski, R. Beacham, M. Jose-Benitez, T. A. Moore, G. Burnell, S. Sugimoto, D. Yesudas, M. C. Wheeler, J. Miguel, S. S. Dhessi, D. McGrouther, S. McVitie, G. Tatara, and C. H. Marrows, *Scientific Reports*, **7**, No. 1640: 1 (2017); doi:10.1038/s41598-017-01748-7
8. S. S. P. Parkin, M. Hayashi, and L. Thomas, *Science*, **320**, No. 5873: 190 (2008); doi:10.1126/science.1145799
9. A. B. Shevchenko and M. Yu. Barabash, *Physica B: Condensed Matters*, **556**: 114 (2019); https://doi.org/10.1016/j.physb.2018.12.025
10. A. B. Shevchenko, M. Yu. Barabash, and I. M. Zabolotnyi, *Results in Physics*, **16**: 102988(5) (2020); https://doi.org/10.1016/j.rinp.2020.102988
11. A. B. Shevchenko and M. Yu. Barabash, *J. Nano- Electron. Phys.*, **12**, No. 4: 04039(3) (2020); https://doi.org/10.21272/jnep.12(4).04039
12. M.-M. Song, W.-J. Song, H. Bi, J. Wang, W.-L. Wu, J. Sun, and M. Yu, *Biomaterials*, **31**, No. 7: 1509 (2010); doi:10.1016/j.biomaterials.2009.11.034

13. С. В. Вонсовский, М. И. Канцельсон, *Квантовая физика твердого тела* (Москва: Наука: 1983).
14. С. В. Вонсовский, *Магнетизм* (Москва: Наука: 1971).
15. A. B. Shevchenko and M. Yu. Barabash, *Nanoscale Research Letters*, **10**: 470(5) (2015); https://doi.org/10.1186/s11671-015-1175-x
16. A. B. Shevchenko and M. Yu. Barabash, *Nanoscale Research Letters*, **11**: 473(6) (2016); https://doi.org/10.1186/s11671-016-1680-6
17. A. B. Shevchenko and M. Yu. Barabash, *Results in Physics*, **13**: 102294(4) (2019); https://doi.org/10.1016/j.rinp.2019.102294
18. A. B. Shevchenko and M. Yu. Barabash, *Appl. Nanoscience*, **9**: 595 (2019); https://doi.org/10.1007/s13204-018-0644-9
19. А. Б. Шевченко, *Успехи физ. мет.*, **2**, № 2: 115 (2018); doi:10.15407/ufm.19.02.115
20. А. Малоземов, Дж. Слонзуски, *Доменные стенки в материалах с цилиндрическими магнитными доменами* (Москва: Мир: 1982).
21. Ю. А. Куфаев, Э. Б. Сонин, *ЖЭТФ*, **95**, № 4: 1523 (1989).
22. V. L. Dorman, V. L. Sobolev, and A. B. Shevchenko, *Journal of Magnetism and Magnetic Materials*, **94**, No. 3: 293 (1991); https://doi.org/10.1016/0304-8853(91)90090-W
23. V. L. Dorman, V. L. Sobolev, and A. B. Shevchenko, *Journal of Magnetism and Magnetic Materials*, **124**, Nos. 1–2: 221 (1993); https://doi.org/10.1016/0304-8853(93)90091-F
24. А. П. Шпак, А. Б. Шевченко, А. Б. Мельник, *ЖТФ*, **74**, № 3: 81 (2004).

REFERENCES

1. W. Hong, S. Lee, H. J. Chang, E. S. Lee, Y. Cho, *Biomaterials*, **106**: 78 (2016); 10.1016/j.biomaterials.2016.08.020
2. M. F. Contreras, R. Sougrat, A. Zaher, T. Ravasi, and J. Cosel, *Int. Journ. Nanomed.*, **10**: 2141 (2015); https://doi.org/10.2147/IJN.S77081
3. W. Zhou, J. Um, Ya. Zhang, A. Nelson, Z. Nemati, J. Modiano, B. Stalder, and R. Franklin, *IEEE Journal of Electromagnetics, RF and Microwaves in Medicine and Biology*, **3**, No. 2: 134 (2018); doi:10.1109/JERM.2018.2889049
4. A. B. A. Nana, T. Marimuthu, P. P. D. Kondiah, Y. E. Choonara, L. C. DuToit, and V. Pillay, *Cancers*, **11**, No. 12: 1 (2019); https://doi.org/10.3390/cancers11121956
5. D. Shore, A. Ghemes, O. Dragos-Pinzaru, Z. Gao, Qi Shao, A. Sharma, J. Um, I. Tabakovic, J. C. Bischof, and B. J. H. Stadler, *Nanoscale*, **11**, No. 31: 14607 (2019); https://doi.org/10.1039/C9NR01182J
6. P. D. McGary, L. Tan, J. Zou, B. Stadler, P. R. Downey, and A. B. Flatau, *Journ. Appl. Phys.*, **99**, No. 8: 08B310-1 (2006); https://doi.org/10.1063/1.2167332
7. S. Lepadatu, H. Saarikoski, R. Beacham, M. Jose-Benitez, T. A. Moore, G. Burnell, S. Sugimoto, D. Yesudas, M. C. Wheeler, J. Miguel, S. S. Dhessi, D. McGrouther, S. McVitie, G. Tatara, and C. H. Marrows, *Scientific Reports*, **7**, No. 1640: 1 (2017); doi:10.1038/s41598-017-01748-7
8. S. S. P. Parkin, M. Hayashi, and L. Thomas, *Science*, **320**, No. 5873: 190

(2008); doi:10.1126/science.1145799
9. A. B. Shevchenko and M. Yu. Barabash, *Physica B: Condensed Matters*, **556**: 114 (2019); https://doi.org/10.1016/j.physb.2018.12.025
10. A. B. Shevchenko, M. Yu. Barabash, and I. M. Zabolotnyi, *Results in Physics*, **16**: 102988(5) (2020); https://doi.org/10.1016/j.rinp.2020.102988
11. A. B. Shevchenko and M. Yu. Barabash, *J. Nano- Electron. Phys.*, **12**, No. 4: 04039(3) (2020); https://doi.org/10.21272/jnep.12(4).04039
12. M.-M. Song, W.-J. Song, H. Bi, J. Wang, W.-L. Wu, J. Sun, and M. Yu, *Biomaterials*, **31**, No. 7: 1509 (2010); doi:10.1016/j.biomaterials.2009.11.034
13. S. V. Vonsovsky and M. I. Kantselson, *Kvantovaya Fizika Tverdogo Tela* [Quantum Solid State Physics] (Moscow: Nauka: 1983) (in Russian).
14. S. V. Vonsovsky, *Magnetizm* [Magnetism] (Moscow: Nauka: 1971) (in Russian).
15. A. B. Shevchenko and M. Yu. Barabash, *Nanoscale Research Letters*, **10**: 470(5) (2015); https://doi.org/10.1186/s11671-015-1175-x
16. A. B. Shevchenko and M. Yu. Barabash, *Nanoscale Research Letters*, **11**: 473(6) (2016); https://doi.org/10.1186/s11671-016-1680-6
17. A. B. Shevchenko and M. Yu. Barabash, *Results in Physics*, **13**: 102294(4) (2019); https://doi.org/10.1016/j.rinp.2019.102294
18. A. B. Shevchenko and M. Yu. Barabash, *Appl. Nanoscience*, **9**: 595 (2019); https://doi.org/10.1007/s13204-018-0644-9
19. A. B. Shevchenko, *Usp. Fiz. Met.*, **2**, No. 2: 115 (2018) (in Russian); doi:10.15407/ufm.19.02.115.
20. A. P. Malozemoff and J. C. Slonczewski, *Domennyye Stenki v Materialakh s Tsilindricheskimi Magnitnymi Domenami* [Magnetic Domain Walls in Bubble Materials] (Moscow: Mir: 1982) (Russian translation).
21. Yu. A. Kufaev and Eh. B. Sonin, *JETP*, **68**, No. 4: 879 (1989).
22. V. L. Dorman, V. L. Sobolev, and A. B. Shevchenko, *Journal of Magnetism and Magnetic Materials*, **94**, No. 3: 293 (1991); https://doi.org/10.1016/0304-8853(91)90090-W
23. V. L. Dorman, V. L. Sobolev, and A. B. Shevchenko, *Journal of Magnetism and Magnetic Materials*, **124**, Nos. 1–2: 221 (1993); https://doi.org/10.1016/0304-8853(93)90091-F
24. A. P. Shpak, A. B. Shevchenko, and A. B. Melnik, *Zh. Tekhn. Fiz.*, **74**, No. 3: 81 (2004) (in Russian).

G. V. Kurdyumov Institute for Metal Physics of the N.A.S. of Ukraine,
36, Academician Vernadsky Blvd.,
UA-03142 Kyiv, Ukraine

[1] **Fig. 1.** Temperature dependences of relative entropy $\eta_e = \frac{S_e - S_{DW}}{S_e}$ of the electron subsystem for cylindrical iron nanowire with different diameters: *1*—$d_e = 1$ nm; *2*—$d_e = 1.5$ nm; *3*—$d_e = 2$ nm; *4*—$d_e = 2.5$ nm; *5*—$\eta_e = 0.667$.

[2] **Fig. 2.** Temperature dependences of relative heat capacity $\xi_e = \frac{c_e - c_{DW}}{c_e}$ of the electron subsystem for cylindrical iron nanowire with different diameters: *1*—$d_e = 1$ nm; *2*—$d_e = 1.5$ nm; *3*—$d_e = 2$ nm; *4*—$d_e = 2.5$ nm; *5*—$\eta_e = 0.667$.

---

[3] **Fig. 3.** Temperature dependences of relative entropy $\eta_m = \frac{S_m - S_{DW}}{S_m}$ of the magnon subsystem for cylindrical iron nanowire with different diameters: *1*— $d_m = 1$ nm; *2*— $d_m = 1.5$ nm; *3*— $d_m = 2$ nm; *4*—$\eta_m = 0.667$.

[4] **Fig. 4.** Temperature dependences of relative heat capacity $\xi_m = \frac{c_m - c_{DW}}{c_m}$ of the magnon subsystem for cylindrical iron nanowire with different diameters: *1*— $d_m = 1$ nm; *2*— $d_m = 1.5$ nm; *3*— $d_m = 2$ nm; *4*—$\eta_m = 0.667$.

[5] **Fig. 5.** Temperature dependences of relative entropy $\eta_{ph} = \frac{S_{ph} - S_{DW}}{S_{ph}}$ of the phonon subsystem for cylindrical iron nanowire with different diameters: *1*— $d_{ph} = 0.3$ nm; *2*— $d_{ph} = 0.35$ nm; *3*— $\eta_{ph} = 0.667$; *4*— $d_{ph,cr_S} = 0.3803$ nm.

[6] **Fig. 6.** Temperature dependences of relative heat capacity $\xi_{ph} = \frac{c_{ph} - c_{DW}}{c_{ph}}$ of the phonon subsystem for cylindrical iron nanowire with different diameters: *1*— $d = 0.3$ nm; *2*— $d = 0.35$ nm; *3*— $d = 0.38$ nm; *4*— $\xi_{ph} = 0.667$; *5*— $d_{ph,cr_c} = 0.39$.

Наносистеми, наноматеріали, нанотехнології
Nanosistemi, Nanomateriali, Nanotehnologii
2021, т. 19, № 4, сс. 823–830

PACS numbers: 72.80.Ey, 73.20.Hb, 73.40.Kp, 73.40.Lq, 81.15.Jj, 85.60.Bt, 85.60.Dw

Фоточутливі діоди Шотткі графіт/*n*-Si, виготовлені методом електронно-променевого випаровування

М. М. Солован[1], Г. М. Ямрозик[1], А. І. Мостовий[1], В. В. Брус[2], П. Д. Мар’янчук[1]

[1]*Чернівецький національний університет імені Юрія Федьковича,*
вул. Коцюбинського, 2,
58012 Чернівці, Україна
[2]*Nazarbayev University,*
53, Kabanbay Batyr,
010000 Nur-Sultan City, Kazakhstan

Вперше виготовлено фоточутливі діоди Шотткі графіт/*n*-Si шляхом електронно-променевого випаровування графіту на підкладинки з Si *n*-типу провідности. Показано, що створені фоточутливі діоди Шотткі графіт/*n*-Si мають висоту потенціяльного бар’єру у 0,46 еВ і такі фотоелектричні параметри: напруга холостого ходу $V_{oc} = 0{,}33$ В, струм короткого замикання $I_{sc} = 0{,}38$ мА, коефіцієнт заповнення $FF = 0{,}35$ за освітлення у 80 мВт/см^2. Їхні чутливість до електромагнетного випромінення та чутливість щодо виявлення знаходяться на рівні світових аналогів; тому такі діоди Шотткі можуть бути успішно використані для виготовлення фотоприймачів.

This paper presents the results of studies of the physical properties of photosensitive Schottky graphite/*n*-Si diodes fabricated by deposition of the thin graphite films by the electron beam evaporation in a universal vacuum system Leybold–Heraeus L560 from compressed pellets of graphite powder onto the substrates of *n*-type Si. The current–voltage characteristics (at different temperatures) are measured. The dominant mechanisms of the current transfer through the Schottky diodes in forward biases are determined. As revealed, the dominant current-transport mechanism is conditioned by the generation–recombination processes. The photosensitive Schottky graphite/*n*-Si diodes possess produce a maximum short-circuit current $I_{sc} = 0.38$ mA, an open-circuit voltage $V_{oc} = 0.33$ V, and a fill factor $FF = 0.35$ under standard illumination conditions (80 mW/cm^2). The sensitivity (R) and detectivity (D^*) are determined. As established, the studied Schottky graphite/*n*-Si diodes can be successfully used as ultraviolet-radiation detectors in the photodiode mode of operation.

Ключові слова: графіт, діод Шотткі, фотоприймач, тонкі плівки, механізми струмоперенесення.

Key words: graphite, Schottky diode, photodetector, thin films, current transfer mechanisms.

(Отримано 4 січня 2021 р.)

1. ВСТУП

Принциповими засадами технічного проґресу є розвиток енергетики, автоматизація виробництва та розробка нових матеріялів. Такі нові матеріяли мають відповідати складним вимогам сучасної техніки стосовно або окремих, достатньо чітко виражених характеристик, або комплексів властивостей.

Карбон — це один з найпоширеніших елементів у Всесвіті за масою після Гідроґену, Гелію й Оксиґену. Також це — один з найпоширеніших елементів на нашій планеті. Атоми Карбону мають властивість гібридизації своїх електронних орбіталей у формуванні хемічних зв'язків, що приводить до наявности різних його алотропних форм. Найпоширенішими з них є графіт та діямант, які мають кардинально різні фізичні властивості.

Графітові стрижні використовувалися у кристалічних детекторах примітивних радіоприймачів. Однак широке застосування вуглецевих і вуглецевмісних матеріялів в електроніці й оптоелектроніці розпочалося після відкриття сімейства вуглецевих наноматеріялів: фуллеренів, вуглецевих нанотрубок і графенів, за що було присуджено дві Нобелівські премії з фізики в 1998 та 2010 роках.

Створення напівпровідникових приладів зі стабільними параметрами та відтворюваними характеристиками пов'язане з вибором матеріялів, що відповідають певним вимогам [1, 2].

Недавно графіт було використано для виготовлення новітніх, екологічно чистих і дешевих наноструктурованих тонкоплівкових компонентів електронних приладів нового покоління [3, 4].

Більше того, нещодавні дослідження морфологічних і структурних властивостей нарисованих графітових плівок показують, що вони складаються з розупорядкованих зв'язаних графітових мікро- та наночастинок і нанопластівців з моно- та кількох графенових шарів. Тому такі плівки є двовимірними наноструктурованими об'єктами [5].

Наші попередні дослідження показали, що робочі елементи електронних пристроїв можуть бути створені на основі тонких плівок графіту. Зокрема, ми показали можливість виготовлення тонких плівок графіту двома методами: простим методом перенесення графітової плівки, нарисованої на соляній (NaCl) підкладинці, для виготовлення високоякісних фоточутливих бар'єрних структур «олівець на напівпровіднику» [6, 7] та методом електронно-променевого випаровування [7, 8]. Цими методами нами було виготовлено фоточутливі структури графіт/SiC [9, 10] і графіт/CdTe [11, 12].

Оскільки силіцій є основним матеріялом сучасної напівпровідникової електроніки, силової електроніки та геліоенергетики, актуальним є завдання створити діоди Шотткі графіт/Si і дослідити їхні електричні та фотоелектричні властивості.

2. ЕКСПЕРИМЕНТАЛЬНА ЧАСТИНА

Для виготовлення діод Шотткі використовували монокристалічний силіцій n-типу провідности з орієнтацією поверхні (100) товщиною у 330 мкм. Значення питомого опору та концентрації носіїв заряду для цих кристалів за кімнатної температури (295 К) становили $\rho = 6$ Ом·см і $n = 7{,}4 \cdot 10^{14}$ см$^{-3}$ відповідно. Глибина залягання рівня Фермі для базового матеріялу ($E_c - E_F = 0{,}27$ еВ) визначалася з виразу для концентрації рівноважних електронів: $n = 2(2\pi m_n kT/h^2)^{3/2}\exp\{-(E_c - E_F)/(kT)\}$. Щоб уникнути рекомбінації на тиловій стороні n-силіцію та забезпечити хороше збирання фотоґенерованих носіїв заряду, ми використовували підкладинки, які вже мали тиловий контакт із вбудованим внутрішнім полем, що був виготовлений шляхом напорошення шару власного гідроґенізованого аморфного силіцію (a-Si:H) товщиною у $\cong 10$ нм для пасивації поверхні підкладинки. Наступний шар сильнолеґованого Фосфором гідроґенізованого аморфного силіцію n^+ (a-Si:H) товщиною у $\cong 20$ нм був нанесений для створення ізотипного переходу з висотою бар'єру у $\cong 0{,}1$ еВ на задній стороні Si, а останнім наносили шар Al методом термічного випаровування.

Виготовлення діод Шотткі графіт/n-Si було проведено осадженням тонкої графітової плівки на підкладинку Si(100) розміром 5×5×0,33 мм в універсальній вакуумній установці Leybold–Heraeus L560 шляхом випаровування електронним пучком чистого масивного полікристалічного графіту. Інтенсивність пучка електронів, швидкість осадження та товщина плівки контролювалася за допомогою контролера осадження INFICON XTC. Упродовж процесу осадження залишковий тиск у вакуумній камері був близько $5 \cdot 10^{-5}$ мбар. Процес осадження тривав 1,5 хв. із середньою швидкістю осадження у 0,27 нм/с (товщина плівки складала близько 25 нм) за температури підкладинки у 723 К. Тонкі графітові плівки одночасно наносили на скляну підкладинку для аналізи їхніх електричних і оптичних властивостей. Електричні та кінетичні параметри тонких графітових плівок вимірювали за допомогою чотирьох і шістьох зондових методів відповідно.

Спектер пропускання тонких графітових плівок на скляних підкладинках вимірювали за допомогою спектрофотометра СФ-2000. Експериментальні дані були виміряні в діяпазоні довжин хвиль від 200 до 1100 нм з кроком у 1 нм.

Спектер пропускання тонких графітових плівок лінійно зростає від 60 до 85% із збільшенням довжини хвилі від 300 до 1100 нм.

Для тонкої графітової плівки питома електрична провідність, концентрація електронів і їхня Голлова рухливість були виміряні за кімнатної температури: $\sigma = 5{,}8$ Ом$^{-1}$·см$^{-1}$, $n = 5\cdot10^{20}$ см$^{-3}$, $\mu_H = 6\cdot10^{-2}$ см^2·В$^{-1}$·с$^{-1}$ відповідно. Чистий полікристалічний графіт, використаний в якості мішені для електронно-променевого випаровування, має на два порядки вищу Голлову рухливість електронів у 7,9 см^2·В$^{-1}$·с$^{-1}$.

Вольт-амперні характеристики досліджуваних діод Шотткі вимірювали за стандартною методикою з використанням точного фемто/піко-амперметра Keysight B2985A із вбудованим джерелом (±1000 В); в якості вольтметра використовували Agilent 34410A.

3. РЕЗУЛЬТАТИ ТА ЇХ ОБГОВОРЕННЯ

На рисунку 1 показано темнову ВАХ діоди Шотткі графіт/n-Si за кімнатної температури. Досліджувані діоди Шотткі графіт/n-Si мали яскраво виражені діодні характеристики з коефіцієнтом випрямлення $RR \approx 5\cdot10^2$.

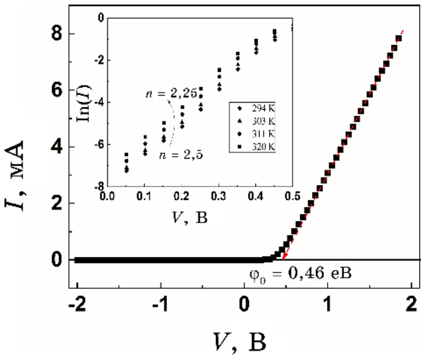

Рис. 1. Вольт-амперні характеристики діод Шотткі графіт/n-Si, виміряні за кімнатної температури. На вставці — прямі гілки ВАХ діод Шотткі графіт/n-Si у напівлогаритмічному масштабі.[1]

Висота потенціяльного бар'єру $\varphi_0 = 0{,}46$ еВ ($\varphi_0 = eV_{bi}$, де V_{bi} — контактна ріжниця потенціялів) діод Шотткі графіт/n-Si оцінювалася шляхом екстраполяції прямолінійної ділянки ВАХ до перетину з віссю напруги.

Для встановлення домінувальних механізмів струмоперенесення в діодах Шотткі графіт/n-Si проаналізовано температурні залежності ВАХ (вставка на рис. 1). Аналіза прямих гілок ВАХ діод Шотткі графіт/n-Si, побудованих у напівлогаритмічному масштабі, показала, що на залежності $\ln I = f(V)$ спостерігаються прямолінійні ділянки, що свідчить про експоненційну залежність струму від напруги.

В даному випадку виміряні ВАХ описуються за допомогою стандартної формули:

$$I = I_0 \exp\left(\frac{qV}{nkT}\right), \tag{1}$$

де I_0 — струм наситу, n — коефіцієнт неідеальности, k — Больцманнова стала, T — абсолютна температура.

Значення коефіцієнта неідеальности n ($\Delta\ln(I)/\Delta(V) = e/(nkT)$) змінюється від 2,5 до 2,25 ($3kT/e < V < 0{,}5$ В) з підвищенням температури від 294 до 320 К. Значення показника неідеальности, близькі до 2, дають можливість припустити, що основний механізм струмоперенесення визначається ґенераційно-рекомбінаційними процесами в області просторового заряду, а саме значення n змінюється від 2,5 до 2,25 з підвищенням температури в інтервалі 295–320 К (вставка на рис. 1). Це свідчить про те, що у вище запропонований домінувальний механізм струмоперенесення, який зумовлений ґенераційно-рекомбінаційними процесами в області просторового заряду, роблять внесок електрично активні поверхневі стани, розміщені на металурґійній роздільчій межі досліджуваної діоди [13].

Дослідженнями освітлених ВАХ показано, що такі діоди Шотткі є фоточутливими, як видно з рис. 2, при освітленні білим світлом інтенсивністю у 80 мВт/см^2; зворотній струм I_{light} зростає в порівнянні з його величиною у темряві I_{dark} майже на два порядки.

Четвертий квадрант освітленої ВАХ є найбільш важливим, оскільки він визначає всі фотоелектричні параметри (рис. 3); з нього видно, що діоди Шотткі графіт/n-Si мають такі фотоелектричні параметри: напруга холостого ходу $V_{oc} = 0{,}33$ В, струм короткого замикання $I_{sc} = 0{,}38$ мА, коефіцієнт заповнення $FF = 0{,}35$ за інтенсивности освітлення у 80 мВт/см^2.

Оцінити продуктивність фотоприймача більш кількісно можна за допомогою визначення чутливости до електромагнетного випромінення (R) і чутливости щодо виявлення (D^*), які відобра-

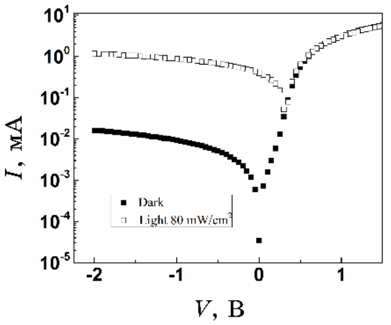

Рис. 2. Темнова та світлова (інтенсивність освітлення у 80 мВт/см^2) ВАХ діод Шотткі графіт/*n*-Si.[2]

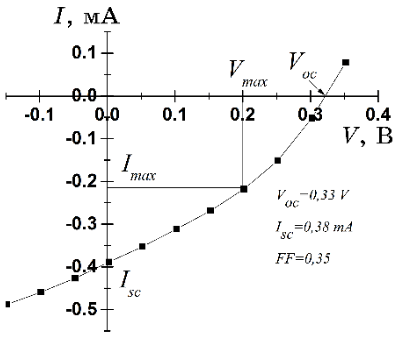

Рис. 3. Четвертий квадрант освітленої ВАХ діод Шотткі графіт/*n*-Si.[3]

жають чутливість фотоприймача до падного випромінення [14]:

$$R = (I_{light} - I_{dark})/P_{opt} \, , \qquad (2)$$

$$D^* = R\sqrt{A/(2qI_{dark})} \, , \qquad (3)$$

де A — активна площа фотоприймача.

На вставках до рис. 4, *а*, *б* наведено $R \quad f(V_{rev})$ і $D^* = f(V_{rev})$; з них видно, що чутливість (R) при збільшенні зворотнього зміщення V_{rev} плавно збільшується, що зумовлено розширенням області просторового заряду (збільшенням висоти потенціяльного бар'єру), унаслідок чого зростає ефективність розділення фотоґенерованих електрон-діркових пар, а чутливість щодо виявлення (D^*), яка описує нормовану потужність опромінення, потрібну для одержання сиґналу від фотоприймача на рівні шуму, зменшується, що зумовлено зростанням темнового зворотнього струму I_{dark}, який є електричним шумом у даному випадку.

Варто зазначити, що значення чутливости щодо виявлення,

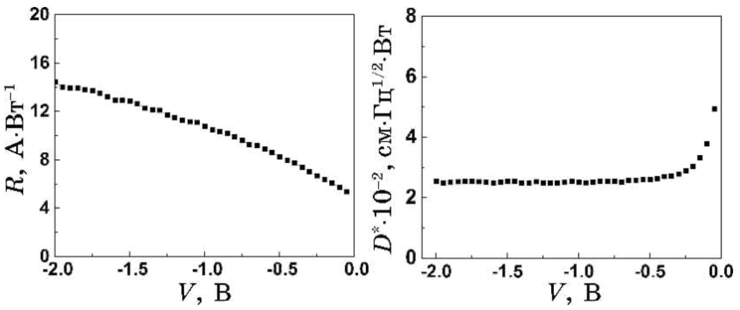

а *б*

Рис. 4. Залежності чутливости до електромагнетного випромінення (R) та чутливости щодо виявлення (D^*) від напруги для діод Шотткі графіт/n-Si при зворотньому зміщенні.[4]

одержане для даних діод Шотткі, не поступається значенням, які одержано для фотодіод на основі InGaAs, PbS, PbSe, а також на декілька порядків перевищує відповідні значення для фотодіод на основі HgCdZnTe [15].

4. ВИСНОВКИ

Вперше виготовлено фоточутливі діоди Шотткі графіт/n-Si методом електронно-променевого випаровування.

Встановлено, що виготовлені фоточутливі діоди Шотткі графіт/n-Si мають висоту потенціяльного бар'єру у 0,46 еВ, а домінувальні механізми струмоперенесення за прямих зміщень добре описуються в рамках ґенераційно-рекомбінаційного моделю за участю поверхневих станів.

Показано, що створені методом електронно-променевого випаровування фоточутливі діоди Шотткі графіт/n-Si мають такі фотоелектричні параметри: напруга холостого ходу $V_{oc} = 0{,}33$ В, струм короткого замикання $I_{sc} = 0{,}38$ мА, коефіцієнт заповнення $FF = 0{,}35$ за освітлення у 80 мВт/см^2, а їхня чутливість до електромагнетного випромінення та чутливість щодо виявлення знаходяться на рівні світових аналогів. Тому такі діоди Шотткі можуть бути успішно використані для виготовлення фотоприймачів.

ЦИТОВАНА ЛІТЕРАТУРА–REFERENCES

1. Z. I. Alferov, *Semiconductors*, **32**: 1 (1998);
https://doi.org/10.1134/1.1187350
2. C. Xie, Y. Wang, Z. X. Zhang, D. Wang, and L. B. Luo, *Nano Today*, **19**:

41 (2018); https://doi.org/10.1016/j.nantod.2018.02.009
3. R. K. Arun, V. Gupta, P. Singh, G. Biswas, and N. Chanda, *Chemistry Select*, **4**: 152 (2019); https://doi.org/10.1002/slct.201802960
4. N. Kurra and G. U. Kularni, *Lab on a Chip*, **13**: 2866 (2013); https://doi.org/10.1039/C3LC50406A
5. Y. Wang and H. Zhou, *Energy Environ. Sci.*, **4**: 1704 (2011); https://doi.org/10.1039/C0EE00759E
6. V. V. Brus and P. D. Maryanchuk, *Carbon*, **78**: 613 (2014); https://doi.org/10.1016/j.carbon.2014.07.021
7. M. M. Solovan, H. M. Yamrozyk, V. V. Brus, and P. D. Maryanchuk, *East Eur. J. Phys.*, **4**: 154 (2020); https://doi.org/10.26565/10.26565/2312-4334-2020-4-19
8. V. V. Brus et al., *Nanotechnology*, **31**: 505706 (2020); https://doi.org/10.1088/1361-6528/abce55
9. M. N. Solovan, G. O. Andrushchak, A. I. Mostovyi, T. T. Kovaliuk, V. V. Brus, and P. D. Maryanchuk, *Semiconductors*, **52**: 236 (2018); https://doi.org/10.1134/S1063782618020185
10. M. M. Solovan, H. P. Parkhomenko, and P. D. Marianchuk, *Journal of Physical Studies*, **23**: 4801 (2019); https://doi.org/10.30970/jps.23.4801
11. V. V. Brus, P. D. Maryanchuk, M. I. Ilashchuk, J. Rappich, I. S. Babiychuk, and Z. D. Kovalyuk, *Solar Energy*, **112**: 78 (2015); https://doi.org/10.1016/j.solener.2014.11.023
12. V. V. Brus and P. D. Maryanchuk, *Appl. Phys. Lett.*, **104**: 173501 (2014); https://doi.org/10.1063/1.4872467
13. B. L. Sharma and R. K. Purohit, *Semiconductor Heterojunctions* (Oxford–New York: Pergamon Press: 1974).
14. X. Zhang, D. Hu, Z. Tang, and D. Ma, *Applied Surface Science*, **357**: 1939 (2015); https://doi.org/10.1016/j.apsusc.2015.09.146
15. P. Long, S. Varadaraajan, J. Matthews, and J. F. Schetzina, *Optoelectronics Review*, **10**: 251 (2002).

---

[1]*Yuriy Fedkovych Chernivtsi National University,*
2, Kotsyubynsky Str.,
UA-58012 Chernivtsi, Ukraine
[2]*Nazarbayev University,*
53, Kabanbay Batyr,
010000 Nur-Sultan City, Kazakhstan

[1] **Fig. 1.** Current–voltage characteristics of the Schottky graphite/*n*-Si diodes measured at room temperature. The inset shows the forward I–V characteristic of the Schottky graphite/*n*-Si diodes on semi-logarithmic scale.

[2] **Fig. 2.** Dark and light (with illumination intensity of 80 mW/cm^2) I–V characteristics of the Schottky graphite/*n*-Si diodes.

[3] **Fig. 3.** The fourth quadrant of the illuminated I–V characteristic of the Schottky graphite/*n*-Si diodes.

[4] **Fig. 4.** Dependences of sensitivity (R) and detectivity (D^*) on voltage for the Schottky graphite/*n*-Si diodes at reverse bias mode.

Наносистеми, наноматеріали, нанотехнології
Nanosistemi, Nanomateriali, Nanotehnologii
2021, т. 19, № 4, сс. 831–840

PACS numbers: 68.37.-d, 78.20.Ci, 78.40.-q, 78.66.-w, 78.67.Sc, 81.07.Pr, 82.35.Np

Low Cost and Excellent Optical Properties of PEO Doped with $CoFe_2O_4$ Nanoparticles for Optoelectronics Applications

Marwa Sajjad and Ahmed Hashim

College of Education for Pure Sciences,
Department of Physics,
University of Babylon,
Hillah, Iraq

Magnetic films of the polyethylene oxide (PEO) and cobalt ferrite nanoparticles' ($CoFe_2O_4$ NPs) nanocomposites are fabricated for magnetic, electronic, and optical applications with low cost and low weight. The structural and optical properties of PEO/$CoFe_2O_4$ nanocomposites are investigated. The results indicate that the absorbance (A), absorption coefficient (α), extinction coefficient (k), refractive index (n), real (ε_1) and imaginary (ε_2) parts of dielectric constant, and optical conductivity (σ) of PEO are increased with increasing of the $CoFe_2O_4$ NPs content, while the transmittance (T) and energy band gap (E_g) are decreased as $CoFe_2O_4$ NPs concentration increases. Finally, the results show that PEO/$CoFe_2O_4$ nanocomposites may be used for the flexible optoelectronics fields.

Магнетні плівки нанокомпозитів з оксиду поліетилену (ПЕО) та наночастинок кобальтового фериту ($CoFe_2O_4$ НЧ) виготовляються для магнетних, електронних і оптичних застосувань з низькою вартістю та низькою вагою. Досліджено структурні й оптичні властивості нанокомпозитів ПЕО/$CoFe_2O_4$. Результати показують, що спектральна поглинальна здатність (A), коефіцієнт поглинання (α), коефіцієнт екстинкції (k), показник заломлення (n), реальна (ε_1) й уявна (ε_2) частини діелектричної константи, а також оптична провідність (σ) ПЕО збільшуються зі збільшенням вмісту $CoFe_2O_4$ НЧ, тоді як коефіцієнт пропускання (T) та ширина забороненої енергетичної зони (E_g) зменшуються у міру збільшення концентрації $CoFe_2O_4$ НЧ. Нарешті, результати показують, що нанокомпозити PEO/$CoFe_2O_4$ можуть використовуватися для областей трансформовної (гнучкої) оптоелектроніки.

Key words: polyethylene oxide, ferrite, nanocomposites, absorbance, energy gap, optoelectronics.

Ключові слова: оксид поліетилену, ферит, нанокомпозити, спектральна поглинальна здатність, енергетична щілина, оптоелектроніка.

(Received 16 January, 2021; in revised form, 19 January, 2021)

1. INTRODUCTION

Nanocomposites are a relatively new class of materials with ultrafine phase dimensions, typically of the order of a few nanometres. The objectives for preparation of enhanced performance nanomaterials are to obtain a homogeneous distribution of the nanoparticles within the polymer matrix, and to promote a strong interfacial adhesion between the matrix and the nanofiller. Nanocomposites could dramatically induce improvements in mechanical and electrical properties, heat resistance, radiation resistance and other ones because of the nanometre-size dispersion of the inorganic fillers in the organic matrix. An immense amount of research and development has been devoted to characterizing and understanding the mechanical and physical properties of such nanocomposites. In recent years, studies on the optical, thermal and electrical properties of polymer nanocomposites have attracted much attention in view of their important applications in optical devices. The optical properties of polymers can be enormously modified by addition of nanoparticles, which react effectively with the host matrix due to their very large surface areas with respect to macro- and microparticles [1].

Organic polymers show ample evidence of optical, electronic and optoelectronic properties and are at length used in optical devices like lenses, optical waveguides, optical switches, light emitting diodes and nonlinear optical applications extended use of optical polymers; therefore, it is advantageous to have polymers with a property, like refractive index, within a certain range [2].

Polyethylene oxide (PEO) is a linear and semi-crystalline polymer. Because PEO is a linear polymer, the regularity of structure unit permits a high crystallinity degree. The chemical structure of PEO contains of polar group –O– that can interact/associate with the cations of metal salt. Thus, PEO can solvate different types of salts. However, the reactivity is very low because of its structural unit has C–H, C–C, C–O bonds. Due to this, it is stabilized chemically and electrochemically. However, a high concentration of crystalline phase within PEO polymer confines the conductivity [3].

Recently, attention in nanosize spinel ferrites has significantly increased due to their importance in understanding the fundamentals in nanomagnetism. Ferrite with remarkable magnetic and microwave absorbing properties has been widely used in the fields of data storage devices, magnetic sensors, actuators, biotechnology, and audio tapes. Ferrite properties strongly depend on the chemical composition, cation distribution, sintering temperature and time, additive amount of the cations and methods of preparation [4].

$CoFe_2O_4$ has received special attention because of its chemical stability, large magnet astrictive coefficient, mechanical hardness high coercivity, moderate saturation magnetization, and large magnetocrystalline anisotropy. The magnetic properties are dependent to the particle size. The energy of a magnetic particle was overall associated on the uniaxial anisotropy, magnetization direction, and easy axis aligned with the direction of external field. $CoFe_2O_4$ is a hard magnetic material with high coercivity and suitable magnetization. These characteristics, along with their tremendous physical and chemical stability, make $CoFe_2O_4$ nanoparticles suitable for applications such as high-density digital recording disks and lithium batteries [5]. This paper aims to investigate a new type of nanocomposites to use it for semiconductors and optoelectronics applications.

2. MATERIALS AND METHODS

Magnetic nanocomposites samples of polyethylene oxide (PEO) and cobalt ferrite nanoparticles ($CoFe_2O_4$ NPs) nanocomposites were fabricated by using casting technique. The PEO solution was prepared by dissolving 0.4 gm in 50 ml of distilled water by using magnetic stirrer. The $CoFe_2O_4$ NPs were added to the PEO solution with different weight percentages: 1.5, 3 and 4.5 wt.%. The optical properties of PEO/$CoFe_2O_4$ nanocomposites were measured by using the double beam spectrophotometer (Shimadzu, UV-1800Å, Japan) in wavelength 200–800 nm.

3. RESULTS AND DISCUSSION

The variation of optical absorbance of PEO/$CoFe_2O_4$ nanocomposites as function of wavelength is shown in Fig. 1. The optical absorption analysis is an important tool to obtain optical band gap energy of crystalline matter, corresponds to the electron excitation from the valence band to the conduction band, and can be used to determine the nature and value of the band gap. The PEO/$CoFe_2O_4$ nanocomposites showed high absorbance in UV region due to the behaviour of $CoFe_2O_4$ nanoparticles, which are may be used as UV shielding and low-weight electronics applications. An amount of $CoFe_2O_4$ nanoparticles is required to reduce the value of gap energy in nanocomposites, and it has different effect depending on type of polymer matrix. The insertion of the $CoFe_2O_4$ nanoparticles into the PEO films has a double effect because it increases the energy of the $CoFe_2O_4$ gap and decreases that of the polymer and increase in charge-carriers' numbers [6–15]. The absorption coefficient (α) of nanocomposites is determined by [16]:

$$\alpha = 2.303A/t, \tag{1}$$

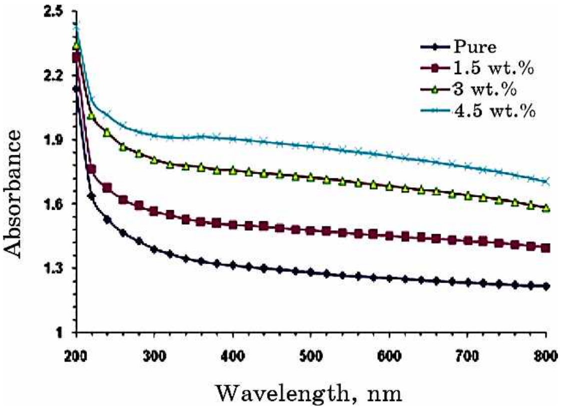

Fig. 1. Variation of optical absorbance of nanocomposites as function of wavelength.

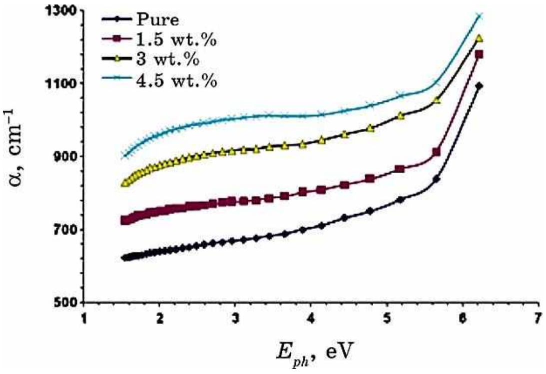

Fig. 2. Variation of absorption coefficient for nanocomposites with photon energy.

where *A* is the absorbance of sample, and *t* is the sample thickness.

Figure 2 shows the variation of absorption coefficient for PEO/$CoFe_2O_4$ nanocomposites with photon energy of the incident light. As shown in this figure, the absorption coefficient of PEO/$CoFe_2O_4$ nanocomposites is high at high energies. This means that the electron transition has high possibility; *i.e.*, the energy of incident photon is enough to transit the electron from the valence band to the conduction band, which due to the energy of the incident photon is greater than the energy band gap. When the values of the absorption coefficient of material are high $\alpha > 10^4$ cm^{-1}, it is expected that direct transition of electron. While, when the values of the absorption coefficient of material are low ($\alpha < 10^4$ cm^{-1}), it is expected that indirect transition of electron. The values of absorption coefficient of PEO/$CoFe_2O_4$ nanocomposites are low ($\alpha < 10^4$) cm^{-1}; the transition of electron is indirect. The absorption coefficient of nanocomposites increases with the increasing of the concentrations of $CoFe_2O_4$ nanoparticles. This is attributed to increasing number of charge carriers [16], as shown in Fig. 3, and, hence, increase the absorbance and absorption coefficient.

The non-direct transition model for amorphous semi-conductors is defined as follows [17]:

$$\alpha h\upsilon = B(h\upsilon - E_g)^r ; \qquad (2)$$

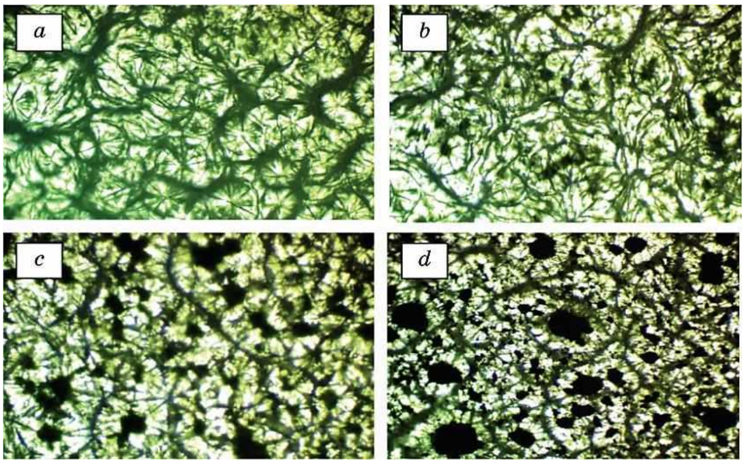

Fig. 3. Microscope images of PEO/$CoFe_2O_4$ nanocomposites (×10): *a*—for PEO; *b*—for 1.5 wt.% $CoFe_2O_4$ NPs; *c*—for 3 wt.% $CoFe_2O_4$ NPs; *d*—for 4.5 wt.% $CoFe_2O_4$ NPs.

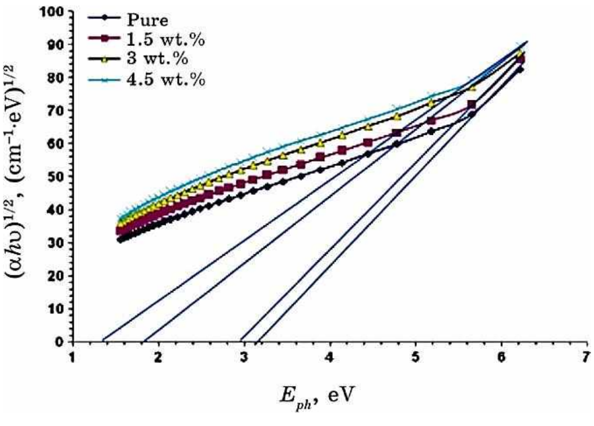

Fig. 4. Values of energy band gap for allowed indirect transition.

here, B is a constant, $h\upsilon$ is the photon energy, E_g is the energy band gap, and $r = 2$ or 3 for allowed and forbidden indirect transition, respectively.

Figures 4 and 5 show the values of energies band gap for allowed and forbidden indirect transition, respectively. These figures show that the values of energy gap for allowed and forbidden indirect transition decrease with increasing $CoFe_2O_4$ nanoparticles' concentration; this decrease is due to $CoFe_2O_4$ nanoparticles' content, which is responsible for the formation of some defects in the films. These defects produce the localized states in the optical band gap and overlap. These overlaps give an evidence for decreasing energy band gap, when the $CoFe_2O_4$ nanoparticles' content is increased in the polymeric matrix. In other words, the decreased optical gap reflects the increase in the degree of disorder in the films [17, 18]. The extinction coefficient k is given by

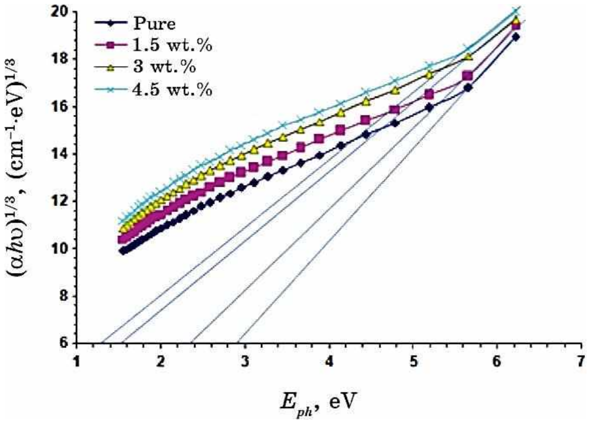

Fig. 5. Values of energy band gap for forbidden indirect transition.

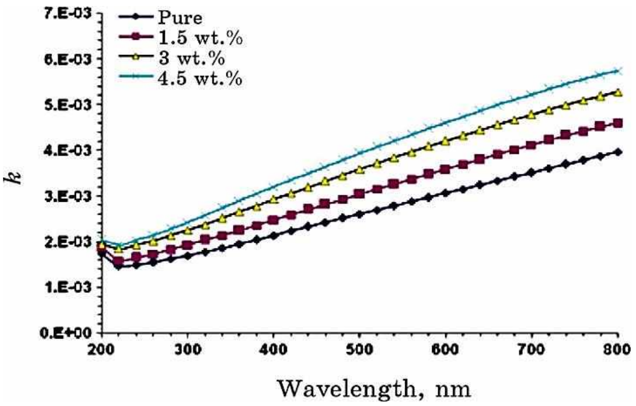

Fig. 6. Variation of extinction coefficient for nanocomposites with wavelength.

using the equation [18]:

$$k = \alpha\lambda/(4\pi). \qquad (3)$$

The refractive index n can be calculated by using the equation [19]:

$$n = (1 + R^{1/2})/(1 - R^{1/2}). \qquad (4)$$

Figure 6 shows the variation of extinction coefficient for PEO/$CoFe_2O_4$ nanocomposites as a function of wavelength. This figure shows that the extinction coefficient of PEO increases with the increasing of the $CoFe_2O_4$ nanoparticles' concentration; this is due to the increase in optical absorption and photon dispersion in the polymer matrix [19].

The refractive index of PEO/$CoFe_2O_4$ nanocomposites as a function of wavelength is shown in Fig. 7. As shown in this figure, the refractive index of PEO increases with the increasing of the $CoFe_2O_4$ nanoparticles concentrations. It is decreased with the increase of the wavelength. This behaviour is attributed to the increase of the density of nanocomposites.

When the incident light interacts with a sample, it has high refractivity at UV-region; hence, the values of refractive index will be increased [19].

The real (ε_1) and imaginary (ε_2) parts of dielectric constant of PEO/$CoFe_2O_4$ nanocomposites are given by the following equations [20]:

$$\varepsilon_1 = n^2 - k^2, \qquad (5)$$

$$\varepsilon_2 = 2nk. \qquad (6)$$

The dielectric constant (with real and imaginary parts) of PEO/$CoFe_2O_4$ nanocomposites is shown in Figs. 8 and 9. From these figures, it is clear that the increase in $CoFe_2O_4$ concentration leads to increase of absorption coefficient and refractive index and subsequently leads to increase of the real and imaginary parts of dielectric constant of PEO [20].

The optical conductivity of PEO/$CoFe_2O_4$ nanocomposites is determined by the equation [21]:

$$\sigma = \alpha nc/(4\pi). \qquad (7)$$

Figure 10 shows the variation of optical conductivity with the wavelength for the PEO/$CoFe_2O_4$ nanocomposites. This figure shows that the optical conductivity of PEO/$CoFe_2O_4$ nanocomposites is decreased with the increase of the wavelength; this behaviour attributed to the optical conductivity depends strongly on the wavelength of the radiation incident on the samples of nanocomposites; the increased optical

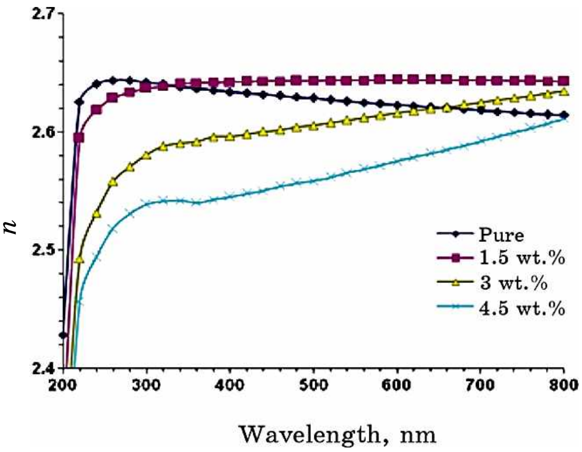

Fig. 7. Refractive index of PEO/$CoFe_2O_4$ nanocomposites as a function of wavelength.

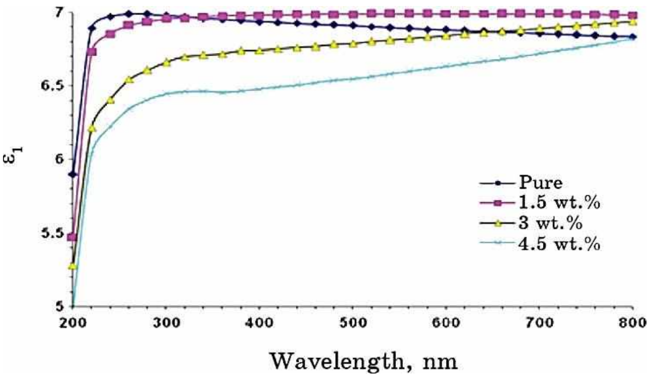

Fig. 8. Real dielectric constant of PEO/$CoFe_2O_4$ nanocomposites.

conductivity at low wavelength of photon is due to high absorbance of nanocomposites in that region and, hence, increase of the charge transfer excitations.

The optical conductivity spectra indicate that the samples are transparent within the visible and near infrared regions. In addition, the optical conductivity of PEO is increased with the increase of $CoFe_2O_4$ nanoparticles' concentration. This behaviour is related to the creation of localized levels in the energy gap; the increase of $CoFe_2O_4$ nanoparticles' concentration increase the density of localized stages in the band structure. Hence, increase of the absorption coefficient consequently increases the optical conductivity of PEO/$CoFe_2O_4$ nanocomposites [21–24].

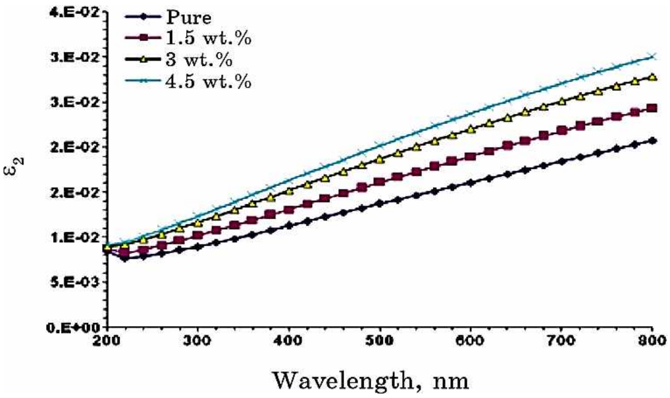

Fig. 9. Imaginary dielectric constant of PEO/$CoFe_2O_4$ nanocomposites.

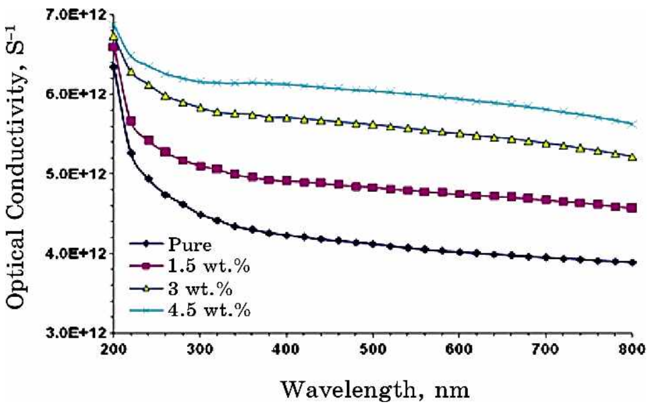

Fig. 10. Variation of optical conductivity with the wavelength of nanocomposites.

4. CONCLUSIONS

In this work, the structural and optical properties of PEO/$CoFe_2O_4$ nanocomposites have been investigated to use in optoelectronics applications such as sensors, solar cells, capacitors, transistors, diodes, *etc*.

The results indicated to the absorbance, absorption coefficient, extinction coefficient, refractive index, dielectric constant parts and optical conductivity of PEO, which are increased with the increase in $CoFe_2O_4$ nanoparticles concentration, while the transmittance and energy band gap are decreased with the increase in $CoFe_2O_4$ nanoparticles' concentration.

The PEO/$CoFe_2O_4$ nanocomposites have higher absorbance in the UV-region.

REFERENCES

1. Z. M. Elimat, A. M. Zihlif, and M. Avella, *J. of Experimental Nanoscience*, **3**, No. 4: 259 (2008).
2. K. Das, P. Pendke, and J. M. Keller, *Res. J. of Recent Sci.*, **5**: 79 (2016).
3. E. M. Abdelrazek, A. M. Abdelghany, and S. I. Badr, *J. Mater. Res. Technol.*, **7**, No. 4: 419 (2018).
4. M. T. Jamil, J. Ahmad, S. H. Bukhari, T. Sultan, M. Y. Akhter, H. Ahmad, and G. Murtaza, *J. of Ovonic Research*, **13**, No. 1: 45 (2017).
5. M. A. Golsefidi, F. Yazarlou, M. Naeimi Nezamabad, B. Naeimi Nezamabad, and M. Karimi, *J. Nanostruct.*, **6**, No. 2: 121 (2016); doi:10.7508/jns.2016.02.003
6. A. Hashim and Z. S. Hamad, *Egypt. J. Chem.*, **63**, Iss. 2: 461 (2020); doi:10.21608/EJCHEM.2019.7264.1593
7. K. H. H. Al-Attiyah, A. Hashim, and S. F. Obaid, *Inter. J. of Plastics Techno.*, **23**, No. 1: (2019); https://doi.org/10.1007/s12588-019-09228-5
8. A. Hashim, K. H. H. Al-Attiyah, and S. F. Obaid, *Ukr. J. Phys.*, **64**, No. 2: 157 (2019); https://doi.org/10.15407/ujpe64.2.157
9. H. Ahmed, H. M. Abduljalil, and A. Hashim, *Transactions on Elect. and Electronic Mater.*, **20**: 218 (2019); https://doi.org/10.1007/s42341-019-00111-z
10. A. Hashim and N. Hamid, *J. of Bionanoscience*, **12**, No. 6: 788 (2018); doi:10.1166/jbns.2018.1591
11. B. Abbas and A. Hashim, *Inter. J. of Emerging Trends in Eng. Res.*, **7**, No. 8: 131 (2019); https://doi.org/10.30534/ijeter/2019/06782019
12. A. Hashim and Z. S. Hamad, *J. of Bionanoscience*, **12**, No. 4: 504 (2018); doi:10.1166/jbns.2018.1561
13. N. H. Al-Garah, F. L. Rashid, A. Hadi, and A. Hashim, *J. of Bionanoscience*, **12**, No. 3: 336 (2018); doi:10.1166/jbns.2018.1538
14. A. Hashim and A. Jassim, *Sensor Letters*, **15**, No. 12: 1003 (2017); doi:10.1166/sl.2018.3915
15. I. R. Agool, F. S. Mohammed, and A. Hashim, *Advances in Environmental Biology*, **9**, No. 11: 1 (2015).
16. A. Hashim and Q. Hadi, *J. of Inorganic and Organometallic Polymers and Materials*, **28**, Iss. 4: 1394 (2018); https://doi.org/10.1007/s10904-018-0837-4
17. A. Hashim and Q. Hadi, *J. of Mater. Sci.: Materials in Electronics*, **29**: 11598 (2018); https://doi.org/10.1007/s10854-018-9257-z
18. A. Hashim, *J. of Inorganic and Organometallic Polym. and Mater.*, **30**: 3894 (2020); https://doi.org/10.1007/s10904-020-01528-3
19. A. Hashim and A. Jassim, *J. of Bionanoscience*, **12**, No. 2: 170 (2018); doi:10.1166/jbns.2018.1518
20. A. Hashim, Y. Al-Khafaji, and A. Hadi, *Transactions on Elect. and Electronic Mater.*, **20**, No. 6: 530 (2019); https://doi.org/10.1007/s42341-019-00145-3
21. A. Hadi, A. Hashim, and Y. Al-Khafaji, *Transactions on Elect. and Electronic Mater.*, **21**, No. 3: 283 (2020); https://doi.org/10.1007/s42341-020-00189-w
22. A. Hashim, A. J. Kadham, A. Hadi, and M. A. Habeeb, *Nanosistemi, Nanomateriali, Nanotehnologii*, **19**, Iss. 2: 327 (2021); https://doi.org/10.15407/nnn.19.02.327
23. A. Hashim and Z. S. Hamad, *Nanosistemi, Nanomateriali, Nanotehnologii*, **18**, Iss. 4: 969 (2020); https://doi.org/10.15407/nnn.18.04.969
24. A. Hazim, A. Hashim, and H. M. Abduljalil, *Nanosistemi, Nanomateriali, Nanotehnologii*, **18**, Iss. 4: 983 (2020); https://doi.org/10.15407/nnn.18.04.983

Наносистеми, наноматеріали, нанотехнології
Nanosistemi, Nanomateriali, Nanotehnologii
2021, т. 19, № 4, сс. 841–853

PACS numbers: 71.15.Mb, 71.20.Rv, 76.60.-k, 78.30.-j, 78.40.-q, 78.67.Sc, 82.35.Np

Exploring the Optical, Electronic, and Spectroscopic Properties of Yttrium Oxide Doped PVA/PEG Blend for Low Cost and Lightweight Electronics Applications

Hind Ahmed and Ahmed Hashim

College of Education for Pure Sciences,
Department of Physics,
University of Babylon,
Hillah, Iraq

This paper is focused on the structural, electronic, and spectroscopic properties of PVA–PEG–Yttrium oxide blend (64 atoms), by using density functional theory (DFT) at the B3LYP level with 6-311G basis set. All calculations are performed with Gaussian 09 program and Gaussian view 5.0.8 program. The geometric properties include improving geometric optimization of bonds and angles. As the electronic properties, there are considered such as ionization potential, electron affinity, chemical hardness, chemical softness, electronegativity, total energy, cohesive energy, energy gap, electrophilicity, and density of states (DOS). In addition, the spectral properties are involved (IR, Raman, NMR, and UV-Visible). The results show that the 6-311G basis sets are efficient and strongly suggested for heavy metals and give good relaxation for the structure. The results state that the yttrium oxide has the low LUMO–HOMO energy gap, and it gives more biological activity ratios. The obtained results indicate that the PVA–PEG–Yttrium oxide blend can be used in different fields for electronics and photonics applications.

Цю статтю зосереджено на структурних, електронних і спектроскопічних властивостях суміші полівініловий спирт (ПВС)/поліетиленгліколь (ПЕГ) із домішкою Y_2O_3 (64 атоми) із використанням теорії функціоналу густини (ТФГ) на рівні B3LYP із базисним набором 6-311G. Всі розрахунки виконуються за допомогою програми Gaussian 09 і програми Gaussian View 5.0.8. Геометричні властивості включають поліпшення геометричної оптимізації зв'язків і кутів. В якості електронних властивостей розглядаються: потенціял йонізації, спорідненість електронів, хемічна цупкість, хемічна м'якість, електронеґативність, повна енергія, когезійна енергія, енергетична щілина, електрофільність і густина електронних станів. Крім того, задіяні спектральні властивості (ІЧ, Раманові, ЯМР і у видимому й ультрафіолетовому діяпазонах світла).

Результати показують, що базисні набори 6-311G є ефективними та настійно пропонуються для важких металів і дають хорошу релаксацію для структури. Результати показують, що оксид Ітрію має низьку енергетичну щілину LUMO–HOMO, і він дає більше коефіцієнтів біологічної активности. Одержані результати свідчать про те, що суміш оксиду ПВС–ПЕГ–оксид Ітрію може використовуватися в різних областях для застосування електроніки та фотоніки.

Key words: PVA/PEG blend, Y_2O_3 admixture, NMR, spectral properties, DFT, 6-311G basis, electronics.

Ключові слова: суміш полівініловий спирт/поліетиленгліколь, домішка Y_2O_3, ЯМР, спектральні властивості, ТФГ, 6-311G-базис, електроніка.

(Received 19 January, 2021; in revised form, 22 January, 2021)

1. INTRODUCTION

Yttrium oxide is promising for chemical catalysis devices and for optoelectronics. It is used for biological imaging applications [1]. Yttrium oxides are the two most important ceramic materials, which have wide technological applications ranging from electronics, optics, and mechanical engineering to catalyst support [2]. Yttrium and yttrium oxide has been studied both experimentally and theoretically owing to their possible applications [3]. Nanocomposites are a new-fangled class of materials made with nanosize fillers. Nanosize inorganic particles mixed with organic polymer are called organic–inorganic hybrids [4]. Polymer matrixes reinforced with nanosize phase (nanofillers) such as nanoparticles, nanotubes, nanosheets, and nanofibers, *etc.*, called polymer nanocomposites, have the physical properties of these composites mainly depending on the contact of polymer molecules with nanofillers [5]. Transition metal oxides are known for their great change in effects of chemical and physical properties. Several of those materials undergo phase transitions with interesting structural, electronic, and magnetic behaviours [6]. In nature, there is a water-soluble and easily degradable material; it is polyvinyl alcohol (PVA). Hence, it acts as an eco-friendly polymer [7]. It may be applied naturally to create thin films with metal oxide. Strong absorption properties are revealed for PVA polymer in the range 300 to 500 nm in the ultraviolet (UV) spectra [8]. There are many studies on some properties of doped polymers like structural, optical, electrical, and electronic properties [9–36]. DFT is proven as very successful in calculating the structural properties of condensed systems and electronic properties of simple metals [37]. That distinguishes the method of density functional theory is choosing the shape of function to compute the energy of bonding and exchange [38].

2. THEORETICAL PART

The total energy for a system is the sum of total kinetic and potential energies at the optimized structure such that the total energy of the molecule must be at the lowest value because the molecule is at the equilibrium point. This means the resultant of the effective forces is zero. Cohesive energy is defined as 'the energy necessary to detaching the condensed material into separated atoms'. The relation (1) is used to compute the cohesive energy, which means 'the difference between energy per atom of the bulk material at equilibrium and energy of a free atom in its ground state' [39]:

$$E_{\text{coh}} = \left(\frac{E_{tot}}{n}\right) - E_{free} - E_0\,, \tag{1}$$

where E_{tot} is the total energy, E_{free} is the free-atoms' energy, n is number of atoms, E_0 is the vibrational energy of ground states (zero-point).

The HOMO (the molecular orbitals of highest energy that is occupied by electrons) and LUMO (the molecular orbitals of lowest energy that is not occupied by electrons) are main orbitals in calculations of such properties as the molecular interaction and the ability of molecule to absorb a light. According to Koopmans' theorem, the band gap is given as follows [40]:

$$E_g = E_{\text{LUMO}} - E_{\text{HOMO}}. \tag{2}$$

For the molecule, there is the magnitude of energy needed to eliminate the electron from atom or isolated molecule and identified as energy difference between the positive charge energy $E_{(+)}$ and neutral one $E_{(n)}$ by the following relation:

$$IP = E_{(+)} - E_{(n)}. \tag{3}$$

When electrons are additional to neutral atoms to form a negative ion, it is stated as 'the energy difference between the neutral energy $E_{(n)}$ and the negative charge energy $E_{(-)}$' by the following relation:

$$EA = E_{(n)} - E_{(-)}. \tag{4}$$

In molecular orbital (MO) theory within the limitation of Koopmans' theorem, the orbital energies of the frontier orbitals are given as follow:

$$IP = -E_{\mathrm{HOMO}}, \tag{5}$$

$$EA = -E_{\mathrm{LUMO}}. \tag{6}$$

The chemical hardness (η) is a measure of the range of resistance to the transfer of charges [40, 41]. It is theoretically defined as 'the second derivative of electron energy in relation to the number of electrons N' for a constant external potential $V(r)$ [41]:

$$\eta = \frac{1}{2}\left[\frac{\partial^2 E}{\partial N^2}\right]_V = \frac{1}{2}\left[\frac{\partial \mu}{\partial N}\right]_V = -\frac{1}{2}\left[\frac{\partial X}{\partial N}\right]_V. \tag{7}$$

Finite-difference approximation for the chemical hardness gives:

$$\eta = \frac{IP - EA}{2}. \tag{8}$$

The chemical softness, S, is a 'property of molecules that measures the degree of chemical reactivity'. It is the converse of the chemical hardness (η) [42]:

$$S = \frac{1}{2\eta}\left[\frac{\partial^2 N}{\partial E^2}\right]_V = \left[\frac{\partial N}{\partial \mu}\right]_V. \tag{9}$$

The fundamental variation principle within the density functional theory is the electron chemical potential, where the reactivity indicator is related to how the electron energy E of molecules is changed with changing the number of electrons (N) and the external potential. Chemical potential μ is defined as [43]:

$$\mu = \left[\frac{\partial E}{\partial N}\right]_V, \tag{10}$$

where V is the potential of nuclei.

Then, we might define the electronegativity: 'It is well-defined as the force of an atom in a molecule to pull electrons to itself by Pauling' as the negative of the electron chemical potential [41]:

$$X = -\mu = -\left[\frac{\partial E}{\partial N}\right]_V. \tag{11}$$

R. Mulliken indicates electronegativity as 'the average energy of the ionization and electron affinity' as follows [39]:

$$X = \frac{IP + EA}{2}. \tag{12}$$

According to Koopmans' theorem, 'it is defined as the negative value for average of the energy levels of the HOMO and LUMO' [37]:

$$X = \frac{E_{\text{HOMO}} + E_{\text{LUMO}}}{2}\,. \tag{13}$$

A measure of the stabilization in energy when the structure obtains the added electron charges from the environment is defined as electrophilicity [43]:

$$\omega = \kappa/(2\eta)\,. \tag{14}$$

3. RESULTS AND DISCUSSION

Figure 1 shows the 'optimized structure' of PVA–PEG–Yttrium ox-

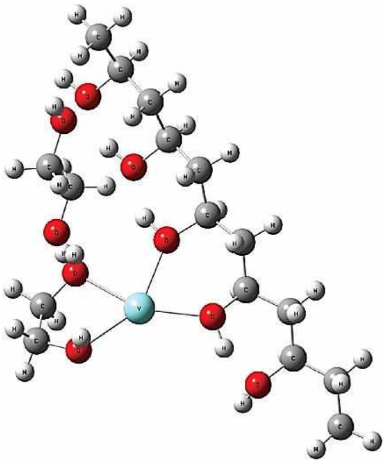

Fig. 1. Optimizing geometries of PVA–PEG–Yttrium oxide (64 atoms).

TABLE 1. Average bond lengths in [Å] and angles in [degrees].

The geometric parameters	The optimizable bonds	Values
Bonds, Å	(C–C)	1.53851
	(C–O)	1.47131
	(C–H)	1.09826
	(O–H)	1.01348
	(Y–O)	2.31069
Angles, deg.	(O–Y–O)	67.13225
	(C–C–C)	118.26195
	(C–O–H)	105.47317

ide, which obtained by the 'DFT method' with using 'three-parameter hybrid-functional' of Becke B3LYP with 6-311G basis sets.

Table 1 shows the geometric parameters of PVA–PEG–Yttrium oxide (64 atoms) including the bond length in [Ångström] and bond angle in [degrees] by the Gaussian 09-programs by using the DFT with the B3LYP/6-311G level. The calculated values of bonds in present work are in a well agreement with previous theoretical studies [44, 45].

Figure 2 and Table 2 show the results of FTIR obtained by using the Gaussian view 5.0-program and density functional theory (DFT) with 6-311G basis sets. Yttrium oxide produces variations in spectrum of PVA–PEG that comprises variation in the intensities and shift in several bonds. These changes are credited to bindings of Yt-

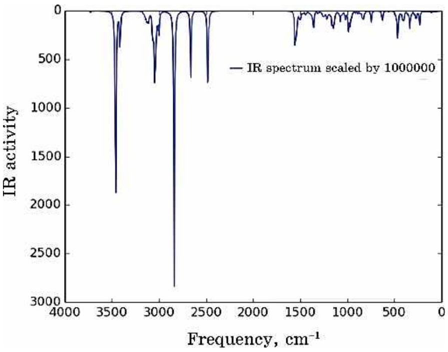

Fig. 2. IR spectrum of PVA–PEG–Yttrium oxide (64 atoms) at the B3LYP/6-311G basis set.

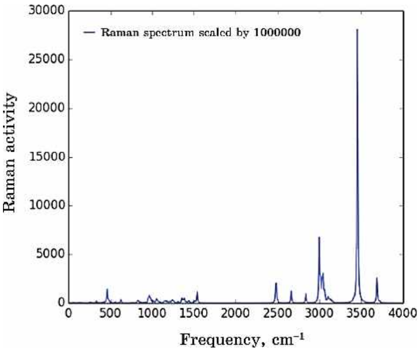

Fig. 3. Raman intensities of PVA–PEG–Yttrium oxide (64 atoms) as a function of vibrational frequency using DFT/6-311G.

TABLE 2. IR frequencies with their assignments of PVA–PEG–Yttrium oxide.

Assignment	Type of vibrational mode	Frequency, cm^{-1}	Typical vibrational frequency, cm^{-1}
Y–O	stretching	200–390	200–400 [42, 43]
C–C	stretching and bending	730–1560	700–1600 [46]
C–O	stretching	1140	1000–1280 [47]
C–O–C	bending	1250	1238–1291 [47]
$-CH_2$	in-plane bending	1355	1340–1465 [47]
C–H	symmetric stretching	3055–3046	3020–3080 [48]
O–H	stretching	3226–3631	3200–3640 [49]

trium oxide with polymers.

Figure 3 shows the Raman spectrum of PVA–PEG–Yttrium oxide (64 atoms). It is shown in this figure that the active region in IR spectrum is similar with less activity in Raman spectrum [45]. Intensities in Raman spectrum rely on probability that a particular wavelength photon will be absorbed.

Gauge-Independent Atomic Orbital (GIAO) method is used in the present NMR calculations, and chemical shifts of the structure are calculated at the same level. Absolute isotropic magnetic shielding is converted into chemical shifts by referencing to the shielding of a standard compound TMS computed at the same level. The chemical shifts are stated in p.p.m. relation to TMS for ^{1}H spectra as shown in Fig. 4.

Figure 5 shows the visible and ultraviolet spectra reliant on upon the electronic structures of the molecule. In Figure 5, absorption intensity of PVA–PEG–Yttrium oxide (64 atoms) has high UV-Vis spectra because adding the oxide leads to an increase in intensity of absorbance. As a result, this is due to moving electrons from valence level to the conduction band at these energies.

Table 3 shows the energy gap for PVA–PEG–Yttrium oxide (64 atoms). This result is in a good agreement with that in Refs. [44,

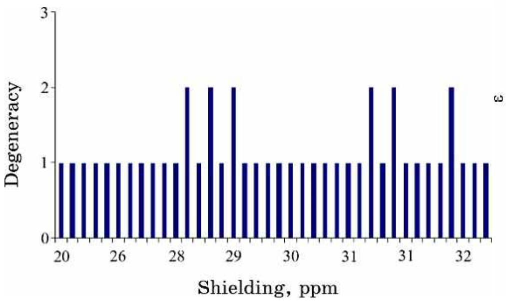

Fig. 4. Nuclear magnetic resonance of PVA–PEG–Yttrium oxide (64 atoms) in infrared spectrum as a function of vibrational frequency.

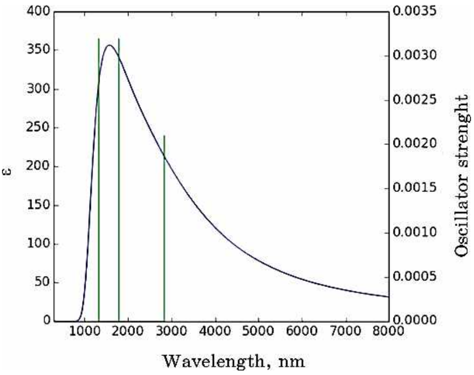

Fig. 5. UV-Vis spectrum for PVA–PEG–Yttrium oxide (64 atoms) using B3LYP/6-311G.

TABLE 3. The values of energy gap in [eV] for the studied structures.

PVA–PEG–Y_2O_3 (64 atoms)		
E_{HOMO}, eV	E_{LOMO}, eV	E_g, eV
3.02	0.008	3.028

46] and refers that PVA–PEG–Yttrium oxide needs high energy to donating or accepting an electron. Figure 6 illustrates the 3*D* distribution of HOMOs and LUMOs for the studied structures. From these results, the calculated energy gap decreases with increasing the number of atoms.

Table 4 illustrates the results for the total energy E_{tot} in [a.u.] and some electronic properties. The total ground state energy E_{tot}

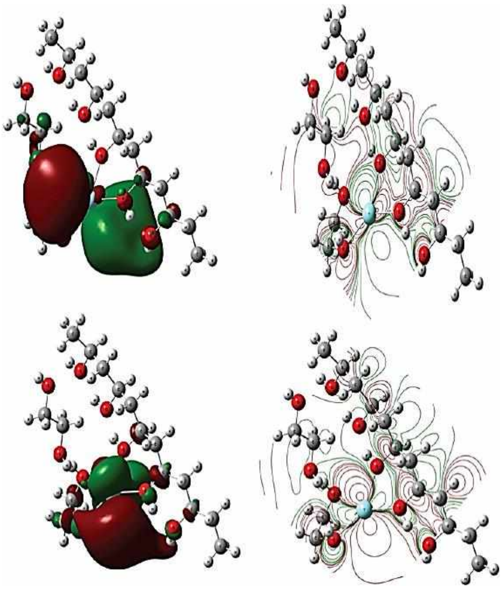

Fig. 6. The distribution of HOMO (up) and LUMO (down) for PVA–PEG–Yttrium oxide blend containing 64 atoms.

TABLE 4. The values of some electronic properties in [eV] of the studied structures.

Property	PVA–PEG–Y_2O_3 (64 atoms)
total energy	–1347.381
cohesive energy	–7.8947
ionization potential	3.02
electron affinity	0.008
electronegativity	1.514
chemical hardness	1.506
chemical softness	0.33
chemical potential	–1.514
electrophilicity	0.760
polarizability, a.u.	213.58

for PVA–PEG–Yttrium oxide is approximated by the summation of all E_{tot} for all atoms in the structure. It is identified that the frontier molecular orbitals, the high occupied molecular orbitals HOMO, and the low unoccupied molecular orbitals LUMO, show an important part for the reactant molecules in chemical reactions. It may be concluded that less negative E_{coh} value for structures might be concerned with its higher LUMO energy level because it does not need high energy to lose electrons from external orbitals. An interesting conclusion may be drawn from these investigations, namely, this factor can affect the value of cohesive energies. Here, the system with larger E_{coh} is more stable. The ionization energy I_E and electron affinity E_A for PVA–PEG–Yttrium oxide are calculated according to Koopmans' theorem. These values show that the PVA–PEG–Yttrium oxide needs to high energy to donating or accepting an electron to become cation or anion because of the high value of I_E and low value of E_A. The calculated values of electronegativity E_N and electrochemical hardness H show that structures have small capability to electron transfer. The low value of the electronic softness S is a reflection to the large separation between the valence band and conduction band. High hardness refers to high excitation energies required to electron transfer for PVA–PEG–Yttrium oxide.

In Table 4, PVA–PEG–Yttrium oxide has large absolute value of chemical potential with low value of ω. Therefore, these are weak nanocomposites to interact with other surrounding species or molecule. The nanocomposites, which have high values of polarizability, will be more effective, less stable, more softness and will have small energy gap.

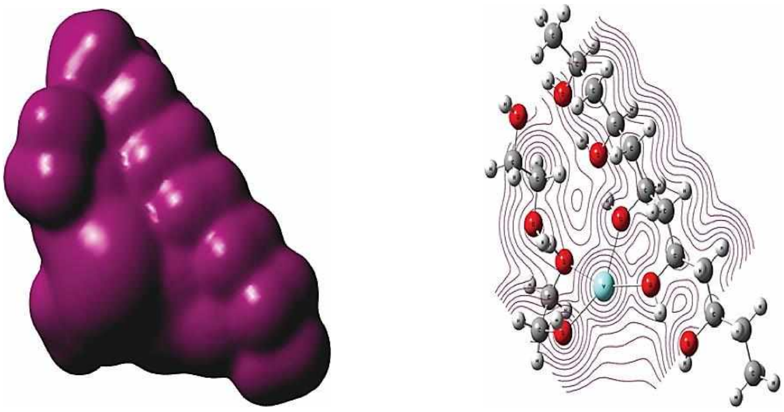

Fig. 7. The electron density distribution for PVA–PEG–Yttrium oxide containing 64 atoms.

Figure 7 illustrates the three-dimensional shape of electron density (ED) distribution surfaces for the structures. The ED is distributed owing to distribution of all atoms in the space of the nanocomposites giving the total density of the electrons.

Figure 8 illustrates the electrostatic potential (ESP) distribution surfaces for PVA–PEG–Yttrium oxide calculated from the total self-consistent field approximation. The ESP distributions for the structures are caused by repulsive forces or by attracting regions around each nanocomposite. In general, the ESP surfaces for PVA–PEG–Yttrium oxide (64 atoms) are dragged toward the positions of

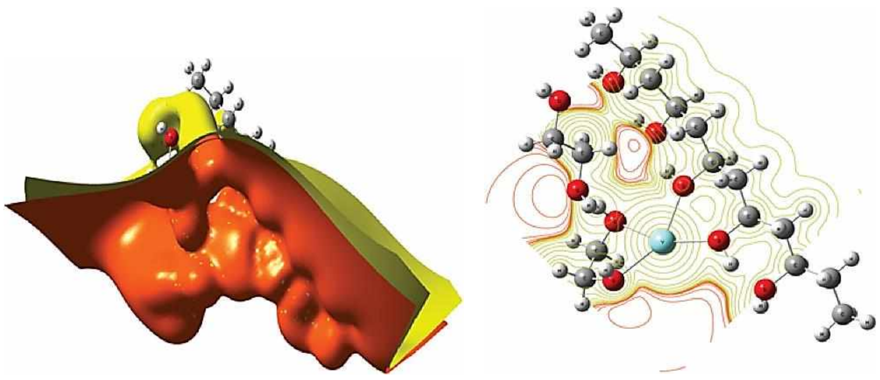

a *b*

Fig. 8. The electrostatic potential distribution surface for PVA–PEG–Yttrium oxide (64 atoms) (left: counter 2*D*; right: 3*D*).

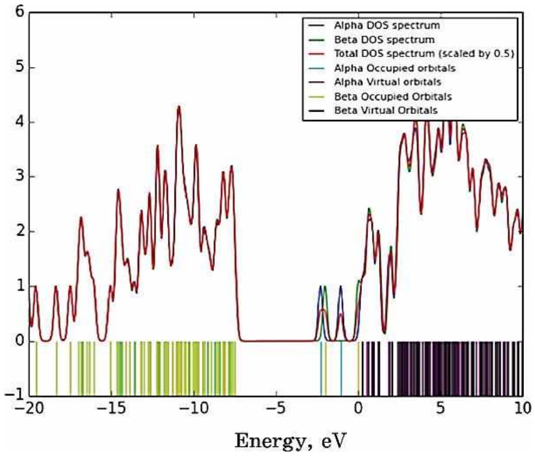

Fig. 9. Electron density of states as a function of bond length for PVA–PEG–Yttrium oxide (64 atoms).

negative charges in each molecule, which are the oxygen atoms of high electronegativity (of 3.5 eV).

Further studying the strength of the reactions can be done by analysing the orbital interactions between the PVA–PEG–Yttrium oxide blend atoms in expression for the DOS, as shown in Fig. 9. The high density of states at a specific energy level refers to the many cases in the structure available for occupations.

4. CONCLUSIONS

The B3LYP/6-311G density functional theory validity is proved in studying the geometry optimization and calculating the geometrical parameters.

Energy gap is a useful inclusive property. Soft molecules have small energy gaps and their electron density changes more easily than in hard molecules.

The ESP is dragged towards the active sites in PVA–PEG–Yttrium oxide structures.

The PVA–PEG–Yttrium oxide structures can be used for different optoelectronics applications.

REFERENCES

1. S. K. Kannan and M. Sundrarajan, *Bull. of Mater. Sci.*, **38**, No. 4: 945 (2015).
2. W. Y. Ching and Y. N. Xu, *Phys. Rev. B*, **59**, No. 20: 12815 (1999).
3. Z. Yang and S. J. Xiong, *J. of Phys. B: Atomic, Mol. and Optic. Phys.*, **42**, No. 24: 245101 (2009); https://doi.org/10.1088/0953-4075/42/24/245101
4. D. Kumar, S. K. Jat, P. K. Khanna, N. Vijayan, and S. Banerjee, *Int. J. of Green Nanotechno.*, **4**, No. 3: 408 (2012).
5. S. K. Sharma, J. Prakash, K. Sudarshan, D. Sen, S. Mazumder, and P. K. Pujari, *Macromolecules*, **48**, No. 16: 5706 (2015).
6. K. Hermann and M. Witko, *Oxide Surfaces* (Ed. D. Woodruff) (Elsevier: 2001), vol. **9**, p. 136.
7. J. Lee, D. Bhattacharyya, A. J. Easteal, and J. B. Metson, *Current Appl. Phys.*, **8**, No. 1: 42 (2008).
8. S. Ram and T. K. Mandal, *Chem. Phys.*, **303**, Nos. 1–2: 121 (2004).
9. A. Hashim, Y. Al-Khafaji, and A. Hadi, *Transactions on Elect. and Electronic Mater.*, **20**: 530 (2019); https://doi.org/10.1007/s42341-019-00145-3
10. A. Hadi, A. Hashim, and Y. Al-Khafaji, *Transactions on Elect. and Electronic Mater.*, **21**: 283 (2020); https://doi.org/10.1007/s42341-020-00189-w
11. A. Hashim, A. J. Kadham, A. Hadi, and M. A. Habeeb, *Nanosistemi, Nanomateriali, Nanotehnologii*, **19**, Iss. 2: 327 (2021); https://doi.org/10.15407/nnn.19.02.327
12. A. Hashim and Z. S. Hamad, *Nanosistemi, Nanomateriali, Nanotehnologii*, **18**, Iss. 4: 969 (2020); https://doi.org/10.15407/nnn.18.04.969

13. A. Hazim, A. Hashim, and H. M. Abduljalil, *Nanosistemi, Nanomateriali, Nanotehnologii*, **18**, Iss. 4: 983 (2020); https://doi.org/10.15407/nnn.18.04.983
14. A. Hashim, *J. of Inorganic and Organometallic Polym. and Mater.*, **30**: 3894 (2020); https://doi.org/10.1007/s10904-020-01528-3
15. A. Hashim and Z. S. Hamad, *Egypt. J. Chem.*, **63**, Iss. 2: 461 (2020); DOI: 10.21608/EJCHEM.2019.7264.1593
16. K. H. H. Al-Attiyah, A. Hashim, and S. F. Obaid, *Int. J. of Plastics Techno.*, **23**, No. 1: 39 (2019); https://doi.org/10.1007/s12588-019-09228-5
17. A. Hashim, K. H. H. Al-Attiyah, and S. F. Obaid, *Ukr. J. Phys.*, **64**, No. 2: 157 (2019); https://doi.org/10.15407/ujpe64.2.157
18. H. Ahmed, H. Abduljalil, and A. Hashim, *Transactions on Elect. and Electronic Mater.*, **20**: 218 (2019), https://doi.org/10.1007/s42341-019-00111-z
19. A. Hashim and N. Hamid, *J. of Bionanoscience*, **12**, No. 6: 788 (2018); doi:10.1166/jbns.2018.1591
20. B. Abbas and A. Hashim, *Int. J. of Emerging Trends in Eng. Res.*, **7**, No. 8: 131 (2019); https://doi.org/10.30534/ijeter/2019/06782019
21. A. Hashim and Z. S. Hamad, *J. of Bionanoscience*, **12**, No. 4: 504 (2018); doi:10.1166/jbns.2018.1561.
22. N. H. Al-Garah, F. L. Rashid, A. Hadi, and A. Hashim, *J. of Bionanoscience*, **12**, No. 3: 336 (2018); doi:10.1166/jbns.2018.1538
23. A. Hashim and A. Jassim, *Sensor Letters*, **15**, No. 12: 1003 (2017); doi:10.1166/sl.2018.3915
24. I. R. Agool, F. S. Mohammed, and A. Hashim, *Advances in Environmental Biology*, **9**, No. 11: 1 (2015).
25. F. A. Jasim, A. Hashim, A. G. Hadi, F. Lafta, S. R. Salman, and H. Ahmed, *Research Journal of Applied Sciences*, **8**, Iss. 9: 439 (2013).
26. F. A. Jasim, F. Lafta, A. Hashim, M. Ali, and A. G. Hadi, *J. of Eng. and Applied Sciences*, **8**, No. 5: 140 (2013).
27. A. Hashim, H. M. Abduljalil, and H. Ahmed, *Egypt. J. Chem.*, **62**, Iss. 9: 1659 (2019); doi:10.21608/EJCHEM.2019.7154.1590
28. A. Hashim and M. A. Habeeb, *Transactions on Elect. and Electronic Materials*, **20**: 107 (2019); doi:10.1007/s42341-018-0081-1
29. H. Ahmed, H. M. Abduljalil, and A. Hashim, *Transactions on Elect. and Electronic Mater.*, **20**: 206 (2019); https://doi.org/10.1007/s42341-019-00100-2
30. H. Ahmed, A. Hashim, and H. M. Abduljalil, *Egypt. J. Chem.*, **62**, Iss. 4: 1167 (2019); doi:10.21608/EJCHEM.2019.6241.1522
31. A. Hashim, H. M. Abduljalil, and H. Ahmed, *Egypt. J. Chem.*, **63**, Iss. 1: 71 (2020); doi:10.21608/EJCHEM.2019.10712.1695
32. H. Ahmed and A. Hashim, *Egypt. J. Chem.*, **63**, Iss. 3: 805 (2020); doi:10.21608/EJCHEM.2019.11109.1712
33. A. Hashim and Z. S. Hamad, *J. of Bionanoscience*, **12**, Iss. 4: (2018); doi:10.1166/jbns.2018.1551
34. D. Hassan and A. Hashim, *J. of Bionanoscience*, **12**, Iss. 3: (2018); doi:10.1166/jbns.2018.1537.
35. D. Hassan and A. Hashim, *J. of Bionanoscience*, **12**, Iss. 3: (2018); doi:10.1166/jbns.2018.1533.
36. H. Ahmed and A. Hashim, *Int. J. of Sci. & Techno. Res.*, **8**, Iss. 11: (2019).

37. J. Baima, A. Erba, M. Rйrat, R. Orlando, and R. Dovesi, *J. of Phys. Chem. C*, **117**, No. 24: 12864 (2013).
38. F. Jensen, *The J. of Chem. Phys.*, **116**, No. 17: 7372 (2002).
39. D. Young, *Computational Chemistry: A Practical Guide for Applying Techniques to Real World Problems* (John Wiley & Sons Inc: 2001); DOI:10.1002/0471220655
40. H. W. Hugosson, *A Theoretical Treatise on the Electronic Structure of Designer Hard Materials* (Doctoral dissertation) (Acta Universitatis Upsaliensis: 2001).
41. W. J. Hehre, L. Radom, P. R. Schleyer, and J. A. Pople, *Ab initio Molecular Orbital Theory* (New York: John Wiley & Sons Inc.: 1986).
42. M. Oftadeh, S. Naseh, and M. Hamadanian, *Comp. and Theor. Chem.*, **966**: Nos. 1–3: 20 (2011).
43. K. Sadasivam and R. Kumaresan, *Comp. and Theor. Chem.*, **963**, No. 1: 227 (2011).
44. A. B. Rahane, P. A. Murkute, M. D. Deshpande, and V. Kumar, *J. of Phys. Chem. A*, **117**, No. 26: 5542 (2013).
45. B. Dai, K. Deng, and J. Yang, *Chem. Phys. Letters*, **364**, Nos. 1–2: 188 (2002).
46. T. Larbi, K. E. El-Kelany, K. Doll, and M. Amlouk, *J. of Raman Spectroscopy*, **51**, No. 2: 232 (2020).
47. H. K. Lin, C. B. Wang, H. C. Chiu, and S. H. Chien, *Catalysis Letters*, **86**, Nos. 1–3: 63 (2003).
48. P. Atkins and J. De Paula, *Physical Chemistry for the Life Sciences* (Oxford, USA: Oxford University Press: 2011).
49. E. Kavitha, N. Sundaraganesan, and S. Sebastian, *Indian J. of Pure and Appl. Phys.*, **48**, No. 1: 20 (2010).

Наносистеми, наноматеріали, нанотехнології
Nanosistemi, Nanomateriali, Nanotehnologii
2021, т. 19, № 4, сс. 855–863

PACS numbers: 61.05.cp, 68.37.Hk, 78.30.Hv, 78.67.Bf, 81.07.Bc, 81.16.Hc, 81.70.Pg

Preparation and Characterization of Zinc Oxide Nanoparticles *via* the Thermal Decomposition

Douaa Alhaddad[1], Farouk Kndil[1], and Ahmad Falah[1,2]

[1]*Department of Chemistry,*
Damascus University,
Mousalam Baroudy Str.,
Damascus, Syria
[2]*Faculty of Pharmacy,*
Arab International University (AIU),
Al-Mazzeh Highway,
Damascus, Syria

Zinc oxide nanoparticles are successfully synthesized *via* a thermal decomposition of the Schiff base complexes [(bis-N-(4-metoxy-benzylidene)-2-nitro-1,4 diaminobenzene) Zn(II)], [D1, Zn(II)] as precursor *via* calcification at the temperature of 600°C for 3 hours in an electrical furnace and the air in the presence of non-ionic surfactant [secondary alcohol ethoxylate (TERGITOL™ 15-S-40 (70%)] and polymer polyvinylpyrrolidone (PVP). ZnO nanoparticles are obtained with average size of the crystals of 36.8 nm. The as-synthesized products are characterized by powder x-ray diffraction (XRD), scanning electron microscopy (SEM), Fourier transform infrared spectroscopy (FT-IR); elemental analysis of the particles is performed by energy dispersive x-ray spectroscopy (EDX).

Наночастинки оксиду Цинку успішно синтезуються за допомогою теплового розкладання комплексів Шиффових основ [(біс-N-(4-метоксі-бензиліден)-2-нітро-1,4 діамінобензол) цинк(II)], [D1, Zn(II)] як провісника через кальцифікацію за температури у 600°C протягом 3 годин в електричній печі та повітрі в присутності нейонної поверхнево-активної речовини [вторинний спиртовий етоксилат (TERGITOL™ 15-S-40 (70%)] і полімерний полівінілпірролідон (ПВП). Наночастинки ZnO одержують із середнім розміром кристалів у 36,8 нм. Щойно синтезовані продукти характеризуються порошковою рентґенівською дифракцією (XRD), сканувальною електронною мікроскопією (SEM), інфрачервоною спектроскопією на основі перетвору Фур'є (FT-IR); елементна аналіза частинок проводиться за допомогою рентґеноспектральної спектроскопії на основі методи енергетичної дисперсії (EDX).

Key words: thermal decomposition, Schiff base complexes, Zinc oxide nanoparticles, Schiff bases of *p*-anisaldehyde.

Ключові слова: термічне розкладання, комплекси Шиффових основ, наночастинки оксиду Цинку, Шиффові основи *p*-анісового альдегіду.

(Received 14 December, 2020; in revised form, 19 December, 2021)

1. INTRODUCTION

Recently, syntheses of materials of nanosizes have attracted attentions attributed to their unique mechanical, physical, optical, and magnetic properties [1]. The properties of nanomaterials stimulate various applications in different technological fields such as electronics, catalysis, magnetic data storage, energy storage, structural components, and ceramics [2]. Among inorganic material, Zinc oxide (ZnO) [3] is semiconducting material with direct band gap of 3.3 eV at room temperature and with unique properties such as optical transparency, electric conductivity, piezoelectricity and near-UV emission [4]. This metal oxide has a variety of applications including chemical sensors [5], catalysts [6], UV light-emitters [7], photovoltaics [8], and cantilevers [9]. Several approaches have been engaged to synthesize ZnO nanocrystals such as thermal methods [10], electrochemical methods [11], sol–gel methods [12], solid-state reactions [13], chemical reduction and decomposition route [14], sonochemical methods [15]. Most of these approaches require tedious processes, expensive substrates, sophisticated equipment and rigorous experimental circumstances. Recently, metal oxides' nanoparticles have been synthesized *via* thermal decomposition method of Schiff base complexes [16] that returns to this method not only avoided usage of the template and complex apparatus, but also affectivity in the shape control of the preparation product. By selecting a proper precursor with a rational calcining procedure, products with unique size and shapes could be obtained. This method also has extra advantages, including operational simplicity, high purity and high yield of product, low-energy consumption and no special equipment required [17]. However, in this work, ZnO nanoparticles have been synthesized *via* thermal decomposition of Schiff base complexes [D1, Zn(II)] as precursor by calcification in electrical furnace with non-ionic surfactant and polymer polyvinylpyrrolidone (PVP).

2. EXPERIMENTAL PROCEDURE

2.1. Materials

Zinc nitrate 6-hydrat (10196-18-6), ethanol solution (16368), 2-nitro-1,4-phenylenediamine (N21200), *p*-anisaldehyde (A88107), non-ionic surfactant [secondary alcohol ethoxylate (TERGITOL™ 15-S-40 (70%)] (STS0003) and polymer polyvinylpyrrolidone (PVP40), all the chemical reagents, were obtained from Sigma-Aldrich.

2.2. Preparation Ligand [Bis-N-(4-Metoxy-Benzylidene)-2-Nitro-1,4 Diaminobenzene]

The symmetrical Schiff base (D1) was prepared by refluxing (0.05 mole) of *p*-anisaldehyde and (0.025 mole) of 2-nitro-1,4-phenylenediamine in (30 ml) of dried ethanol for 4 h and cooling the reaction mixture. The Schiff base was separated as orange needles and was recrystallized twice from methanol (yield 90%). The compound is stable at room temperature.

Figure 1 shows the chemical preparation of ligand (D1):

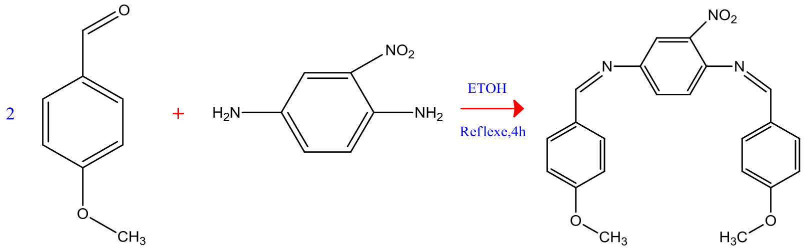

Fig. 1.

2.3. Preparation of [D1, Zn(II)] Complex

Ligand D1 (2 mmole) was dissolved in 15 mL of ethanol, mixed with $Zn(NO_3)_2 \cdot 6H_2O$ (2 mmole, in ethanol) at 100°C and stirred for 2 h. The dark orange precipitates were washed several times using distilled water and dried in the air.

2.5. Synthesis of ZnO Nanoparticles

Ligand D1 (2 mmole) was dissolved in 15 ml of ethanol, mixed with $Zn(NO_3)_2 \cdot 6H_2O$ (2 mmole, in ethanol) at 100°C and stirred for 30 min. Then, we added 7 gr of non-ionic surfactant and stirred continuously for 1 h. Finally, we add 3 gr of polymer polyvinylpyrrolidone (PVP). ZnO nanocrystals were produced by subjecting the previous prepared complex [D1, Zn(II)] to thermal treatment at a relatively low temperature (600°C) in the air, and after keeping the thermal treatment at 600°C for 3 h. The white nanocrystals of ZnO were cooled at room temperature, and then washed with ethanol and distilled water for three times and dried in the air.

3. RESULTS AND DISCUSSION

3.1. Characterization by Using FT-IR Spectroscopy

Compounds have been clearly characterized by using Fourier transform infrared spectroscopy (FT-IR). The structure of Schiff base ligand was confirmed with disappearance of the amine and aldehyde group and in the oxides; the corresponding peaks appeared in Fig. 2, *a* show FT-IR spectra of the precursors. Characteristic peaks at 1.635 cm^{-1} are attributed to the C=N stretching, and 1560, 1348 cm^{-1} belongs to nitrogroup NO_2. The strong broad peak around 3463 cm^{-1} belongs to N–H group as result of tautomeric isomerism, and at 3136 cm^{-1}, due to aromatic C–H.

FT-IR spectra of prepared nanoparticles are given in Fig. 2, *b*. Strong broad peak around 479 cm^{-1} shows a distinct stretching mode of ZnO crystal. The broad absorption band of O–H stretching ($\cong$ 3500 cm^{-1}) is due to adsorbed water on the external surface of the samples during handling to record the spectra.

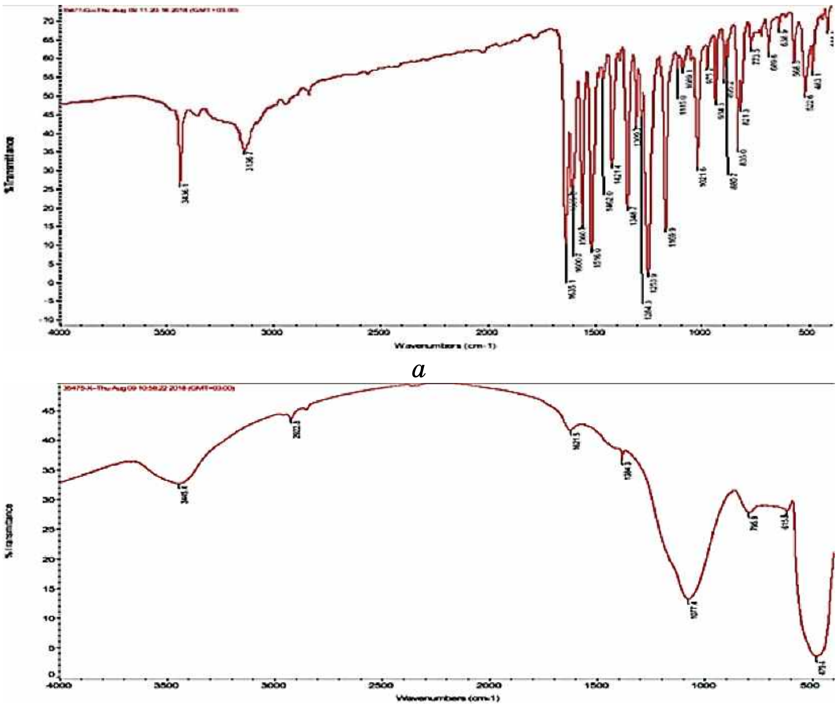

a

b

Fig. 2. FT-IR spectra of Schiff base ligand [D1] (*a*); FT-IR spectra of ZnO nanoparticles (*b*).

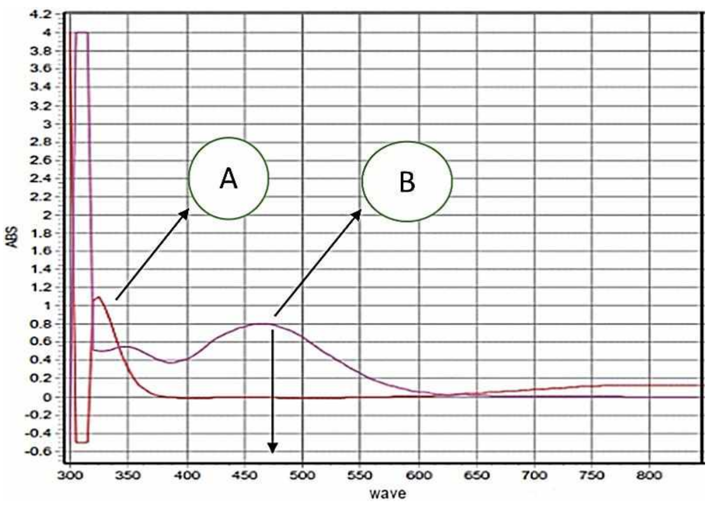

Fig. 3. Line (A)—UV-vis spectra for Schiff base ligand [D1]; line (B)—UV-vis spectra for [D1, Zn (II)] complex.

3.2. UV-Vis Spectroscopy

The complexes have been confirmed by UV-vis spectroscopy, which show shifts in the absorption peaks between ligand and their complexes because of differences in electronic transitions.

In Figure 3, there are line (A) of UV-vis spectra of Schiff base ligand [D1], and line (B), *i.e.*, line (A) for [D1, Zn(II)] complex. The ligand displays typical ligand-centred $\pi \to \pi^*$-transitions at 325 nm. Upon co-ordination with Zinc ions, there are minor changes of these bands. The visible spectra of complexes are clearly shown with line (B); for Zn(II) complex, absorption appears at 465 nm, and they can be assigned to $d \to d$-electron transition or metal to ligand charge transfer (MLCT).

3.3. Thermogravimetric Analysis of the Schiff Base Complexes

In Figure 4, the thermal behaviour of Zn(II) complex has been studied (by means of the TGA) under N_2 atmosphere from room temperature to 950°C with the heating rate of 10°C per minute. We can observe that the thermal decomposition ends at 600°C for the Zn(II) complex. There is no mass loss up to ≈ 250°C for confirming the absence of any crystalline water (solvent) molecules in the complexes, Zn(II) complex loses ≈ 99% of its weight *via* two thermal stages. The increasing weight after thermal decomposition temperature is definitely due to formation of Zinc oxide.

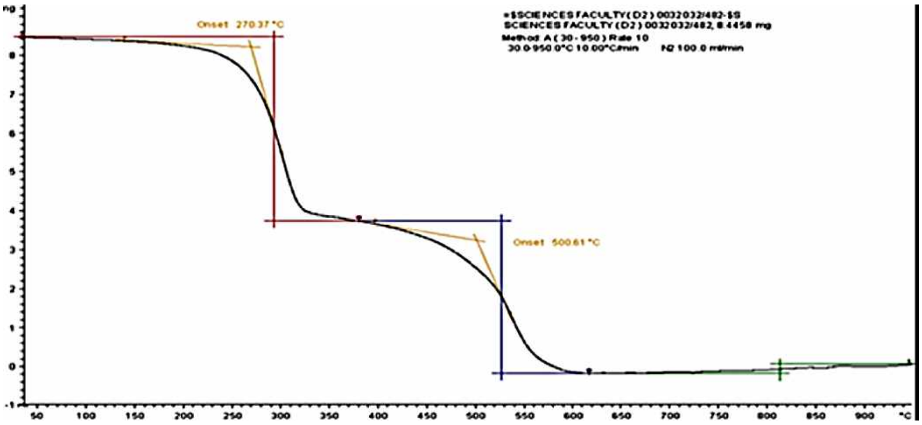

Fig. 4. TGA curve for Zn(II) complex.

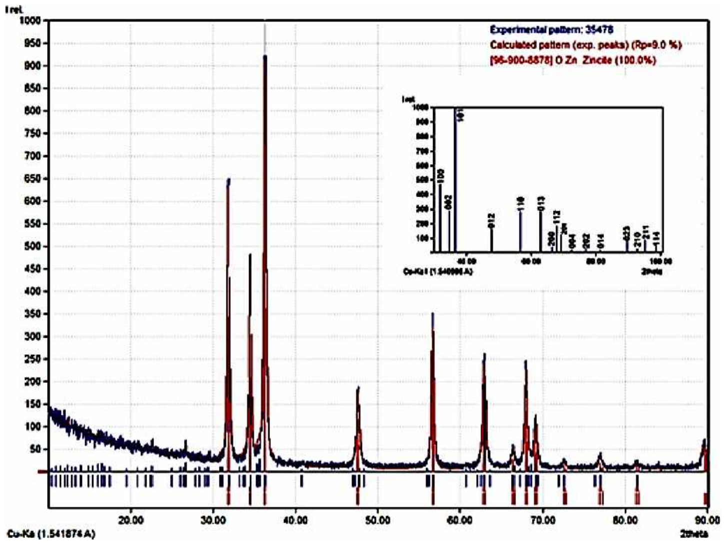

Fig. 5. XRD spectrum for Zinc oxide.

3.4. X-Ray Structural Analysis for the Oxides

The phase identification of crystalline structure of the nanoparticles was characterised by x-ray powder diffraction. The synthesized sample was analysed by the CuK_α x-ray diffractometer for confirming the presence of ZnO and identification of the structure.

Figure 5 shows the XRD patterns of ZnO nanoparticle synthesized. The different peaks are observed at $2\Theta = 31.94°$ (100), 34.55° (002), 36.45° (101), 47.65° (102), 56.75° (110), 62.95° (103), 66.45° (200), 68.10° (112) and 69.20° (201), which are indexed to the hexagonal wurtzite structure (COD Card No. 96-900-8878) (space group: $P63m$) with lattice constants $a = b = 3.2494$ Å and $c = 5.2054$ Å. The presence of the (100), (002) and (101) planes in XRD patterns indicates the formation of high purity of the ZnO nanoparticles. Further, no peaks due to impurities were observed. Strong intensity and narrow width of the ZnO diffraction peaks indicate that the resulting product was highly crystalline [18]. Average size of ZnO nanoparticles can be estimated using the Debye–Scherrer equation, which gives a relationship between peak broadening in XRD and particle size that is demonstrated by the following equation: $D_c = k\lambda/(\beta\cos\theta)$, where D_c is the crystal nanoparticle size, k is Scherrer's constant (0.89), λ is x-ray wavelength (0.15406 nm), β is the width of the XRD peak at half height, and θ is the Bragg diffraction angle [19]. By Match program [20] and using the Scherrer's equation, the average crystalline size of ZnO nanoparticles is found of 38.22 nm.

3.5. Energy Dispersive X-Ray Spectrometry (EDX)

The chemical stoichiometry of ZnO nanoparticle was investigated with EDX. This analysis was performed on three different areas randomly across the investigated sample to determine the Zinc and Oxygen ratio. Figure 6 shows the content of Zn, O and C elements in the sample. As detected, it is indicating the high purity of the synthesized ZnO. The Oxygen-to-Zinc weight ratio was found quantitatively from ≈ 1 to 4, and atomic ratio was found from ≈ 1 to 1, respectively, indicating the stoichiometric formation of ZnO, while 4% Carbon weight ratio attributed to EDX sample holder.

3.6. Scanning Electron Microscopy (SEM) Measurement

The SEM image of prepared nanoparticles is given in Fig. 7. The diameter of the nanoparticles is found to be in the range of 16–60 nm, and they are nearly spherical in shape.

4. CONCLUSION

In summary, we have synthesized ZnO nanoparticles using direct thermal decomposition method. The preparation process of ZnO nanoparticles is quite facile. XRD pattern indicates the formation of ZnO nanoparticles of pure hexagonal wurtzite structure with average particle size found to be of 38.22 nm. Here, we report a simple, green, low-cost, and reproducible process for the synthesis. In this

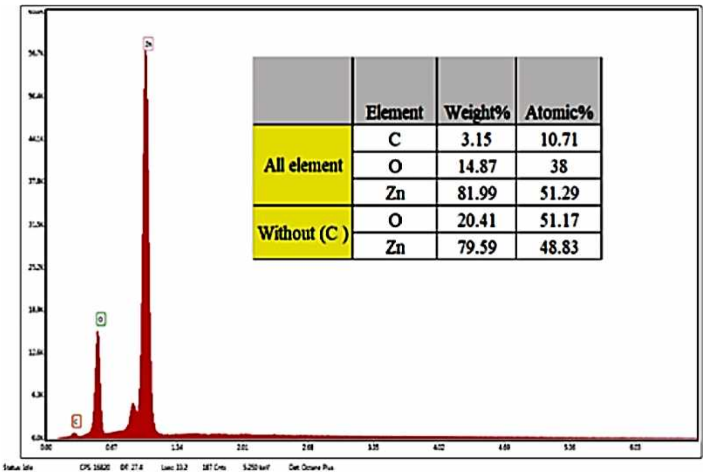

	Element	Weight%	Atomic%
All element	C	3.15	10.71
	O	14.87	38
	Zn	81.99	51.29
Without (C)	O	20.41	51.17
	Zn	79.59	48.83

Fig. 6. Energy dispersive spectrum indicating the chemical composition of freshly prepared for ZnO nanoparticles.

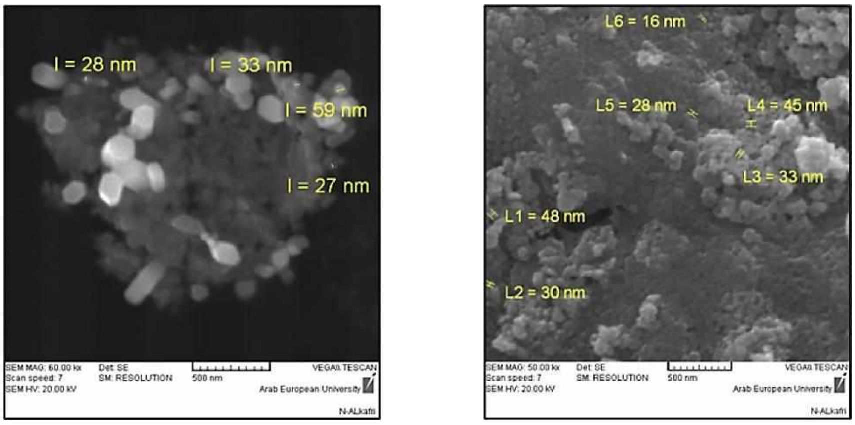

Fig. 7. SEM image of ZnO nanoparticles.

process, surfactant (C12-14-secondary alcohol ethoxylate) was used as both the medium and the stabilizing reagent, while polyvinylpyrrolidone (PVP) can serve as a surface stabilizer, growth modifier, and nanoparticle dispersant.

5. HIGHLIGHTS

The XRD pattern confirmed the crystalline nature of ZnO nanoparticles. As revealed from FT-IR pattern, the ZnO bonding and the functional groups responsible for reduction of ZnO nanoparticles are presented. Structural morphology of ZnO nanoparticles was studied by SEM analysis.

COMPLIANCE WITH ETHICAL STANDARDS

This study was funded by Damascus University. Authors declares that they have no conflict of interest.

REFERENCES

1. L. J. Lauhon, M. S. Gudiksen, D. Wang, and C. M. Lieber, *Nature*, **420**, No. 6911: 57 (2002); doi:10.1038/nature01141
2. A.Weibel, R. Bouchet, P. Bouvier, and P. Knauth, *Acta Materialia*, **54**, No. 13: 3575 (2006).
3. M. Frietsch, F. Zudock, J. Goschnick, and M. Bruns, *Sen. and Act. B: Chem.*, **65**, Nos. 1–3: 379 (2000).
4. T. Kawano and H. Imai, *Crystal Growth & Design*, **6**, No. 4: 1054 (2006).
5. J. Tamaki, *Sensor Letters*, **3**, No. 2: 89 (2005).
6. M. Kurtz, J. Strunk, O. Hinrichsen, M. Muhler, K. Fink, B. Meyer, and C. Wöll, *Angewandte Chemie International Edition*, **44**, No. 18: 2790 (2005).
7. C. L. Yang, J. N. Wang, W. K. Ge, L. Guo, S. H. Yang, and D. Z. Shen, *Journal of Appl. Phys.*, **90**, No. 9: 4489 (2001).
8. M. Izaki, K. T. Mizuno, T. Shinagawa, M. Inaba, and A. Tasaka, *Journal of the Electrochemical Society*, **153**, No. 9: C668 (2006).
9. S. H. Lee, S. S. Lee, J. J. Choi, J. U. Jeon, and K. Ro, *Microsystem Technologies*, **11**, No. 6: 416 (2005).
10. H. Chang, M. Kao, C. Jwo, C. Kuo, Y. Yeh, and W. Tzeng, *Journal of Alloys and Compounds*, **504**, Suppl. 1: S376 (2010); https://doi.org/10.1016/j.jallcom.2010.04.127
11. S. J. Chen, X. T. Chen, Z. Xue, L. H. Li, and X. Z. You, *Journal of Crystal Growth*, **246**, Nos. 1–2: 169 (2002).
12. X. Liu, B. Geng, Q. Du, J. Ma, and X. Liu, *Materials Science and Engineering: A*, **448**, Nos. 1–2: 7 (2007).
13. M. Epifani, G. De, A. Licciulli, and L. Vasanelli, *Journal of Materials Chemistry*, **11**, No. 12: 3326 (2001).
14. C. Xu, Y. Liu, G. Xu, and G. Wang, *Materials Research Bulletin*, **37**, No. 14: 2365 (2002).
15. L. Gou and C. J. Murphy, *Nano Letters*, **3**, No. 2: 231 (2003).
16. A. D. Khalaji, *Journal of Cluster Science*, **24**, No. 1: 209 (2013).
17. S. Farhadi and J. Safabakhsh, *Journal of Alloys and Compounds*, **515**, No 1: 180 (2012).
18. D. Das, B. Nath, P. Phukon, and S. K. Dolui, *Colloids and Surfaces B: Biointerfaces*, **11**, No. 1: 556 (2013).
19. A. Janaki, E. Sailatha, and S. Gunasekaran, *Spectrochimica Acta. Part A: Molecular and Biomolecular Spectroscopy*, **144**, No. 2: 17 (2015).
20. *Match! - Phase Analysis using Powder Diffraction. Crystal Impact GbR* (Dr. H. Putz & Dr. K. Brandenburg GbR, Kreuzherrenstr. 102, D-53227 Bonn, Germany); http://www.crystalimpact.com/match

Наносистеми, наноматеріали, нанотехнології
Nanosistemi, Nanomateriali, Nanotehnologii
2021, т. 19, № 4, сс. 865–871

PACS numbers: 07.07.Df, 68.37.Hk, 78.30.Jw, 78.67.Sc, 82.35.Np, 84.32.Tt

Synthesis of PVA/PAA/$SrTiO_3$ Nanostructures for Pressure Sensors

Abeer Ghalib Hadi[1,2], Zainab Al-Ramadhan[1], and Ahmed Hashim[2]

[1]*College of Education,*
Department of Physics,
University of Mustansiriyah,
Baghdad, Iraq
[2]*College of Education for Pure Sciences,*
Department of Physics,
University of Babylon,
Hillah, Iraq

In this work, new types of nanocomposites are fabricated from $SrTiO_3$-doped PVA–PAA blend for a high-sensitivity, flexible, high corrosion-resistance, and low-cost pressure sensor. The microscopy images, FT-IR studies and pressure-sensor application of PVA/PAA/$SrTiO_3$ nanocomposites are examined. The PVA/PAA/$SrTiO_3$ nanocomposites are tested for pressure sensor with range from 80 bar to 160 bar. The results indicate that the PVA/PAA/$SrTiO_3$ nanocomposites have high sensitivity for pressure.

У цій роботі нові типи нанокомпозитів виготовлено із суміші полівініловий спирт (ПВС)–поліакриламід (ПАА), леґованої $SrTiO_3$, для дешевого давача тиску високої чутливости, гнучкого, високого опору корозії. Перевірено зображення мікроскопії, дослідження інфрачервоною спектроскопією на основі перетвору Фур'є (FT-IR) і застосування для давача тиску нанокомпозитів ПВС/ПАА/$SrTiO_3$. Нанокомпозити ПВС/ПАА/$SrTiO_3$ випробувано для давача тиску з діяпазоном від 80 бар до 160 бар. Результати вказують на те, що нанокомпозити ПВС/ПАА/$SrTiO_3$ мають високу чутливість щодо тиску.

Key words: polymer blend, PVA, $SrTiO_3$, nanocomposites, pressure sensor.

Ключові слова: полімерна суміш, полівініловий спирт, $SrTiO_3$, нанокомпозити, сенсор тиску.

(Received 16 January, 2021; in revised form, 23 January, 2021)

1. INTRODUCTION

Nanotechnology is promising as a fast growing area with its technological application for the reason of developed new substance in nanosize. It can be proved a boon, because it has a large possibility to get benefits in fields as information and communication technology, drug improvement, water decontamination [1]. In the class of new materials, polymer nanocomposites have grabbed more attention due to their enhanced electrical, optical and magnetic properties. These materials possess increased modulus and flame resistance, and are capable to preclude oxidation and agglomeration. These enhancements in properties are due to interaction between nanoparticles and polymer matrix. Addition of nanoparticles in polymer matrix improves lifetime of nanoparticles, modifies the surface of nanoparticles by passivation defect states, provide low cost, ease of device fabrication and tuneable optical and electronic properties [2]. Polymers have stability after chemical and physical doping with high mechanical properties [3]. Integration of macro- and nanocomposites has led to the development of a new class of nanocomposite materials, which find vital approach in medicine, biology, industry and defence. Polymers and organic materials have been receiving a great deal of attention for their unique features offering to realize lightweight, environmental friendly, flexible and cost effective electronic devices [4]. Polyvinyl alcohol (PVA) is a polymer with carbon chain backbone attached with hydroxyl groups. These OH groups can be a source of hydrogen bonding and hence assist in the formation of polymer blends. PVA is non-toxic, water-soluble synthetic polymer, which is widely used in the polymer blends due to its good physical and chemical properties, excellent film forming characteristics, emulsifying capability, non-carcinogenic, biodegradable and biocompatible qualities. These unique characteristics enable it for its applicability in pharmaceutical fields, as drug coating agents, material for surgical structures and cosmetic industries [5]. This work aims to prepare of PVA/PAA/$SrTiO_3$ nanocomposites for low-cost pressure sensors.

2. MATERIALS AND METHODS

In this work, the materials used are PVA (88 wt.%) and polyacrylamide (PAA) (12 wt.%) in a polymer blend and the $SrTiO_3$ nanoparticles as additive. To get a homogeneous solution PVA–PAA blend, magnetic stirrer is used in mixing process when each of the PVA and PAA polymers are dissolved in distilled water. $SrTiO_3$ nanoparticles are added to solution with concentrations of 0, 1.8, 3.6, 5.4 and 7.2 wt.%. To prepare the PVA/PAA/$SrTiO_3$ nanocomposites, the casting method is used. Films of PVA–PAA/$SrTiO_3$ nanocomposites are prepared by dissolving 1 g of PVA and PAA with 88:12 ratio in 30 ml of distilled water. The sample is placed between copper plate, and load is applied on two plates where sample between them. The capacitance for different applied load in a range 80–160 bar is measured by using LCR meter type HIOKI 3532-50 LCR HI TESTER at 100 Hz, which locally manufactured.

3. RESULTS AND DISCUSSION

Figure 1 shows microscopy examination of PVA/PAA/$SrTiO_3$ nano-

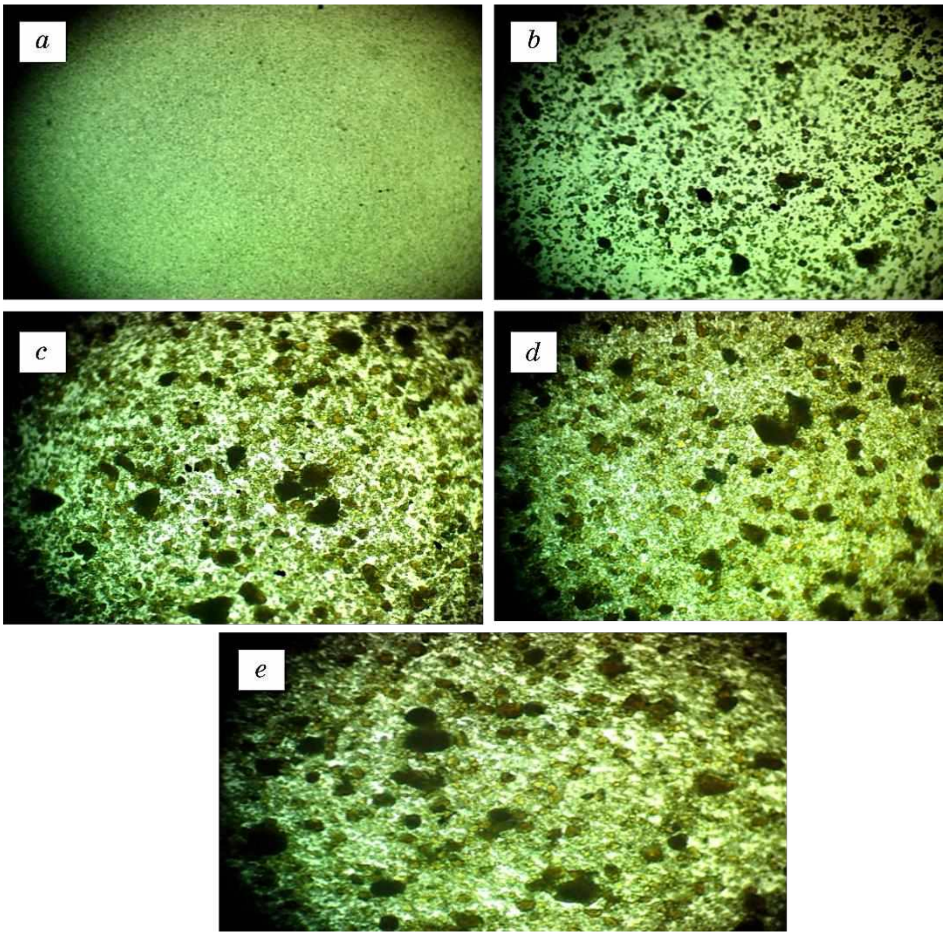

Fig. 1. Microscopy images (×10): (*a*) pure blend; (*b*) 1.8 wt.% $SrTiO_3$ nanoparticles; (*c*) 3.6 wt.% $SrTiO_3$ nanoparticles; (*d*) 5.4 wt.% $SrTiO_3$ nanoparticles; (*e*) 7.2 wt.% $SrTiO_3$ nanoparticles.

composites. The microscopy examination shows the distribution of the $SrTiO_3$ nanoparticles in the polymer PVA–PAA blend. When adding the $SrTiO_3$ nanoparticles to the polymer PVA–PAA blend, the concentrations of the charge carriers, which are absorbing the photons, will increase as shown in Fig. 1, *a*, *b*, *c*, *d* and *e*.

Figure 1 shows that the $SrTiO_3$ nanoparticles are aggregated as clusters at lower content. When increasing the ratio of $SrTiO_3$ nanoparticles, they form paths network inside the PVA/PAA blend.

Figure 2 shows the FT-IR spectra of PVA/PAA/$SrTiO_3$ nanocom-

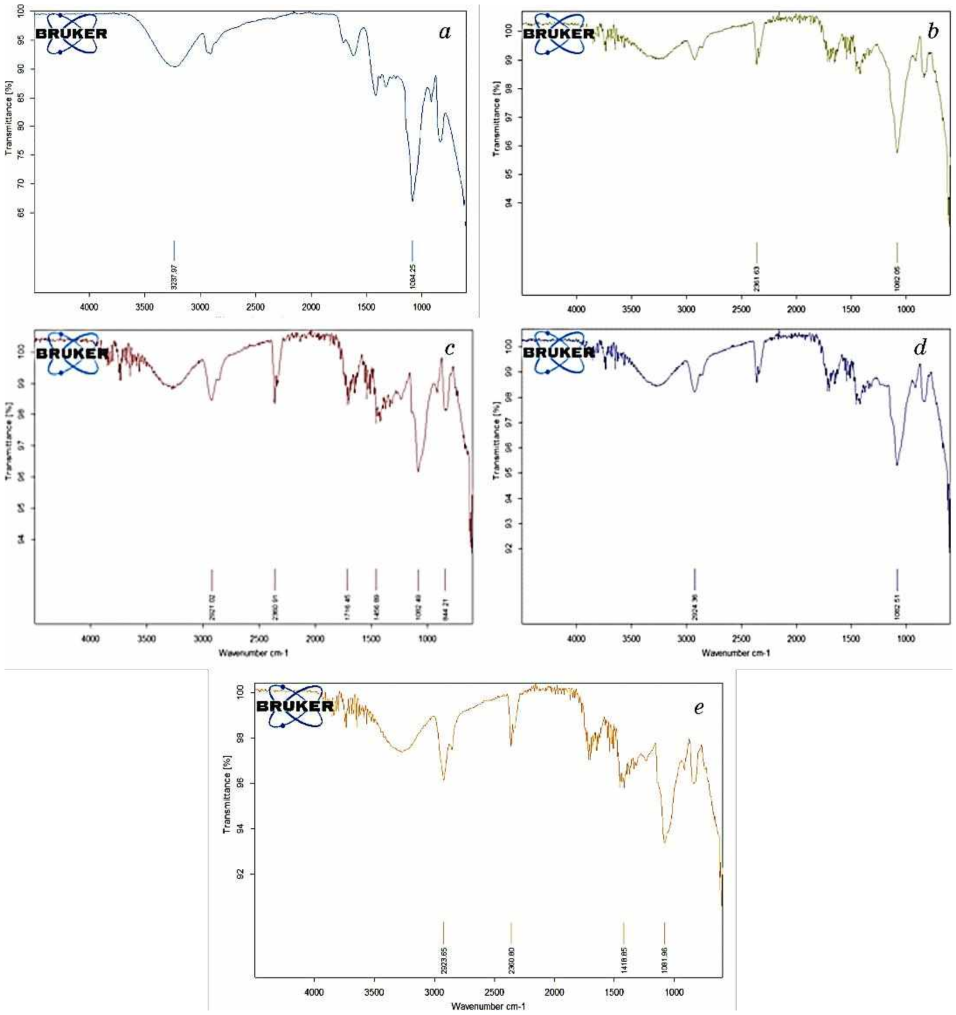

Fig. 2. FT-IR spectra of PVA/PAA/$SrTiO_3$ nanocomposites: (*a*) pure blend; (*b*) 1.8 wt.% $SrTiO_3$ nanoparticles; (*c*) 3.6 wt.% $SrTiO_3$ nanoparticles; (*d*) 5.4 wt.% $SrTiO_3$ nanoparticles; (*e*) 7.2 wt.% $SrTiO_3$ nanoparticles.

posites.

The FT-IR studies of nanocomposites manifest the interactions in nanocomposites. They show broad bands at 3237.97 cm^{-1}. The large bands observed between 3550 and 3200 cm^{-1} are linked to the stretching O–H from the intermolecular and intramolecular hydrogen bonds. The vibrational band observed between 2840 and 3000 cm^{-1} refers to the stretching C–H from alkyl groups. This correlation was calculated through the ratio of the intensities associated with vibrational bands of C–O (1710 cm^{-1}) and bending vibrations related to CH$_2$ groups at $\delta = 1460$ cm^{-1} that remains almost constant [6]. The peaks at 1418–1424 cm^{-1} were assigned to the C–O groups of polymers matrix. The band observed at 2920 cm^{-1} is characteristic of an asymmetry-stretching mode of CH$_2$ group. The strong band around 1086–1090 cm^{-1} for all samples of nanocomposites is attributed to the stretching mode of C–O group. The two strong bands observed at around 1420 cm^{-1} and 841 cm^{-1} are attributed to the bending and stretching modes of CH$_2$ group, respectively [7].

As noted from the FT-IR studies, there are no interactions between PVA–PAA blend and SrTiO$_3$ nanoparticles.

Figure 3 shows a variation of the electrical capacitance for PVA/PAA/SrTiO$_3$ nanocomposites with the pressure for different concentrations of SrTiO$_3$ nanoparticles.

As shown, the electrical capacitance of PVA–PAA blend increases as the pressure increases. There is an explanation of this behaviour: the SrTiO$_3$ nanoparticles are aggregated as clusters in the

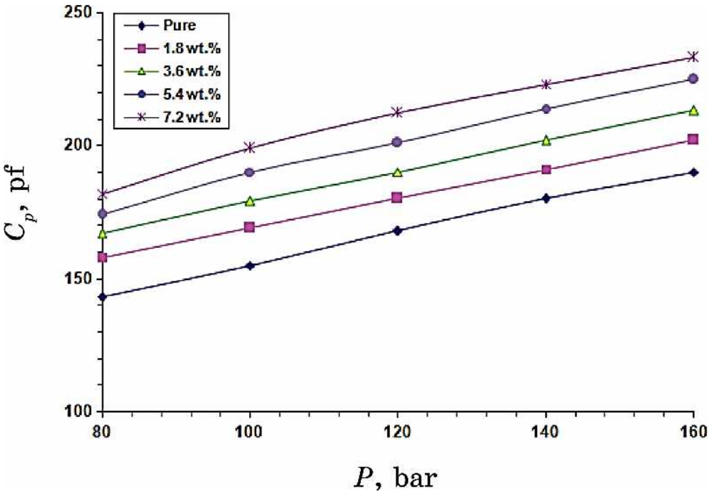

Fig. 3. Variation of the electrical capacitance for PVA/PAA/SrTiO$_3$ nanocomposites with the pressure for different concentrations of SrTiO$_3$ nanoparticles.

PVA/PAA blend and, hence, the electrical resistance is high. Applying the pressure causes a decrease in the distance between filler particles inside the matrix and an increase in the number of conductive paths that leads to decrease in the resistance of composites. Hence, the resistance is low, and the electrical capacitance of PVA/PAA/$SrTiO_3$ nanocomposites will increase [8–14].

4. CONCLUSIONS

In the present work, synthesis of PVA/PAA/$SrTiO_3$ nanocomposites has been investigated.

The microscopy images, FT-IR analysis and pressure sensor application were examined.

Finally, the results show that the electrical capacitance of PVA/PAA/$SrTiO_3$ nanocomposites increases with the rise in pressure that makes the PVA/PAA/$SrTiO_3$ nanocomposites useful for pressure sensors' applications with low cost, lightweight and high sensitivity.

REFERENCES

1. S. Pişkin, A. Palantöken, and M. Yılmaz, *Int. Conf. on Emer. Trends in Eng. and Techno. (December 7–8, 2013, Patong Beach, Phuket, Thailand).*
2. C. Tyagi and A. Sharma, *AIP Conf. Pro.*, **1728**: 020151 (2016); doi:10.1063/1.4946202
3. S. E. Islam and A. M. Abdelrhman, *J. Mater. Res. Technol.*, **8**, No. 2: 1944 (2019).
4. A. Hazim, A. Hashim, and H. M. Abduljalil, *Nanosistemi, Nanomateriali, Nanotehnologii*, **18**, Iss. 4: 983 (2020); https://doi.org/10.15407/nnn.18.04.983
5. A. Hashim and Z. S. Hamad, *Nanosistemi, Nanomateriali, Nanotehnologii*, **18**, Iss. 4: 969 (2020); https://doi.org/10.15407/nnn.18.04.969
6. H. S. Mansur, C. M. Sadahira, A. N. Souza, and A. A. P. Mansur, *Engineering C*, **28**: 539 (2008).
7. K. Karthikeyan, N. Poornaprakash, N. Selvakumar, and Jeyasubrmanian, *J. of Nanostructured Polymers and Nanocomposites*, **5**, No. 4: 83 (2009).
8. A. Hashim and A. Hadi, *Ukrainian J. of Phys.*, **63**, No. 8: 754 (2018); https://doi.org/10.15407/ujpe63.8.754
9. A. Hashim and Q. Hadi, *Sensor Letters*, **15**, No. 11: 951 (2017); doi:10.1166/sl.2017.3892
10. A. Hashim, M. A. Habeeb, A. Hadi, Q. M. Jebur, and W. Hadi, *Sensor Letters*, **15**, No. 12: 998 (2017); doi:10.1166/sl.2018.3935
11. A. Hashim and A. Hadi, *Ukrainian J. of Physics*, **62**, No. 12: 1050 (2017); doi:10.15407/ujpe62.12.1050
12. A. Hashim and A. Hadi, *Sensor Letters*, **15**, No. 12: 1019 (2017); doi:10.1166/sl.2017.3910

13. A. Hashim, A. J. K. Algidsawi, H. Ahmed, A. Hadi, and M. A. Habeeb, *Nanosistemi, Nanomateriali, Nanotehnologii*, **19**, Iss. 1: 91 (2021); https://doi.org/10.15407/nnn.19.01.091
14. A. Hashim, A. J. K. Algidsawi, H. Ahmed, A. Hadi, and M. A. Habeeb, *Nanosistemi, Nanomateriali, Nanotehnologii*, **19**, Iss. 2: 353 (2021); https://doi.org/10.15407/nnn.19.02.353

Наносистеми, наноматеріали, нанотехнології
Nanosistemi, Nanomateriali, Nanotehnologii
2021, т. 19, № 4, сс. 873–881

PACS numbers: 72.80.Tm, 78.20.Ci, 78.30.Jw, 78.67.Sc, 81.07.Pr, 82.35.Np

Novel Pressure Sensors Prepared from PVA–CMC–TiC Nanocomposites: Fabrication and Characterization

Ahmed Hashim and Qassim Hadi

College of Education for Pure Sciences,
Department of Physics,
University of Babylon,
Hillah, Iraq

In this paper, preparation of new pressure sensors with low cost and lightweight, and their structural and dielectric properties are investigated. The pressure sensors are prepared from polyvinyl alcohol (PVA; 50 wt.%) and carboxyl methylcellulose (CMC; 50 wt.%) with different concentrations (1, 2 and 3 wt.%) of titanium-carbide nanoparticles. The dielectric properties are measured in the frequency range from 100 Hz to 5 MHz. The experimental results show that the dielectric constant and dielectric loss of PVA–CMC–TiC nanocomposites are decreased with increase in frequency of applied electric field. The A.C. electrical conductivity increases with increasing the frequency. The dielectric constant, dielectric loss, and A.C. electrical conductivity of PVA–CMC blend are increased with increase of concentration of TiC nanoparticles. The results of pressure sensor application show that the electrical resistance of PVA–CMC–TiC nanocomposites decreases with increase in pressure.

У цій роботі досліджено приготування нових датчиків тиску з низькою вартістю та невеликою вагою, а також їхні структурні та діелектричні властивості. Датчики тиску готуються з полівінілового спирту (ПВС; 50 ваг.%) і карбоксильної метилцелюлози (КМЦ; 50 ваг.%) з різною концентрацією (1, 2 і 3 ваг.%) наночастинок карбіду Титану. Діелектричні властивості вимірюються в діяпазоні частот від 100 Гц до 5 МГц. Експериментальні результати показують, що діелектрична проникність і діелектричні втрати нанокомпозитів ПВС–КМЦ–TiC зменшуються зі збільшенням частоти прикладеного електричного поля. Електропровідність змінного струму збільшується зі збільшенням частоти. Діелектрична проникність, діелектричні втрати й електропровідність змінного струму суміші ПВС–КМЦ збільшуються зі збільшенням концентрації наночастинок TiC. Результати застосування датчика тиску показують, що електричний опір нанокомпозитів ПВС–КМЦ–TiC понижується зі збільшенням тиску.

Key words: nanocomposite, titanium carbide, conductivity, pressure sensor.

Ключові слова: нанокомпозит, карбід Титану, провідність, датчик тиску.

(Received 17 November, 2020)

1. INTRODUCTION

Recently there has been a constant search for new materials that possess high dielectric permittivity and good mechanical properties for important technological applications. Polymers are materials with low-density flexible, easy to fabricate and superior in dielectric breakdown strength and mechanically more compliant than the ceramics, but its dielectric values are much lower than those of the ceramics [1].

The addition of inorganic nanoparticles to polymers allows the modification of the polymer physical properties as well as the implementation of new features in the polymer matrix. With decreasing particle size, the ratio of surface/volume increases, so that surface properties become crucial. Smaller the particles are, more important will be the surface properties, thereby influencing interfacial properties, agglomeration behaviour, and the physical properties of the particles. The intensity of these properties changes depending upon the nature, composition, concentration and size of the nanoparticles [2].

Addition of small amount of nanomaterial could improve the performance of polymeric materials due to their small size, large specific surface area, quantum confinement effects, and strong interfacial interactions. Among these polymers, polyvinyl alcohol (PVA) is a polymer that has been studied intensively due to its good film forming and physical properties, high hydrophilicity, processability, biocompatibility, and good chemical resistance. Polyvinyl alcohol is a good insulating material with low conductivity; hence, it is very useful in microelectronic industry. Its electrical conductivity depends on the thermally generated carriers and the addition of suitable dopants. Moreover, the PVA polymer extends the industrial applications in optical, pharmaceutical, medical, and membrane fields. PVA is a semi-crystalline material with several interesting physical properties, which are very useful in technical applications [1, 3]. Polymer nanocomposites containing semiconductor nanoparticles are shown to be significant for building electronic and optoelectronic devices, such as solar cells, light-emitting diodes, optical limiters, and various types of sensors [4–6].

Many of the modern technologies require materials with unusual combinations of properties that cannot be met by conventional metal alloys, ceramics and polymers. Nanocomposite development provides for new technologies and business opportunities in many sectors of aerospace, automobile, electronics and biotechnology industries.

Titanium carbide (TiC) is widely used as a reinforcing particle to produce metal matrix composites due to its hardness, chemical inertia, high melting point and stability. Composites comprising titanium carbide metal matrix can be characterized by a good wear resistance with a relatively low coefficient of friction [7].

2. EXPERIMENTAL PART

The nanocomposites of PVA–CMC–TiC were prepared by dissolving 1 gm of PVA–CMC blend in 20 ml of distilled water with concentration: 50 wt.% PVA and 50 wt.% CMC by using magnetic stirrer to mix the polymers for 1 hour to obtain solution that is more homogeneous. The TiC nanoparticles were added to polymers' mixture with different concentrations (1, 2 and 3 wt.%). The casting method is used to prepare the samples of PVA–CMC–TiC nanocomposites in the template (Petri dish has diameter of 10 cm). The samples were prepared with thickness range 117–140 μm.

The dielectric properties of PVA–CMC–TiC nanocomposite samples are studied with frequency range from 100 Hz to $5\cdot10^6$ Hz by using LCR meter type (HIOKI 3532-50 LCR HI TESTER). The pressure sensor of samples is investigated by measuring the resistance between two electrodes on the top and bottom of the sample for different pressures' range 80–200 bar.

The dielectric constant, ε', of nanocomposites is defined by using the following equation [8]:

$$\varepsilon' = \frac{C_p}{C_o}, \tag{1}$$

where C_p is parallel capacitance and C_o is vacuum capacitor.

The dielectric loss, ε'', of nanocomposites is written by following equation [8]:

$$\varepsilon'' = \varepsilon' D, \tag{2}$$

where D is dispersion factor.

The A.C. electrical conductivity is defined by following equation [9]:

$$\sigma_{\text{A.C.}} = w\varepsilon''\varepsilon_0, \tag{3}$$

where w is the angular frequency.

3. RESULTS AND DISCUSSION

The FT-IR spectra for pure polymer blend and PVA–CMC–TiC nanocomposite films are shown in Fig. 1. In the spectra of nanocomposites, the broad and strong band centred at 3366 cm^{-1} is assigned to the stretching vibration of hydroxyl group OH. The band observed at 1601 cm^{-1} is assigned to the stretching vibrational band of C=O. The two bands observed at 1416 and 1356 cm^{-1} are assigned as CH_3 bending vibration and CH_2 stretching, respectively. The band at 1056 cm^{-1} arises from the C–O stretching vibration, while the band at 917 cm^{-1} results from CH_2 rocking vibration [10]. The TiC nanoparticles cause changes in spectra of PVA–CMC, which include shift in some bonds and change in the intensities. These changes attributed to interactions of nanoparticles with polymers. The FT-IR studies show the non-interactions between PVA–CMC polymer matrix and TiC nanoparticles [11].

The variation of dielectric constant for PVA–CMC–TiC nanocomposites with frequency at different concentrations of TiC nanoparticles is shown in Fig. 2.

The polarized molecules or atoms in dielectric medium can align in accordance with the applied electric field, which implies electro-

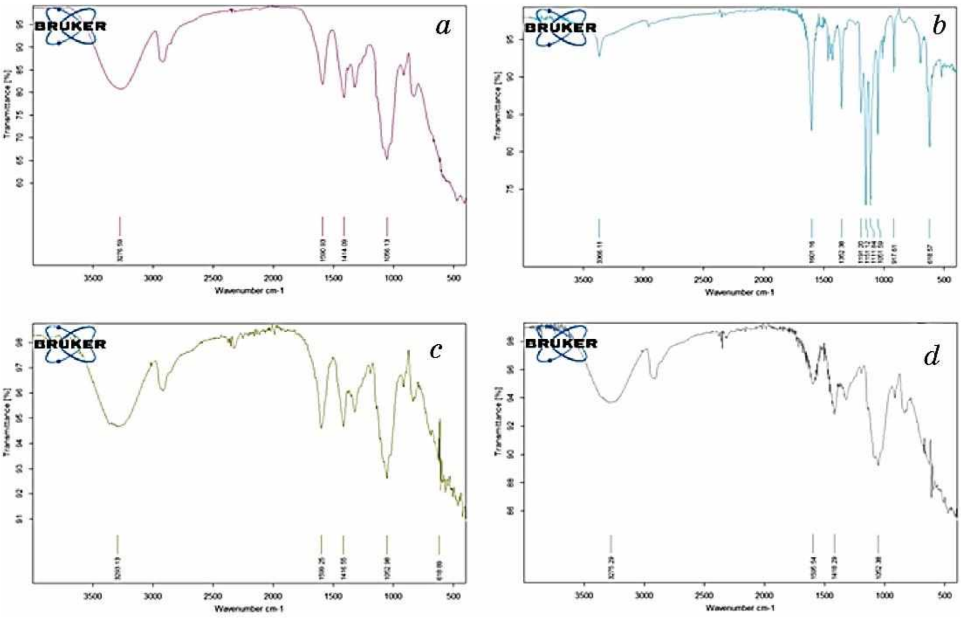

Fig. 1. FT-IR spectra for PVA–CMC–TiC nanocomposites: *a*) pure blend; *b*) 1 wt.% TiC nanoparticles; *c*) 2 wt.% TiC nanoparticles; *d*) 3 wt.% TiC nanoparticles.

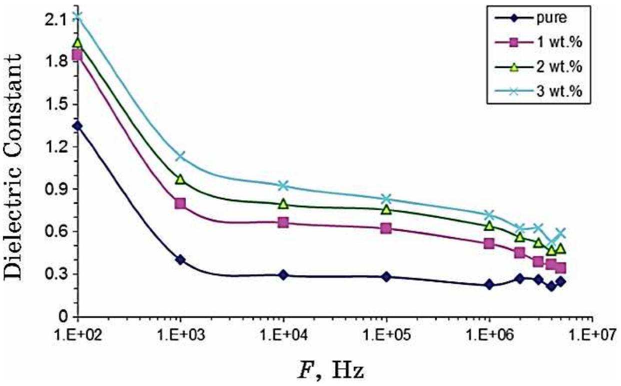

Fig. 2. Variation of dielectric constant for PVA–CMC–TiC nanocomposites with frequency at room temperature.

magnetic energy to be transferred into materials. In Figure 2, the behaviour of frequency-dependent dielectric constant of PVA–CMC–TiC nanocomposites at room temperature is illustrated. The plot inferred that the value of dielectric constant has a strong influence in radiofrequency region. At lower frequencies, high values are noticed that indicates that the four polarizations are active, whereas at higher frequencies, due to the high periodic field reversal resulting in inertia of the dipolar moments, causes the reduction in the values. An independent frequency trace is noticed beyond 1 kHz but a substantial modification is achieved by the incorporation of TiC nanoparticles in the matrix. A giant polarizability is noticed because the particles are relatively free to move in extended trajectories between the electrodes. The TiC exhibits a strong ionic polarization due to the titanium and carbon ions and has a high value of static permittivity, so that the increment in the values of relative permittivity for the composites due to these mobile charge carriers is expected.

Figure 3 shows the frequency-dependent dielectric loss of PVA–CMC–TiC at room temperature. This curve possessed a similar trace as the plot of dielectric constant, and the changes in steepness are observed at the same frequency region. This phenomenon can be identified as interfacial polarization (IP) where the high values are presented at the low-frequency region. At higher frequencies, the dipoles cause an inertia results from the electrical heterogeneity known as Maxwell–Wagner–Sillars effect [12].

As shown in Figures 2, 3, the dielectric constant of PVA–CMC blend increases with increase in TiC nanoparticles' concentration; this behaviour could be interpreted from both interfacial polarization inside the nanocomposite in applied alternating electric field and increase of the charge carriers.

The dielectric loss increases with increase in concentrations for nanoparticles. The increase of dielectric loss of PVA–CMC blend with increase in TiC nanoparticles' concentration for related to the increase of the number for charge carriers. At low concentrations of TiC nanoparticles, they are formed as clusters; when the concentra-

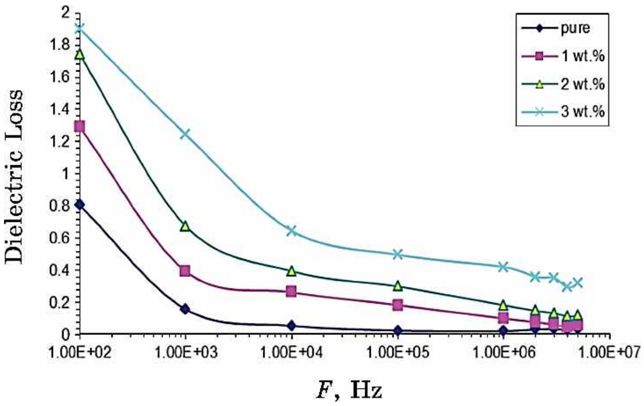

Fig. 3. Variation of dielectric loss for PVA–CMC–TiC nanocomposites with frequency at room temperature.

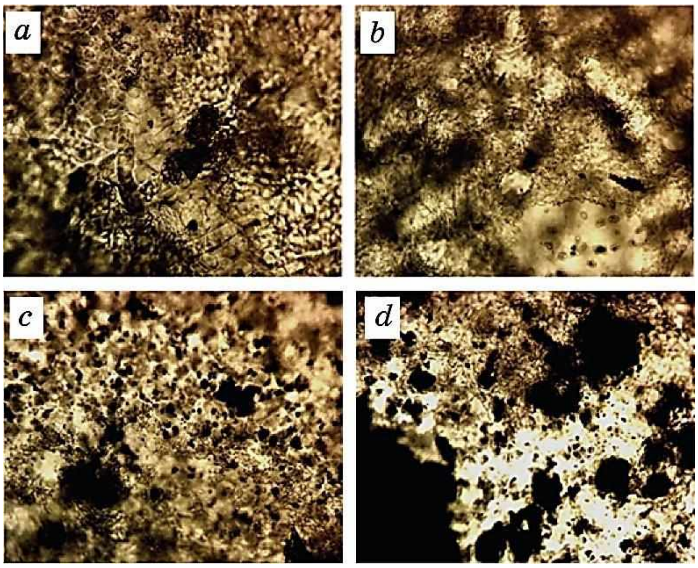

Fig. 4. Photomicrographs (×10) for PVA–CMC–TiC nanocomposites: *a*) for pure; *b*) for 1 wt.% TiC nanoparticles; *c*) for 2 wt.% TiC nanoparticles; *d*) for 3 wt.% TiC nanoparticles.

tion of TiC nanoparticles increases, the nanoparticles form a continuous network in the nanocomposite [11], as shown in Fig. 4. In Figure 4, the TiC nanoparticles' arrangement in PVA–CMC polymer matrix is shown at magnification power (×10). The TiC nanoparticles are aggregated as clusters at low concentrations. When increasing the concentrations of TiC nanoparticles, the nanoparticles form a continuous network inside the PVA–CMC blend [11].

The variation of A.C. electrical conductivity for PVA–CMC–TiC nanocomposites with frequency for different TiC nanoparticles' concentrations is shown in Fig. 5. The increase in A.C. conductivity is due to increase in the composition of the TiC nanoparticles' concentration in polymer matrix resulting in relatively more number of free charges carries. These charge carriers move in the amorphous polymer matrix, and hence the conductivity increases. Thus, there is a relation between the amorphous nature of the polymer film and the conductivity [13].

In addition, the A.C. conductivity increases as TiC nanoparticles' concentration increases. This result can be attributed to an increase in the conductivity because of the increase in the charge carrier density in the polymer blend and the increase of the free charge carrier number [14].

Figure 6 shows variation of resistance for PVA–CMC–TiC nanocomposites with compression stress. Pressure sensors, which are widely applied in automation equipment, robot arms, touch panels, and cell phones, have been developed on the basis of piezoresistive, piezoelectric, and capacitive principle. Pressure sensors need high sensitivity and strong discriminatory abilities for wide applications

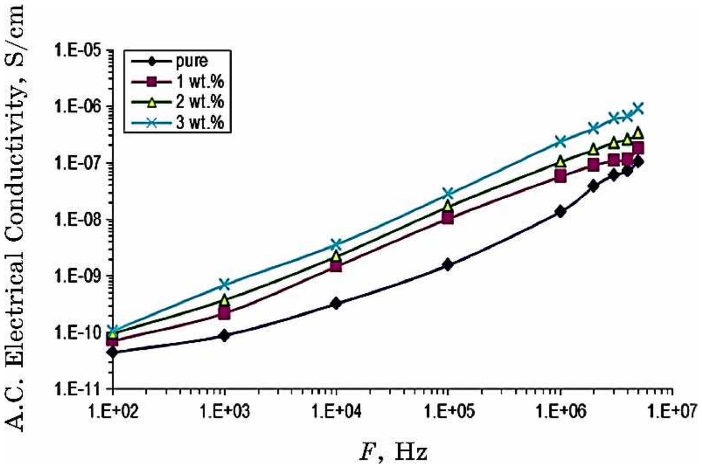

Fig. 5. Variation of A.C. electrical conductivity for PVA–CMC–TiC nanocomposites with frequency at room temperature.

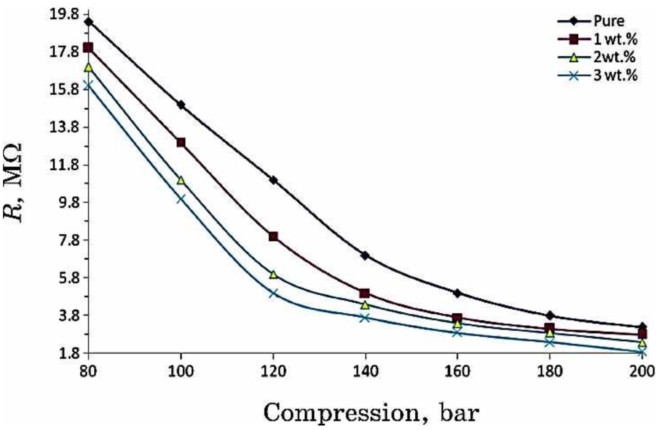

Fig. 6. Variation of resistance for PVA–CMC–TiC nanocomposites with compression.

[15]. As shown in Figure 6, the resistance for PVA–CMC–TiC nanocomposites decreases with increases in compression stress. This behaviour can be explained as follows: when stress is applied, it will change the local dipole distributions and induce an electric field; the induced electric field accumulates the charges at both the top and the bottom of the sample [16].

4. CONCLUSIONS

The dielectric constant, dielectric loss, and A.C. electrical conductivity of PVA–CMC blend increase with increasing titanium carbide nanoparticles' concentration.

The dielectric constant and dielectric loss of PVA–CMC–TiC nanocomposites decrease with increase of the frequency.

The A.C. electrical conductivity increases with increase of the frequency.

The PVA–CMC–TiC nanocomposites films have high sensitivity for pressure.

REFERENCES

1. I. R. Agool, K. J. Kadhim, and A. Hashim, *International Journal of Plastics Technology*, **20**, Iss. 1: 121 (2016); https://doi.org/10.1007/s12588-016-9144-5
2. T. Badapanda, V. Senthil, S. Anwarb, L. S. Cavalcante, N. C. Batista, and E. Longo, *Current Applied Physics*, **13**: 1490 (2013).
3. R. Etefagha, S. M. Rozatia, E. Azhirb, N. Shahtahmasebib, A. S. Hosseinib, and P. Madahib, *Scientia Iranica F*, **24**, No. 3: 1717 (2017).

4. I. R. Agool, K. J. Kadhim, and A. Hashim, *International Journal of Plastics Technology*, **21**, Iss. 2: 397 (2017); DOI:10.1007/s12588-017-9192-5
5. I. R. Agool, K. J. Kadhim, and A. Hashim, *International Journal of Plastics Technology*, **21**, Iss. 2: 444 (2017); https://doi.org/10.1007/s12588-017-9196-1
6. A. Hashim and Q. Hadi, *Journal of Inorganic and Organometallic Polymers and Materials,* **28**, Iss. 4: 1394 (2018); https://doi.org/10.1007/s10904-018-0837-4
7. L. Benea and J.-P. Celis, *Materials*, **9**, Iss. 4: 269 (2016); https://doi.org/10.3390/ma9040269
8. R. Divya, M. Meena, C. K. Mahadevan, and C. M. Padma, *Journal of Engineering Research and Applications*, **4**, Iss. 5: 1 (2014).
9. T. Sankarappa and M. Prashantkumar, *International Journal of Advanced Research in Physical Science*, **1**, No. 2: 1 (2014).
10. A. F. Mansour, S. F. Mansour, and M. A. Abdo, *IOSR Journal of Applied Physics*, **7**, No. 2: 60 (2015).
11. A. Hashim, I. R. Agool, and K. J. Kadhim, *Journal of Materials Science: Materials in Electronics*, **29**, Iss. 12: 10369 (2018); https://doi.org/10.1007/s10854-018-9095-z
12. J. J. Mathen, G. P. Joseph, and J. Madhavan, *IJEDR*, **4**, No. 3: 1054 (2016); https://www.ijedr.org/papers/IJEDR1603167.pdf
13. M. B. Nanda Prakash, A. Manjunath, and R. Somashekar, *Advances in Condensed Matter Physics*, **2013**: ID 690629 (2013).
14. A. Hashim and A. Hadi, *Ukrainian Journal of Physics*, **62**, No. 12: 1050 (2017); https://doi.org/10.15407/ujpe62.12.1050
15. C.-C. Su, C.-H. Li, N.-K. Chang, F. Gao, and S.-H. Chang, *Sensors*, **12**: 10034 (2012).
16. T. H. Kim, *M. Sc. Thesis* (Uni. California: 2015).

Наносистеми, наноматеріали, нанотехнології
Nanosistemi, Nanomateriali, Nanotehnologii
2021, т. 19, № 4, сс. 883–891

PACS numbers: 07.07.Df, 72.80.Tm, 78.20.Ci, 78.30.Jw, 78.67.Sc, 81.07.Pr, 82.35.Np

Synthesis and Characterization of Novel PVA–Starch–Y_2O_3 Bionanocomposites for Pressure Sensors

Ahmed Hashim and Ali Jassim

College of Education for Pure Sciences,
Department of Physics,
University of Babylon,
Hillah, Iraq

Synthesis of the polyvinyl alcohol (PVA)–starch (ST)–yttrium oxide (Y_2O_3) nanocomposites and studying their structural and dielectric properties are considered for the sake of high-sensitive pressure sensors. The nanocomposites are prepared by casting method. The PVA–ST blend is prepared with following concentrations: 85 wt.% polyvinyl alcohol, 15 wt.% starch. The effect of yttrium-oxide nanoparticles' concentration on the structural and dielectric properties of PVA–ST blend is studied. The dielectric properties of PVA–ST–Y_2O_3 nanocomposites are examined in frequency range from 100 Hz to 5 MHz. The results show that dielectric constant and dielectric loss of nanocomposites are decreased with increase in frequency of applied electric field. The A.C. electrical conductivity increases with increase in frequency. The dielectric parameters (dielectric constant, dielectric loss, and A.C. electrical conductivity) of PVA–ST blend are increased with increase in yttrium-oxide nanoparticles' concentration. The PVA–ST–Y_2O_3 nanocomposites are tested for pressure-sensor application. The results show that the electrical resistance of PVA–ST–Y_2O_3 nanocomposites decreases with increase in pressure.

Синтеза нанокомпозитів полівініловий спирт (ПВС)–крохмаль (К)–оксид Ітрію (Y_2O_3) та вивчення їхніх структурних і діелектричних властивостей розглядаються заради високочутливих датчиків тиску. Нанокомпозити готують методом лиття. Суміш ПВС–К готується з наступними концентраціями: 85 ваг.% полівінілового спирту, 15 ваг.% крохмалю. Досліджено вплив концентрації наночастинок оксиду Ітрію на структурні та діелектричні властивості суміші ПВС–К. Діелектричні властивості нанокомпозитів ПВС–К–Y_2O_3 досліджуються в діяпазоні частот від 100 Гц до 5 МГц. Результати показують, що діелектрична постійна та діелектричні втрати нанокомпозитів зменшуються зі збільшенням частоти прикладеного електричного поля. Електропровідність змінного струму збільшується зі збільшенням частоти. Діелектричні параметри (діелектрична константа, діелектричні втрати та електропровідність змінного струму) суміші ПВС–К збільшуються зі збільшенням концентрації наночастинок оксиду Ітрію. Нанокомпозити ПВС–К–Y_2O_3 тестуються на застосування датчиків тиску. Результати показують, що електричний опір нанокомпозитів ПВС–К–Y_2O_3 спадає зі збільшенням тиску.

Key words: conductivity, structure, Y_2O_3, nanocomposite, pressure sensor.

Ключові слова: електропровідність, структура, Y_2O_3, нанокомпозит, датчик тиску.

(Received 17 November, 2020)

1. INTRODUCTION

Organic–inorganic nanocomposites are extremely promising for applications in light-emitting diodes, photodiodes, photovoltaic cells, smart microelectronic device, and gas sensors among others. The properties of nanocomposites films can be adjusted by varying the composition. Their fabrication shares the same advantages of organic device technology such as low-cost production and the possibility of device fabrication on large area and flexible substrates.

PVA is a potential material having high dielectric strength, good charge storage capacity and dopant-dependent electrical and optical properties. It has carbon chain backbone with hydroxyl groups attached to methane carbons. These OH groups can be a source of hydrogen bonding and hence assist the formation of polymer composite [1].

Starch is the most abundant carbohydrate reserve in plants and is found in leaves, flowers, fruits, seeds, different types of stems and roots. Starch biochemical chain responsible for starch synthesis involves glucose molecules produced in plant cells by photosynthesis. Starch is formed in the chloroplasts of green leaves and amyloplasts, organelles responsible for the starch reserve synthesis of cereals and tubers [2].

Yttrium oxide, as an important member among rare-earth compounds, has been actively studied in the recent years. It is one of the most promising elements for the fabrication of optoelectronics devices and chemical catalysis. Y_2O_3 can be used as high-efficient additives and functional composite materials like yttria-stabilized zirconia films. This material could be synthesized *via* several methods, including cathodic electrodeposition, gas-phase condensation, precipitation, sol–gel, pyrolysis, solvothermal and hydrothermal syntheses [3]. The addition of inorganic nanoparticles to polymers allows the modification of the polymer physical properties as well as the implementation of new features in the polymer matrix [4].

Pressure sensors have a great significance for industrial equipment, and they are widely used for the control and monitoring of thousands of applications such as biomedical, environment, space, and automobiles. Furthermore, piezoresistive pressure sensors have been proposed to detect the strain by applying pressure to change the resistance of test patterns. Materials typically used for piezoresistive pressure sensors are silicon, polysilicon thin films, bonded metal foils, sputtered thin films, and inkjet printing films. Generally, piezoresistive pressure sensors are the most commonly employed technology in the pressure sensor market owing to their advantages of high sensitivity and low cost [5].

The idea of connecting two or more different constituents into one substance gives almost infinite possibilities to create new engineering materials characterized by variety of different properties. Composite materials, because of these diverse properties, are successfully used in almost all areas of industry and science [6–9]. One advantage of nanoparticles as polymer additives appearing to have is that compared to traditional additives, namely, loading requirements are quite low [10].

2. THEORETICAL PART

The dielectric constant, ε', of PVA–ST–Y_2O_3 bionanocomposites is defined by the following equation [11]:

$$\varepsilon' = C_p / C_o\,, \qquad (1)$$

where C_p is parallel capacitance and C_o is vacuum capacitance.

The dielectric loss, ε'', of PVA–ST–Y_2O_3 bionanocomposites is written by the equation as follows [12]:

$$\varepsilon'' = \varepsilon' D, \qquad (2)$$

where D—dispersion factor of PVA–ST–Y_2O_3 nanocomposites.

The A.C. electrical conductivity of PVA–ST–Y_2O_3 bionanocomposites is determined by the equation [12]:

$$\sigma_{\mathrm{A.C.}} = w\varepsilon''\varepsilon_0, \qquad (3)$$

where w—the angular frequency.

3. EXPERIMENTAL PART

The nanocomposite films are prepared from PVA–ST blend with different of yttrium-oxide nanoparticles' concentrations by casting method. The PVA–ST blend is prepared by dissolving 1 gm of polyvinyl alcohol and starch in 20 ml of distilled water with concentrations: 85 wt.% PVA and 15 wt.% ST by using magnetic stirrer to mix the polymers for 1 hour to obtain solution that is more homogeneous. The Y_2O_3 nanoparticles added to polymers' mixture with different concentrations 1, 2 and 3 wt.%. The samples of PVA–ST–Y_2O_3 nanocomposites are casted in the template (Petri dish has diameter of 10 cm). The samples are prepared with thickness range 120–142 μm.

FT-IR spectra (Fig. 1) were tested in wave number range 500–4000 cm^{-1} by FT-IR (Bruker Company, German origin, type Vertex-70). The nanocomposites' samples are examined by using the optical microscope (supplied from Olympus name (ToupView) type (Nikon-73346)) with magnification (×10). The dielectric properties of PVA–ST–Y_2O_3 nanocomposites' samples are tested within the frequency range from 100 Hz to $5 \cdot 10^6$ Hz by using LCR meter type (HIOKI 3532-50 LCR HI TESTER). The pressure-sensor application of nanocomposites is investigated by measuring the resistance between two electrodes on the top and bottom of the sample for different pressures' range 80–200 bar.

4. RESULTS AND DISCUSSION

The FT-IR spectra of PVA–ST–Y_2O_3 nanocomposites are shown in Fig. 1. As shown in Fig. 1, the broad peak around 3250 cm^{-1} indicates stretching of hydroxyl groups (O–H). The peak at 1087 cm^{-1} is due to the C–O stretch of secondary alcoholic groups [13].

Figure 2 shows the dependence of real dielectric constant on the frequency at room temperature. It verifies that value of dielectric constant for PVA–ST–Y_2O_3 nanocomposites is high at low frequencies since electric dipoles have enough relaxation time to be supported with the field. Thus, there is a high dielectric constant. However, relaxation time decreases with increase in frequency as dipoles do not get sufficient time to be supported with the field, and the dielectric constant decreases. The values of dielectric constant for PVA–ST–Y_2O_3 nanocomposites rise with a dopant concentration of yttrium-oxide nanoparticles.

This rise in dielectric-constant values could be ascribed by Maxwell–Wagner interfacial polarization [14] and increasing number of charge carries as shown in Fig. 3. This figure shows that the Y_2O_3 nanoparticles are aggregated as clusters at low concentrations. When increasing the concentration of Y_2O_3 nanoparticles, the nanoparticles form a paths' network inside the PVA–ST blend.

The variation of dielectric loss for PVA–ST–Y_2O_3 nanocomposites

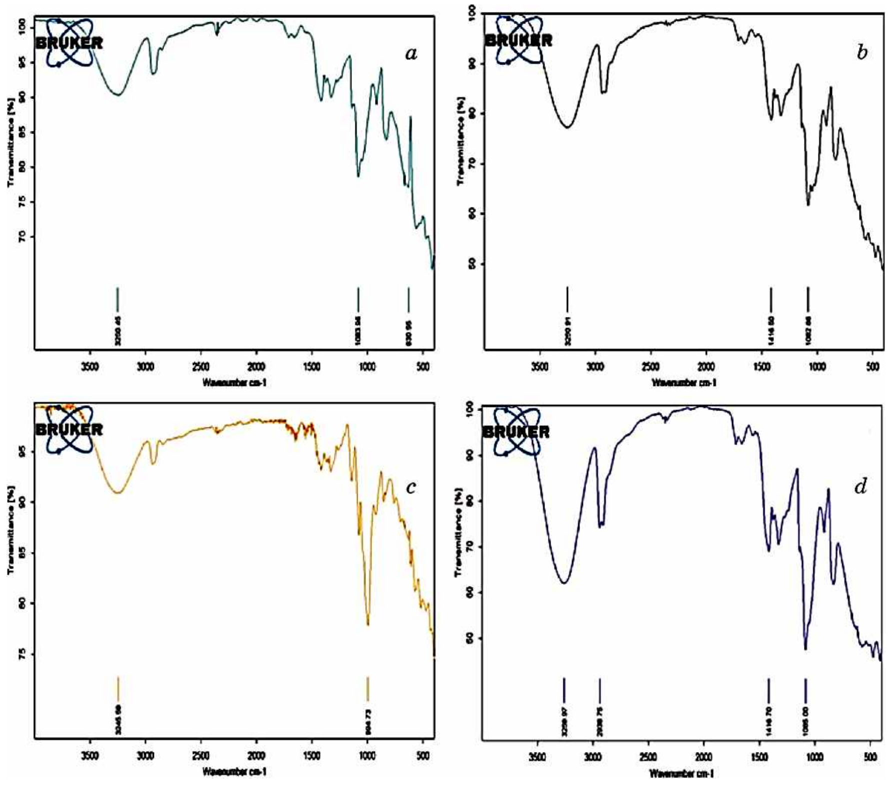

Fig. 1. FT-IR spectra for PVA–ST–Y_2O_3 nanocomposites; *a*—pure blend; *b*—1 wt.% Y_2O_3 nanoparticles; *c*—2 wt.% Y_2O_3 nanoparticles; *d*—3 wt.% Y_2O_3 nanoparticles.

with frequency at room temperature with different concentrations of yttrium-oxide nanoparticles is shown in Fig. 4. It is clear from the graph that loss decreases with frequency. The higher value of the dielectric loss for PVA–ST–Y_2O_3 nanocomposites at the higher concentration of yttrium-oxide nanoparticles can be understood regarding electrical conductivity, which is related to the dielectric loss. Moreover, polyvinyl alcohol is polar polymer with polar bonds and shows flexible polar groups since the bond rotating having intense dielectric α-transition [14].

Figure 5 shows the variation of A.C. electrical conductivity for PVA–ST–Y_2O_3 nanocomposites with frequency at room temperature. As the yttrium-oxide nanoparticles' concentration is increased, the inorganic filler molecules start bridging the gap separating the two localized states and lowering the potential barrier between them, thereby, facilitating the transfer of charge carriers between two localized states.

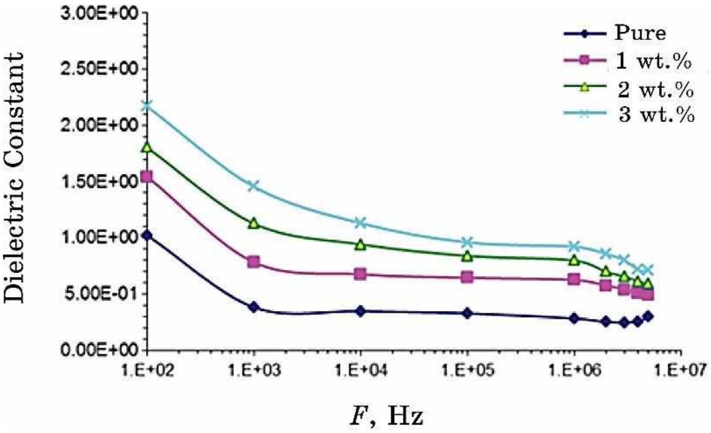

Fig. 2. Variation of dielectric constant for PVA–ST–Y_2O_3 nanocomposites with frequency at room temperature.

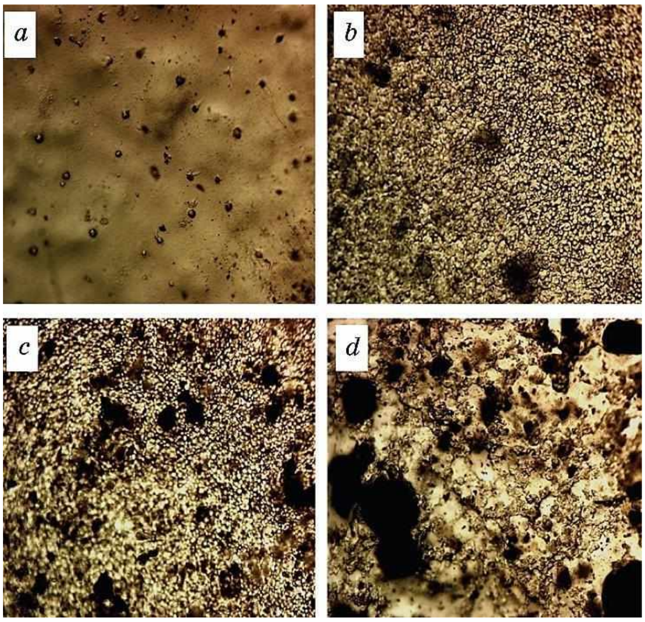

Fig. 3. Photomicrographs (×10) for PVA–ST–Y_2O_3 nanocomposites: (*a*) for pure blend; (*b*) for 1 wt.% Y_2O_3 nanoparticles; (*c*) for 2 wt.% Y_2O_3 nanoparticles; (*d*) for 3 wt.% Y_2O_3 nanoparticles.

The frequency-dependent conductivity is conditioned by the hopping of charge carriers in the localized state. The term hopping refers to the sudden displacement of charge carriers from one position

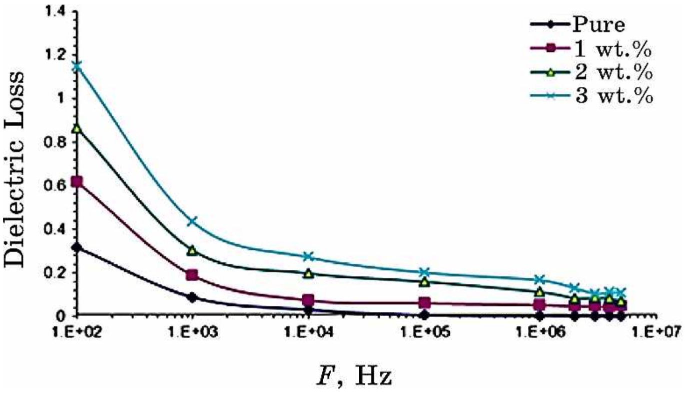

Fig. 4. Variation of dielectric loss for PVA–ST–Y_2O_3 nanocomposites with frequency at room temperature.

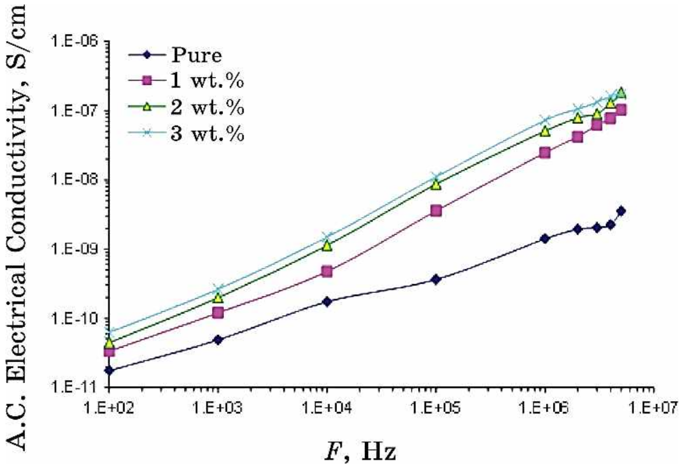

Fig. 5. Variation of A.C. electrical conductivity for PVA–ST–PbO_2 nanocomposites with frequency.

to another neighbouring site and, in general, includes both jumps over a potential barrier and quantum mechanical tunnelling [15].

Figure 6 shows the variation of electrical resistance for PVA–ST–Y_2O_3 nanocomposites with compression stress. From the figure, the electrical resistance of nanocomposites decreases with increasing the pressure. Typical piezoelectric polymers have a crystalline region that has an internal dipole moment. These dipole moments are randomly oriented without any mechanical or electrical poling process, and the net dipole moment is zero in these conditions. When stress is applied to the stacked polymer chain region, it will change

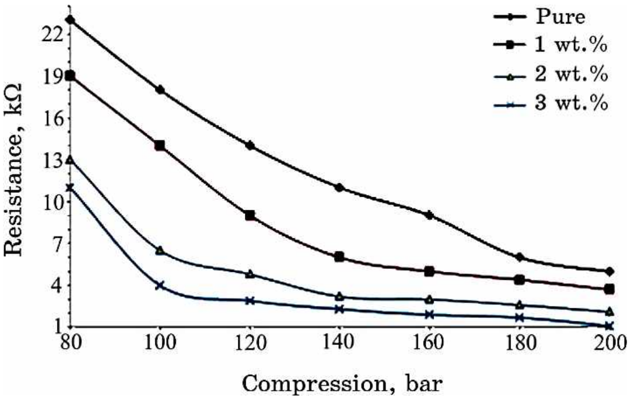

Fig. 6. Variation of electrical resistance for PVA–ST–Y_2O_3 nanocomposites with compression stress.

the local dipole distributions and induce an electric field in the stack. The induced electric field accumulates the charges at both the top and the bottom of the film [16].

5. CONCLUSIONS

The dielectric properties (dielectric constant, dielectric loss, and A.C. electrical conductivity) of PVA–ST–Y_2O_3 nanocomposites increase with an increase the yttrium-oxide nanoparticles' concentration.

The dielectric constant and dielectric loss of PVA–ST–Y_2O_3 nanocomposites are decreased with an increase of the frequency, while the A.C. electrical conductivity increases with an increase of the frequency.

The electrical resistance of PVA–ST–Y_2O_3 nanocomposites decreases with an increase in pressure, and these samples have high sensitive for pressure.

REFERENCES

1. E. Sheha, H. Khoder, T. S. Shanap, M. G. El-Shaarawy, M. K. El Mansy, *Optik*, **123**, No. 13: 1161 (2012).
2. R. P. Ellis, M. P. Cochrane, M. F. B. Dale, C. M. Duffus, A. Lynn, I. M. Morrison, R. D. M. Prentice, J. S. Swanston, and S. A. Tiller, *J. of the Sci. of Food and Agriculture*, **77**, No. 3: 289 (1998).
3. M. Aghazadeh, M. Ghaemi, A. N. Golikand, T. Yousefi, and E. Jangju, *Int. Scholarly Research Network*, **2011**: ID 542104 (2011); doi:10.5402/2011/542104
4. I. R. Agool, K. J. Kadhim, and A. Hashim, *International Journal of Plas-*

tics Technology, **20**, Iss. 1: 121 (2016); https://doi.org/10.1007/s12588-016-9144-5

5. J.-C. Wang, R. S. Karmakar, Y.-J. Lu, C.-Y. Huang, and K.-C. Wei, *Sensors*, **15**: 818 (2015).
6. A. J. K. Algidsawi, A. Hashim, and H. J. K. Algidsawi, *European Journal of Scientific Research*, **65**, No. 1: 74 (2011).
7. M. A. Habbeb, A. Hashim, and Abdul-Raheem K. AbidAli, *European Journal of Scientific Research*, **61**, No. 3: 367 (2011).
8. H. Abduljalil, A. Hashim, and A. Jewad, *European Journal of Scientific Research*, **63**, No. 2: 231 (2011).
9. B. Hussien, A. J. K. Algidsawi, and A. Hashim, *Australian Journal of Basic and Applied Sciences*, **5**, No. 7: 933 (2011).
10. B. H. Rabee and A. Hashim, *European Journal of Scientific Research*, **60**, No. 2: 247 (2011).
11. B. H. Rabee and A. Hashim, *European Journal of Social Sciences*, **32**, No. 3: 316 (2012).
12. A. J. K. Algidsawi, H. J. K. Algidsawi, A. Hashim, and Ghaleb Abd Al-Wahab Ali, *Australian Journal of Basic and Applied Sciences*, **5**, No. 11: 1463 (2011).
13. J. Koteswararao, R. Abhishek, S. V. Satyanarayana, G. M. Madhu, and V. Venkatesham, *eXPRESS Polymer Letters*, **10**, No. 11: 883 (2016).
14. S. S. More, R. J. Dhokane, and S. V. Mohril, *IOSR Journal of Applied Physics*, **8**, Iss. 3: 28 (2016).
15. R. Divya, M. Meena, C. K. Mahadevan, and C. M. Padma, *Journal of Engineering Research and Applications*, **4**, Iss. 5: 1 (2014).
16. T. H. Kim, *M. Sc. Thesis* (Uni. California: 2015).

Наносистеми, наноматеріали, нанотехнології
Nanosistemi, Nanomateriali, Nanotehnologii
2021, т. 19, № 4, сс. 893–903

PACS numbers: 07.07.Df, 68.37.Hk, 72.80.Tm, 78.20.Ci, 78.67.Sc, 82.35.Np, 92.60.jk

Humidity Sensing Performance of Polymer Blend–Titanium Nitride Nanocomposites: Structural, Electrical, and Optical Properties

Ahmed Hashim and Zinah Sattar Hamad

College of Education for Pure Sciences,
Department of Physics,
University of Babylon,
Hillah, Iraq

Synthesis of new nanocomposite films of both the PVA–PAA blend and the PVA–PAA blend doped by titanium nitride nanoparticles is investigated for the sake of humidity sensors with low cost, light weight, flexibility and high sensitivity. The structural, electrical, and optical properties of PVA–PAA–TiN nanocomposites are studied. The results concerning electrical properties of PVA–PAA–TiN nanocomposites show that the electrical conductivity of PVA–PAA blend increases from $4.3\cdot10^{-11}$ S/cm to $6.1\cdot10^{-9}$ S/cm, if the titanium-nitride nanoparticles' concentration increases to 6 wt.%. In addition, the electrical conductivity of all samples of PVA–PAA–TiN nanocomposites increases by one order, when temperature increases from 50°C to 80°C. The activation energy for PVA–PAA blend decreases from 0.57 eV to 0.29 eV, when titanium-nitride nanoparticles' concentration increases. The optical-properties' results show that the transmittance of PVA–PAA blend decreases (to 83.5%) with increasing the titanium-nitride nanoparticles' concentration. The results concerning PVA–PAA–TiN-nanocomposites' applications for the sake of humidity sensors show that the PVA–PAA–TiN nanocomposites have high sensitivity for relative humidity.

Синтеза нових нанокомпозитних плівок як суміші полівініловий спирт (ПВС)–поліакрилова кислота (ПАК), так і суміші ПВС–ПАК, леґованої наночастинками нітриду Титану, досліджується заради датчиків вологости з низькою вартістю, невеликою вагою, гнучкістю та високою чутливістю. Досліджено структурні, електричні й оптичні властивості нанокомпозитів ПВС–ПАК–TiN. Результати щодо електричних властивостей нанокомпозитів ПВС–ПАК–TiN показують, що електропровідність суміші ПВС–ПАК збільшується з $4{,}3\cdot10^{-11}$ См/см до $6{,}1\cdot10^{-9}$ См/см, якщо концентрація наночастинок нітриду Титану збільшується до 6 ваг.%. Крім того, електропровідність всіх зразків нанокомпозитів

ПВС–ПАК–TiN збільшується на один порядок, коли температура підвищується від 50°C до 80°C. Енергія активації суміші ПВС–ПАК зменшується від 0,57 еВ до 0,29 еВ, коли концентрація наночастинок нітриду Титану збільшується. Результати щодо оптичних властивостей показують, що прозорість суміші ПВС–ПАК понижується (до 83,5%) зі збільшенням концентрації наночастинок нітриду Титану. Результати щодо застосування нанокомпозитів ПВС–ПАК–TiN заради датчиків вологости показують, що нанокомпозити ПВС–ПАК–TiN мають високу чутливість до відносної вологости.

Key words: humidity sensors, nanocomposites, titanium nitride, conductivity, transmittance.

Ключові слова: датчики вологости, нанокомпозити, нітрид Титану, електропровідність, прозорість.

(Received 23 November, 2020)

1. INTRODUCTION

Humidity has an important influence on several industrial processes such as electronic, food or pharmaceutical manufacturing, food storage, *etc*. All these processes, which can be affected by humidity, require continuous monitoring of air humidity. In addition, proper humidity levels can be critical to the quality of the product and having the right humidity level can contribute to diminishing energy consumption [1]. Humidity sensors have gained advanced applications in industrial processing and environmental control. For manufacturing, highly sophisticated integrated circuits in semiconductor industry, humidity levels are constantly monitored in wafer processing. There are many domestic applications, such as intelligent control of the living environment in buildings, cooking control for microwave ovens, and intelligent controller. In automobile industry, humidity sensors are used in rear window defoggers and motor assembly lines. In medical field, humidity sensors are used in respiratory equipment, sterilizers, pharmaceutical processing, and biological products. In agriculture, humidity sensors are used for greenhouse air conditioning, plantation protection (dew prevention), soil moisture monitoring. In general industry, humidity sensors are used for humidity control in chemical gas purification, dryers, ovens, film desiccation, paper and textile production, and food processing. Humidity sensor plays an important role in every part of the Earth and automated industrial processes [2].

Several kinds of humidity sensors are available based on different transduction principles, such as resistive, capacitive, optical, and surface acoustic wave. However, resistive-type sensors have the advantage to be cheaper and easier to read out over the other ones. Typically, rigid substrates like ceramic, glass, or silicon are used as the fundamental building blocks of humidity sensors; but, recent advancements in the field of printed electronics show increased potential for the substitution of rigid substrates by flexible ones, since the latter potentially reduce the cost of sensors and offer good mechanical flexibility. Examples of flexible sensors integrating additional electronic functions like readout electronics, thermal compensation systems, and other sensors have opened a new route towards multifunctional sensors fabricated on flexible substrate [3]. Inorganic–organic nanocomposites are extremely promising for applications in light-emitting diodes, microelectronic packaging, automobiles, medicine, drug delivery, injection moulded products, optical integrated circuits, sensors, fire-retardants, membranes, aerospace, coatings adhesives, packaging materials, consumer goods, *etc*. [4–10].

The properties of nanocomposites films can be adjusted by varying the composition. Their fabrication shares the same advantages of organic device technology, such as low cost production and the possibility of device fabrication on large area and flexible substrates. Polyvinyl alcohol (PVA) is a potential material having high dielectric strength, good charge storage capacity and dopant-dependent electrical and optical properties. It has carbon chain backbone with hydroxyl groups attached to methane carbons. These OH groups can be a source of hydrogen bonding and hence assist the formation of polymer composite [11]. Polyacrylic acid (PAA) is a non-toxic, hydrophilic and biocompatible superabsorbent polymer with a three dimensional (3*D*) network. PAA was chosen as a host polymer in this research due to its fascinating behaviours such as excellent stability in acidic and basic media, high ionic conductivity, strong adhesive properties, superior selectivity and permeability and high ability to associate with a variety of multivalent metal ions in solution. PAA can suppress the crystallization and form stable complexes with metal. The main reason for choosing PAA as a host polymer is because of its high charge density based on carboxylic (–COOH) functional group. This functional group favours the bond formation, for example, ionic, covalent, hydrogen and coordination ones, which can be used to form complexation with the nanoparticles [12]. Lim *et al.* [13] studied the polyvinyl alcohol nanocomposites containing reduced graphene oxide coated with tannic acid for humidity sensor. The results showed that the PVA nanocomposites showed excellent humidity sensing properties over the wide relative humidity range and the long-term stability due to the conductive property of the reduced GO and the enhanced mechanical strength by the effective incorporation of rGO-TA into the

PVA matrix [13].

2. MATERIALS AND METHODS

Nanocomposites films of polyvinyl alcohol–polyacrylic acid blend and polyvinyl alcohol–polyacrylic acid blend doped with titanium nitride nanoparticles were prepared by using casting method. The films of PVA–PAA–TiN nanocomposites were prepared by dissolving 1 gm of PVA and PAA in 30 ml of distilled water with concentrations 85 wt.% PVA and 15 wt.% PAA by using magnetic stirrer to mix the polymers for 1 hour to obtain solution that is more homogeneous. The TiN nanoparticles were added to PVA–PAA blend with concentrations 1.5, 3, 4.5 and 6 wt.%. The samples of nanocomposites were prepared with thickness range 115–122 μm. The D.C. electrical conductivity of films was measured by measuring the D.C. electrical resistance by using the Keithley electrometer type 2400 source mater at different temperature 50–80°C. The optical properties of PVA–PAA–TiN nanocomposites were measured by using the double beam spectrophotometer (Shimadzu, UV-1800Å) in wavelength 240–820 nm. The each one of PVA–PAA–TiN nanocomposites samples was placed in box and the water vapour was used as a source of humidity. The control network monitored and controlled variations in humidity. The electrical resistance of PVA–PAA–TiN nanocomposites for different-humidity range 40–90% was measured by using the Keithley electrometer type 2400 source mater.

The D.C. electrical conductivity (σ) of PVA–PAA–TiN nanocomposites can be calculated by using the equation [14]:

$$\sigma = L/(RS), \tag{1}$$

where S—the open cross-sectional area, L—the length, and R—the electrical resistance of a sample.

The electrical conductivity of PVA–PAA–TiN nanocomposites increases with increasing temperature according to the relation [15]:

$$\sigma = \sigma_0 \exp\left(-\frac{E_a}{k_B T}\right), \tag{2}$$

σ—conductivity at temperature T, σ_0—conductivity at absolute temperature zero, E_a—activation energy, k_B—Boltzmann constant.

3. RESULTS AND DISCUSSION

Figure 1 shows the variation of D.C. electrical conductivity of

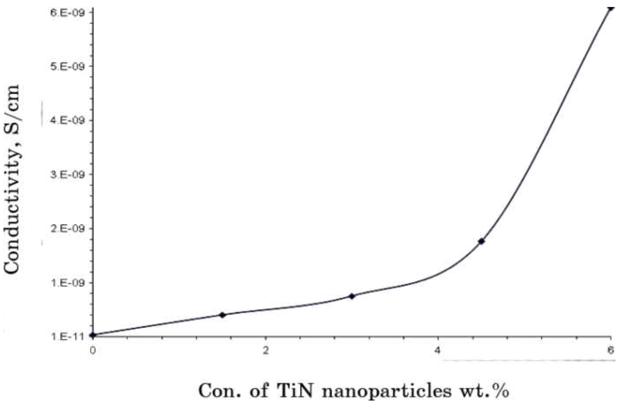

Fig. 1. Variation of D.C. electrical conductivity of PVA–PAA blend with concentration of TiN nanoparticles at 50°C.

PVA–PAA blend with concentrations of TiN nanoparticles at 50°C. The D.C. electrical conductivity of PVA–PAA blend is increasing with the increase in TiN nanoparticles' concentration and is noticeably increasing, when the concentration of TiN nanoparticles reach to 4.5 wt.%.

The increase of electrical conductivity with increasing TiN nanoparticles' concentration is attributed to the increase of the charge-carriers' number with increasing TiN concentration [16]. When the concentration of TiN nanoparticles reaches to 4.5 wt.%, the TiN nanoparticles form a continuous network in the nanocomposite as shown in Fig. 2. At low concentrations of TiN nanoparticles (1.5 wt.% and 3 wt.%), the nanoparticles are located in clusters, the clusters are contacted at concentration of 4.5 wt.% for PVA–PAA nanocomposites [17].

The effect of temperature on the D.C. electrical conductivity of PVA–PAA–TiN nanocomposites is shown in Fig. 3. This figure shows that the electrical conductivity of all samples is increased with increase the temperature. The behaviour of electrical conductivity with temperature attributed to the increase the mobility and number of charge carriers inside the PVA–PAA–TiN nanocomposites [18], where PVA–PAA chains and TiN nanoparticles could act as traps for the moving charge carriers by hopping process, the increase in temperature causes to moving the polymers chains and releasing the trapped charges [19]. So, the increase of current in PVA–PAA–TiN nanocomposites with the increase of the temperature is attributed to two parameters: mobility and number of charge carriers. The increase is exponential [20].

Figure 4 shows the variation of $\ln\sigma$ with $1000/T$ for PVA–PAA–TiN nanocomposites to calculate the activation energy for nanocom-

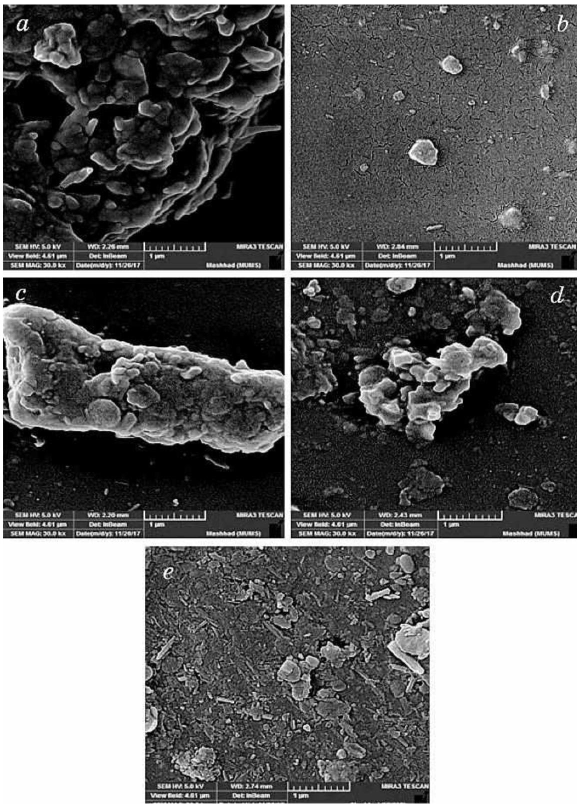

Fig. 2. SEM images of PVA–PAA blend and PVA–PAA blend doped with titanium-nitride nanoparticles: (*a*) pure PVA–PAA blend; (*b*) 1.5 wt.% TiN nanoparticles; (*c*) 3 wt.% TiN nanoparticles; (*d*) 4.5 wt.% TiN nanoparticles; (*e*) 6 wt.% TiN nanoparticles.

posites. The experimental results show that the activation energy values are ranging from 0.576 eV to 0.295 eV for PVA–PAA–TiN nanocomposites. The high value of activation energy for PVA–PAA blend attributed to existence of free ions in the polymers. The decrease of activation energy of PVA–PAA–TiN nanocomposites with the increase of the nanoparticles' concentration related to increase in localization of charge carriers causing higher electrical conductivity that is attributed to effect of space charge contribution, which may play an important role in the charges' transport [21, 22].

The variation of activation energy with TiN nanoparticles concentration is shown in Fig. 5. The activation energy of PVA–PAA–TiN nanocomposites decreases with the increase of the TiN nanoparticles' concentration for all samples of nanocomposites. This behav-

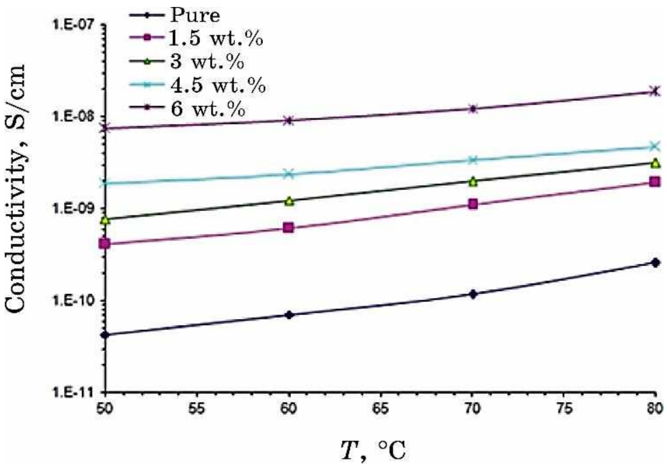

Fig. 3. Effect of temperature on the D.C. electrical conductivity of PVA–PAA–TiN nanocomposites.

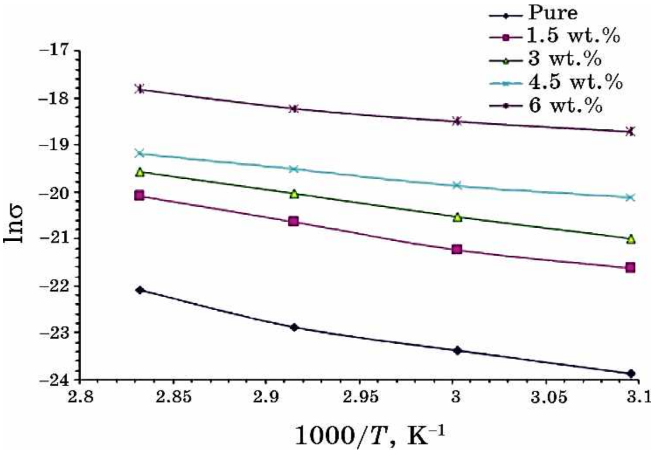

Fig. 4. Variation of lnσ with 1000/T for PVA–PAA–TiN nanocomposites.

iour is due to creating local energy levels in the energy gap, which act as traps for charge carriers [22]. At high TiN nanoparticles' concentration, the activation energy has lower values, which are attributed to formation a continuous network of nanoparticles in the nanocomposite [23].

Figure 6 shows the variation of transmittance for PVA–PAA–TiN nanocomposites with wavelength of the incident light. The figure shows that decrease in transmission of all samples at UV region; this is due to the excitations of donor level electrons to the conduction band at these energies.

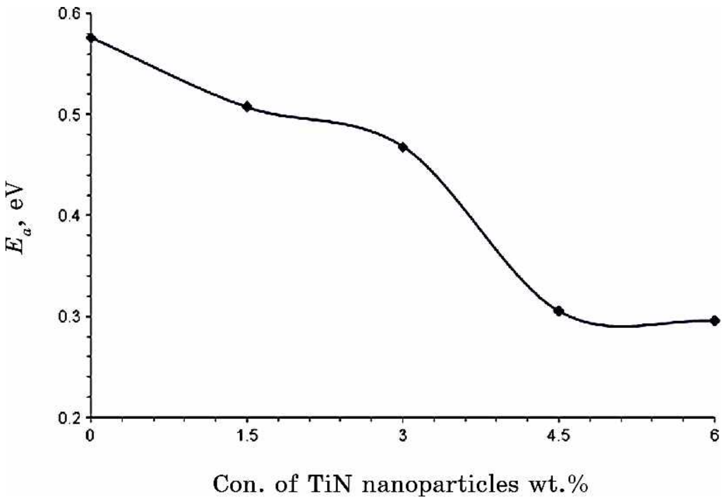

Fig. 5. Variation of activation energy with TiN nanoparticles' concentration.

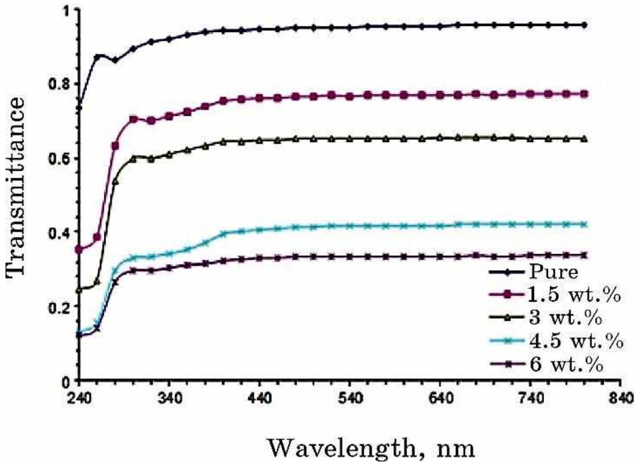

Fig. 6. Variation of transmittance for PVA–PAA–TiN nanocomposites with wavelength of the incident light.

The low transmittance of samples at UV region is attributed to the energy of photon enough to interact with atoms; the electron excites from a lower to higher energy level by absorbing a photon of known energy. The changes in the absorbed and transmitted radiation can decide the types of possible electron transitions [24].

At visible and near infrared regions, the transmittance of all samples has high values. This behaviour attributed to the energy of incident photons does not enough in energy to interact with atoms. Thus, the photons will be transmitted when the wavelength increases [25]; hence, the transmittance increases.

In addition, Figure 6 shows that the transmittance decreases with increase in TiN-nanoparticles' concentration; this is due to the agglomeration of nanoparticles with increasing concentration and increase of the number of charge carriers [26].

Figure 7 shows the variation of electrical resistance for PVA–PAA–TiN nanocomposites with humidity at room temperature. From the figure, the electrical resistance decreases with increase in humidity. This behaviour may be attributed to the following possibilities. (i) At low *RH*, mobility of TiN ions in the composite is restricted due to curling up of polymer chains. As humidity increases, polymer chain uncurls and becomes aligned by absorbing water molecules paving way for faster hopping of charge carriers, resulting in increased sensing response of the composite. (ii) Porosity of the polymers may facilitate absorption of water molecules as *RH* increases causing a decrease in the impedance of the composite [27]. The resistance changes with increasing the humidity levels occur because of adsorption and capillary condensation of water. At low humidity levels, chemisorption takes place leading to the formation of two surface hydroxyls with the charge transport occurring by the hopping mechanism, while, at high humidity levels, water is physisorpted on the top of the chemisorbed layer. When water molecules are available at low humidity, they chemisorb on grain surfaces of the ceramic to form hydroxyl groups as surface charge carriers. When initial water molecules are adsorbed, each water molecule

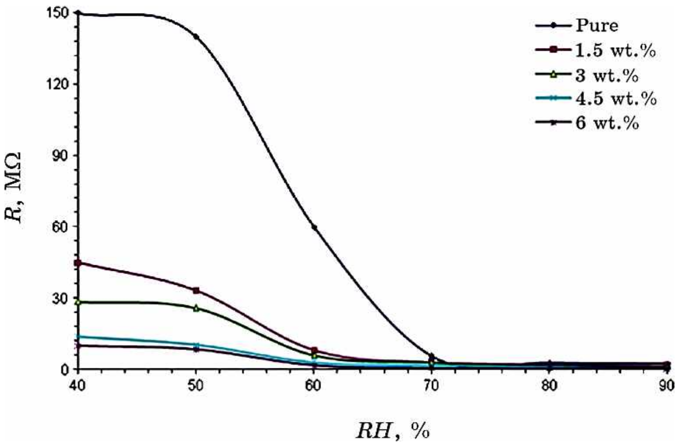

Fig. 7. Variation of electrical resistance for PVA–PAA–TiN nanocomposites with humidity at room temperature.

is hydrogen-bonded to two hydroxyls, and the dominant surface charge carriers will be H_3O^+. When still more water is adsorbed, clustering of the water molecules takes place, forming a liquid-like multilayer film of hydrogen bonded water molecules, where each water molecule is only singly bonded to a hydroxyl group. Since dissociation of H_3O^+ into H_2O and H^+ is energetically favourable in liquid water, the dominant charge carrier in high moisture environment is H^+ [28–30].

4. CONCLUSIONS

The D.C. electrical conductivity of PVA–PAA blend increases with an increase in TiN nanoparticles concentration and temperature.

The activation energy of PVA–PAA blend decreases with an increase in titanium-nitride nanoparticles concentration.

The optical transmittance of PVA–PAA blend decreases with an increase in titanium nitride nanoparticles concentration.

The PVA–PAA–TiN nanocomposites have high sensitivity for relative humidity with low cost and low weight.

REFERENCES

1. J. Ascorbe, J. M. Corres, F. J. Arregui, and I. R. Matias, *Sensors*, **17**, No. 4: 893 (2017); DOI: 10.3390/s17040893
2. L. Chitra, S. Srinivasan, and B. Praveenkumar, *Int. J. of Pure and Appl. Mathematics*, **118**, No. 5: 815 (2018).
3. G. Dubourg, A. Segkos, J. Katona, M. Radović, Sl. Savić, G. Niarchos , C. Tsamis, and V. Crnojević-Bengin, *Sensors*, **17**, No. 8: 1854 (2017); DOI:10.3390/s17081854
4. A. Hashim, I. R. Agool, and K. J. Kadhim, *J. of Materials Science: Materials in Electronics*, **29**, Iss. 12: 10369 (2018); https://doi.org/10.1007/s10854-018-9095-z
5. A. Hashim and Q. Hadi, *J. of Materials Science: Materials in Electronics*, **29**: 11598 (2018); https://doi.org/10.1007/s10854-018-9257-z
6. I. R. Agool, K. J. Kadhim, and A. Hashim, *Int. Journal of Plastics Technology*, **21**, Iss. 2: 397 (2017); https://doi.org/10.1007/s12588-017-9192-5
7. A. Hadi and A. Hashim, *Ukrainian Journal of Physics*, **62**, No. 12: 1044 (2017); doi: 10.15407/ujpe62.12.1044
8. A. Hashim and A. Hadi, *Ukrainian Journal of Physics*, **62**, No. 12: 1050 (2017); https://doi.org/10.15407/ujpe62.12.1050
9. A. Hashim and A. Hadi, *Ukrainian Journal of Physics*, **62**, No. 11: 978 (2017); doi:10.15407/ujpe62.11.0978
10. A. Hashim and A. Hadi, *Ukrainian Journal of Physics*, **63**, No. 8: 754 (2018); https://doi.org/10.15407/ujpe63.8.754
11. E. Sheha, H. Khoder, T. S. Shanap, M. G. El-Shaarawy, and M. K. El Mansy, *Optik*, **123**, Iss. 13: 1161 (2012); https://ui.adsabs.harvard.edu/abs/2012Optik.123.1161S

12. C. Wen Liew, H. M. Ng, A. Numan, and S. Ramesh, *Polymers*, **8**, No. 5: 179 (2016); https://doi.org/10.3390/polym8050179
13. M. Y. Lim, H. Shin, D. M. Shin, S. S. Lee, and J. C. Lee, *Polymer*, **84**: 89 (2016); https://doi.org/10.1016/j.polymer.2015.12.048
14. I. R. Agool, K. J. Kadhim, and A. Hashim, *International Journal of Plastics Technology*, **20**, No. 1: 121 (2016); https://doi.org/10.1007/s12588-016-9144-5
15. I. R. Agool, K. J. Kadhim, and A. Hashim, *International Journal of Plastics Technology*, **21**, Iss. 2: 444 (2017); https://doi.org/10.1007/s12588-017-9196-1
16. Ch. Srikanth, Ch. Sridhar B, B. M. Nagabhushana, and R. D. Mathad, *Int. Journal of Engineering Research and Applications*, **4**, Iss. 10: 38 (2014).
17. S. D. Meshram, R. V. Rupnarayan, S. V. Jagtap, V. G. Mete, V. S. Sangawar, *International Journal of Chemical and Physical Sciences*, **4**, Spec. Iss.: 83 (2015); https://www.ijcps.org/0Site/SP3/P16.pdf
18. M. Pandey, G. M. Joshi, K. Deshmukh, and J. Ahmad, *Journal of Advanced Materials Letters*, **6**, No. 2: 165 (2015); DOI: 10.5185/amlett.2015.5639
19. J. Ramesh Babu and K. Vijaya Kumar, *International Journal of Chem. Tech. Research*, **7**, No. 1: 171 (2014–2015); https://www.sphinxsai.com/2015/ch_vol7_no1/2/(171-180)%20014.pdf
20. S. P. Ansari and F. Mohammad, *The IUP Journal of Chemistry*, **III**, No. 4: 7 (2010).
21. P. A. Fartode, S. S. Yawale, and S. P. Yawale, *International Journal of Chemical and Physical Sciences*, **4**, Spec. Iss.: 60 (2015); https://www.ijcps.org/0Site/SP3/P11.pdf
22. R. Divya, M. Meena, C. K. Mahadevan, and C. M. Padma, *International Journal of Engineering Research & Technology*, **3**, Iss. 7: 722 (2014).
23. M. F. Ahmer and S. Hameed, *International Journal of Advanced Research in Electrical, Electronics and Instrumentation Engineering*, **3**, Iss. 10: 12731 (2014); DOI: 10.15662/ijareeie.2014.0310048
24. A. P. Indolia and M. S. Gaur, *Polymer Research*, **20**: 43 (2013); https://doi.org/10.1007/s10965-012-0043-y
25. P. Phukan and D. Saikia, *International Journal of Photoenergy*, **2013**: ID 728280 (2013).
26. G. A. M. Amin and M. H. Abd-El Salam, *Journal of Materials Research Express*, **1**, No. 2: 025024 (2014).
27. S. Kotresh, Y. T. Ravikiran, H. G. Raj Prakash, and S. C. Vijaya Kumari, *Nanosystems: Phys., Chem., Math.*, **7**, No. 4: 732 (2016); DOI:10.17586/2220-8054-2016-7-4-732-739
28. V. Jeseentharani, B. Jeyaraj, J. Pragasam, A. Dayalan, and K. Seetharamaiah Nagaraja, *Sensors & Transducers Journal*, **113**, Iss. 2: 48 (2010).
29. H. Ahmed, H. M. Abduljalil, and A. Hashim, *Transactions on Electrical and Electronic Materials*, **20**: 206 (2019); https://doi.org/10.1007/s42341-019-00100-2
30. A. Hashim and M. A. Habeeb, *Transactions on Electrical and Electronic Materials*, **20**: 107 (2019); doi:10.1007/s42341-018-0081-1

Наносистеми, наноматеріали, нанотехнології
Nanosistemi, Nanomateriali, Nanotehnologii
2021, т. 19, № 4, сс. 905–912

PACS numbers: 78.30.Jw, 78.67.Rb, 81.05.Qk, 81.07.Nb, 82.35.Lr, 82.70.Gg, 83.80.Tc

Structural, Swelling and Water Absorption Properties of New Polymer Blends for Modern Applications

Farhan Lafta Rashid[1] and Ahmed Hashim[2]

[1]*College of Engineering,*
Department of Petroleum,
University of Kerbala
Kerbala, Iraq
[2]*College of Education for Pure Sciences,*
Department of Physics,
University of Babylon,
Hillah, Iraq

In this paper, fabrication of new polymer blends for water absorption in crude oil is used. The polymer blends are prepared from polyvinyl alcohol (60 wt.%) and polyethylene glycol (40 wt.%) with different concentrations of polyvinyl pyrrolidone (10, 20, 30 wt.%). The structural, swelling and water absorption properties of PVA–PEG–PVP blends are studied. The results show that both the swelling ratio and the water absorption of PVA–PEG blend increase with increase in PVP concentration. In addition, the PVA–PEG–PVP blends have good swelling and water-absorption ratio with the time.

У роботі використовується виготовлення нових полімерних сумішей для водопоглинання в сировій нафті. Полімерні суміші готуються з полівінілового спирту (ПВС; 60 ваг.%) і поліетиленгліколю (ПЕГ; 40 ваг.%) з полівінілпірролідоном (ПВП) різною концентрацією (10, 20, 30 ваг.%). Досліджено структурні, набрякні та водопоглинальні властивості сумішей ПВС–ПЕГ–ПВП. Результати показують, що коефіцієнт набрякання та гігроскопічність суміші ПВС–ПЕГ збільшуються зі збільшенням концентрації ПВП. Крім того, суміші ПВС–ПЕГ–ПВП мають хороше співвідношення набрякання та водовбирання з часом.

Key words: polymer blend, crude oil, water absorption, swelling.

Ключові слова: полімерна суміш, сирова нафта, водопоглинання, набряклість.

(Received 16 January, 2021; in revised form, 19 January, 2021)

1. INTRODUCTION

The term 'hydrogel' is used to describe materials, which are three dimensional, hydrophilic, high-molecular-weight polymeric networks capable usually for imbibing large amounts of water or biological fluids or aqueous solutions within their structure near equilibrium without dissolution. The interactions responsible for water sorption by hydrogels are due to hydrophilic nature of functional groups on the polymer backbone, which can be non-ionic (–OH, –O–, $-NH_2$, –CONH–, –CHO) or ionic ($-SO_3H$, –COOH, –COONa, $-COONH_4$, $-NR_2HX$, *etc.*), and the existence of capillary areas and differences in osmotic pressure. The forces, which make hydrogel dissolution impossible, are presented by covalent bonds between individual polymer chains, hydrophobic and electrostatic interactions. Hydrogels have numerous functional properties such as high water absorptivity, optical clarity, inherent compatibility in biological (aqueous) fluids (*i.e.*, biocompatibility), soft tissue-like behaviour, oxygen permeability and elasticity, *etc*. Because of these versatile properties, they are important in different fields including pharmaceuticals, biotechnology, agriculture, food processing and electronics. Recently many researchers have focused on modifying hydrogels with a view to enhance their water absorbency, gel strength, and absorption rate [1].

In recent years, polymeric gels are the objects of intensive studies. Highly swollen polymers or copolymers are highly hydrophilic, three-dimensional crosslinked polymeric structures, which are able to swell in the aqueous environment. Hydrogels have found numerous uses ranging from daily life applications, mainly due to their high water absorption capacity to the development of new materials for many different purposed applications. Hydrogels are inherently soft, hydrophilic, porous, and elastic polymeric systems. The use of polymer hydrogels as biopotential sorbent or carriers for the removal of the model molecules from aqueous solutions or controlled release studies of them has been continued to attract considerable attention in recent years. Hydrogels are polymers in three-dimensional network arrangement, which are able to retain large amount of water. In order to keep the spatial structure, the polymer chains are usually physically or chemically crosslinked. Due to their swelling capacity, hydrogels can be easily rinsed to remove reagents residues. On the other hand, the big water content that makes hydrogels such a special class of materials. The importance of hydrogels in the biomaterial field is justified by some unique characteristics: the elastomeric and soft nature of the hydrogels. Crosslinked polymers capable of imbibing large volumes of water have found widespread applications in bioengineering, biomedicine, and food industry and water purification and separation process. Due to its swelling ability in water, hydrophilicity, biocompatibility, and no toxicity, hydrogels have been utilized in a wide range of biological, medical, pharmaceutical, environmental applications [2].

By the most used definition, hydrogels are polymer networks, which are capable of absorbing and retaining large amounts of water and biological fluids. The physical and chemical features of hydrogels are extremely important for choice of their specific applications. Normally, the behaviour of hydrogels depends on external conditions, in which such materials are exposed. Thus, it is important to characterize the hydrogel properties in conditions similar to that it will be applied. Important characteristic of hydrogels is the biocompatibility. Because of this, hydrogels had been applied in biomedical field. For instance, as prolonged or controlled drug delivery systems, contact lenses, biosensors, catheters, and tissue engineering and organ reconstruction scaffolds are exceedingly common. Hydrogels can be formed by either chemical or physical crosslinking process or just by entangling of polymer chains. Galactomannan, dextran, alginate, pectin, and chondroitin sulphate are good examples of natural polymers applied on hydrogel formulations. Among the synthetic ones, polyvinyl alcohol (PVA), polyhydroxyethyl methacrylate (polyHEMA), polyethylene oxide (PEO) and poly-*N*-isopropyl acrylamide (PNIPAAm) may be cited from a plenty of others [3].

PVA is a non-toxic, water-soluble synthetic polymer and has good physical and chemical properties and film-forming ability. The use of this polymer is important in many applications such as controlled drug delivery systems, membrane preparation, recycling of polymers and packaging. Studies of the mechanism of dissolution and changes in crystallinity and swelling behaviour of PVA and its physical gel-forming capabilities have been carried out. PVA has bioinertness, and it has many uses in medical applications such as artificial pancreas, haemodialysis, nanofiltration, synthetic vitreous and implantable medical device. Antithrombotic property, cell compatibility, blood compatibility and biocompatibility of PVA have been studied extensively [4]. There are several studies of different polymer blend [5–7] like PVA and its blends [8–15]. Polyvinyl pyrrolidone (PVP) is a well known biologically and eco-friendly polymer and has been developed for biomedical applications. To improve its mechanical properties, PVP is usually blended with other polymers, which also enhances its biocompatibility and water uptake. It has been pointed out that polymers or copolymers containing carboxylic acid groups are highly desirable in biomaterials as such groups represent functionality useful for yielding a wide variety of biomedical products. The swelling of hydrogels bearing weak acid moieties depends on the acid content in the hydrogel, as well as on several other variables such as the crosslinking density, pH, and ionic strength. Polymer blends are aiming to bring together different polymers completing each other favourable properties. Blending different polymers and yet conserving their individual properties in the final mixture is an extremely attractive inexpensive and advantageous way of obtaining new structural materials. The advantages of polymer blend systems for controlled release applications may include easy fabrication of devices, manipulation of device properties (hydration, degradation rate and mechanical strength), drug loading and utilization of the dispersed phase domains as micro reservoirs for enhanced release properties [1].

3. MATERIALS AND METHODS

The polymer blend of PVA–PEG were prepared with weight percentage of polyvinyl alcohol (60 wt.%) and polyethylene glycol (40 wt.%) by dissolving 1 gm of PVA and PEG in 20 ml of distilled water by using magnetic stirrer to mix the polymers for 1 hour to obtain more homogeneous solution. PVP was added with different concentrations: 10, 20 and 30 wt.%. The casting method was used to prepare the samples PVA–PEG–PVP blend. The samples prepared with thickness range 120–140 μm. The structural, swelling and water absorption properties were studied. The pre-weighed dry samples were immersed in distilled water for 2 minutes at room temperature. The swollen polymer blend were then removed from distilled water and weighed after removing surface water. The swelling ratio was calculated as follows [16]:

$$\text{Swelling ratio} = (W_2 - W_1)/W_1\,, \tag{1}$$

where W_2 is the weight of swelled sample, and W_1 is the weight of dry sample.

The pre-weighed dry samples were immersed in distilled water at room temperature and periodically weighed after soaking the surface water. The water absorption was calculated as follows [16]:

$$\text{Water absorbtion [\%]} = 100 \cdot (W_t - W_1)/W_1\,; \tag{2}$$

here, W_t is the weight of swelled sample at time t.

4. RESULTS AND DISCUSSION

The water absorption and swelling dependency of the PVA–PEG blend on PVP amount is shown in Fig. 1 and Fig. 2.

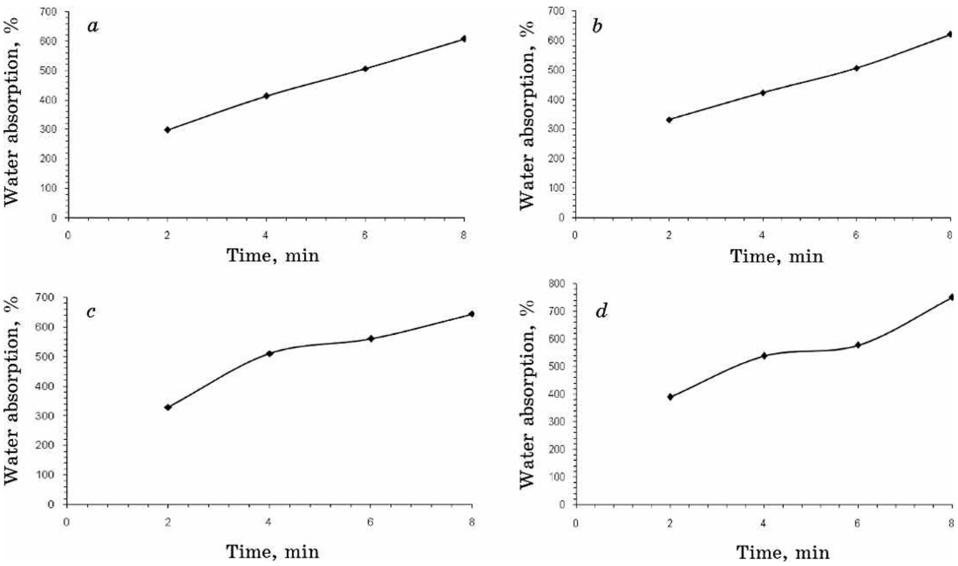

Fig. 1. Effect of PVP concentration on water absorption of PVA–PEG blend: *a*) for PVA–PEG blend; *b*) for 10 wt.% PVP; *c*) for 20 wt.% PVP; *d*) for 30 wt.% PVP.

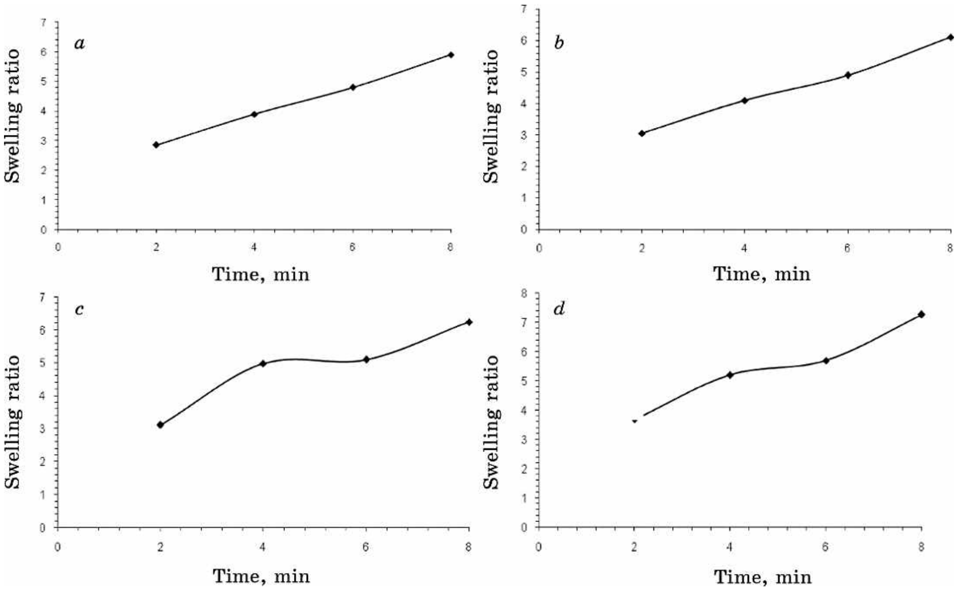

Fig. 2. Effect of PVP concentration on swelling ratio of PVA–PEG blend: *a*) for PVA–PEG blend; *b*) for 10 wt.% PVP; *c*) for 20 wt.% PVP; *d*) for 30 wt.% PVP.

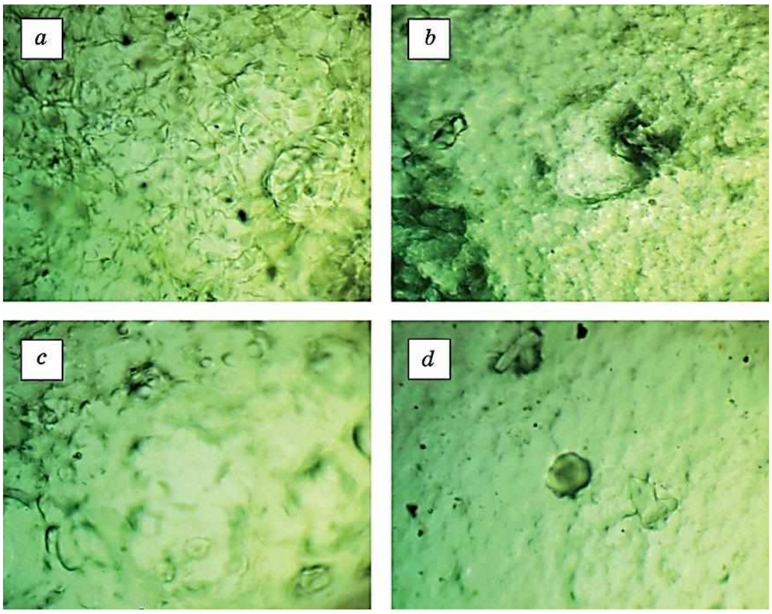

Fig. 3. Photomicrographs (×10) for PVA–PEG–PVP blends: *a*) for PVA–PEG blend; *b*) for 10 wt.% PVP; *c*) for 20 wt.% PVP; *d*) for 30 wt.% PVP.

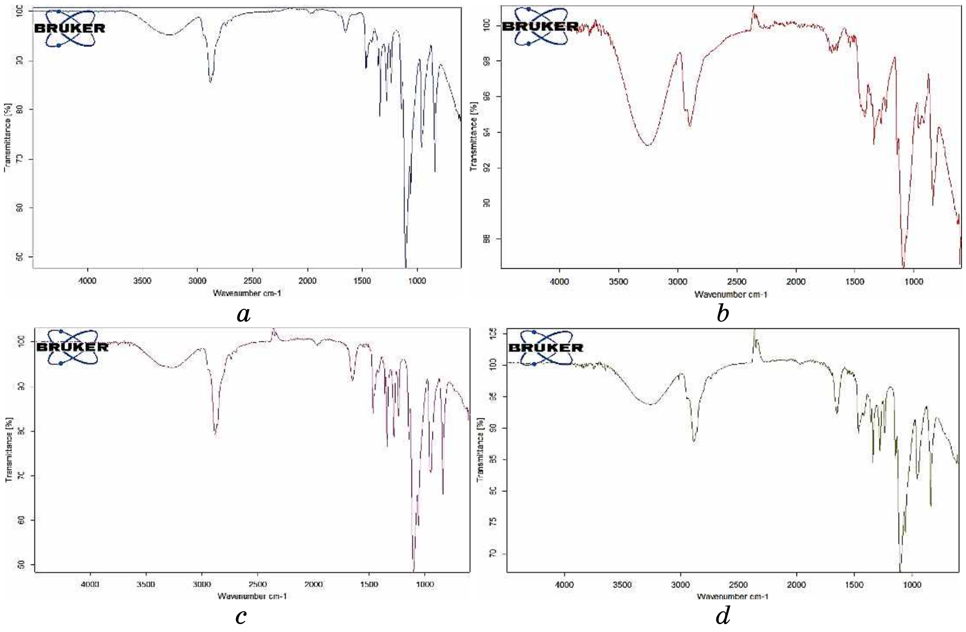

Fig 4. FT-IR spectra of PVA–PEG–PVP blends: *a*) for PVA–PEG blend; *b*) for 10 wt.% PVP; *c*) for 20 wt.% PVP; *d*) for 30 wt.% PVP.

The water absorption and swelling of PVA–PEG blend are considerably increased with the increase of PVP wt.%. This behaviour is attributed to the availability of more sites for crosslinking [17], as shown in Fig. 3.

FT-IR spectra of PVA–PEG–PVP blends for different concentrations of PVP are shown in Fig. 4. It shows broad bands at around 3250 cm^{-1} for samples are observed due to OH groups in the polymers blends chain. The bands at around 1280 cm^{-1} were attributed to the other bonds (C–O–C). The peaks at around 1470 cm^{-1} were assigned to the C–O groups of polymers matrix. The band at around 2890 cm^{-1} was attributed to the C–H groups. The strong band at 1090 cm^{-1} for samples was attributed to the stretching mode of C–O group. The two strong bands observed at around 1465 cm^{-1} and 840 cm^{-1} are attributed to the bending and stretching modes of CH_2 group, respectively [18, 19].

5. CONCLUSIONS

The water absorption of PVA–PEG blend increases with increase of the PVP concentration.

The swelling ratio of PVA–PEG blend increases with increase of the PVP concentration.

The FT-IR studies show that there are no interactions between PVA–PEG polymer blend and PVP.

REFERENCES

1. M. A. Q. Bhuiyan, M. S. Rahman, M. S. Rahaman, M. Shajahan, and N. C. Dafader, *Organic Chem. Curr. Res.*, **4**, Iss. 2: 138 (2015); DOI: 10.4172/2161-0401.1000138
2. S. Kundakci, E. Karadağ, and Ö. B. Üzüm, *J. of Encap. and Adsor. Sci.*, **1**: 7 (2011).
3. E. G. Crispim, J. F. Piai, A. R. Fajardo, E. R. F. Ramos, T. U. Nakamura, C. V. Nakamura, A. F. Rubira, and E. C. Muniz, *eXPRESS Polym. Lett.*, **6**, No. 5: 383 (2012).
4. U. K. Parida, A. K. Nayak, B. K. Binhani, and P. L. Nayak, *J. of Biomater. and Nanobiotechno.*, **2**: 414 (2011).
5. N. H. Al-Garah, F. L. Rashid, A. Hadi, and A. Hashim, *J. of Bionanoscience*, **12**, No. 3: 336 (2018); https://doi.org/10.1166/jbns.2018.1538
6. F. L. Rashid, A. Hadi, N. H. Al-Garah, and A. Hashim, *Int. J. of Pharmaceutical and Phytopharmacological Research*, **8**, Iss. 1: 46 (2018).
7. F. L. Rashid, A. Hashim, M. A. Habeeb, S. R. Salman, and H. Ahmed, *J. of Eng. and Applied Sci.*, **8**, No. 5: 137 (2013).
8. A. Hashim, A. J. Kadham, A. Hadi, and M. A. Habeeb, *Nanosistemi, Nanomateriali, Nanotehnologii*, **19**, Iss. 2: 327 (2021); https://doi.org/10.15407/nnn.19.02.327

9. A. Hashim and Z. S. Hamad, *Nanosistemi, Nanomateriali, Nanotehnologii*, **18**, Iss. 4: 969 (2020); https://doi.org/10.15407/nnn.18.04.969
10. I. R. Agool, F. S. Mohammed, and A. Hashim, *Advances in Environmental Biology*, **9**, No. 11: 1 (2015).
11. A. Hashim and Z. S. Hamad, *Egypt. J. Chem.*, **63**, No. 2: 461 (2020); doi:10.21608/EJCHEM.2019.7264.1593
12. Kh. H. H. Al-Attiyah, A. Hashim, and S. F. Obaid, *Int. J. of Plastics Techno.*, **23**, No. 1: 39 (2019); https://doi.org/10.1007/s12588-019-09228-5
13. A. Hashim, Kh. H. H. Al-Attiyah, and S. F. Obaid, *Ukr. J. Phys.*, **64**, No. 2: 157 (2019); https://doi.org/10.15407/ujpe64.2.157
14. A. Hashim and N. Hamid, *J. of Bionanoscience*, **12**, No. 6: 788 (2018); doi:10.1166/jbns.2018.1591
15. A. Hashim and A. Jassim, *Sensor Letters*, **15**, No. 12: 1003 (2017); https://doi.org/10.1166/sl.2017.3915
16. N. C. Dafader, T. Akter, M. E. Haque, S. P. Swapna, S. Islam, and D. Huq, *African J. of Biotechno.*, **11**, No. 66: 13049 (2012).
17. H. Hosseinzadeh, *Current Chem. Lett.*, **2**: 153 (2013).
18. A. Mohammad, K. Hooshyari, M. Javanbakht, and M. Enhessari, *Iranica J. of En. & Enviro.*, **4**, No. 2: 86 (2013).
19. K. Karthikeyan, N. Poornaprakash, N. Selvakumar, and Jeyasubrmanian, *J. of Nanostr. Polym. and Nanocomp.*, **5**, No. 4: 83 (2009).

Наносистеми, наноматеріали, нанотехнології
Nanosistemi, Nanomateriali, Nanotehnologii
2021, т. 19, № 4, сс. 913–922

PACS numbers: 68.37.Ps, 68.55.jd, 73.61.Ph, 78.40.Me, 82.35.Cd, 82.45.Wx

Fabrication and Characterization of Poly(2-Formylpyrrole) Nanoparticles' Thin Films by Anchoration

Ahmad Al-Hamdan[1], Ahmad Al-Falah[2], Fawaz Al-Deri[1],
and Marwa Al-Kheder[3]

[1]*Department of Chemistry,*
Damascus University,
Damascus, Syria
[2]*Department of Chemistry, Faculty of Pharmacy,*
Arab International University (AIU),
Damascus, Syria
[3]*Department of Chemistry,*
Al-Furat University,
Deir Ez-zor, Syria

The polymer-nanoparticles' thin films are fabricated by anchoring polymer from reaction solution (monomer, alcohol and hydrochloric acid). The thickness of the film increases with time and concentration of monomer and acid, and it decreases at large concentrations of acid. The films have a rough surface and peaks several times greater than the thickness. Thin films are formed on a substrate of gold, ordinary glass and quartz. Film thickness is between 106 nm and 1296 nm. Based on electrochemical impedance spectroscopy, the ohmic resistances of films are of 1090, 235, 176 and 157 (± 12%) Ohm at thicknesses of 780, 487, 102 and 65 nm, respectively, and the double-layer capacitance is of about 149 ± 0.02 μF/cm^2.

Тонкі плівки полімерних наночастинок виготовляються шляхом закріплення полімеру з реакційного розчину (мономер, спирт і соляна кислота). Товщина плівки збільшується з часом і концентрацією мономера та кислоти, і вона зменшується за великих концентрацій кислоти. Плівки мають шерстку поверхню та піки, що в кілька разів перевищують товщину. Тонкі плівки утворюються на підкладинці з золота, звичайного скла та кварцу. Товщина плівки становить від 106 нм до 1296 нм. За даними електрохемічної імпедансної спектроскопії активні електроопори плівок становлять 1090, 235, 176 і 157 (± 12%) Ом за товщини у 780, 487, 102 і 65 нм відповідно, а двошарова ємність становить близько $149 \pm 0{,}02$ μF/cm^2.

Key words: polymer thin films, anchoring, 2-formyl pyrrole, polyformyl pyrrole.

Ключові слова: полімерні тонкі плівки, прикріплення, 2-формільний піррол, поліформіл піррол.

(Received 27 January, 2021; in revised form, 31 December, 2021)

1. INTRODUCTION

Conducting polymers such as polypyrrole, polythiophene, polyfuran and its derivatives have received great attention because of their wide applications [1–3]. They used in sensors, biosensors [4, 5], solar cells [6], optical displays [7], light emitting diodes [8], electrochromic devices [9], capacitors [10], rechargeable batteries [11], enzyme immobilization matrices [12], membranes [13], and gas separation membranes [14]. Conducting-polymers' thin films are the most important applications [15]. The fabrication method of thin films varies according to the polymer and the substrate. Thickness, surface morphology, electrical current-conducting properties and polymer may select the thin films applications [16]. Polypyrrole and poly(2-formylpyrrole) thin films have been widely studied due to their applications [17, 18] in catalysts [17], modified electrode [19], photocatalysts [20], solar cells [19], and medical implants [21]. For best applications, the preparation of thin films of the conductive polymer with good properties is needed [22]. However, the development of effective and precise methods for controlling the organization of the polymer in the solid state has been limited because polymers often fail to assemble into organized structures due to their amorphous character and large molecular weight [23].

In this paper, we fabricated poly(2-formylpyrrole) nanoparticles' thin films by anchoring them from reaction solution. Thickness, surface morphology and electrochemical properties of poly(2-formylpyrrole) films were also studied.

2. EXPERIMENTAL

2.1. Materials

Pyrrole-2-carboxaldehyde 98% sigma, hydrochloric acid 35.5% sigma, and golden electrodes (CBC China).

2.2. Measurements

Thin films were characterized by UV spectrometer of PG model T72 between 400 and 800 nm. Electrochemical impedance spectroscopy (EIS) is applied using in $KClO_4$ (1M) solution, 1 mA/cm^2 and 0.58 V in the range of 0.1–10 kHz (AMEL model 2550). Thin film morphologies were examined with AFM (Nanosurf model eseyscan2).

2.3. Thin Films' Fabrication

The film was fabricated by anchoration in the reaction solution (2-formyl pyrrole (10 mmole, 0.97 g) was dissolved in the methanol (50 ml); then, hydrochloric acid 35.5% (20 ml) was added). The substrate was immersed in the reaction solution after adding the acid, and left in the solution for some time and removed from the solution. The substrate with film was washed with deionized water, then, with alcohol and left to dry without touching the film surface.

Effect of immersed time, acid concentration, and monomer concentration was studied. The thickness of film was determined by weight method.

3. RESULTS AND DISCUSSION

3.1. Characterization of PFPy Thin Films

Figure 1 shows the film images formed at different times, acid, and monomer on glass as substrate. The films seem darker with increas-

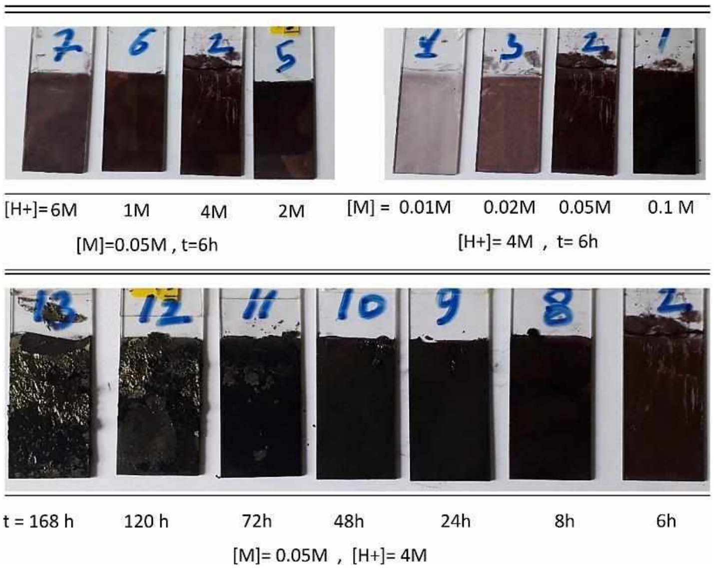

Fig. 1. Film images formed during different times and at many concentrations of acid and monomer on glass.

ing the concentration of acid and monomer concentration and time. After 120 hours, they become more thickness and were easily separated from the substrate to make flakes. This means that, with higher acid or monomer concentration, the polymer precipitated faster, and the films would be more thick and dark.

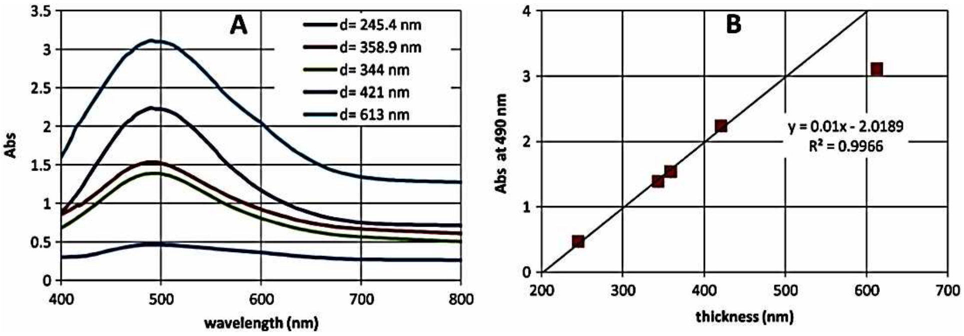

Fig. 2. *a*—absorption spectra of the films; *b*—absorption *vs* film thickness.

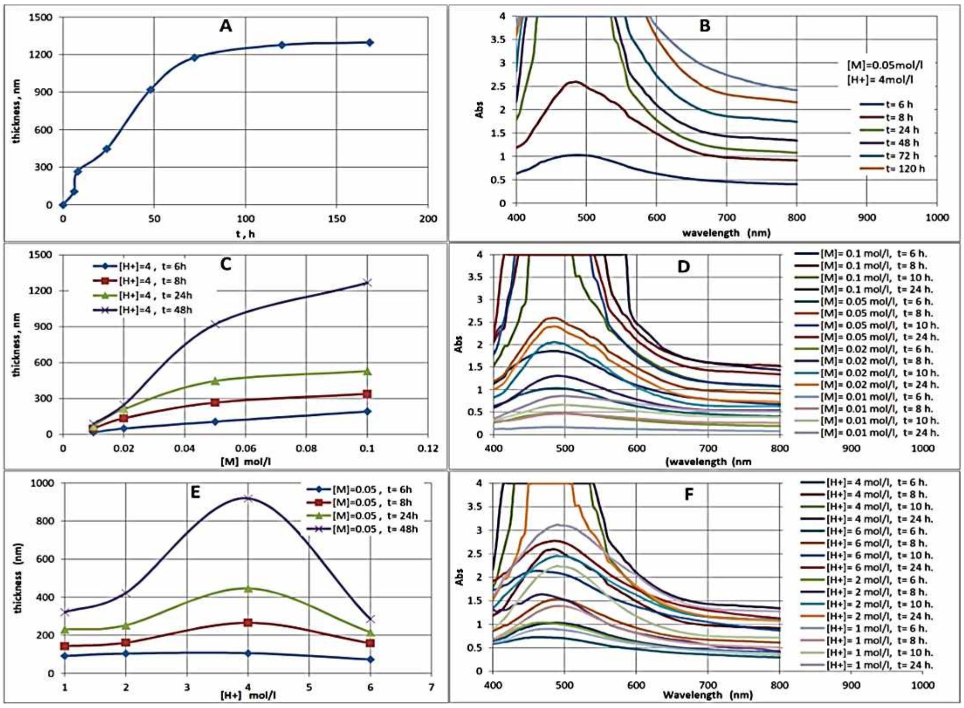

Fig. 3. UV-Vis spectrum (*b*, *d* and *f*) of the films. (*a*, *b* and *c*) thickness *vs* monomer, acid concentration and time.

3.2.1. UV-Vis Spectra

UV-Vis spectra were recorded for dry films on glass in the visible field only. Figure 2, *a* shows the absorption spectra of the films studied at different thicknesses. The films have a maximum absorption peak at 490 nm. Figure 2, *b* shows absorption at 490 nm wavelength *vs* film thickness. By the Beer–Lambert law, the absorption coefficient of the films was linear ($\varepsilon' = 0.01\ \mathrm{nm}^{-1}$).

3.2.2. Effects of Monomer, Acid Concentration and Time on the Anchoring Films

The effects of monomer, acid concentration and time on the fabrication of films were studied. Figure 3 shows UV-Vis spectrum of the films and thickness *vs* monomer, acid concentration and time. Film thickness becomes greater when acid, monomer or time increase, but high concentration of acid gives low thickness because it helps dissolve the polymer and damage the film. The films were fabricated on a substrate of gold, ordinary glass and quartz. No effect of substrate type was observed on the thickness of film.

3.2.3. Surface Morphology

Figure 4 shows the AFM images of the polymer films on glass as substrate. Surfaces of films seem as balls that merge together to

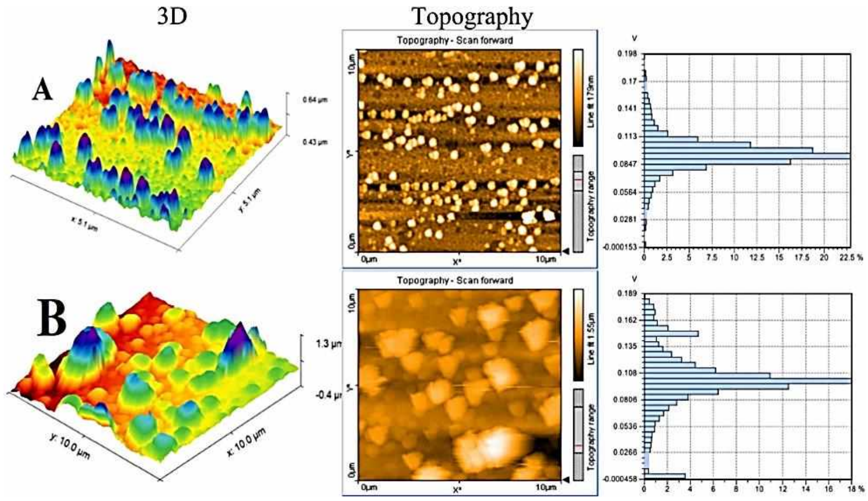

Fig. 4. AFM images (3*D*, topography and elevation distribution) of the polymer films on glass as substrate: *a*) thickness = 106 nm; *b*) thickness = 918 nm.

form rough surface and had a lot of mountains. The surface becomes less rough for more thickness and the mountains become fewer and higher. As noted in Fig. 4, *a*, its thickness is 106 nm, and the maximum height of its mountains is of 197 nm, while, in Fig. 4, *b*, the thickness is 918 nm, and the maximum height of its mountains is of 1550 nm.

From above, making films can be described as follows: when polymer formed and precipitated, the active pointes in surface of substrate absorb polymer chains. They accumulate on surface and grow to join together, and form a rough layer, which seems as joined balls (as in AFM; Fig. 4). Some pointes grow faster and make moun-

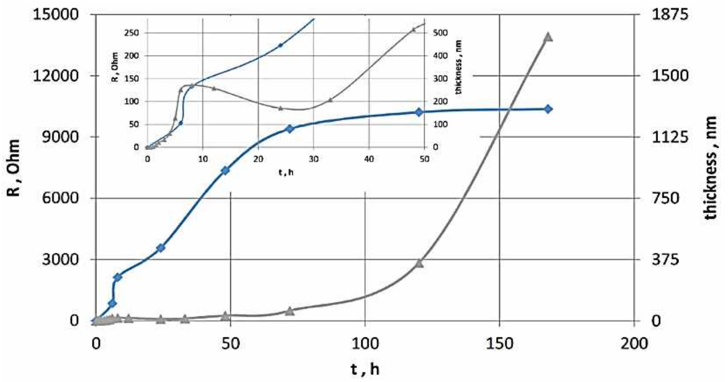

Fig. 5. Time dependence of the electrical resistance and films' thickness of thin films.

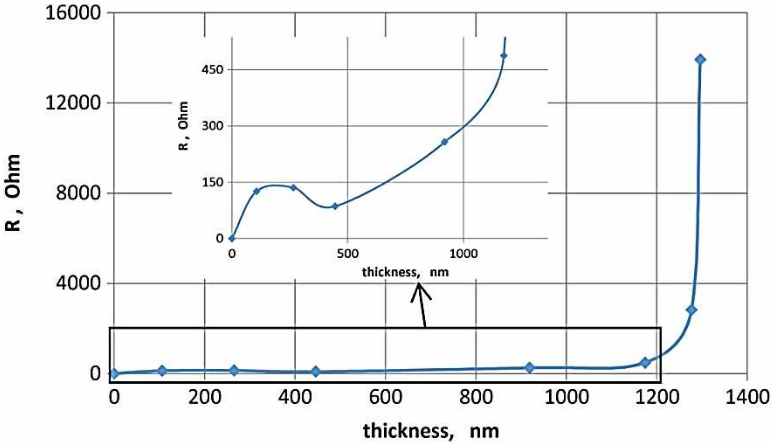

Fig. 6. Films' thickness-dependence of the electrical resistance of thin films.

tains. As well, when polymer chains form faster (by high concentration of monomer or acid), film will be rapidly formed too.

3.3. Studying the Electric Resistance of Films

In order to study the electrical conductivity of films, the electrical resistance between two electrodes of gold, which were immersed in the reaction mixture, was measured *versus* time.

Figure 5 shows the electrical resistance and films' thickness *vs* time, and Fig. 6 shows the electrical resistance *vs* film thickness. At first, the films are thin, and their resistance is low; then, it increases to maximum value. After that, film becomes less resistant because surfaces of films become roughness. When the thickness of the polymer becomes so large, the resistance is increased significantly. This is due to the multilayers in film, which cause additional resistance between the layers.

3.4. Electrochemical Impedance Spectroscopy

Figure 7 shows the electrochemical impedance spectrum (EIS) for four films precipitated on the gold. All curves have semi-circular at high frequencies and linear at low frequencies. With low thickness film, semi-circular part is less clear.

In order to analysis the EIS results, we fitted the impedance data to equivalent electrical circuits (Fig. 8), which consist of a first re-

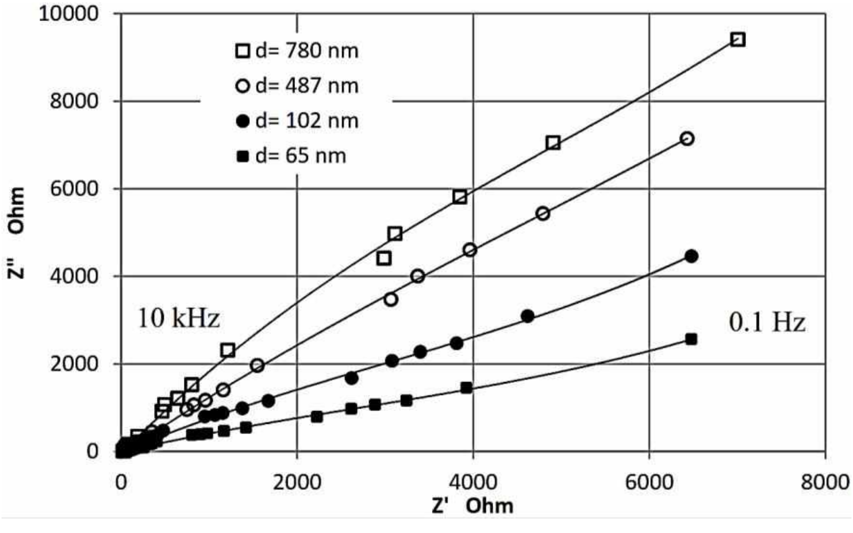

Fig. 7. Nyquist plot for films at gold.

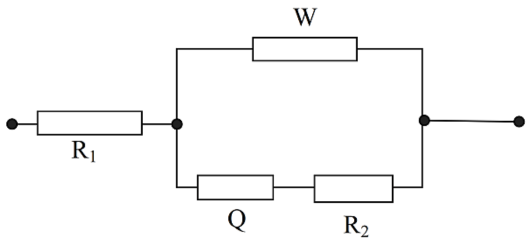

Fig. 8. Equivalent electrical circuits for the films.

TABLE 1. Volumes of electrical circuits.

Thickness, nm	R_1, Ohm	W, mOhm^{-2}	R_2, Ohm	Q, μF/cm^2
780	31±2	740±15.3	1090±56	0.149±0.03
487	30±1	387±8.4	235±42	0.156±0.03
102	29±2	42±3.5	180±27	0.148±0.02
65	32±3	27±1.6	162±18	0.143±0.02

sistance (solution resistance R_1), Warburg impedance (noted W), or capacitance is therefore ascribed to the diffusive capacitance. Warburg impedance is in parallel with the faradic component, which is composed of resistance R_2 serially associated with a capacitance Q. Resistance R_2 is the sum of the charge transfer and the ohmic resistance of film, while Q is the double-layer capacitance (see Table).

4. CONCLUSIONS

Polymer nanoparticles' thin films were fabricated by a simple and easy method by anchoring poly(2-formylpyrrole) in reaction solution. Polymer thin films can be formed on a substrate (glass and gold) by immersing the substrate in the mixture reaction. The thickness of the film increases with time and concentration of monomer and acid, and it decreases at large concentrations of acid. The films had a rough surface and peaks several times greater than the thickness. Electrical resistance of films decreases with the surface roughness and increases with thickness. The best thin films with less resistance can be made by a mixture reaction consisted of monomer concentration 0.01 M, acid 4 M, and for the time of 24 h.

5. HIGHLIGHTS

Novel polymer thin films were fabricated by a simple and easy method by anchoring polymer in reaction solution.

Control of film thickness by procedural factors in the experiment (time and concentration of the reaction materials) is provided.

The used polymer is new and previously unused, easy to prepare and has good properties.

COMPLIANCE WITH ETHICAL STANDARDS

This study was funded by Al-Furat University and Damascus University.
Authors declare that they have no conflict of interest.

ACKNOWLEDGEMENTS

We extend our thanks and gratitude to Prof. Ebrahim Al-Karibi and Prof. Hasan Kalawi for support of this work.

REFERENCES

1. J. Kim, D. Sohn, Y. Sung, and E. R. Kim, *Synthetic Metals*, **132**, Iss. 2: 309 (2003); doi:10.1149/ma2014-02/28/1563
2. M. Gita Rani, *International Journal of Advanced Science and Research*, **3**, Iss. 3: 6 (2018).
3. S. Glenis, M. Benz, E. LeGoff, J. L. Schindler, C. R. Kannewurf, and M. G. Kanatzidis, *Journal of ACS*, **115**, Iss. 26: 12519 (1993); doi:10.1021/ja00079a035
4. S. C. Hernandez, *InterScience*, **19**, Iss. 19–20: 2125 (2007).
5. Y.-P. Zhang, S.-H. Lee, K. R. Reddy, A. I. Gopalan, and K.-P. Lee, *Journal of Applied Polymer Science*, **104**, Iss. 4: 2743 (2007); doi:10.1002/app.25938
6. J. C. Zhang, X. Zheng, M. Chen, X. Y. Yang, and W. L. Cao, *Express Polymer Letters*, **5**, Iss. 5: 401 (2011); doi:10.3144/expresspolymlett.2011.39
7. S. Panero, S. Passerini, and B. Scrosati, *Molecular Crystals and Liquid Crystals: Science and Technology*, **229**, Iss. 1: 97 (1993); doi:10.1080/10587259308032182
8. T. Kasa and F. Gebrewold, *Advances in Physics Theories and Applications*, **62**: 28 (2017); https://www.iiste.org/Journals/index.php/APTA/article/view/35835/36830
9. G. H. Shim and S. H. Foulger, *Photonics and Nanostructures—Fundamentals and Applications*, **10**, Iss 4: 440 (2012); doi:10.1016/j.photonics.2011.12.001
10. A. Rudge, J. Davey, I. Raistrick, S. Gottesfeld, and J. P. Ferraris, *Journal of Power Sources*, **47**, Iss. 1–2: 89 (1994); doi:10.1016/0378-7753(94)80053-7
11. L. Duan, J. Lu, W. Liu, P. Huang, W. Wang, and Z. Liu, *Physicochemical and Engineering Aspects*, **414**, Iss. 2: 98 (2012); doi:10.1016/j.colsurfa.2012.08.033
12. G. Bayramoğlu, M. Karakışla, B. Altıntaş, A. U. Metin, M. Saçak, and

M. Y. Arıca, *Process Biochemistry*, **44**, Iss. 8: 880 (2009); doi:10.1016/j.procbio.2009.04.011

13. H. Gherras, A. Yahiaoui, A. Hachemaoui, A. Belfeda, A. Dehbi, and A. I. Mourad, *Journal of Semiconductors*, **39**, Iss. 10: 102001-1 (2018); doi:10.1088/1674-4926/39/10/102001
14. X. Ding, F. Tan, H. Zhao, M. Hua, M. Wang, Q. Xin, and Y. Zhang, *Journal of Membrane Science*, **570–571**: 53 (2019); doi:10.1016/j.memsci.2018.10.033
15. T. C. Kang, J. K. Park, B. H. Kim, J. J. Lee, H. Choi, H. J. Lee, and J. G. Yook, *Measurement*, **137**, Iss. 1: 272 (2019); doi:10.1016/j.measurement.2019.01.032
16. B. Fernández, R. Pereiro, and A. Sanz-Medel, *Analytica Chimica Acta*, **679**, Iss. 1–2: 7 (2010); doi:10.1016/j.aca.2010.08.031
17. M. Alsultan, J. Choi, R. Jalili, P. Wagner, and G. F. Swiegers, *Molecular Catalysis*, **490**, Iss. 1: 110955 (2020); doi:10.1016/j.mcat.2020.110955
18. A. Al-Hamdan, A. Al-Falah, and F. Al-Deri, *Int. J. Thin Films Sci. Tech.*, **10**, Iss. 2: 101 (2021); http://dx.doi.org/10.18576/ijtfst/100205
19. Y. Fu, Y. Lin, T. Chen, and L. Wang, *Journal of Electroanalytical Chemistry*, **687**, Iss. 1: 25 (2012); doi:10.1016/j.jelechem.2012.09.040
20. J. Huang, X. Liu, Y. Lu, Y. Zhou, J. Xu, J. Li, and W. Song, **184**, Iss 1: 73 (2018); doi:10.1016/j.solmat.2018.04.002
21. E. Klein, K. Huber, O. Paul, and P. Ruther, *Thin Solid Films*, **693**, Iss. 1: 137715 (2019); doi:10.1016/j.tsf.2019.137715
22. D. R. Talham, *Chemical Reviews*, **104**, Iss. 11: 5479 (2004); doi:10.1021/cr030665u
23. R. Ravindranath, P. K. Ajikumar, R. C. Advincula, W. Knoll, and S. Valiyaveettil, *Langmuir*, **22**, Iss. 21: 9002 (2006); doi:10.1021/la060539w

Наносистеми, наноматеріали, нанотехнології
Nanosistemi, Nanomateriali, Nanotehnologii
2021, т. 19, № 4, сс. 923–940

PACS numbers: 61.05.cp, 68.37.Hk, 68.37.Lp, 78.30.Hv, 78.55.Hx, 81.07.Wx, 82.80.Pv

The Effect of Ag Content on the Structural, Optical, and Cytotoxicity Properties of TiO_2 Nanopowders Grown from $TiO(OH)_2$ Precursor by the Chemical Deposition Method

M. Zahornyi[1], N. Tyschenko[1], O. Shyrokov[1], A. Ragulya[1],
O. Kolomys[2], V. Strelchuk[2], K. Naumenko[3], L. Biliavska[3],
S. Zahorodnia[3], M. Kharchuk[3], M. Skoryk[4], A. Kasumov[1],
and A. Ievtushenko[1]

[1]*I. M. Frantsevich Institute for Problems of Materials Science, N.A.S. of Ukraine,*
3, Krzhizhanovsky Str.,
UA-03142 Kyiv, Ukraine
[2]*V. Ye. Lashkaryov Institute of Semiconductor Physics, N.A.S. of Ukraine,*
45, Nauky Prosp.,
UA-03028 Kyiv, Ukraine
[3]*D. K. Zabolotny Institute of Microbiology and Virology, N.A.S. of Ukraine,*
154, Acad. Zabolotny Str.,
UA-03143 Kyiv, Ukraine
[4]*'NanoMedTech' LLC,*
68, Antonovych Str.,
UA-03680 Kyiv, Ukraine

A series of Ag/TiO_2 is prepared by the chemical deposition method using silver nitrate and suspension of $TiO(OH)_2$ following sonication and treatment up 600°C. Silver nanoparticles are deposited on the surface and inside of TiO_2 nanoparticles depending on the Ag concentration. The Ag/TiO_2 composites are characterized by x-ray diffraction, transmission electron microscopy, scanning electron microscopy, Raman and photoluminescence spectroscopies. The optical activity of Ag/TiO_2 with significant attenuation of photoluminescence in the range of 480–600 nm, a shift of mode E_g from 143 to 150 cm^{-1} and FWHM from 12 to 19 cm^{-1} are revealed due to decreasing of TiO_2 crystallites. The optical activity is increased after loading with Ag because metal particles offer electron traps to decrease the recombination of holes and electrons, especially, with Ag loading of 8 wt.%. The obtained results indicate lower toxicity of nanoparticles in the glycerine + water suspension; regardless of the introduction of silver molecules in amount of 4 or 8 wt.%, their CC_{50} values are of 50 μg/mL and 3.9–58.5 μg/mL for the MDBK and MDCK cells, respectively. Instead, TiO_2 nanoparticles in C_2H_5OH + 1.3-propanediol with the introduction of silver molecules are significantly more toxic for the MDBK cells compared to the pure TiO_2; their CC_{50} values are of 6.5 and 4 μg/mL.

Серію Ag/TiO_2 одержано методом хемічного осадження з використанням нітрату срібла та суспензії $TiO(OH)_2$ після ультразвукового та термооброблення до 600°C. Наночастинки срібла осідають як на поверхні, так усередині наночастинок самого TiO_2 в залежності від концентрації Ag. Композити Ag/TiO_2 було охарактеризовано дифракцією Рентґенівських променів, просвітлювальною електронною мікроскопією, сканувальною електронною мікроскопією, Рамановою та фотолюмінесцентною спектроскопіями. Показано оптичну активність Ag/TiO_2 із значним ослабленням фотолюмінесценції в діяпазоні 480–600 нм, зсувом моди E_g від 143 до 150 см$^{-1}$ і FWHM від 12 до 19 см$^{-1}$ внаслідок зменшення кристалітів TiO_2. Оптична активність зростає зі збільшенням концентрації Ag до 8 мас.%. Одержані результати свідчать про меншу токсичність наночастинок у суспензії гліцерин + вода; незалежно від введення молекул Арґентуму в кількості 4 або 8 мас.%, їх значення CC_{50} становили 50 мкг/мл і 3,9–58,5 мкг/мл для клітин MDBK (нирки бика) та MDCK (нирки собаки) відповідно. Натомість наночастинки TiO_2, розчинені в C_2H_5OH + 1,3-пропандіолі при введенні молекул Арґентуму, були значно більш токсичними для клітин MDBK у порівнянні з чистим TiO_2; їхні значення CC_{50} становили 6,5 та 4 мкг/мл.

Key words: Ag/TiO_2, irradiation, Raman spectra, photoluminescence, defects, optical activity, cytotoxicity.

Ключові слова: Ag/TiO_2, опромінення, Раманові спектри, фотолюмінесценція, дефекти, оптична активність, цитотоксичність.

(Received 2 February, 2021)

1. INTRODUCTION

Titanium dioxide was used as a photocatalyst and has attracted scientific interest for many years [1–3]. Heterogeneous photocatalytic oxidation is a promising technique for the complete oxidation of dilute organic pollutants in the waste gas stream. Many organics, bacteria, virus can be oxidized to CO_2 and H_2O at room temperature with TiO_2 catalysts in the air when illuminated with UV or near-UV light. The UV light excites electrons from the valence band to the conduction band. The resulting electron/hole pairs can then migrate to the surface and initiate redox reactions with adsorbed organics.

Nowadays, different kinds of methods, including shape, size, and facet control, element doping have been developed to effectively enhance the photocatalytic performance through increasing the broad absorption of sunlight, prolonging the lifetime of photoinduced carriers, and enhancing the optical activity and photocatalytic stability of TiO_2. For example, *via* shape control, doping with metal or nonmetal elements, dye-sensitization, and construction of heterostructured photocatalyst systems by combining them with plasmonic metals (*i.e.*, Ag, Au, Pd, Pt) or other semiconductors [4–10]. Noble metal nanoparticles (NPs) can show SPR (surface plasmonic resonance), which can be tailored by engineering the shape, size, and surroundings [7–10]. Therefore, noble metal NPs cannot only strongly absorb visible light but also can serve as an electron sink and source of active reaction sites [11].

Morphology-controlled rutile titanium (IV) oxide (TiO_2) and anatase TiO_2 usually prepared by a hydrothermal method and their surfaces were selectively loaded with Au, Ag, and Au–Ag bimetallic nanoparticles (NPs) by photo-deposition to obtain visible light-responsive photocatalysts [12].

The authors [13–14] note that when doped with metals (rare earth) elements, it is possible to shift to the visible region, but the photocatalytic activity decreases, especially in the UV range. For the electronic interaction, nitrogen is good because electrons can pass for the dopant of the orbitals 2*p* or 3*p* to the 3*d* orbital Ti, and the width of the forbidden band decreases.

TiO_2 powders doped with Ag, Fe enhanced the photocatalytic and bactericidal activity [15–18]. For example, Ag concentration from 2.46 to 6.0 wt.% showed increasing of bacteriophage virus inactivation rate 7 times. Therefore, the duration of the disinfection process reduced from 5 to 0.75 min [15]. Der-Shing Lee, Yu-Won Chen have shown the optimum Ag loading (2 wt.%) for excellent methylene blue destruction under UV-light irradiation [18].

The bactericidal effect on bacillus Kochi has been studied using TiO_2–Ag–SiO_2 photocatalyst [17]. The synthesized composite characterized by a higher surface area 164 $m^2 \cdot g^{-1}$ in comparison with P25. Thus, the ability to inactivate composite photocatalyst occurs over a wide spectral range of UV irradiation with an intensity of 2.5 $mV \cdot cm^{-2}$. However, the high absorbance of visible light does not always increase the photocatalytic activity. Sometimes, cation doping leads to a certain number of defects in TiO_2, which can act as centres for the recombination of charges.

Ag–TiO_2 were coated on glass substrates with different dopant concentrations (1%, 3%, 5%, 7% and 10%) and annealed at 550°C [19]. The crystalline structure and phase formation of Ag–TiO_2 was examined using XRD. The HRTEM analysis of pure and 5% Ag-doped TiO_2 thin films was revealed that the particles are spherical with sizes around 23.8 and 11.6 nm, respectively. The Raman spectrometer was also used to identify the phase formation and vibrational modes in the prepared silver-doped TiO_2 coatings. Ag-doped TiO_2 nanoparticles show characteristic photoluminescence (PL) corresponding to the visible spectral range with excitation at 325 nm.

The intensity of luminescence emission decreases with doping of silver ions due to decreasing bandgap TiO_2 from 3.2 to 2.7 eV.

Considering the methods of synthesis and study of nanocomposite properties with oxide NPs, especially of TiO_2–Ag (Au), has not yet received information on the effectiveness of their use. The reason for all would be to use expensive isopropoxide (butoxide), precursors. Using cheap $TiCl_4$ as the precursor of TiO_2 does not allow obtaining the composite system with the required properties due to the complexity of the control of the hydrolysis process, the difficulties associated with the removal and the highly reactive reaction by-products (HCl). However, methods of surface modification of TiO_2 in the synthesis of composites in most cases do not cause difficulties and apply industrial processes.

Therefore, the modification of TiO_2 with Ag has attracted interest for optical and photocatalytic applications. The silver ion-doped TiO_2 attracts much attention due to its outstanding photocatalytic activity and antibacterial activity. However, the withdrawal of nanosize powder catalyst particles from the liquid suspension is difficult. This leads to the formation of secondary pollution and can be catalyst loss activity.

The present paper focuses on the surface structure, cytotoxicity, spectroscopic features (light irradiation 325, 488 nm) of Ag/TiO_2 series prepared by chemical deposition method using silver nitrate, and suspension of $TiO(OH)_2$. The effect of Ag-loading at 4 wt.% and 8 wt.% on the microstructure, Raman and photoluminescence properties are studied and discussed.

2. EXPERIMENTAL

2.1. Synthesis of TiO_2/Ag

The raw material for obtaining the sample was a suspension of hydrated titanium dioxide $TiO(OH)_2$ (metatitanic acid), which is a product of the intermediate stage of processing of titanium concentrates and slags at the plant 'Sumykhimprom'. The suspension was heated at 600°C with a heating rate of 5°C/min to obtain TiO_2 powder. Nanosize particles of titanium dioxide modified with silver were obtained in aqueous solutions of $TiO(OH)_2$ by adding alkali to form anatase modification with a range of silver concentrations from 0 to 8 wt.% . Samples number TiO_2, ATO4 (4 wt.% Ag), ATO8 (8 wt.% Ag).

2.2. Characterization

The crystalline nature and phase formation of Ag–TiO_2 powders are known using powder x-ray diffractometer (DRON 3M) with cobalt anode tube. Mira 3 Tescan with EDX (Oxford INCA *x*-act) was used to study morphology and elemental analysis. The particle shape and size are found with high-resolution transmission electron microscopy (TEM JEM-1400). TEM study of the morphological features of nanoparticles was conducted. The obtained suspensions were mixed actively for 5 min. The drops of the finished suspensions were placed on copper grids coated with a formvar film, which was reinforced with carbon. The samples of nanoparticles dried at room temperature were analysed using a TEM JEM-1400 (Jeol, Japan) at an accelerating voltage of 80 kV. Electron diffraction of nanoparticles was performed on TEM with the same accelerating voltage, with the introduction of a field aperture and removal of an objective aperture. Raman spectroscopy, photoluminescence emission spectra of powders (Horiba Jobin-Yvon T64000) was used to study the structural properties of silver ions doped TiO_2 powders using Ar–Cr laser at 488 nm for Raman and He–Cd laser at 325 nm for PL.

2.3. CYTOTOXICITY ASSAY

MTT-assay was used for the analysis of cell viability [19]. The MDCK cells (Madin–Darby canine kidney cells) obtained from the Institute of Epidemiology and Infectious Diseases Named after L. V. Gromashevsky of the Academy of Medical Sciences of Ukraine and the MDBK cells (Madin–Darby bovine kidney cells) obtained from the tissue culture collection of the Institute of Virology of the Bulgarian Academy of Sciences were used.

Cells were maintained in sterile plastic falcon (Sarstedt, Germany) in a growth medium composed of 45% DMEM (Sigma, USA), 45% RPMI 1640 (Sigma, USA) and 10% foetal bovine serum (Sigma, USA) heat inactivated at 56°C, with antibiotic gentamycin (100 μg/mL) (Sigma, USA).

For the study, the attached cells were trypsinizated for 3–5 min, and then cells were counted and distributed in 96-well plate with density 30.000–50.000 cells in each well. The plate was incubated for 24 h at 37°C in a 5% CO_2 atmosphere to allow the cells to attach to the bottom of the well. After 24 h of growing, monolayer of the MDBK and MDCK cells in 96-multiwell plates were incubated with TiO_2 nanoparticles (NPs) at concentrations of 100, 10.0, 1.0, and 0.1 μg/mL. Nanoparticles were diluted in growth medium for cell cultures. Control cells were incubated with fresh medium lacking NPs for 72 h. A total of 20 μL of MTT solution 3-(4.5-dimethylthiazol-2-yl)-2.5-diphenyl tetrazolium bromide (Sigma-Aldrich, USA) was added to wells and cells were incubated at 37 °C and 5% CO_2 for 3–4 h, then the medium was removed and 150 μL of 96% ethanol was added. The plates were read using a Multiskan FC (Thermo Scientific, USA) with a 538-nm test wavelength. The percentage of cell viability under the condition of TiO_2 NPs action was calculated using formula:

$$\%\ \text{of cell viability (or mitochondrial activity)} = A/B\cdot 100,$$

where A is the mean optical density of the studied samples at a certain concentration, and B is the mean optical density of the control cell samples. NPs concentration, at which cell viability was inhibited by 50% (CC_{50}), was estimated in comparison to the control cells not treated with NPs.

3. RESULTS AND DISCUSSION

3.1. XRD Analysis

X-ray diffraction (XRD) patterns used to examine the phase identification and structural properties of the Ag–TiO_2 powders. Figure 1 shows the XRD pattern of Ag doped TiO_2 powders. The observed XRD patterns of all Ag–TiO_2 series well matched with standard JCPDS File No: 894921. XRD results clearly show that the Ag–TiO_2 powders revealed the formation of a tetragonal anatase. The TiO_2 powders showed several diffraction peaks at $2\theta = 25.34°$, 37.83°, 48.11°, 53.94°, 55.15°, 62.79° were indexed as (101), (004), (200), (105), (211), respectively, which close to values [20]. In our observation, the diffraction pattern of Ag–TiO_2 powders exhibit, no oth-

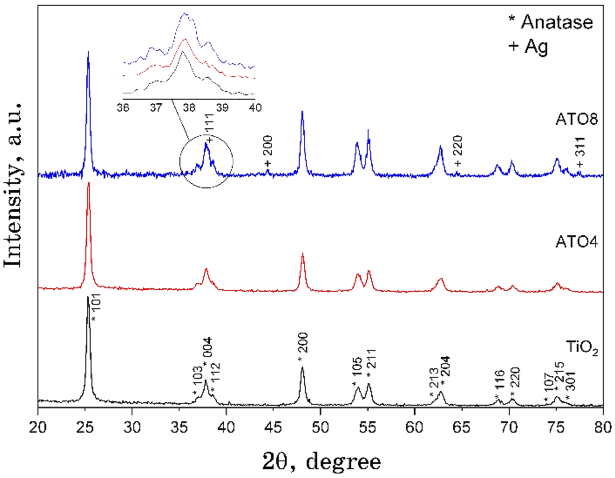

Fig. 1. XRD patterns of TiO_2–Ag

er peaks related to the brookite or rutile phase, which indicates that the powders are in a single anatase phase. In case of lower amount of Ag doped TiO_2 (4 wt.%), no extra peak assigned to Ag was founded, feasibly due to highly dispersion. However, at higher amount of Ag (8 wt.%) doping, the weak diffraction signal is appeared at $2\theta = 38.15°$, $44.38°$, $64.45°$, and $77.32°$ corresponding to metallic Ag (JCPDS #89–3722) having a cubic crystalline structure with parameter lattice $a = 4.0862$ close to [21]. When the doping of Ag, a strain is induced in the TiO_2 crystal lattice due to the occurrence of ionic radii mismatch, the ionic radii of Ag^+ (1.26 Å) being greater than Ti^{4+} (0.68 Å) permits only a little amount of Ag^+ going into the periodic crystal lattice of TiO_2 by replacing the Ti^{4+} ions [20] changing of the lattice periodicity. In addition, the parameter FWHM at $2\theta = 25.3°$ is decreased from 0.4101 to 0.3815 (Table 1) may be due to defects contribution on the surface of TiO_2.

3.2. EDX

The EDX method (Fig. 2) found that the content of elements for pure TiO_2: Ti—54.25 wt.%; O—43.93 wt.%, S—0.5 wt.%. The S content can be explained as follows, the raw material $TiO(OH)_2$ synthesized by a specific technology of the plant 'Sumykhimprom' in sulphuric acid. Therefore, even with repeated washing powder, the sulphur residue is in the raw material. The content of elements for doped TiO_2: Ti—46.27 wt.%; O—49.69 wt.%, S—0.14 wt.%, Ag—3.3 wt.%. There is also an amount of carbon. The results obtained by the EDX method indicate the non-stoichiometry of oxide nanopowders ($Ti/O < 2$).

3.3. TEM

The morphology of materials such as shape and particle size is analysed by TEM. Figure 3, *a–c* show the morphologies of the Ag/TiO_2 samples. Ag nanoparticles on TiO_2 support were dispersed and the sizes of Ag nanoparticles were 35–40 nm. There was no clear correlation between Ag loading and Ag particle size because Ag particles were very homogeneously distributed. Moreover, the sizes of TiO_2 initial particles were 20–30 nm. After loading of Ag, the sizes of TiO_2 particles decreased to 13–20 nm. A 'ball-shaped' particles of silver with developed crystalline structure in TiO_2 (diffraction electrons) were observed.

The results in Figure 4 show that TiO_2 can be present in tetragonal phase (defected state), and Ag phase with a cubic crystalline structure (sample ATO8), which correlate with XRD results.

TABLE 1. The structural parameters of TiO_2, and Ag/TiO_2 powders.

Sample	2θ	*FWHM*	*d*, Å	Phase
TiO_2	25.32	0.3895	3.5170	*
	36.93	0.5045	2.4339	*
	37.79	0.4968	2.3806	*
	38.58	0.4422	2.3335	*
	48.04	0.4245	1.8940	*
	53.91	0.6804	1.7007	*
	55.06	0.4757	1.6680	*
	62.16	0.5637	1.4934	*
	62.72	0.5476	1.4813	*
	68.82	0.5391	1.3642	*
	70.31	0.6221	1.3390	*
	74.03	0.4632	1.2806	*
	75.07	0.5369	1.2654	*
	76.01	0.7301	1.2520	*
ATO4	25.34	0.3831	3.5151	*
	36.93	0.4868	2.4341	*
	37.84	0.5308	2.3777	*
	38.55	0.4492	2.3355	*
	48.08	0.4309	1.8925	*
	53.95	0.5664	1.6997	*
	55.10	0.4767	1.6667	*
	62.13	0.6087	1.4941	*
	62.68	0.7564	1.4822	*
	68.84	0.6463	1.3638	*
	70.39	0.4573	1.3376	*
	74.04	0.5725	1.2804	*
	75.08	0.6040	1.2652	*
	76.03	0.6777	1.2518	*
ATO8	25.31	3.5185	0.3676	*
	36.92	2.4348	0.4257	*
	37.80	2.3799	0.3955	*
	38.12	2.3609	0.1922	+
	38.57	2.3341	0.2670	*
	44.32	2.0437	0.2485	+
	48.05	1.8937	0.3689	*
	53.88	1.7017	0.4026	*
	55.08	1.6674	0.4144	*
	62.10	1.4947	0.5067	*
	62.71	1.4816	0.4412	*
	64.44	1.4459	0.1512	+
	68.76	1.3653	0.5403	*
	70.29	1.3392	0.4155	*
	74.01	1.2808	0.4600	*
	75.08	1.2652	0.5057	*
	76.04	1.2516	0.3850	*
	77.36	1.2335	0.1786	+

Note: ATO—argentum titanium dioxide, *—anatase, +—Ag.

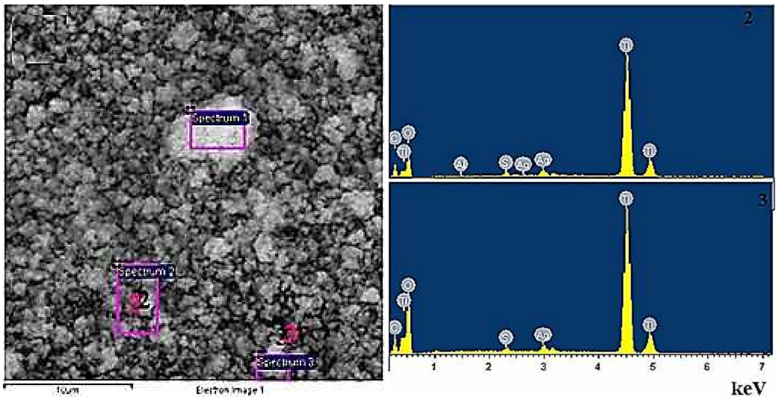

$TiO_2 + 4\%$ Ag
a

b

Fig. 2. SEM micrograph (*a*) and EDX spectra 2–3 (*b*) of the ATO4 powder.

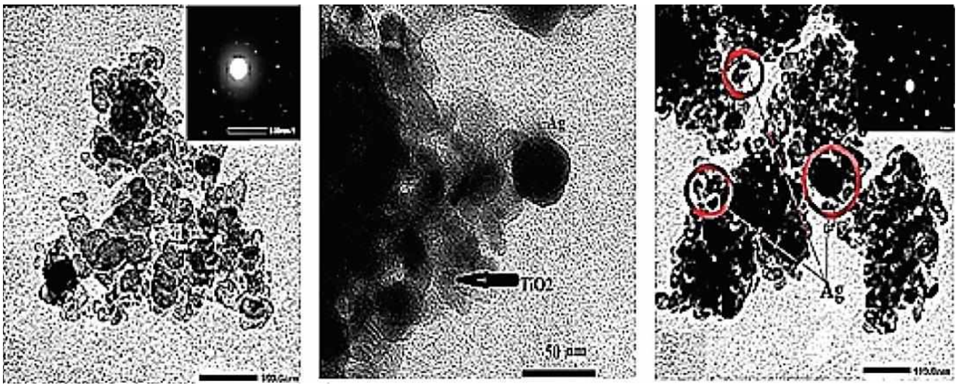

a *b* *c*

Fig. 3. TEM images of pure TiO_2 (*a*), ATO4 (*b*), and ATO8 (*c*) powders.

The hydroxyl group content on the TiO_2 surface samples is important for antimicrobial and photocatalytic properties because in the process of UV irradiation OH groups on the defective surface of TiO_2 are active due to hole capture with subsequent formation of $\cdot$OH radicals for the destructive of toxic organic substances or pathogens. Besides, the presence of silver provides an efficient process of photogeneration of electrons, their transfer from the conduction band Ag to the TiO_2 with the subsequent formation of the Schottky barrier, which inhibits the rate of recombination of photogenerated charges.

Ag and TiO_2 have different work functions, ($\Phi TiO_2 = 4.2$ eV, $\Phi Ag = 4.6$ eV) and hence, when silver is in contact with TiO_2, elec-

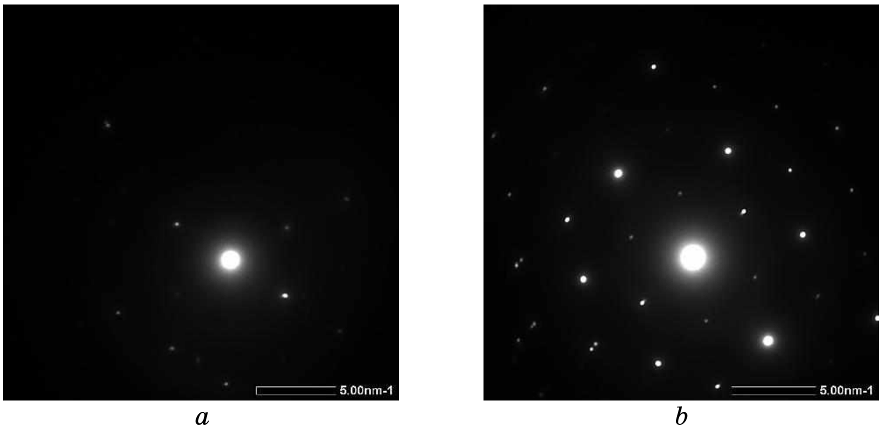

Fig. 4. Electron diffraction of pure TiO_2 (*a*), ATO8 (*b*) powder.

trons will transfer from TiO_2 to silver. These electrons transfer to silver, and loads on the surface of silver will be scavenged by the electron acceptor, thus decrease the recombination between electrons and holes; thereby, silver atoms act as electron traps. The electron-hole recombination is the main reason for low efficiency of TiO_2 photocatalysts [20–24]. Therefore, the existence of silver atom in Ag/TiO_2 can facilitate the transport of more holes to the surface and enhance the optical activity. The Ag particles on TiO_2 act as electron-hole separation centres. The photo-generated electrons transferred from the TiO_2 conduction band to metallic silver particles on TiO_2 are thermodynamically possible, because the Fermi level of TiO_2 is higher than that of silver metals [23, 24]. The Schottky barrier is formed at the Ag–TiO_2 contact region, which improved the charge separation and thus retards the recombination of the photo-generated electrons and holes. The photogenerated electrons accumulated on the surface of Ag have a good fluidity and can be transferred to oxygen molecules, which is absorbed on the surface of Ag.

3.4. Raman

Figure 5 shows the Raman spectra of Ag doped TiO_2 powders. The powders showed several Raman bands located at 142 cm^{-1} (E_g), 196 cm^{-1} (E_g), 396 cm^{-1} (B_{1g}), 513 cm^{-1} ($A_{1g}+B_{1g}$), and 636 cm^{-1} (E_g), which is close to [25]. The strong and sharp Raman peak located at 142 cm^{-1}, which denotes the formation of the anatase phase [21, 25]. In our observation, the Raman spectra of Ag–TiO_2 powders exhibit no other peaks for the brookite/rutile phase, which confirms

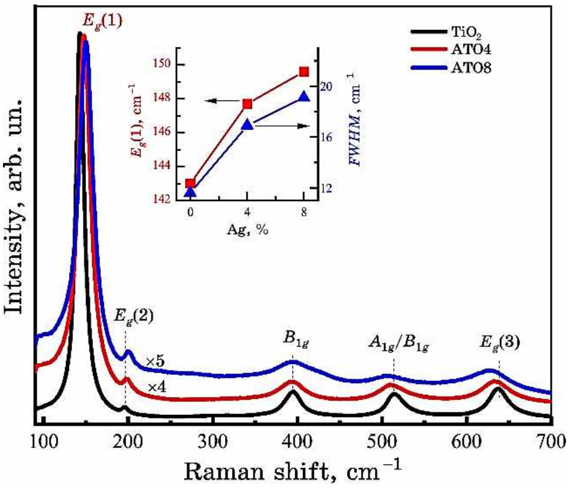

Fig. 5. Raman spectra of TiO_2 (*1*), ATO4 (*2*), ATO8 (*3*) powders.

that all powders are in a single anatase phase (correlation with XRD). The peak intensities found to decrease whereas the width of peak increases because of the lattice distortion and presence of defect levels. The most intense band E_g (1) is shifted in the high-frequency side from 142 to 149 cm^{-1}, while its half-width (FWHM) increases from 11 to 19 cm^{-1}. Lattice deformation, defects and crystallite size have a strong influence on the shear, expansion of peaks and the intensity of Raman peaks [26].

According to the calibration curve [27], we obtained that the average size of anatase crystallites for doped powders is 10 and 8 nm at a silver content of 4 and 8 wt.%, respectively. As well known, the doping with metal ions in the optimal concentration prevents the growth of nanocrystallites [28]. The decrease in the size of TiO_2 particles when replacing Ti^{4+} ions with Ag^{+} ions is associated with the passivation of the boundaries of TiO_2 grains by doping impurity ions, which leads to a violation of structural symmetry, and hence to reduce nanoparticle sizes [29]. TEM images of the samples are confirmed too. The doping by the silver to maintain charge neutrality creates oxygen vacancies in the TiO_2 lattice. If the silver ion replaces the Ti^{4+} ion during doping, the bonds of the Ti–O–Ti complex will be distorted and new bonds of the Ag–O–Ti or Ag–O–Ag complexes will be formed. Therefore, the disruption of Ti–O–Ti bonds and the formation of new Ag–O bonds will affect the combination-active modes and will lead to the expansion and shift of the bands for Raman TiO_2 doped with silver.

There is a high-frequency shift and increase in the half-width of the E_g (1) band at 142 cm^{-1} and E_g (2) band at 196 cm^{-1}, while the

B_{1g} band at 636 cm^{-1} and A_{1g} /B_{1g} at 513 cm^{-1} show a low-frequency shift and a significant increase in half-width in the Raman spectra of silver-doped nanopowders. A wide complex band in the range of 220–300 cm^{-1} is due to the processes of multiphonon scattering [30]. Since in the Raman spectra all oscillations move mainly oxygen atoms, the introduction of silver atoms changes the local coordination of oxygen around Ti^{4+}.

The appearance of structural defects because of doping, which leads to a distortion of octahedra of crystal structure TiO_6, the occurrence of oxygen vacancies, Ti^{4+} ions, surface states, must be accompanied by changes in radiative recombination due to changes in the electronic structure within the bandgap. This primarily refers to the recombination of autolocalized excitons at TiO_6 centres and radiation associated with different *F*-centres due to the presence of oxygen vacancies [31]. The location of the radiation bands, as well as changes in their positions and intensities, depend on the size of TiO_2 nanocrystals and the concentration of the doping impurity, which determine the type and density of donor and acceptor centres on the oxide surface and, as a consequence, photoluminescence spectra [32].

3.5 PL Spectra

Figure 6 shows the photoluminescence analysis of Ag/TiO_2 doped series. The addition of silver atoms leads to a significant (15 times)

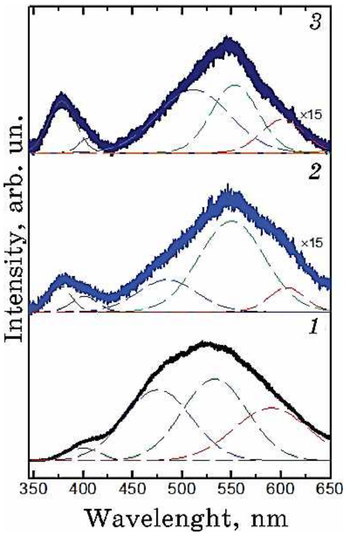

Fig. 6. PL spectra of TiO_2 (*1*), ATO4 (*2*), ATO8 (*3*) powders.

quenching of photoluminescence. For TiO_2 powder with 8 wt.% silver atoms, it has a more pronounced character than with an Ag content of 4 wt.%. This attenuation of the photoluminescence intensity indicates a general decrease in the mutual recombination of photoinduced charge carriers. The doping by silver atoms causes not only general damping of the PL intensity but also a shift and decrease in the band intensity in the region of 480–490 nm, which corresponds to the recombination of autolocalized excitons due to distortion of the TiO_6 octahedron.

The latter is possible both due to the displacement of Ti and O atoms due to substitution by a much larger Ag atom and due to a change in their ionic state, which is manifested in the interatomic bonds in the TiO_6 octahedron. The nature of TiO_6 distortions, in turn, affects the possibility of autolocalization of excitons and, thus, the increase in the probability of photogenerated charges coming to the surface, which can further improve the photocatalytic reactions involving TiO_2. In addition, there is a redistribution of intensity between the bands due to the recombination of autolocalized excitons and the radiation of F-centres. The high-frequency shift of all these lines may be due to changes in the size of the nanocrystallites, which is confirmed by the results of Raman spectroscopy. The oxygen vacancies in the TiO_2 lattice are a kind of intrinsic defect, which creates intermediate energy states within the bandgap of titania. These oxygen vacancies act as photoinduced electron (e^-) and hole (h^+) pair recombination centres. Therefore, this emission has occurred from the recombination of e^-/h^+ pair via oxygen vacancies.

Thus, oxygen vacancies form both in the volume of nanocrystals and on their surface, it is possible to form several localized electronic states for anatase. In addition, it should also be noted that in the process of photochemical transformations the formation of new donor and acceptor levels. Thus, the energy electron structure within the bandgap in nanocrystalline doped Ag/TiO_2 samples can be complex. Therefore, it contributes to the sensitization of semiconductor nanoparticles to visible light, thus, improves the relaxation of electronic excitation, and therefore complicates the understanding of the nature and dynamics of photochemical transformations necessary to create conditions that reduce losses of photogenerated charge carriers.

3.6. Cytotoxicity of Suspensions with Powders TiO_2–AG

Determination of the cytotoxicity of titanium dioxide (TiO_2) with different percentages of argentum (Ag) is an integral component of any drug development process. The research was carried out using

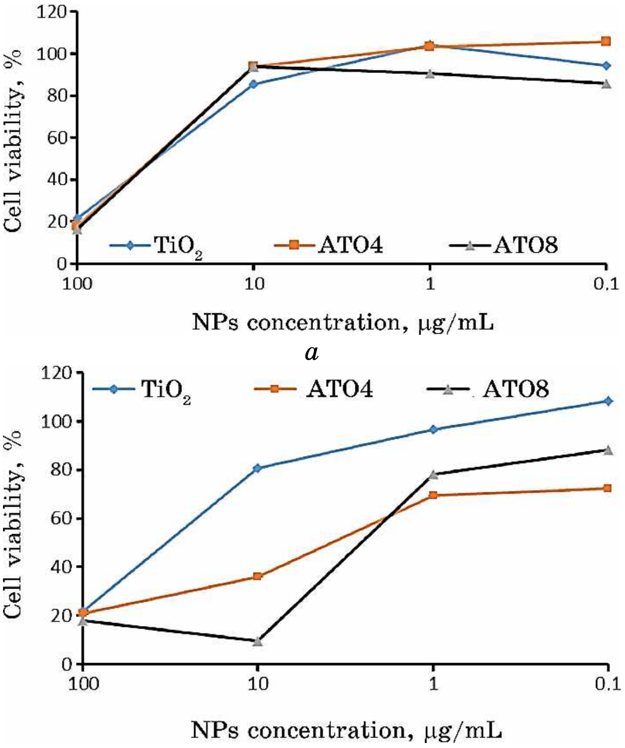

b

Fig. 7. The effects of the TiO_2 NPs in glycerine + water suspension (*a*) and in a C_2H_5OH + 1,3-propandiol suspension (*b*) on the viability of the MDBK cells.

the MTT-assay.

It was shown that TiO_2 NPs in glycerine + water suspension possess significant cytotoxicity at concentrations of 100 μg/mL, as MDBK cells viability decreased by more than 84% (Fig. 7, *a*). However, at a concentrations of 10.0÷0.1 μg/mL, they were non-toxic because reduced cell viability by a maximum of 15%. TiO_2 NPs with Ag (4–8 wt.%) in C_2H_5OH + 1.3-propanediol suspension at a concentration of 100 and 10 μg/mL were toxic for MDBK cells, as they suppressed their viability by 65–91% (Fig. 7, *b*).

As shown in Figure 8, *a*, the composition of TiO_2 without Ag, with 4 wt.% and 8 wt.% Ag in glycerine + water were less toxic on the MDCK cells compare to nanoparticles of TiO_2 in the C_2H_5OH + 1.3-propandiol. Thus, these samples do not decrease the cell viability at a concentration from 0.1 to 10 μg/ml. The inhibition of mitochondrial activity detects only at a concentration of 100 μg/ml, the percentage of life were at range from 8 to 33%.

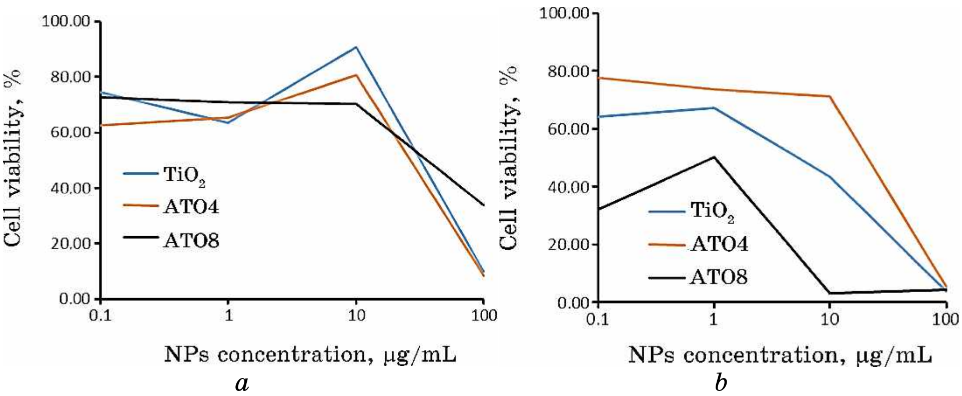

Fig. 8. Viability of the MDCK cells cultivated on the different samples of TiO_2 and TiO_2 with Ag in glycerine + water (*a*) and at C_2H_5OH + 1,3 propandiol (*b*).

Our results on the MDCK cell line clearly show that TiO_2 with 8 wt.% Ag in the C_2H_5OH + 1,3-propandiol was highly toxic at a concentration of 10 and 100 μg/ml. The inhibition of cell viability was 97% (Fig. 8, *b*). Other samples, TiO_2 without Ag and TiO_2 with 4 wt.% Ag were toxic only at a high concentration of 100 μg/ml. Thus, the inhibition of mitochondrial activity was 96%. It should be noted that in minimal dilution inhibition of cell viability decreased to the control sample.

Using the linear regression model in Microsoft Excel (predictor function) [32] and dose-dependent values of the NP cytotoxicity, it was estimated that for MDBK cells the CC_{50} indexes of TiO_2 NPs regardless of the solvent equalled 50 μg/mL (Table 2), while, for MDCK cells, the CC_{50} index of TiO_2 diluted at C_2H_5OH + 1.3-propandiol was lower in 2.5 times as compared with glycerine + water suspension. The obtained results indicate lower toxicity of nanoparticles in the glycerine + water suspension, regardless of

TABLE 2. NPs concentration, at which cell viability was inhibited by 50%.

Solvent—glycerine + water			
Type of cells	TiO_2	ATO4	ATO8
CC_{50} (for the MDBK cells), μg/mL	50	50	50
CC_{50} (for the MDCK cells), μg/mL	42.8	39	58.3
Solvent—C_2H_5OH + 1.3-propandiol			
CC_{50} (for the MDBK cells), μg/mL	50	6.5	4
CC_{50} (for the MDCK cells), μg/mL	17.4	36.9	2.3

the introduction of silver molecules amount of 4 or 8 wt.%, their CC_{50} values were 50 μg/mL and 3.9–58.5 μg/mL for the MDBK and MDCK cells, respectively. Instead, TiO_2 nanoparticles in $C_2H_5OH + 1.3$-propanediol with the introduction of silver molecules were significantly more toxic for the MDBK cells compared to the pure TiO_2 NP, their CC_{50} values were 6.5 and 4 μg/mL.

4. CONCLUSIONS

Nanopowders Ag/TiO_2 successfully obtained by chemical deposition technique. The effect of Ag concentration on the structural, morphological, cytotoxicity and optical properties, PL emission behaviour has been systematically studied. The crystallite size decreased with cumulative concentrations of Ag doping. The crystalline phase of the $Ag–TiO_2$ was confirmed using XRD, and Raman analysis. The average size of pure and 8 wt.% Ag^+ doped TiO_2 particle was determined to be 25–30 and 13–15 nm, respectively, using the TEM images. The optical activity of Ag/TiO_2 with significant attenuation of photoluminescence in the range of 480–600 nm, a shift of mode E_g from 143 to 150 cm^{-1} and FWHM from 12 to 19 cm^{-1} was stated due to decreasing of TiO_2 crystallites to 8 nm. As a result of the cytotoxicity studies, it was shown that the type of solvent depends on the toxicity level of the studied nanoparticles for the cell cultures. Thus, the studied nanocomposites in $C_2H_5OH + 1.3$-propanediol increases the inhibition of cell viability compared to nanoparticles in glycerine + water. In addition, it was determined that increasing the concentration of silver leads to increased cytotoxicity for cell cultures. The results obtained made it possible to determine CC_{50} values, which are the primary test for subsequent antiviral activities.

ACKNOWLEDGEMENTS

This work was partially supported by the research project of N.A.S. of Ukraine ‘The development of photocatalytic nanocomposites for viruses inactivation in the air’ (No. 40/20-H) and was partially supported by the research projects of NAS of Ukraine ‘Development of innovative photocatalytic nanostructured materials based on ZnO and TiO_2’ (528/IPM-11/20).

REFERENCES

1. M. N. Ghazzal, H. Kebaili, M. Joseph, D. P. Debecker, P. Eloy, J. De Coninck, and E. M. Gaigneaux, *Appl. Catalys. B: Environm.*, **115**: 276

(2012); doi:10.1016/j.apcatb.2011.12.016
2. A. L. Luna, D. Dragoe, K. Wang, B. Peaunier, E. Kowalska, B. Ohtani, and C. Colbeau-Justin, *The J. Physic. Chem. C*, **121**: 14302 (2017); doi:10.1021/acs.jpcc.7b01167
3. G. V. Sokolsky, M. N. Zahornyi, T. F. Lobunets, N. I. Tyschenko, A. V. Shyrokov, A. V. Ragulya, S. V. Ivanov, N. Gayuk, and V. E. Sokol'skii, *Journal of Chemistry and Technologies*, **27**: 130 (2019); doi:10.15421/081914
4. Yu. B. Pankivskka, L. O. Biliavska, O. Yu. Povnitsa, M. M. Zagornyi, A. V. Ragulia, M. S. Kharchuk, and S. D. Zagorodnya, *Microbiol. J.*, **81**: 73 (2019); doi:10.15407/microbiolj81.05.073
5. J. Li, and N. Wu, *Catalys. Sci. & Technol.*, **5**: 1360 (2015); doi:10.1039/c4cy00974f
6. A. Ievtushenko, N. Karpyna, J. Eriksson, I. Tsiaoussis, I. Shtepliuk, G. Lashkarev, R. Yakimova, and V. Khranovskyy, *Superlattices and Microstructures*, **117**: 121 (2018); doi:10.1016/j.spmi.2018.03.029
7. A. Zaleska-Medynska, *Metal Oxide-Based Photocatalysis. Fundamentals and Prospects for Application* (Book Elsiver: 2018).
8. H. Harada, A. Onoda, T. Uematsu, S. Kuwabata, and T. Hayashi, *Langmuir*, **32**: 6459 (2016); doi:10.1021/acs.langmuir.6b01073
9. O. M. Lavrynenko, M. N. Zahornyi, M. M. Bataiev, Yu. M. Bataiev, O. Yu. Pavlenko, and O. A. Kornienko, *Khimiya, Fizika ta Tekhnologiya Poverkhni*, **11**: 508 (2020); https://doi.org/10.15407/hftp11.04.508
10. P. Nguyen-Tri, V. Nguyen, and T. Nguyen, *Journal of Composites Science*, **3**, No. 2: 34 (2019); doi:10.3390/jcs3020034
11. M. Zahornyi, *Powder Metallurgy and Metal Ceramics*, **3–4**: 130 (2017); doi:10.1007/s11106-017-9880-x
12. Z. Zheng, N. Murakamia, J. Liv, Z. Teng, Q. Zhang, Yu Cao, H. Cheng, and T. Ohno, *ChemCatChem.*, **12**: 3783 (2020); https://doi.org/10.1002/cctc.202000366
13. M. V. Shapovalova, T. A. Khalyavka, N. D. Shcherban, O. Y. Khuzhun, V. V. Permyakov, and S. N. Shcherbakov, *Nanosistemi, Nanomateriali, Nanotehnologii*, **18**, Iss. 3: 681 (2020); https://doi.org/10.15407/nnn.18.03.681
14. T. A. Khalyavka, N. D. Shcherban, V. V. Shymanovska, E. V. Manuilov, V. V. Permyakov, and S. N. Shcherbakov, *Res. on Chem. Intermed.*, **45**: 4029 (2019); doi:10.1007/s11164-019-03888-z
15. H. Moradi, A. Eshaghi, S. R. Hosseini, and K. Ghani, *Ultrason. Sonochem.*, **32**: 314 (2016); doi:10.1016/j.ultsonch.2016.03.025
16. Z. Xiong, J. Ma, W. J. Ng, T. D. Waite, and X. S. Zhao, *Water Research*, **45**: 2095 (2011); doi:10.1016/j.watres.2010.12.019
17. J. Ma, Z. Xiong, T. David Waite, W. J. Ng, and X. S. Zhao, *Micropor. Mesopor. Mater.*, **144**: 97 (2011); doi:10.1016/j.micromeso.2011.03.040
18. H. N. Thi-Tuyet, T. A. Thi-Kim, S. N. Van, and N. The-Vinh, *AIMS Mater. Sci.*, **3**: 339 (2016); doi:10.3934/matersci.2016.2.339
19. K. Satyavani S. Gurudeeban, T. Ramanathan, and T. Balasubramanian, *Avicenna J. Med. Biotechnol.*, **4**: 35 (2012).
20. D. Komaraiah, E. Radha, J. Sivakumar, M.V. Ramana Reddy, and R. Sayanna, *Optical Materials*, **108**: 110401 (2020); https://doi.org/10.1016/j.optmat.2020.110401
21. D. Gogo, A. Namdeo, A. K. Golder, and N. R. Peela, *Int. J. Hydrogen Ener-*

gy, **45**: 2729 (2020); https://doi.org/10.1016/j.ijhydene.2019.11.127
22. C. H. Li, Y. H. Hsieh, W. T. Chiu, C. C. Liu, and C. L. Kao, *Separ. Purif. Technol.*, **58**: 148 (2007); doi:10.1016/j.seppur.2007.07.013
23. J. Wang, H. Zhao, X. Liu, X.Li, P. Xu, and X Han, *Catal. Comm.*, **10**: 1052 (2009); https://doi.org/10.1016/j.catcom.2008.12.060
24. L. Der-Shing and Y. W. Chen, *Journal of the Taiwan Institute of Chemical Engineers*, **45**: 705 (2014); https://doi.org/10.1016/j.jtice.2013.07.007
25. W. F. Zhang, Y. L. He, M. S. Zhang, Z. Yin, and Q. Chen, *J. Phys. D: Appl. Phys.*, **33**: 912 (2000); https://iopscience.iop.org/article/10.1088/0022-3727/33/8/305/pdf
26. S. Sahoo, A. K. Arora, and V. Sridharan, *J. Phys. Chem. C*, **113**: 16927 (2009); https://doi.org/10.1021/jp9046193
27. Yu. M. Shul'ga, D. V. Matyushenko, E. N. Kabachkov, A. M. Kolesnikova, E. N. Kurkin, I. A. Domashnev, and S. B. Brichkin, *ZhTF*, **80**: 142 (2010) (in Russian); Ю. М. Шульга, Д. В. Матюшенко, Е. Н. Кабачков, А. М. Колесникова, Е. Н. Куркин, И. А. Домашнев, С. Б. Бричкин, *ЖТФ*, **80**: 142 (2010).
28. A. Ahmad, J. Thiel, and S. Ismat, *J. Phys.: Conf. Ser.*, **61**: 11 (2007); https://iopscience.iop.org/article/10.1088/1742-6596/61/1/003
29. Sajid I. Mogal, Vimal G. Gandhi, Manish Mishra, Shilpa Tripathi, T. Shripathi, Pradyuman A. Joshi, and Dinesh O. Shah, *Ind. Eng. Chem. Res.*, **53**: 5749 (2014); https://doi.org/10.1021/ie404230q
30. S. M. Mali, C. A. Betty, P. N. Bhosale, and P. S. Patil, *Cryst. Eng. Comm.*, **13**: 6349 (2011); doi:10.1039/C1CE05928A
31. W. F. Zhang, M. S. Zhang, Z. Yin, and Q. Chen, *Appl. Phys. B*, **70**: 261 (2000); https://doi.org/10.1007/s003400050043
32. T. O. Busko, O. P. Dmitrenko, M. P. Kulish, M. A. Zabolotnyi, O. O. Prikhod'ko, N. V. Vityuk, A. M. Yeremenko, N. P. Smirnova, A. C. Nikolenko, V. V. Strel'chuk, B. M. Romanyuk, B. V. Shlapats'ka, *Voprosy Atomnoi Nauki i Tekhniki. Seriya: Fizika Radiatsionnykh Povrezhdeniy i Radiatsionnoye Materialovedenie*, **4**: 3 (2011) (in Ukrainian); Т. О. Буско, О. П. Дмитренко, М. П. Куліш, М. А. Заболотний, О. О. Приходько, Н. В. Вітюк, А. М. Єременко, Н. П. Смірнова, А. С. Ніколенко, В. В. Стрельчук, Б. М. Романюк, В. В. Шлапацька, *Вопросы атомной науки и техники. Серия: Физика радиационных повреждений и радиационное материаловедение*, **4**: 3 (2011); http://dspace.nbuv.gov.ua/handle/123456789/111345
33. S. N. Lapach, A. V. Gubenko, and P. N. Babich, *Statistical Methods in Biomedical Research Using Excel* (Kiev: Morion: 2001).

Наносистеми, наноматеріали, нанотехнології
Nanosistemi, Nanomateriali, Nanotehnologii
2021, т. 19, № 4, сс. 941–952

PACS numbers: 07.07.Df, 33.50.Dq, 42.62.Be, 61.46.Df, 78.67.Hc, 81.07.Ta, 87.64.kv

Gas-Sensing Fluorescent Nanostructured Composites with Coumarin Dyes and CdTe Semiconductor Nanoparticles for Non-Invasive Medical Diagnostics

V. P. Mitsai, Ya. P. Lazorenko, A. G. Misyura, and S. O. Mamilov

Institute of Applied Problems of Physics and Biophysics, N.A.S. of Ukraine,
3, Vasil Stepanchenko Str.,
UA-03142 Kyiv, Ukraine

The paper presents the results of the study of the spectral-luminescent properties of solutions and nanostructured composites, which include some coumarin dyes (coumarin 4, coumarin 7), semiconductor nanocrystals (CdTe quantum dots), as well as values of their spectral shifts depending on the medium. The effect of enhancing the fluorescence intensity of coumarin dyes by CdTe quantum dots through nonradiative energy transfer is revealed. The fluorescence sensitivity of the synthesized systems to ammonia and acetone vapours in the air is shown, that manifests itself by means of the decrease in the fluorescence intensity proportional to the analyte concentration. For ammonia, the response to a vapour concentration of 10 p.p.m. is $13.2 \pm 0.6\%$, and for 5000 p.p.m., it is $74.0 \pm 1.1\%$. For acetone, the response to a vapour concentration of 33 p.p.m. is $0.56 \pm 0.08\%$; for 67 p.p.m., it is $1.2 \pm 0.1\%$, and for 133 p.p.m., it is $2.2 \pm 0.1\%$. Recovery of sensory properties of such systems after desorption of analytes' molecules is revealed. The created nanostructured composites are promising as sensor elements of devices for non-invasive medical diagnostics of several pathologies, such as lung cancer, liver and kidney diseases, diabetes mellitus, heart failure, pancreatitis, by determining the concentrations of their biomarkers in human exhaled air: ammonia and acetone.

У статті наведено результати дослідження спектрально-люмінесцентних властивостей розчинів і наноструктурних композитів, що включають ряд кумаринових барвників (кумарин 4, кумарин 7), напівпровідникових нанокристалів (квантових точок CdTe), а також величини їхніх спектральних зсувів в залежності від середовища. Виявлено ефект підсилення інтенсивности флюоресценції кумаринових барвників квантовими точками CdTe шляхом безвипромінювального переносу енергії. Показано флюоресцентну чутливість синтезованих систем до парів аміяку й ацетону в повітрі, що проявляється у пониженні інтенсивности флюоресценції, пропорційному концентрації аналіту. Для аміяку відгук на концентрацію парів у

10 p.p.m. складав 13,2 ± 0,6%, на 5000 p.p.m. — 74,0 ± 1,1%. Для ацетону відгук на концентрацію парів у 33 p.p.m. складав 0,56 ± 0,08%, на 67 p.p.m. — 1,2 ± 0,1%, а на 133 p.p.m. — 2,2 ± 0,1%. Виявлено відновлення сенсорних властивостей таких систем після десорбції молекул аналітів. Створені наноструктурні композити є перспективними як сенсорні елементи приладів для неінвазивної медичної діягностики ряду патологій, таких як рак легенів, захворювання печінки та нирок, цукровий діябет, серцева недостатність, панкреатит, шляхом визначення концентрацій їхніх біомаркерів у видихуваному повітрі людини — аміяку й ацетону.

Key words: sensor, coumarin dyes, acetone, ammonia, fluorescence, quantum dots.

Ключові слова: сенсор, кумаринові барвники, ацетон, аміяк, флюоресценція, квантові точки.

(Received 4 February, 2021)

1. INTRODUCTION

Studies in the field of molecular spectroscopy and luminescence have received new pulls in connection with the development of works on optical sensorics of chemical compounds [1]. The development of fluorescent gas sensor systems is becoming increasingly important to solve a wide range of problems that require determining the concentrations of various components of the gaseous environment: environmental monitoring (living and working areas), detection of biomarker molecules in human exhaled air, and others. Such sensor systems can be created using micro- and nanotechnology, which will provide miniature, reliable, and relatively inexpensive detectors and sensor systems.

Nanosensors based on nanoparticles and molecules of organic fluorophores placed in organic or inorganic matrices are used to detect gases. Fluorescent optical chemosensors in which the output signal is a change in the fluorescence properties of the sensor material are among the most promising, due to the high sensitivity of the fluorescence signal to certain agents, and as a consequence, the ability to detect ultra-low concentrations of analytes [1–4].

One of the important practical applications of such sensors can be a non-invasive diagnosis of diseases by analysis of exhaled air, which can be an alternative to blood and urine tests. The connection between some pathologies and the increase in the concentration of certain biomarker molecules is well established. Today, some of the most studied and most important biomarkers in exhaled air are ammonia and acetone [5]. Ammonia is a marker of liver and kidney dysfunction, lung cancer, *etc.*, and acetone is a marker of diabetes, pancreatitis, heart failure, lung cancer, *etc.* [5–8].

The use of coumarin dyes as fluorophores is promising, which is based on information about their spectral-luminescent properties, as well as the ability to intermolecular interactions and the formation of proteolytic forms [9]. There are many reports of studies of coumarin fluorophores in sensors that are sensitive to ammonia vapour [1, 9], but due to several disadvantages (low selectivity, low sensitivity limit, *etc.*), they have not yet found practical application. In [10, 11], it was shown that some coumarin dyes show fluorescent sensitivity to the presence of acetone in liquids, but there are no data on the study of their sensor properties to acetone vapours currently. Therefore, it is important to further study coumarin dyes to create highly sensitive fluorescent sensors of ammonia and acetone in a gaseous medium.

To increase the sensitivity of such fluorescent sensors, it is of interest to investigate the use of the effects of enhancing the fluorescence of organic dyes located near nanoparticles. According to the works [12–16], nanoparticles of metals or semiconductors (quantum dots) near fluorophores can significantly increase the intensity of their radiation due to non-radiative, so-called Förster resonance energy transfer (FRET) from nanoparticles to fluorophores molecules. When two objects (donor and acceptor) converge to the distance of the Förster radius (approximately, of 10 nm) and the fluorescence spectrum of the donor overlaps with the absorption spectrum of the acceptor, the probability of energy transfer without radiation increases significantly between them.

This paper is concerned with the creation of gas-sensing fluorescent nanostructured composites with coumarin dyes and semiconductor nanoparticles CdTe and the study of their optical properties and sensory sensitivity to acetone and ammonia vapours.

2. EXPERIMENTAL

We used such materials and reagents: ethanol 96%, acetone ('extra pure'), ammonia solution 10% (aqueous), coumarin 4 (chemical formula 7-Hydroxy-4-methylcoumarin, produced by Avocado), coumarin 7 (chemical formula 3-(2-Benzimidazolyl)-7-N,N-(diethylamino)–coumarin, Alpha-Aconis), CdTe quantum dots (produced by BukNano-Tech) with a particle size of 2.3 nm, a quantum yield of 30%, and luminescence at wavelengths of 530–535 nm, stabilized by the surfactant thioglycolic acid (TGA), pH = 11; silica gel 60 (pore size 6 nm) with a specific surface area of 500 ± 50 m^2/g and a particle size of 37–63 μm (UkrOrgSyntez), hydrophilic pyrogenic silica 'Aerosil' brand A-380 with a specific surface area of $3.8 \cdot 10^2$ m^2/g, polymer ethylene-vinyl acetate (EVA). The materials of the sorbents were selected due to their developed surface, which determines their high sorption properties.

Recording of absorption spectra and fluorescence excitation spectra were performed on the Specord M40 UV-VIS spectrophotometer (manufactured by Carl Zeiss Jena). Fluorescence spectra were measured using the SL40-2 spectrometer (Solar TII). Kinetics of fluorescence was obtained on the FLx800T fluorimeter (BioTek Instruments) and on the Specord M40 UV-VIS. The Justor 1100DG (manufactured by Nichiryo) and the Research (Eppendorf) manual pipettes were used to dispense a given volume of liquid substances. Reagents were weighed on the electronic scales AD50 (Axis).

The semiconductor laser with a wavelength of 405 nm and the ultraviolet 370–375 nm LED were used as sources of fluorescence excitation for measuring fluorescence spectra.

Alcohol solutions of coumarin dyes at concentrations of 10^{-3} M and 10^{-4} M were prepared by dissolving in ethanol a dry portion of the dye. Samples of composite structures of two types were created. In the first case, the formation of composite structures involved the layer-by-layer application of their components. On a heated to 80°C glass substrate, EVA polymer was applied, after that, on the polymer layer, a layer of silica gel 60 was immobilized. On the resulting two-layer composite, the mixture of the solution of coumarin 7 in ethanol (concentration 10^{-3} M) with the aqueous solution of colloidal quantum dots CdTe in the ratio (1:1) was applied. The resulting composite was dried at a temperature of 65–70°C. The obtained samples were translucent with a matte surface and had a size of $7\times35\pm2$ mm and a thickness of 80 ± 5 μm (without substrate). In the second case, samples were created by applying a layer of Aerosil A-380 with immobilized coumarin 4 to the glass substrate. Immobilization of coumarin 4 on Aerosil was performed by sorption from the ethanolic solution of the dye with concentrations of 10^{-3} M and 10^{-4} M, followed by drying at room temperature.

Air mixtures with the required concentration of the analyte (acetone or ammonia) were obtained by the static volumetric method of preparation of gas mixtures, similar to that described in the international standard ISO 6144:2003 [17].

Measurement of the fluorescence response of nanostructured composite samples to the presence of certain concentrations of analytes in the gas samples was performed as follows. The synthesized samples were fixed in the quartz gas cuvette, which was placed in the measuring compartment of the fluorimetric device. Next, the fluorescence intensity kinetics of the samples was recorded. A certain volume of the prepared air mixture with the given concentration of analyte was cyclically pumped through the cuvette for a definite time at the first stage of the measurement. On the second, there was a pumping of clean air through the cuvette. The difference in the fluorescence intensity of the sample before pumping the gas mixture and at the end of pumping was considered the fluorescent response of the sample. All data were registered in automatic mode with further processing on PC. Fluorescence excitation was performed at 485 nm and registration was at 528 nm for the samples with coumarin 7. Fluorescence excitation was performed at 340 nm and registration was at 360–600 nm for the samples with coumarin 4.

3. RESULTS AND DISCUSSION

We investigated the spectral-optical properties of ethanolic solutions of fluorescent dyes, aqueous solutions of quantum dots, as well as their donor-acceptor mixtures. The absorption spectra and the fluorescence spectra of ethanolic solutions of coumarin 7 and coumarin 4 dyes are presented in Fig. 1 and Fig. 2. Absorption (D) was measured in absolute units of optical density, and fluorescence (I) was measured in relative units of intensity.

The absorption spectrum of the ethanolic solution of coumarin 7 (Fig. 1 (*1*)) has a wide band in the range of 370–480 nm with a maximum near $\lambda_{\max} = 430$ nm. The fluorescence spectrum (Fig. 1 (*2*)) has a band with a maximum at $\lambda_{\max} = 508$ nm. The widths of the bands (full width at half maximum—FWHM) were $\Gamma = 150$ nm and $\Gamma = 51$ nm, respectively. The concentration of the dye coumarin 7 in ethanol was 10^{-3} M; the excitation of fluorescence was at $\lambda = 405$ nm.

The absorption spectrum of the ethanolic solution of coumarin 4 (Fig. 2 (*1*)) has a band in the range of 260–400 nm with a maximum $\lambda_{\max} = 324$ nm. The fluorescence spectrum (Fig. 2 (*2*)) has a band with a maximum at $\lambda_{\max} = 453$ nm. The widths of the bands were $\Gamma = 45$ nm and $\Gamma = 57$ nm, respectively. The concentration of the coumarin 4 dye in ethanol was 10^{-4} M; the excitation of fluorescence was at $\lambda = 370$–375 nm.

We have performed experiments to detect the effect of CdTe quantum dots on the fluorescence of the ethanolic solution of coumarin 7. The results showed an increase in fluorescence of coumarin 7 in ethanol by 57% when it mixed with the solution of CdTe quantum dots in a ratio of 1:1. This evidences that FRET takes place because there is an overlap of the fluorescence band of quantum dots and the absorption band of coumarin 7.

We will use the obtained spectra of coumarin 7 and coumarin 4 in ethanol solutions to compare with the spectra of composite structures, which include these dyes. It will allow us to study the spectral behaviour of molecules of these dyes depending on the molecular environment. It should be noted that our experimental data on ethanolic solutions of the studied dyes coincide with the known spectra [18] that indicates the reliability of our results.

A study of the spectral-optical properties of the samples was performed in order to determine the spectral ranges for the experi-

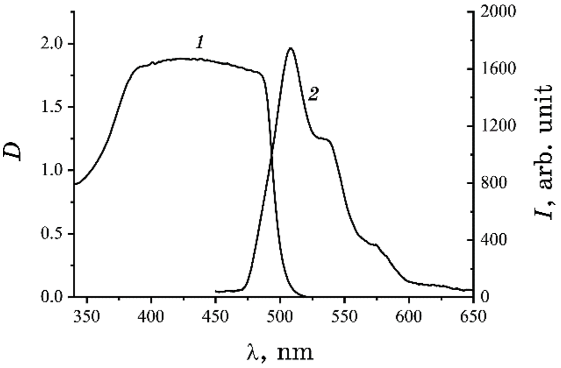

Fig. 1. Spectra of optical absorption (*1*) and fluorescence (*2*) of ethanolic solution of coumarin 7 with a concentration of 10^{-3} M.

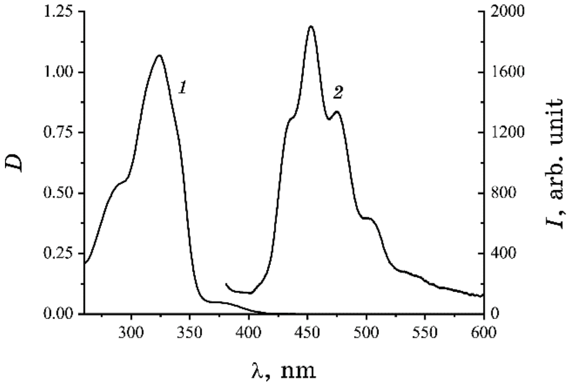

Fig. 2. Spectra of optical absorption (*1*) and fluorescence (*2*) of ethanolic solution of coumarin 4 with a concentration of 10^{-4} M.

mental study of the sensory properties of the synthesized samples of nanostructured composites based on coumarin dyes, CdTe quantum dots, and silicate matrices.

The spectra of matrices without fluorophores (polymer ethylene-vinyl acetate (EVA) with a layer of silica gel 60 as well as Aerosil A-380) obtained by us showed the practical absence of their own fluorescence at the wavelengths of the fluorescence range of coumarin dyes and quantum dots. This indicates that the fluorescence of the synthesized samples is due to the fluorescence of coumarin 4 or coumarin 7 molecules and CdTe quantum dots, and not the matrix material.

Figure 3 shows the absorption and fluorescence spectra of the synthesized composite structures with coumarin 7. As can be seen in Fig. 3 (*1*), the sample based on EVA and silica gel 60 with coumarin 7 and quantum dots of CdTe has a wide absorption band of 404–550 nm, with

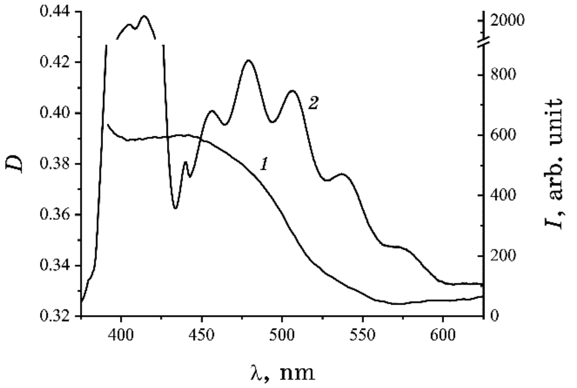

Fig. 3. The spectra of optical absorption (*1*) and fluorescence (*2*) of the sample of composite structures based on EVA and silica gel 60 with coumarin 7 and CdTe quantum dots.

a maximum of about $\lambda_{\max} = 441$ nm. After 550 nm, the absorption spectrum reaches a value of approximately $D = 0.33$, due to the scattering of light by the sample. The fluorescence spectrum of the sample (Fig. 3 (*2*)) has a band with a maximum $\lambda_{\max} = 478$ nm. The fluorescence bandwidth was $\Gamma = 118$ nm. The intense band in the range of 385–430 nm corresponds to the excitation radiation of the laser $\lambda = 405$ nm. The width of the absorption band because of the shape of the spectrum could not be determined exactly, it is approximately 80 nm. For such samples, a bathochromic (red) shift of the absorption band is observed in comparison with the ethanolic solution of coumarin 7 (Fig. 1) by 11 nm, while for the fluorescence band, a hypochromic (blue) shift of 30 nm.

Since the samples based on Aerosil A-380 with coumarin 4 were opaque due to high light scattering by Aerosil, instead of absorption spectra, fluorescence excitation spectra were measured, which generally essentially correspond to the absorption spectra of fluorescent substances [19]. Figure 4 shows the fluorescence and fluorescence excitation spectra of the synthesized composite structures with coumarin 4. The sample has a fluorescence excitation band of 310–360 nm with a maximum $\lambda_{\max} = 340$ nm (Fig. 4 (*1*)). The fluorescence excitation bandwidth was $\Gamma = 45$ nm. The fluorescence spectrum of the sample (Fig. 4 (*2*)) has a band of approximately 400–600 nm. The intense band in the region of 360–450 nm corresponds to the excitation radiation of the laser $\lambda = 405$ nm (horizontal section $I = 2168$ corresponds to the ‘upper counts’ of the device). The position of the maximum and the width of the fluorescence band are difficult to establish due to the illumination of the excitation radiation in this area. For such samples, a bathochromic shift of the fluorescence excitation band by 16 nm is observed in comparison with the absorption band in the ethanolic solution of

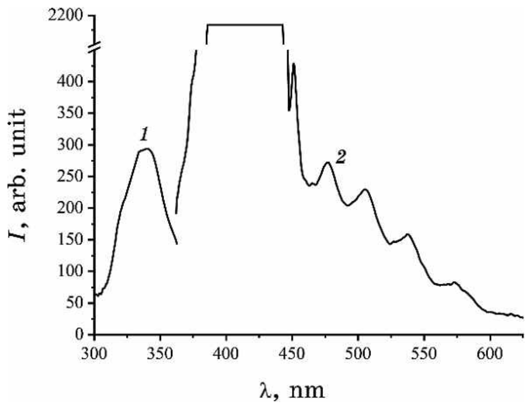

Fig. 4. The spectra of fluorescence excitation (*1*) and fluorescence (*2*) of the sample of composite structures based on Aerosil A-380 with coumarin 4.

coumarin 4 (Fig. 2).

The presence of shift of fluorescence bands of coumarin dye molecules in SiO_2 matrices (silica gel 60 and Aerosil A-380) relative to ethanol is explained by us that the medium of the matrixes has a higher polarity because the spectral behaviour of coumarin dyes depends on the polarity of the medium [20].

The study of the sensory properties of the created composite structures to ammonia and acetone was carried out, that is the fluorescence response of the samples interacting with analyte molecules in the air. The concentration of ammonia and acetone in the air was considered as the base, *i.e.*, equal to zero, because in pure air the concentrations of these VOCs were much lower than those studied. Our experiments showed the presence of an evident sensory response of samples with coumarin 7 to ammonia and with coumarin 4 to acetone (in air medium), which corresponds to a decrease in fluorescence intensity.

Figure 5 shows the fluorescence kinetics of the synthesized composite structures with coumarin 7 when they interact with ammonia molecules in the air. 500 ml of the air mixture with 5000 ppm (*i.e.*, $million^{-1}$) of ammonia was pumped in the time interval of 620–1100 seconds, and a decrease in fluorescence by 72% is observed. The cuvette with the sample was pumped with clean air in the time interval of 1100–2500 seconds, during which the fluorescence intensity of the sample was restored. Already in 1400 seconds, the fluorescence intensity was restored to 90% of the initial level. We interpret these results as follows. When air with ammonia is pumped, the process of sorption of ammonia molecules on the developed pore surface of the matrix element, silica gel 60, takes place. These molecules interact with immobilized molecules of coumarin 7 dye, re-

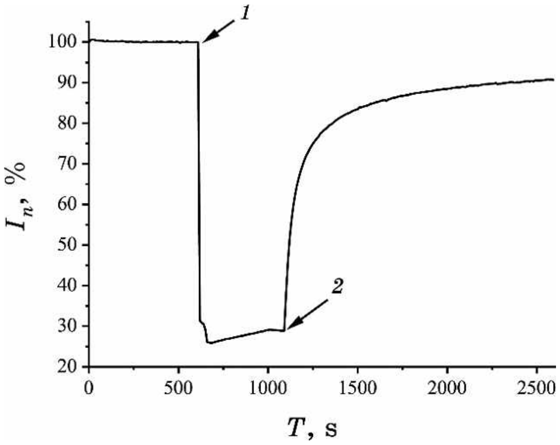

Fig. 5. The kinetics of fluorescence (normalized to 100%) of composite structures based on EVA and silica gel 60 with coumarin 7 and quantum dots of CdTe when interacting with ammonia in the concentration of 5000 ppm in air. *1*—the beginning of pumping the air mixture with ammonia; *2*—the beginning of pumping pure air.

sulting in a decrease in fluorescence intensity. This is due to the presence of a specific chemical interaction of ammonia molecules with coumarin cations and the formation of coumarin anion-ammonium cation complexes [1] that indicates a static mechanism of fluorescence quenching. The reverse process of desorption of ammonia molecules occurs during pumping with clean air, with the fluorescence signal of the sample is restored.

Figure 6 shows the kinetics of the fluorescence of the synthesized composite structures with coumarin 4 when interacting with acetone molecules in air. 1000 ml of the air mixture with 133 ppm of acetone was pumped during a time interval of 120–240 seconds, and the fluorescence was gradually decreased by approximately 2.2%. The cuvette with the sample was pumped with pure air in the time interval 240–470 seconds, and the fluorescence intensity of the sample was restored. Already after 230 seconds of the pumping, the fluorescence intensity was almost completely restored to the value of 99.8% of the initial one. We explain the mechanisms of falling and restoring the fluorescence intensity of such samples similarly: the sorption–desorption processes of acetone molecules on the pore surface of Aerosil A-380 and quenching of the fluorescence of dye molecules take place. However, the quenching of coumarin 4 fluorescence, unlike to coumarin 7, occurs due to the non-radiative deactivation of the excited state of coumarin 4 molecules by acetone molecules, the so-called dynamic quenching of fluorescence [10].

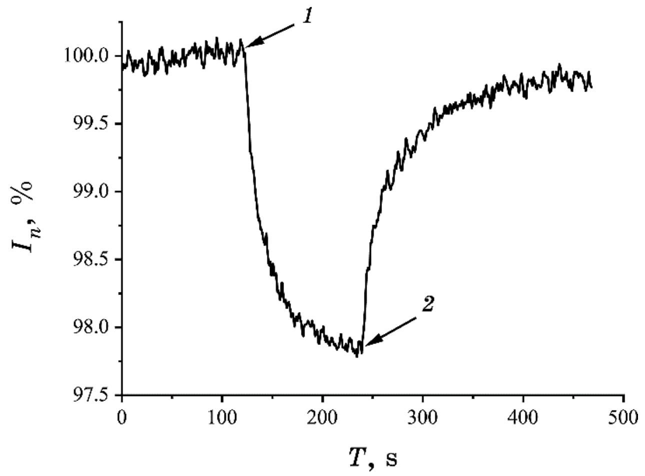

Fig. 6. The kinetics of fluorescence (normalized to 100%) of composite structures based on Aerosil A-380 with coumarin 4 when interacting with acetone in the concentration of 133 ppm in air. *1*—the beginning of pumping the air mixture with acetone; *2*—the beginning of pumping pure air.

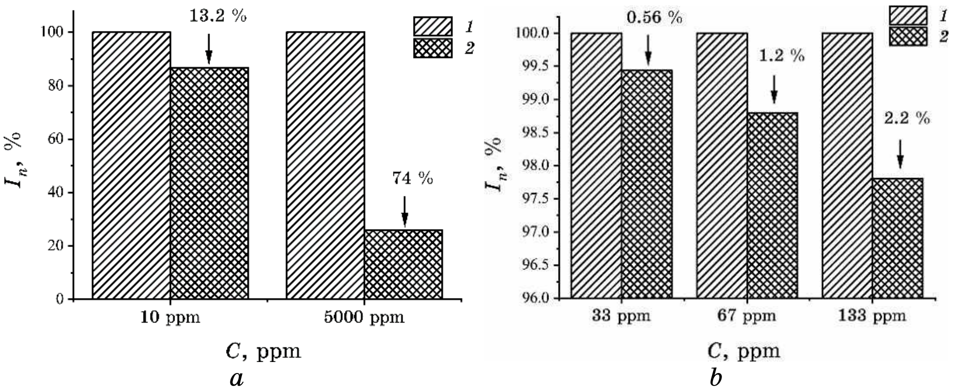

a *b*

Fig. 7. Bar charts of the fluorescent responses (normalized to 100%) of the composite structures with coumarin 7 (*a*) for ammonia concentrations of 10 ppm and 5000 ppm, and with coumarin 4 (*b*) for acetone concentrations of 33 ppm, 67 ppm, and 133 ppm. *1*—the initial fluorescence intensity of the sample; *2*—the fluorescence intensity after interaction with the analyte.

Figure 7 shows the fluorescent responses of the composite structures with coumarin 7 (Fig. 7, *a*) and coumarin 4 (Fig. 7, *b*) for different concentrations of ammonia and acetone in the air, respectively. As can be seen in Fig. 7, *a*, the response to 10 ppm of ammonia was $13.2 \pm 0.6\%$, and to 5000 ppm was $74.0 \pm 1.1\%$. The response to 33 ppm of acetone was $0.56 \pm 0.08\%$, to 67 ppm was $1.2 \pm 0.1\%$, and to 133 ppm was 2.2 ± 0.1% (Fig. 7, *b*). For both samples, the correlation of the value of the fluorescent response with the value of the concentration of analyte molecules in the air is observed.

Thus, we have shown the presence of a significant fluorescent response of the samples, as well as we demonstrated an evident correlation between the value of the fluorescence signal decrease of the samples and the change in analyte concentration in the air and the ability to restoring after ventilation. All this suggests that the composite structures created by us have a significant sensory sensitivity to ammonia molecules (composite with coumarin 7) and acetone molecules (composite with coumarin 4).

4. CONCLUSIONS

The spectral-optical properties of ethanolic solutions of fluorescent dyes of coumarin 7 and coumarin 4 as well as synthesized nanostructured composites, which include these dyes, are obtained. The presence of a significant shift of the spectral bands of coumarin dyes in the matrices of the synthesized samples in relation to the spectral bands of these dyes in ethanol has been demonstrated. This indicates a significant effect of matrix molecules on the electronic structure of the energy levels of coumarin dyes molecules. It was found that when mixing the CdTe quantum dots (fluorescence band position $\lambda_{max} = 530$ nm) with the ethanolic solution of coumarin 7 dye, the fluorescence intensity of the dye increased by 57%. This made it possible to increase the fluorescence intensity signal of the synthesized samples with coumarin 7 as well as to increase the sensory sensitivity of such samples to ammonia molecules. It has been shown that the composite structures with coumarin dyes developed by us show fluorescent sensitivity to molecules of ammonia (concentrations range 10–5000 ppm) and acetone (concentrations range 33–133 ppm) in the air. This sensitivity is due to static fluorescence quenching of QD (CdTe)—coumarin 7 complexes or dynamic fluorescence quenching of coumarin 4 molecules by molecules of the analytes.

The presence of a significant response of the synthesized by us nanostructured composites to ammonia and acetone molecules, as well as the ability to repeatedly restore the signal after aeration of samples with clean air, gives prospects for the use of these materials in portable sensors for non-invasive disease diagnosis, environmental monitoring.

REFERENCES

1. N. I. Selivanov, *Vliyanie Mezhmolekulyarnykh Vzaimodeistviy na Fotoprotsessy Zameshchennykh Akridina, Kumarina i Nil'skogo Krasnogo v Rastvorakh i Tonkikh Plenkakh* [Influence of Intermolecular Interactions on Photoprocesses of Substituted Acridine, Coumarin and Nile Red in Solutions

and Thin Films] (Authors abstract of Disser. for Cand. Chem. Sci.) (Tomsk: National Research Tomsk State University: 2015) (in Russian).
2. S. N. Shtykov and T. Yu. Rusanova, *Russ. Chem. J.*, **52**, No. 2: 92 (2008) (in Russian).
3. Yu. A. Toporova, A. O. Orlova, V. G. Maslov, A. V. Baranov, and A. V. Fedorov, *Sci. and Tech. J. of Information Technologies, Mechanics and Optics*, **63**, No. 5: 36 (2009) (in Russian).
4. T. L. Mako, J. M. Racicot, and M. Levine, *Chem. Rev.*, **119**, No. 1: 322 (2019); https://doi.org/10.1021/acs.chemrev.8b00260
5. S. Das and M. Pal, *J. Electrochem. Soc.*, **167**: 037562 (2020); https://doi.org/10.1149/1945-7111/ab67a6
6. Y. Y. Broza, X. Zhou, M. Yuan, D. Qu, Y. Zheng, R. Vishinkin, M. Khatib, W. Wu, and H. Haick, *Chem. Rev.*, **119**, No. 22: 11761 (2019); https://doi.org/10.1021/acs.chemrev.9b00437
7. V. Saasa, T. Malwela, M. Beukes, M. Mokgotho, C. P. Liu, and B. Mwakikunga, *Diagnostics*, **8**, No. 12: 1 (2018); https://doi.org/10.3390/diagnostics8010012
8. E. V. Stepanov, *Proceedings of the Prokhorov General Physics Institute*, **61**: 1 (2005) (in Russian).
9. R. M. Gadirov, L. G. Samsonova, T. N. Kopylova, N. I. Selivanov, V. P. Hilya, and V. V. Ishchenko, *Proceedings of the Higher Educational Institutions. Physics*, **56**, No. 2: 89 (2013) (in Russian).
10. V. K. Sharma, D. Mohan, and P. D. Sahare, *Spectrochim. Acta A*, **66**: 111 (2007); https://doi.org/10.1016/j.saa.2006.02.032
11. N. Cabaleiro, I. de la Calle, C. Bendicho, and I. Lavilla. *Talanta*, **129**: 113 (2014); https://doi.org/10.1016/j.talanta.2014.05.033
12. V. P. Mitsai, A. G. Misyura, S. V. Kryvets, and Ya. P. Lazorenko, *J. Nano-Electron. Phys.*, **8**, No. 4(1): 04032-1 (2016); https://doi.org/10.21272/jnep.8(4(1)).04032
13. H. Zhu, Y. Yang, K. Wu, and T. Lian, *Annu. Rev. Phys. Chem.*, **67**: 259 (2016); https://doi.org/10.1146/annurev-physchem-040215-112128
14. S. Luker and D. E. Reiter, *Semicond. Sci. Tech.*, **34**, No. 6: 063002 (2019); https://doi.org/10.1088/1361-6641/ab1c14
15. N. M. Vykhnan, O. V. Kopach, H. M. Okrepka, and Yu. B. Khalavka, *Chernivtsi University Scientific Herald: Chemistry*, **640**: 114 (2013) (in Ukrainian).
16. M. Chern, J. C. Kays, S. Bhuckory, and A. M. Dennis, *Methods Appl. Fluores*, **7**, No. 1: 012005 (2019); https://doi.org/10.1088/2050-6120/aaf6f8
17. *ISO 6144:2003, Gas Analysis—Preparation of Calibration Gas Mixtures—Static Volumetric Method*.
18. A. Bavali, P. Parvin, and S. Z. Mortazavi, *Appl. Optics*, **53**, No. 24: 5398 (2014); https://doi.org/10.1364/AO.53.005398
19. J. R. Albani, *Structure and Dynamics of Macromolecules: Absorption and Fluorescence Studies* (Elsevier Science: 2004); https://doi.org/10.1016/B978-0-444-51449-3.X5000-X
20. E. V. Seliverstova, *Vliyanie Mezhmolekulyarnykh Vzaimodeistviy na Ehlektronnyye Protsessy v Organicheskikh Nanostrukturah* [Influence of Intermolecular Interactions on Electronic Processes in Organic Nanostructures] (Thesis of Disser. for the Degree of PhD. 6D060400 – Physics) (Karaganda: Academician E. A. Buketov Karaganda University: 2013) (in Russian).

Наносистеми, наноматеріали, нанотехнології
Nanosistemi, Nanomateriali, Nanotehnologii
2021, т. 19, № 4, сс. 953–965

PACS numbers: 68.35.-p, 68.37.Hk, 81.05.Pj, 87.19.rd, 87.85.J-, 87.85.Lf, 87.85.Qr

Features of Mineralization of Hydroxyapatite on the Surface of Calcium-Silicophosphate Glass-Ceramic Materials *in vivo*

O. V. Savvova[1], O. I. Fesenko[1], O. V. Babich[2], O. A. Nikolchenko[3], H. K. Voronov[1], and Yu. O. Smyrnova[1]

[1]*O. M. Beketov National University of Urban Economy in Kharkiv,*
17, Marshal Bazhanov Str.,
UA-61002 Kharkiv, Ukraine
[2]*SRI 'Ukrainian Scientific Research Institute of Ecological Problems',*
6, Bakulin Str.,
UA-61002 Kharkiv, Ukraine
[3]*Sytenko Institute of Spine and Joint Pathology, N.A.M.S. of Ukraine,*
80, Pushkinska Str.,
UA-61024 Kharkiv, Ukraine

The features of mineralization of hydroxyapatite (HAp) on the surface of calcium-silicophosphate glass-ceramic materials *in vivo* are analysed. It is found that the implantation of biomaterials based on BS-11 and ASZ-5 bioactive glass-ceramic materials characterized by a strengthened structure and an adjustable level of resorption implements the chemical and biochemical mechanisms of formation of the apatite-like layer. The peculiarities of compositions and technologies for obtaining bioactive glass–ceramic materials for replacement of bone defects are analysed. The conditions for the formation of an apatite-like layer *in vivo* on the surface of glass-ceramic materials are established. These ones include crystallization process of fine-dispersed HAp, ensuring the reactivity of glass-ceramic materials due to destruction of them, initiation of the nucleation of non-stoichiometric HAp on the surface of materials. As determined, the stimulation of the adsorption process of proteins on the surface of the ASZ-5 and BS-11 glass-ceramic materials is realized by ensuring the values of the surface microroughness index $R_a = 2.6$ and 6.0 μm and the surface free energy of 51.5 and 74.6 MJ/m^2, respectively. For the developed glass-ceramic materials based on calcium-silicophosphate glasses, the formation of a sitallized structure under conditions of low-temperature heat treatment makes it possible to provide their operational properties close to those for bone cortical tissue ($K_{1C} = 2.44$ and 2.8 MPa·m$^{1/2}$, $HV = 7800$ and 3800 MPa, $\sigma_{\text{compr}} = 160$ MPa). This fact allows us to consider them as promising when creating implants, which can be used to replace the statically and dynamically loaded areas of bone tissue in orthopaedics and maxillofacial surgery. This one, together with the shortened periods of resorption and mineralization of bone tissue, will increase the efficiency of prosthetics by halving the rehabilitation period for patients and avoiding the necessity for repeated operations.

Проаналізовано особливості мінералізації гідроксиапатиту (ГАп) на поверхні кальцій-силікофосфатних склокристалічних матеріялів *in vivo*. Встановлено, що за імплантації біоматеріялів на основі біоактивних склокристалічних матеріялів БС-11 та АСЗ-5, які характеризуються зміцненою структурою та реґульованим рівнем резорбції, реалізується хемічний і біохемічний механізми формування апатитоподібного шару. Проаналізовано особливості складів і технології одержання біоактивних склокристалічних матеріялів для заміщення дефектів кістки. Встановлено умови формування апатитоподібного шару в умовах *in vivo* на поверхні склокристалічних матеріялів: реалізація процесу кристалізації тонкодисперсного ГАп, забезпечення реакційної здатности склокристалічних матеріялів за рахунок деструкції їх, ініціяція зародкоутворення нестехіометричного ГАп на поверхні матеріялів. Визначено, що стимулювання процесу адсорбції протеїнів на поверхні склокристалічних матеріялів реалізується за рахунок забезпечення значень показника мікрошерсткости поверхні склокристалічних матеріялів АСЗ-5 і БС-11 $R_a = 2{,}6$ і 6,0 мкм та вільної енергії поверхні 51,5 і 74,6 мДж/м^2 відповідно. Для розроблених склокристалічних матеріялів на основі кальцій-силікофосфатних стекол формування ситалізованої структури в умовах низькотемпературного термічного оброблення уможливлює забезпечити їхні експлуатаційні властивості, які наближені до таких властивостей для кісткової кортикальної тканини ($K_{1C} = 2{,}44$ та 2,8 МПа·м$^{1/2}$, $HV = 7800$ і 3800 МПа, $\sigma_{\text{стиск}} = 160$ МПа), дає змогу вважати їх перспективними для створення імплантатів, що можуть бути використані для заміни статично та динамічно навантажених ділянок кісткової тканини у ортопедії та щелепно-лицевій хірургії. Це разом зі скороченими строками резорбції та мінералізації кісткової тканини дасть змогу підвищити ефективність протезування за рахунок скорочення вдвічі періоду реабілітації пацієнтів і виключення повторних операцій.

Key words: glass-ceramic materials, biomaterials, *in vivo*, apatite-like layer, bone tissue.

Ключові слова: склокристалічні матеріяли, біоматеріяли, *in vivo,* апатитоподібний шар, кісткова тканина.

(Received 11 February, 2021)

1. INTRODUCTION

The development of medical science and technology requires the creation of materials for obtaining bone tissue substitutes of a new generation, intended for long-term functioning in the body [1]. Materials for the manufacture of implants must ensure biocompatibility for a long time, namely, do not change the physicochemical properties, do not cause chronic inflammation, and do not show a carcinogenic effect, not subject to calcification. However, it should be emphasized that, along with the ability to calcify, mineralization of calcium-containing compounds plays an important role in the restoration of the function of bone tissues and their formation [2]. Therefore, to ensure the biocompatibility of the implant, it is important to correct these processes, which are similar in their mechanism. The effectiveness of the functioning of bone endoprostheses is ensured by the formation of a strong adhesion layer in the implant–bone system, which is realized due to the mineralization of apatite-like structures. To achieve the latter, it is important to take into account the theoretical approach to substantiating the calcification of biomaterials.

The primary stages of calcification, in the cellular approach, are associated either with the presence of already dead cells (as in the case of treated biological tissues), or with the death of recipient cells that adhere to the biomaterial. At present, a theory based on the formation of calcium–phospholipid–phosphate complexes is being widely tested, the reason for the formation of which is the affinity of acidic phospholipids for calcium ions. It is envisaged that the presence of such complexes in metastable solutions of calcium and phosphates provokes the precipitation of insoluble crystals of hydroxyapatite (HAp) [3].

The concentration theory allows one to take into account and evaluate the role of the concentration of calcium and phosphate ions in the intercellular fluid. Known physicochemical theories associate the formation of heterogeneous nucleation centres of HAp crystals with the macromolecular stereoconfiguration of collagen or consider the transformation of crystalline HAp precursors such as amorphous calcium phosphate (ACP) [3]. The concentration theory is clearly realized in the implantation of biomaterials based on bioactive ceramic [4] and glass-ceramic materials characterized by a strengthened structure and an adjustable level of resorption [5].

The complexity of the simultaneous providing with high strength of the implant–bone bond for a short time depends primarily on the bioactivity of the glass material and its ability to form a thin apatite-like layer on its surface [6, 7]. This can be achieved by heterogeneous nucleation of apatite crystals by the presence of Si–OH, Ti–OH, Zr–OH structural elements on the surface of materials. At the stage of collagen fibre synthesis and at the initial stages of bone biomineralization, silicon is associated with calcium, initiating the process of deposition of bone minerals, and is an important ‘transitional’ element in the formation and development of cartilage and bone structures.

It should be noted that the identification of mineralization products is important from the point of view of the fact that the crystal-chemical structure of the resulting hydroxyapatite also depends on the composition of the physiological medium, because during the growth the crystals capture impurities of cations from the medium and form nonstoichiometric solid solutions. Therefore, it is worth talking about the appearance of apatite-like structures on the surface of calcium phosphate biomaterials, rather than pure hydroxyapatite. Obviously, these structures are close to bone ones, since the chemical composition of bone hydroxyapatite somewhat differs from the stoichiometric composition of natural and artificial analogues in the Ca:P ratio, as well as in the presence of ion impurities, the total content of which may exceed 5%.

The use of bioactive resorption glass-ceramic materials [8], which are close to bone tissue in chemical and phase composition, as bone tissue substitutes can significantly reduce the time of their fusion with bone tissue. However, the high level of resorption of such materials can lead to the formation of an inhomogeneous, fragile bonding layer between the implant and the bone, especially under stress. Therefore, it is a detailed study of the mineralization process of bioactive glass-ceramic materials during the entire *in vivo* period that will make it possible to assess the effectiveness of the use of implants with different resorption periods.

2. EXPERIMENTAL

2.1. AIM Setting and Research Methodology

The aim of this work is to determine the features of the mineralization of hydroxyapatite on the surface of calcium silicophosphate glass-ceramic materials *in vivo*.

The phase composition of the materials was studied using x-ray phase (DRON-3M diffractometer) and petrographic (NU-2E optical microscope) methods of analysis.

The structure of the surface layer of glass-ceramic materials (GCM), which was removed after implantation, was investigated using x-ray spectral analysis (scanning electron microscope RES Tesla 3 LMU with a resolution of 1 nm using an Oxford X-max 80 mm energy dispersive spectrometer).

Evaluation of the hydrolytic destruction of the developed materials was carried out in non-enzymatic media using the extreme (*ES*) and simulated solutions (*SS*) tests according to ISO 10993-14-2011 by weight loss in the corresponding B_{ES} and B_{SS} solutions.

The surface free energy (SFE) value of the experimental materials was determined by the Owens–Wendt–Rabel–Kaelble method, according to which the surface energy of a solid includes two components: dispersive and polar ones. This method provides for the calculation of the SFE based on the contact angle between the material surface and various liquids, followed by the calculation of its two surface free energy components using the Mathcad computer software. To improve the accuracy of the obtained values, six liquids with known polar and non-polar components of surface tension were used. Surface microrelief was determined as the arithmetic mean of the deviation of the surface profile (R_a) using a Surtronic 3+ profilometer.

Vickers hardness (HV) and fracture toughness index (fracture viscosity, K_{1C}) were determined by indenting the Vickers pyramid under the load of 5000 g on it for 10 measurements using a TMV-1000 device. Compressive strength (σ_{compr} [MPa]) was determined according to GOST 8462-85.

Histological analysis of bone tissue regeneration was performed after the GCM-based implant was inserted into the distal metaphysis of the femur of rats on the first, 7th, 14th and 28th days after implantation. After each term, the activity of alkaline phosphatase was determined by the kinetic method in the serum of rats. The studies were carried out on the base of the laboratory of connective tissue morphology of the Sytenko Institute of Spine and Joint Pathology N.A.M.S. of Ukraine.

2.2. Peculiarities of Compositions and Technology of Bioactive Glass-Ceramic Materials

To study the peculiarities of the formation of an apatite-like layer on the surface of bioactive glass-ceramic materials (GCM) *in vivo*, materials differing in structure and resorption capacity were chosen BS-11 [9] and ASZ-5 [10].

To obtain BS-11 and ASZ-5 GCM, the glasses based on calcium silicophosphate systems with SiO_2 content in the range of 47–55 wt.%, the degree of connectivity of the silicon-oxygen framework (f_{Si}) 0.28 and the CaO/P_2O_5 ratio 1.7–4.0 were synthesized (Table 1). This is to ensure their biological activity by finely dispersed crystallization of HAp and initiation of its nucleation on the surface of materials *in vivo*. The glasses contain Al_2O_3 and B_2O_3 to provide structural strength, which determines their ability to resorption and mechanical loads.

ZnO, ZrO_2, TiO_2, CaF_2 and CeO_2 as nucleation catalysts were added into the AS-5 glass to control the apatite formation processes. To approximate the glass composition to the composition of natural bone tissue in the process of mineralization, the trace elements (Cu_2O, V_2O_5, MoO_3, CoO, SrO, La_2O_3) of 0.1 wt.% were introduced.

TABLE 1. Generalized chemical composition of glasses (in [wt.%]) and the ratio of phase-forming components.

Marking of Glass	Glass-Forming Components		Phase-Forming Components		Modifiers			Doping Constituents
	SiO_2	$Al_2O_3 + B_2O_3$	$CaO + CaF_2 + P_2O_5$	CaO/P_2O_5	R_2O	RO	RO_2	
BS-11	55.0	10.0	25.0	4.0	10.0	—	—	—
AS-5	47.0	6.0	29.4	1.7	10.5	2.6	4.4	0.1

AS-5 and BS-11 experimental glasses were obtained by glass technology: melted under identical conditions at temperatures of 1523 and 1723 K in corundum crucibles, followed by the cooling on a metal plate. To obtain GCM by ceramic technology, there were used powders of model glasses milled to a residue on sieve No. 063 of no more than 5%. The samples were prepared by the method of semi-dry pressing, formed in the form of cylinders with a diameter of 4 mm and a height of 10 mm using a 2% solution of carboxymethyl cellulose as a temporary binder.

To increase the fracture toughness of the GCM, zirconia stabilized with yttrium oxide was additionally introduced into the AS-5 glass composition. Such a sample of GCM was marked with ASZ-5 and was used for further research. The transformation strengthening of the glass matrix was carried out due to the controlled transition of tetragonal ZrO_2 to the monoclinic phase, which is accompanied by volume increase of 3 vol.% [11, 12].

Heat treatment of materials was carried out at 1023 K during 30 min for ASZ-5 and at 1323 K during 30 min for BS-11. After heat treatment, the GCMs were characterized by insignificant porosity (up to 10%), which is a consequence of sintering of narrow-fraction glass powders with a particle size of ≤ 60 μm.

2.3. Characterization of Bioactive Glass-Ceramic Materials

Glass-ceramic materials are characterized by a fine-dispersed volume-crystallized structure with a HAp content of 55–60 vol.% (Table 2). Providing the sitallization process of the initial glasses under the conditions of low-temperature short-time heat treatment makes it possible to form a high-strength structure of GCM, which is capable of withstanding variable dynamic loads. Along with this, in the glass structure, in addition to the presence of calcium phosphates, sybotaxic groups of future apatite-like crystalline phases

TABLE 2. Characteristics of the GCM composition, structure and destruction.

Indicators		Marking of Samples	
		BS-11	ASZ-5
The crystalline phase content (HAp), vol.%		55.0	60.0
The degree of the silicon–oxygen framework bonding (f_{Si})		0.28	0.28
Roughness (R_a), μm		6.0	2.0
Surface free energy, mJ/m^2		51.50	74.59
Material destruction, wt.% (ISO 10993-14-2001)	B_{ES}	0.20	0.44
	B_{SS}	2.00	2.96

are formed, which are potential nucleators during the formation of a mineralized layer *in vivo* on the implant surface.

Stimulation of the protein adsorption process on the surface of the GCM is realized by ensuring the values of the structural strength index $f_{\mathrm{Si}} = 0.28$ and the surface microroughness indicators (Table 2). This will provide an increase in the SFE index *in vivo* by increasing the proportion of the electrostatic component of the chemical bond in the glass.

The ASZ-5 GCM is characterized by the highest values of weight loss, despite its location in a low-silica area. With a simultaneously higher HAp content, this material, in comparison with BS-11, is characterized by a higher reactivity and ability to accelerate the formation of an apatite-like layer *in vivo*. These assumptions are the basis for studies on the features of nucleation and growth of non-stoichiometric hydroxyapatite (*n*HAp) on the surface of calcium silicophosphate glass-ceramic materials *in vivo*.

3. RESULTS AND DISCUSSION

3.1. Hydration and Nucleation of Apatite on the Surface of Bioactive GCM *in vivo*

In the first hours of *in vivo* contact, hydrolysis and condensation processes occur on the GCM surface. The materials are hydrolysed with the formation of a gel-like silica-rich layer saturated with OH^- groups. The structural elements ≡Si–OH provide areas for heterogeneous nucleation of apatite crystals.

The study of the surface morphology of the implant material and bone tissue showed that, for the BS-11 GCM on the 1st day of exposure, the hydrolysis process with the formation of ≡Si–OH bonds and their subsequent polycondensation $\equiv\mathrm{Si{-}OH} + \mathrm{HO{-}Si}\equiv \rightarrow \equiv\mathrm{Si{-}O{-}}$

Si≡ + H_2O are observed. The result is the formation of a thin gel-like layer of silicic acid in the form of nanoinhomogeneities over the entire surface of the material under study and individualized spheres of amorphous calcium phosphate (ACP) (Fig. 1, *a* I, II) as a precursor of *n*HAp crystals. For the ASZ-5 GCM, against the general background of spheres of the silica-gel layer (Fig. 1, *b* I), single crystals, which have a plate-like shape, are observed (Fig. 1, *b* II). A manifestation of the intensification of the nucleation process of *n*HAp crystals is a change in the parameters of the crystal lattice of apatite-like structures and the morphology of crystals, which change during the growth of crystals.

At the initial stages of growth (7–14 days), both materials under study are characterized by the formation of solid solutions with a structure that is very different from the structure of *n*HAp. How-

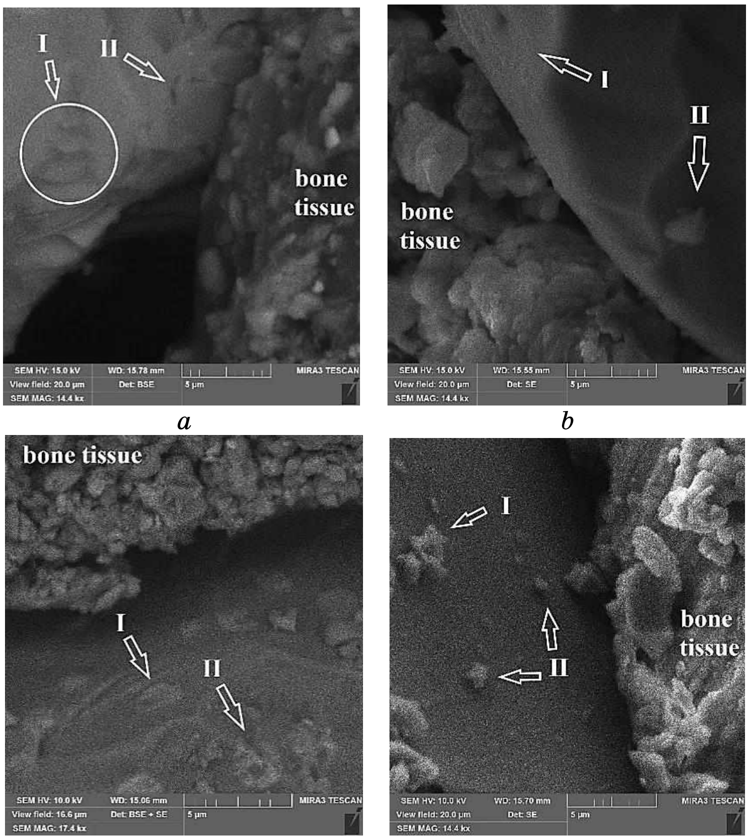

a *b*

c *d*

Fig. 1. Surface structure of bioactive GCM: BS-11 (*a*); ASZ-5 (*b*) after 1 day of exposure; BS-11 (*c*); ASZ-5 (*d*) after 7 days of exposure.

ever, the growth of crystals for the experimental GCM, as well as the mechanism of nucleation, is significantly different.

Thus, on the 7th day, BS-11 GCM is still characterized by the presence of a silica-gel layer and an accumulation of nanoinhomogeneities, which form flat (Fig. 1, *c* I) and convex spheres (Fig. 1, *c* II). A decrease in the size of inhomogeneities and an increase in their number indicate the formation of a significant number of crystallization nuclei. For ASZ-5 GCM, during the mentioned period, the simultaneous presence of a silica-gel layer and platy crystals (Fig. 1, *d* I) is observed; they form aggregates of different sizes (Fig. 1, *d* II).

3.2 Growth of Crystals on the Surface of Bioactive GCM *in vivo*

After 14 days of implantation, the BS-11 GCM is a multiphase system, which consists of individual spherical and platy crystals ranging in size from 0.5 to 5 μm (Fig. 2, *a* I) and their clusters of about 10 μm, which form a single crystalline block. The presence of a significant amount of spherulites is evidence of the formation of amorphous calcium phosphate (Fig. 2, *a* II), which is a precursor of the formation of native bone.

For the ASZ-5 GCM, inhomogeneities are represented by spherulites, which form ridges and spalls (Fig. 2, *b* I). This process is accompanied by a phase rearrangement of ACP, followed by levelling of the surface and the formation of a layer-by-layer structure of the material with the presence of platy crystals of *n*HAp (Fig. 2, *b* II).

After 28 days of implantation, the formation of *n*HAp aggregates is observed in the structure of the BS-11 and ASZ-5 GCM implants (Fig. 2, *c*, *d* I), which are similar to crystals for mature lamellar bone (Fig. 2, *c*, *d* II). At the implant–bone interface, it is observed the formation of a transition layer containing, like the implant material, crystals of the platy structure of carbonate hydroxyapatite (CHAp). This is due to the incorporation of carbonate ions into the apatite lattice, which affects the mineralization process.

The intensification of nucleation for the ASZ-5 GCM makes it possible to form CHAp on their surface even on the 28th day *in vivo*. They are crystals from prismatic to acicular of a hexagonal syngony, assembled into aggregates (Fig. 2, *d* II). Crystals of CHAp are present in the form of plates ranging in size from 50×20 nm to 25×(2–5) nm, which are oriented in a certain way with respect to the axis of collagen fibres.

3.3. Mineralization of Bioactive GCM *in vivo*

For experimental GCM, due to an increase in the calcium concentra-

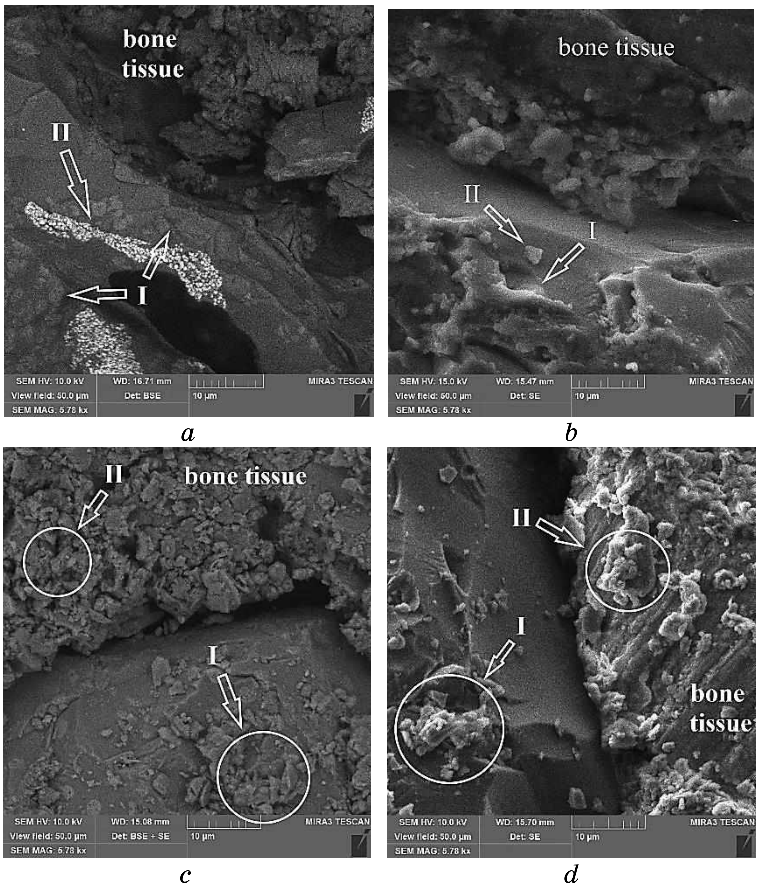

Fig. 2. Surface structure of bioactive GCM: BS-11 (*a*); ASZ-5 (*b*) after 14 days of exposure; BS-11 (*c*); ASZ-5 (*d*) after 28 days of exposure.

tion and accompanying factors in the environment, the process of appearance of CHAp crystals around the implant (osteoinduction) is 'triggered'.

The confirmation of the fact that, after the formation of the bioactive GCM–collagen bond, osteoblasts mineralize the osteoid area formed by the synthesis and secretion of matrix bubbles, is the appearance of an alkaline phosphate phase in high concentrations. The microenvironment inside the matrix bubbles promotes the formation of *n*HAp crystals.

Thus, according to the results of biochemical analysis of the blood serum of rats after implantation of the BS-11 and ASZ-5 GCM samples, the dynamics of alkaline phosphatase activity was found in accordance with the stages of bone tissue regeneration of the implants:

on the 7th day, 411.80 ± 27.60 U/L; on the 14th day, 952.50 ± 63.30 U/L; on the 30th day, 828.00 ± 98.60 U/L. It was established that, on the 7th and 14th days, the activity of alkaline phosphatase increases that indicates its release by osteoblasts during bone formation. On the 30th day, a slowdown in this process shows the gradual completion of the process of bone tissue remodelling.

Mineralization of new bone tissue, as well as its growth (osteoconduction), on the surface of GCM-based implants is possible, when a significant surface area of contact between the biological fluids and the implant is provided, that is, with a sufficient porosity ($\geq 30\%$) of the latter.

Even on the 30th day of implantation, microscopically, the area of removal of the pin on histopreparations of animals with an implant based on the BS-11 GCM was represented by a cavity, on the perimeter of which mainly newly formed trabeculae from coarse fibrous and lamellar bone tissue, areas of fibroreticulate tissue of an osteogenic nature and centres of dense connective tissue were determined (Fig. 3, *a*). In the bone tissue that forms the cavity paries for a given period, even in the cortical part, there is lamellar bone tissue, which has a significant density of osteocytes in narrow lacunae that surround the intercellular matrix. The boundary between the regenerate and the maternal bone is clearly defined.

30 days after the operation, the formation of lamellar bone tissue, the trabeculae of which were directed along the surface of the injected material, was noted around the site of implantation of the ASZ-5 GCM. It was on this basis the newly formed bone could be distinguished from the maternal one. The reorganization of the bone regenerate is evidenced by the presence of clastic structures of osteons, irregular cement lines (Fig. 3, *b*).

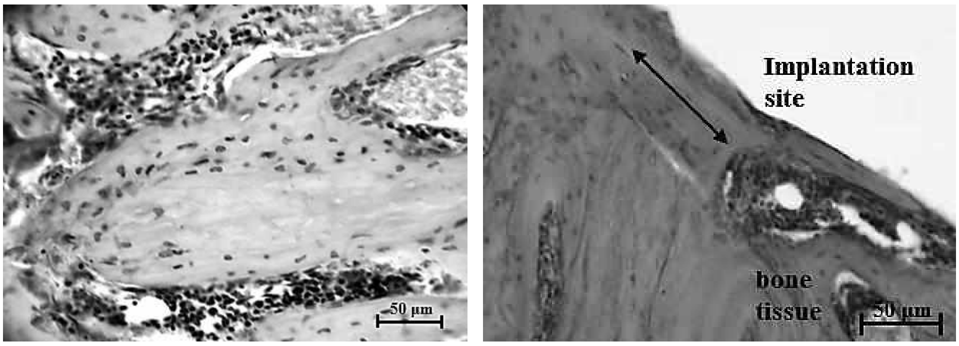

a *b*

Fig. 3. Fragment of the distal metaphysis of the rat femur after injection of BS-11 (*a*) and ASZ-5 (*b*) samples.

With the use of the developed materials as implants, regeneration has a more favourable course, as evidenced by the restoration of the bone structure on the 30th day of observation, when a part of the regenerate (50% for BS-11 GCM and 70% for ASZ-5 GCM) in the defect is represented by a mature lamellar bone.

Thus, taking into account the mechanical properties of BS-11 and ASZ-5 GCM, which are close to those properties for bone cortical tissue ($K_{1C} = 2.44$ and 2.8 MPa·m$^{1/2}$, $HV = 7800$ and 3800 MPa, $\sigma_{\text{compr}} = 160$ MPa), implants based on them can be used to replace the statically and dynamically loaded areas of bone tissue in orthopaedics and maxillofacial surgery.

The introduction of implants based on bioactive glass-ceramic materials BS-11 and AC3-5 with reduced terms of resorption and mineralization of bone tissue will increase the efficiency of prosthetics by halving the rehabilitation period for patients and eliminating repeated operations.

4. CONCLUSIONS

The regularities of mineralization of calcium-containing compounds during the formation of bone tissue on the surface of bioactive glass-ceramic materials with different resorption periods have been established. It has been determined that the implantation of biomaterials based on bioactive glass-ceramic materials characterized by a strengthened structure and an adjustable level of resorption implements the chemical and biochemical mechanisms of the formation of an apatite-like layer.

The features of the compositions and technologies for obtaining bioactive glass-ceramic materials for replacement of bone defects were analysed. It has been established that the provision of biological activity along with high strength of glass-ceramic materials can be realized by their sitallization and the formation of HAp crystals under conditions of low-temperature one-stage short-time heat treatment of glasses of calcium silicophosphate systems characterized by a SiO_2 content of 45–55 wt.%, $f_{\text{Si}} = 0.28$ and the ratio $CaO/P_2O_5 = 1.7$–4.0.

The conditions for the formation of an apatite-like layer *in vivo* on the surface of the GCM were analysed. These ones include crystallization process of finely dispersed HAp, ensuring the reactivity of the GCM due to their destruction, and initiation of the nucleation of nHAp on the surface of materials.

It was determined that the stimulation of the adsorption process of protein on the surface of the GCM is realized by providing the values of the surface microroughness index for ASZ-5 and BS-11 GCM $R_a = 2.6$ and 6 μm and SFE 51.5 and 74.6 MJ/m^2, respectively.

The features of hydration and nucleation of HAp on the surface of bioactive GCM *in vivo* were established, which consist in the hydrolysis process with the formation of ≡Si−OH bonds, their polycondensation and the formation of a thin gel-like layer of silicic acid in the form of nanoinhomogeneities and individualized spheres and ACP plates (1 day) and aggregates (7 days), forming ridges with the subsequent layer-by-layer structure of the material with the presence of lamellar crystals of *n*HAp (14 days), which are recrystallized into crystals of CHAp, oriented with respect to the axis of collagen fibres (28 days), followed by the formation of the bioactive GCM−collagen bond.

The activity of osteoblasts, which mineralize the osteoid area around the implant based on bioactive GCM, is determined by the activity of alkaline phosphatase. It is confirmed the formation of mature lamellar bone tissue, when using the developed bioactive glass-ceramic materials and the expediency of their use as biocompatible materials for bone tissue regeneration within one month.

REFERENCES

1. D. D. Kiradziyska and R. D. Mantcheva, *Folia Med.*, **61**, No. 1: 34 (2019); doi:10.2478/folmed-2018-0038
2. H. Owara, K. Hoshi, and N. Amizuka, *J. Oral Biosci.*, **50**, No. 1: 1 (2008); https://doi.org/10.1016/S1349-0079(08)80014-X
3. V. I. Sevast'yanov, *Biosovmestimost'* [Biocompatibility] (Moscow: IC VNIIGS: 1999) (in Russian).
4. W. Elshahawy, *Advances in Ceramics—Electric and Magnetic Ceramics, Bioceramics, Ceramics and Environment. Ch. Biocompatibility* (Ed. C. Sikalidis) (Rijeka, Croatia: InTech: 2011); doi:10.5772/18475
5. Ch. Sato, D. Yamazato, M. Sato, H. Takeshima, N. Memtily, Y. Hatano, T. Tsukuba, and E. Sakai, *Sci. Rep.*, **9**: 1 (2019); doi:10.1038/s41598-019-43608-6
6. K. Ravindranadh, *Int. J. Chem. Sci*, **14**, No. 3: 1339 (2016).
7. O. V. Savvova and O. I. Fesenko, *Nanosistemi, Nanomateriali, Nanotehnologii*, **15**, No. 4: 649 (2017) (in Ukrainian); https://doi.org/10.15407/nnn.15.04.0649
8. O. V. Savvova, O. V. Babich, and G.N. Shadrina, *Functional Materials*, **21**, No. 4: 421 (2014); http://dx.doi.org/10.15407/fm21.04.421
9. O. Savvova, O. Babich, M. Kuriakin, A. Grivtsova, and V. Topchiy, *Functional Materials*, **24**, No. 2: 109 (2017); https://doi.org/10.15407/fm24.02.311
10. O. V. Savvova, V. M. Shimon, O. V. Babich, and M. V. Shimon, *Functional Materials*, **27**, No. 4: 767 (2020); https://doi.org/10.15407/fm27.04.767
11. C. C. Barry, *Ceramic Materials: Science and Engineering* (Ed. Norton M. Grant) (Berlin: Springer: 2007).
12. V. V. Lashneva, A. V. Shevchenko, and E. V. Dudnik, *Glass and Ceramics*, **66**, Nos. 3–4: 140 (2009); https://doi.org/10.1007/s10717-009-9148-0

Наносистеми, наноматеріали, нанотехнології
Nanosistemi, Nanomateriali, Nanotehnologii
2021, т. 19, № 4, сс. 967–980

PACS numbers: 28.52.Fa, 42.62.Be, 61.66.-f, 71.20.Nr, 73.20.-r, 73.61.-r, 75.47.-m

Synthesis, Structure and Biomedical Application of Nanosize Composites Based on Oxide Semiconductor and Metal (Review)

M. Zahornyi[1], O. Lavrynenko[1], N. Tyschenko[1], M. Skoryk[2],
A. Kasumov[1], O. Kornienko[1], and A. Ievtushenko[1]

[1]I. M. Frantsevich Institute for Problems of Materials Science, N.A.S. of Ukraine,
3, Academician Krzhizhanovsky Str.,
UA-03142 Kyiv, Ukraine
[2]'NanoMedTech' LLC,
68, Antonovych Str.,
UA-03680 Kyiv, Ukraine

Today, nanocomposites based on magnetite (Fe_3O_4), zinc oxide (ZnO), titanium oxide (TiO_2) doped with metal cations are widely used to create new kinds of biocompatible materials, which are characterized by unique complexes of physical-chemical properties. The semiconducting-nanoparticles' coating by metals leads to their stabilization in corrosive biological media and affects their electrical, magnetic, catalytic, and plasmonic properties too. The achievements during recent years in the field of producing composites based on nanosize particles of different nature are demonstrated in a given review article. The basic methods for materials' preparation, properties, and the possible fields of their application are summarized.

Сьогодні нанокомпозити на основі магнетиту (Fe_3O_4), оксиду Цинку (ZnO), оксиду Титану (TiO_2), леґованих катіонами металів, широко використовуються для створення нових видів біосумісних матеріялів, що характеризуються унікальними комплексами фізико-хемічних властивостей. Покриття напівпровідникових наночастинок металами приводить до стабілізації їх у корозійних біологічних середовищах і впливає також на їхні електричні, магнетні, каталітичні та плазмонні властивості. Досягнення останніх років у галузі виробництва композитів на основі нанорозмірних частинок різної природи продемонстровано в даній оглядовій статті. Підсумовано основні методи підготовки матеріялів, властивості та можливі сфери застосування їх.

Key words: Fe_3O_4, ZnO, TiO_2, nanocomposites, nanoparticles, structure, conductivity, bactericidal action.

Ключові слова: Fe_3O_4, ZnO, TiO_2, нанокомпозити, наночастинки, структура, електропровідність, бактерицидність.

(Received 15 December, 2020)

1. INTRODUCTION

Nowadays, it will not be an exaggeration to attribute the spread of viral infections and ensure the biological safety of the population to the global problems of the XXI century. According to statistics, every year, 15 million people die in the world. Viral infections have a division into new (emergent) and secondary (re-emergent). The second type includes avian influenza viruses (A (H5N1)) (1997), A (H9N2) (1999), A (H7N7) (2003), A (H7N3) (2004), A (H7N9) A (H10N8) (2013), including pandemic virus A (H1N1) pdm09 (2009), coronaviruses (SARS viruses, 2002, Middle Eastern respiratory syndrome MERS-CoV, 2012), *etc*. The urgency of the research topic is due to the need to develop the latest effective means of preventing the spread of viral pathogens that can lead to epidemics and pandemics.

Functional nanocomposites based on metal oxides as TiO_2, ZnO, and Fe_3O_4 doped with noble metals and rare-earth elements (REE) can be a perspective material for the new kind of bioactive photocatalysts creation, whereas, the presence of REE in the structure of the zinc and titanium oxides enhances their photocatalytic activity. The inclusion of noble metal cations in the crystal lattice of iron oxides enhances their optical properties [1–2]. In addition, effect of UV irradiation on metal oxide catalysts promotes to appearance their photobactericidal activity [1–10].

This paper presents the composite nanomaterials for the development of novel water purification technologies. The unique surface, optical, and catalytic properties of nanomaterials based on oxide nanoparticles of different nature are present to the wastewater treatment. The aim is to analyse the state-of-the-art of the given rapidly developed research area.

2. METHODS OF PREPARATION AND PROPERTIES OF COMPOSITES WITH TiO_2 NANOPARTICLES

In the past 10 years, TiO_2 nanopowder through photocatalytic activity, chemical resistance and non-toxic can be used as an effective agent for the treatment of organic and inorganic substances, pathogens of various types in the environment [7–10]. The unique properties of TiO_2, especially nanoscale one, used to address important energy and environmental issues have caused the recent emergence of large scientific works on the synthesis and study of its antivirus properties and then search for ways of its practical application The antiviral activity of TiO_2 anatase nanoparticles against human adenovirus 5 serotypes was between 45% and 95% dependence on particles size [8].

The authors [1–7] note that the doping by metal (rare earth) elements allows shifting to the visible region, but the photocatalytic activity may decrease, especially in the UV range. For the electronic interaction, nitrogen is good because of electrons can pass for the dopant of the orbitals 2*p* or 3*p* to the 3*d* orbital Ti, and the width of the forbidden band decreases. The photocatalytic activity decrease of doped TiO_2 powders in the visible region, especially in the polluted environment is an urgent problem to solve [10–17].

TiO_2 powders doped with Ag, Fe enhance the photocatalytic and bactericidal activities [20–23]. For example, Ag concentration from 2.46 to 6.0 wt.% showed increasing of bacteriophage virus inactivation rate by 7 times. Therefore, the duration of the disinfection process reduced from 5 to 0.75 min [20]. Der-Shing Lee and Yu-Won Chen have shown the optimum Ag loading (2 wt.%) for the excellent methylene blue destruction under UV-light irradiation [24].

The bactericidal effect on the bacillus Kochi has been studied using TiO_2–Ag–SiO_2 photocatalyst [23]. The synthesized composite characterized by a higher surface area of 164 $m^2 \cdot g^{-1}$ in comparison with P25. Thus, the ability to inactivate composite photocatalyst occurs over a wide spectral range of UV irradiation with an intensity 2.5 mV cm^{-2}. However, the high absorbance of visible light does not always increase the photocatalytic activity. Sometimes, the cation doping leads to a certain number of defects in TiO_2, which can act as centres for the recombination of charges.

Nevertheless, this can be avoided if after doping the photocatalyst is annealed additionally. For example, the annealing of TiO_2–Co photocatalyst at 100, 400, 600, and 800°C for 180 min resulted in 30, 50, 90, and 60% photodestruction of 2-chlorophenol, respectively [25]. Thus, the annealing temperature for doped anatase (500–600°C) increases the crystallinity and reduces the recombination of electron–hole pairs.

The presence of Ti^{3+} defects for the synthesized sample could be the reason for bandgap decrease in this semiconductor to 2.75 eV and growth of MO (methyl orange) anode oxidation currents under UV irradiation at high scan rates (above 50 mV/s) and potentials below 500 mV (SCE) comparing with standard samples [15]. The photoelectrocatalytic activity of samples is defined by the dispersity and form nanoparticles.

Thus, the photocatalytic degradation is an efficient and economical method that attracted increasing attention [20–29]. This is because it is particularly useful for cleaning biologically toxic or nondegradable materials such as aromatics, pesticides, petroleum constituents, and volatile organic compounds in wastewater. The contaminant materials are converted largely into stable inorganic compounds such as water, carbon dioxide, and salts, *i.e.*, they undergo mineralization. Additionally, other features such as morphological architecture, the nature of catalyst, and surface properties affecting photocatalysis will be considered when designing a stable and efficient catalyst material.

3. NANOMAGNETITE DOPED WITH NOBLE METALS

Core & shell type nanocomposites are attractive to practical application in biological and medical studies due to the combination of their useful physical-chemical properties such as optical (plasmonic), (super)paramagnetic, catalytic, accompanied with biocompatibility as well.

3.1. Typical Synthesis Methods to Obtain Core and Shell Type Nanocomposites

Generically, the obtaining of core and shell type nanocomposites based on ferromagnetic cores covered with precious (noble) metal shells includes the synthesis of iron oxides nanoparticles and the following formation of noble metal shell on their surface [30]. Nowadays, core & shell type nanocomposites are usually formed *via* as follow:

1) coprecipitation of ferric and ferrous salts in weak-alkaline water dispersion medium and reduction of noble metal shells on their surface [31];

2) microemulsion method [32, 33];

3) separate sedimentation of the nucleating seeds (magnetite and gold) and formation of corresponding composites using organic substance [34].

Less commonly applied methods are closely connected with the x-ray emission [35], laser ablation [36], sonochemical reaction [37], ‘wet’ chemistry [38], and photochemical reduction [39].

According to published data, the process of the formation of cores and shells is possible in two phases system (microemulsion method), as well as in water [38] or organic medium only [39]. Recently, the combined method including the formation of ferromagnetic core in organic medium and formation of noble metal shell — in water was proposed [40].

The carrying out of the surface separated reductive–oxidative reaction on the steel–solutions of noble metals interface may be referred to alternative synthesis procedure to obtain core and shell type nanoparticles [41]. In the first stage of the process, Fe(II)–Fe(III) layered double hydroxides (LDHs) are formed on the steel surface contacting with distilled water in the open-air system. Taking into account strong reductive properties of Fe(II)–Fe(III) LDHs, their following contact with water medium containing noble metal aqua forms leads to phase transformation of LDH into magnetite particles accompanied with reduction of precious metals on their surface or it leads to the inclusion of Ag, Au, Pt or Pd cations into the crystal lattice of magnetite. The concentration of noble metals in the initial solutions influences degree of a core covering and the thickness of the shell at all. The main advantages of the procedure lie in the simplicity of the method, the absence of necessity to use superficially active substances (SAS), various reducing agents, and high concentrated ferric–ferrous solutions to form core particles as well.

To obtain ferromagnetic cores, it is usually applied co-precipitation in the water medium in the presence of inorganic ferrous and ferric salts and base solution NaOH or NH_4OH under standard conditions [42] or in the nitrogen atmosphere by the addition of a reducing agent, for example, sodium citrate [43]. In addition, the reductant simultaneously plays the role of stabilizing substance [44]. Numerous synthesis methods of obtaining ferromagnetic nanoparticles were described in several reviews [45]. Nanosize iron oxides for biomedical applications are usually obtained *via* polyol synthesis, preparation of microemulsions, co-precipitation, decomposition of organic species, *etc*. Thus, nanocomposites based on iron cores and silver shells were produced under the standard conditions in the solution containing argentum nitrate, ferrous salt, borohydride, and sodium citrate [46]. As the determinative factors of obtaining nanocomposites, the sequence of solutions blending, and time of reagents addition was found.

Hydroxylamine, citrate, or sodium borohydride are most commonly used as reducing agents [47]. To reduce the silver layer onto nanomagnetite surface, tartaric acid was used [48]. However, the application of various SAS and organic components to obtain core and shell type nanocomposites is impossible for structures prepared for biomedicine, so in that case, there are preferable to use various biocompatible substances. For example, Fe_3O_4 and Au particles were synthesized *via* a combination of chemical and biological route [49]. Ethanolic extract of *Eucalyptus camaldulensis* was used to reduce aurum on the magnetite surface from the water solution of $HAuCl_4$.

Therefore, we need to develop effective materials for preventing

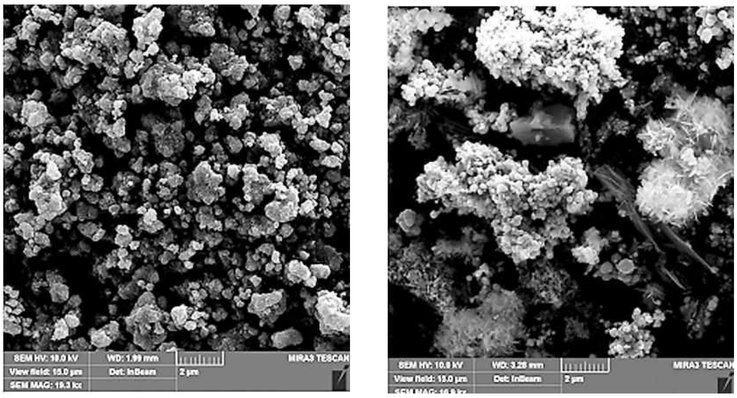

a *b*

Fig. 1. SEM images: *a*—TiO_2–Ag (4 wt.%) (×19300); *b*—Fe_3O_4–Ag (×16900).

the bacteria from environmental because of pandemic spreading. The idea is the creation of functional composites based on magnetite and anatase with cations of Ag, Pt, Pd, which exhibit bactericidal and antiviral activities under the UV irradiation for purification water and air.

Functional nanocomposites based on metal oxides as TiO_2, Fe_3O_4 doped with noble metals and rare-earth elements (REE) can be a perspective material for the new kind of bioactive photocatalysts creation, whereas, the presence of REE in the structure of the zinc and titanium oxides enhances their photocatalytic activity [30]. The inclusion of noble metal cations in the crystal lattice of iron oxides enhances their optical properties [31] accompanied by superparamagnetic properties and high catalytic activity for phospholipids.

Our team synthesized bioactive magnetite and anatase doped cations of Ag, Pt, and Pd with a concentration in the interval 0–5 wt.% (Fig. 1). Noble concentrations influence surface structure and magnetic properties of as-prepared and UV-irradiated nanocomposites doped with Ag, Pt, Pd. EDX analysis testifies composition of TiO_2–Ag (Ti—58.6 wt.%, O—36.69 wt.%, Ag—4.12 wt.%) and Fe_3O_4–Ag (Fe—50.84 wt.%, O—44.92 wt.%, Ag—4.3 wt.%).

According to obtained data, the UV irradiation changes the spine quantity in the structure of the nanocomposites and it shifts the characteristically lines to high energy.

3.2. Study of Adsorption and Phagocytosis of Magnetite Particles by U-937 Cells

Our study of the magnetite nanoparticles adsorption and their phagocytosis by U-937 cells was performed using the Lilly cytochemical method. Incubation of U-937 cells with magnetite particles was performed in phosphate-buffered saline for 15–120 min. According to the obtained data (Fig. 2), magnetite with a nanometer particle size is adsorbed on the cell surface and does not show signs of phagocytosis. The obtained data indicate that, during the entire period of observation in the cells of the control group, there were not detected granules, which include Fe^{2+} and/or Fe^{3+}.

Magnetite obtained on the surface of the iron with particles size 1 μm was identified on the cell surface in the form of both aggregates and individual particles. For 15 min of incubation at the point of contact of magnetite with the cell, there was observed bending of the cytoplasm. Phagocytic magnetite particles are also present in some cells. The amount of phagocytosed and adsorbed magnetite in the cells increased during 2 h of observation. The adsorption of natural microsize magnetite by the cell surface is similar to the ad-

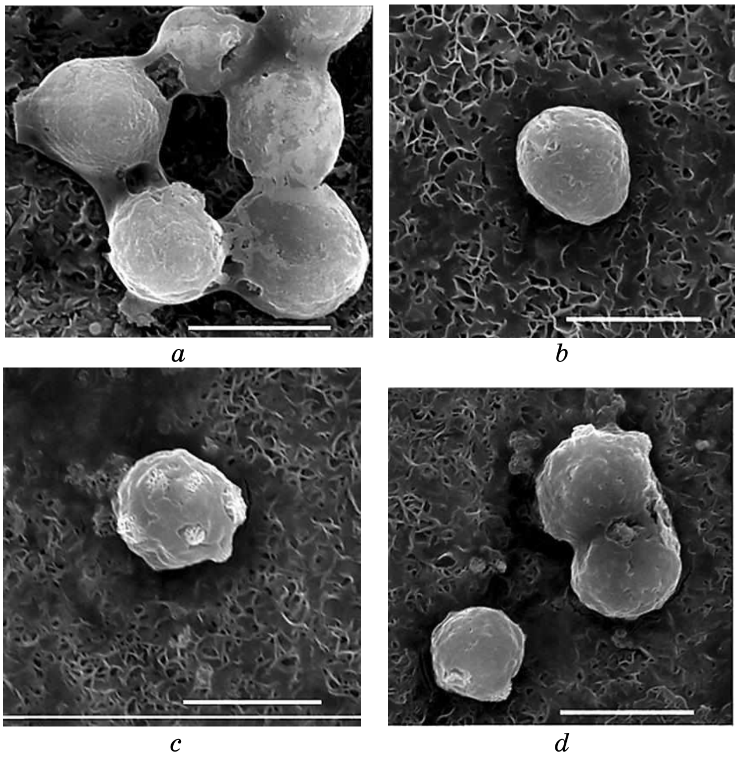

Fig. 2. Cells of the U937 line (human leukemic monocyte lymphoma cell line): *a*, *b*—system cells; in-cells after incubation with nanosize magnetite particles; *c*, *d*—cells after incubation with microsize particles of magnetite. Notice: scale is 10 μm.

sorption of the synthesized analog, but during 120 min of incubation, the amount of phagocytosed and adsorbed natural magnetite in the cells increased and exceeded the values obtained for artificial magnetite. Moreover, in some cells, phagocytosis was accompanied by cell death and disintegration. Based on the obtained results, it is concluded that the magnetite obtained by the method of rotational corrosion dispersion has less biological activity compared to natural and this makes it suitable for further use in various biological systems.

Thus, the study of the interaction of tumour cells of the promonocytic leukaemia line U-937 with magnetite particles obtained by the method of rotational corrosion dispersion, as well as microsize particles of natural magnetite proved their lack of cytotoxic properties. The revealed dependence of the cytotoxic activity of other iron-oxygen-containing minerals on their nature and particle size is due to a possible criterion for the selection of ferromagnetic material concerning its suitability for medical and biological research. Nanosize magnetite particles form a complex with transferrin, a natural transporter of iron, and accumulate in mitochondrial and cytosolic cell fractions. The tested particles of iron–oxygen-containing minerals are recognized as suitable for the creation of nanosize magnetic carriers.

4. MANUFACTURING AND PROPERTIES OF ZnO NANOSTRUCTURES

Among the metal oxide nanoparticles (NPs), ZnO a wurtzite *n*-type semiconductor and which have potential material for biosensing and gas sensing application because of their unusual properties, like direct bandgap (3.37 eV), high exciton binding energy (60 meV), and resistivity (10^{-4} to 10^{5} $\Omega\cdot$cm), including high surface area, high catalytic efficiency, nontoxicity, chemical stability, and strong adsorption ability. ZnO nanostructures (NS) due to their unique properties have the possibility of using in the ultraviolet (UV) photodiodes, piezoelectric devices, chemical sensors, *etc.* [50]. In the last years, ZnO has been more actively studied as a cost-effective and eco-friendly photocatalytic material for the cleaning of the environment from persistent organic pollutants, bacteria [51, 52]. ZnO films and nanostructures were deposited on Si substrates by MOCVD using single-source solid-state zinc acetylacetonate (Zn(AA)) precursor [53]. Doping by silver was realized in-situ *via* adding 1 and 10 wt.% of Ag acetylacetonate (Ag(AA)) to zinc precursor. The MOCVD method of growth allows us to deposit the different types of ZnO nanostructures morphologies (Fig. 3).

It was shown that Ag doping affects the ZnO microstructure *via*

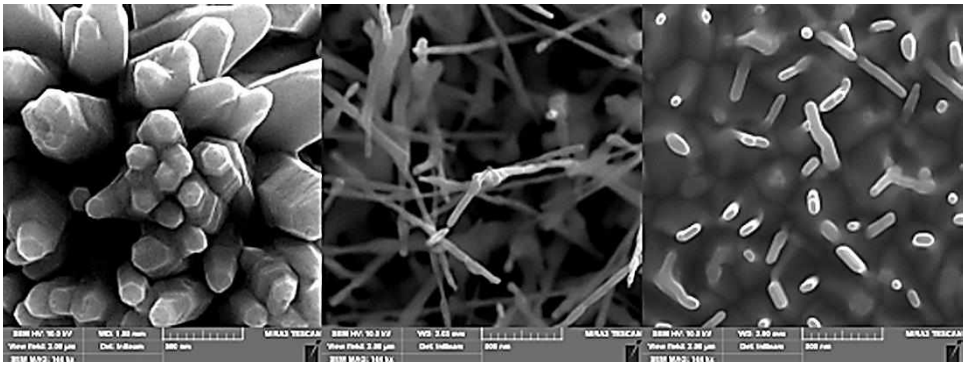

Fig. 3. SEM images of ZnO:Ag nanostructures: nanorods (*a*), nanowires (*b*) and nanoteats (*c*) deposited on Si substrates.

changing the nucleation mode into heterogeneous and thus transforming the polycrystalline films into a matrix of highly *c*-axis textured hexagonally faceted nanorods or nanowires. Ag doping leads to increasing of the work function value from 4.45 to 4.75 eV that is attributed to Ag behaviour as a donor-type impurity. It was observed that near-band photoluminescence of ZnO NS was enhanced with Ag doping because of quenching deep-level emission. Observed considerable amplification of near-band photoluminescence in Ag-doped ZnO NS comparison with undoped ZnO may be caused by surface plasmon resonance, which, as we believe, can be used for the development of the effective photocatalytic devices based on Ag-doped ZnO NS for the disposal of the environment from organic pollutants and bacteria, *etc*.

Besides, the nanosize ZnO particles having a large specific surface and high surface energy, upon settling on the surface of a bacterium, easily destroy the cell membrane and penetrate the microorganism. In this case, the balance of metabolism and energy with the environment is disturbed, and the bacterium death occurs. To increase the bactericidal activity of ZnO-based nanostructures, all types of modifications are used [50–54]. Thus, the creation of structures of ZnO/Au, Ag, Cu leads to an increase in the ROS (super radical oxides) release rate due to the separation of electron-hole pairs at the Schottky barrier and decrease in their recombination, acceleration of the generation of such pairs caused by the influence of surface plasmons and the shift of the absorption edge towards the visible light. In such structures, charge transfer from Au and Ag to ZnO can cause an electrostatic attraction between positively charged metal particles and negatively charged bacteria, increasing bactericidal activity. In addition, noble metals themselves have bactericidal properties of a wide spectrum of action.

The authors of chapter [54] discussed the application of various nanomaterials (such as metal nanoparticles, metal oxides (TiO_2, ZnO, CeO_2, Fe_3O_4), carbon compounds, filtration membranes, *etc.*) in the field of wastewater treatment by photocatalysis. In the last years, most photocatalysts have been specifically devised for application under sunlight, but many researchers focused attention on UV-active systems [54]. Thus, here, we will differentiate between UV- and visible light or sunlight-active nanoscale semiconductors. This chapter [54] also includes a description of the most studied photocatalytic reactions related to water purification, the degradation of emerging pollutants, and disinfection procedures.

Considering the methods of synthesis and study of nanocomposites properties with oxide NPs, especially of TiO_2, has not yet received information on the effectiveness of their use. The reason for all would be to use expensive Ti precursors. Using cheap $TiCl_4$ as the precursor of TiO_2 does not allow us to obtain the composite system with the required properties due to the complexity of the control of the hydrolysis process, the difficulties associated with the removal, and the highly reactive reaction by-products (HCl). However, methods of the TiO_2-surface modifying in the synthesis of composites do not cause difficulties in most cases and could be successfully applied to industrial processes.

Thus, it is a global task to create a composite photogenerator based on TiO_2, ZnO, Fe_3O_4 to control the distribution of $h+$ (generation), and then applying for the effective destruction of toxic organic substances and pathogen microorganisms due to the high concentration of oxide radicals.

5. SUMMARY

Thus, nanosize core & shell type composites containing iron oxide cores (magnetite or maghemite) and noble metal shells (in particular gold or silver) are one of the most perspective materials for biomedical applications due to combinations of magnetic, optical, colloid-chemical properties, as well as because of the possibility to biofunctionalization of the surface of the composite. The variation in the physicochemical characteristics of nanocomposites based on ferrimagnetic cores and a noble metal shells opens for us great possibilities for their usage as a platform for the development of highly effective diagnostic and therapeutic tools with selectivity at the level of individual cells and biomacromolecules. The superparamagnetic properties of Fe_3O_4 and Ag^0 shell composite particles and the photocatalytic properties of TiO_2 nanopowder in combination with the bactericidal and antiviral activity of both, which can be significantly increased under the influence of UV radiation, are the basis for the creation of new protective composite materials. Variation in the material composition of such a composite, the structure of oxide particles and the form of their composition of modifying components will optimize the photoactive composite system, which will show the greatest antiviral activity initiated by the action of UV radiation. The obtained nanocomposite (in the form of powder or film) can be used in the creation of technical means and prevention of the spread of infectious diseases in a confined air environment (transport, public places, and hospitals).

Summarised results show that the photocatalysis of composites TiO_2, ZnO appears to be an interesting approach to water purification, offering the possibility of using sunlight as a sustainable and renewable source of energy. This technology is based on the presence of a semiconductor that can be excited by light with energy higher than its bandgap, inducing the formation of energy-rich electron–hole pairs that can be involved in ORR (oxygen reduction reaction). Recent progress has explored the chemical nature of nanoscale semiconductors to improving their electronic and optical properties, enhancing their photoresponse to visible light. In addition, nanomaterials typically have high reactivity and a high degree of functionalization, large specific surface area, size-dependent properties, *etc*. They can application in water purification.

During doping by Ag, important work function to our TiO_2, Fe_3O_4, and ZnO has, and maybe, the transfer of electron will take place from Ag to conducting band oxide to achieve Fermi level equilibrium following by localized surface plasmon resonance. The features of proposed with us doped oxide nanoparticles (specific nanostructures) due to catching and holding of microorganisms, generation of oxidizing radicals by photocatalysts under UV irradiation, mechanical damaging of microorganisms, and inactivation of microorganisms. We are going step-by-step to discover all components and deliver all evidence of such a concept for the effective antimicrobial guard.

However, the questions that have arisen since the start of the COVID-19 coronavirus pandemic, which spreads mainly with air droplets, suggest that scientists will soon turn their attention to cleaning the water and air from microbiological contaminants. By taking into account the advantages of the photocatalytic properties of ZnO over TiO_2, one can expect the problems that have arisen to be solved in particular thanks to zinc-oxide nanomaterials.

ACKNOWLEDGEMENTS

This work was partially supported by the research project of N.A.S.

of Ukraine 'The development of photocatalytic nanocomposites for viruses inactivation in the air' (No. 40/20-H) and was partially supported by the research projects of N.A.S. of Ukraine 'Development of innovative photocatalytic nanostructured materials based on ZnO and TiO_2' (528/IPM-11/20).

The authors are grateful to thanks Dr. V. Khranovskyy (Department of Physics, Chemistry and Biology, Linköping University, Sweden) for fruitful discussions.

REFERENCES

1. T. H. Han, N. Parveen, J. H. Shim, A. T. N. Nguyen, N. Mahato, and M. H. and Cho, *Industr. & Engineer. Chem. Res.*, **57**: 6705 (2018); doi:10.1021/acs.iecr.7b05314
2. N. A. Jumat, P. S. Wai, J. J. Ching, and W. J. & Basirun, *Polym. and Polym. Compos.*, **25**: 507 (2017); doi:10.1177/096739111702500701
3. http://www.fao.org/docrep/010/ai407e/ai407e26.htm
4. T. J. Brooms, B. Otieno, M. S. Onyango, and A. & Ochieng, *J. Environm. Sci. Health, Part A*, **53**: 99 (2017); doi:10.1080/10934529.2017.1377583
5. M. N. Ghazzal, H. Kebaili, M. Joseph, D. P. Debecker, P. Eloy, J. De Coninck, and E. M. Gaigneaux, *Appl. Catalys. B: Environm.*, **115**: 276 (2012); doi:10.1016/j.apcatb.2011.12.016
6. A. L. Luna, D. Dragoe, K. Wang, B. Peaunier, E. Kowalska, B. Ohtani, and C. Colbeau-Justin, *The J. Phys. Chem. C*, **121**: 14302 (2017); doi:10.1021/acs.jpcc.7b01167
7. M. Zahornyi, *Metall. and Met. Ceram.*, **3–4**: 130 (2017); doi:10.1007/s11106-017-9880-x
8. Yu. B. Pankivskka, L. O. Biliavska, O. Yu. Povnitsa, M. M. Zagornyi, A. V. Ragulia, M. S. Kharchuk, and S. D. Zagorodnya, *Microbiol. J.*, **81**: 73 (2019); doi:10.15407/microbiolj81.05.073
9. J. Li and N. Wu, *Catalys. Sci. & Technol.*, **5**: 1360 (2015); doi:10.1039/c4cy00974f
10. M. Zahornyi, *Functional Nanocomposites Based of Titanium Dioxide* (Saarbrücken: Lambert Academic Publishing: 2018).
11. S. Ghosh, N. A. Kouamé, L. Ramos, S. Remita, A. Dazzi, A. Deniset-Besseau, and H. Remita, *Nature Mater.*, **14**: 505 (2015); doi:10.1038/nmat4220
12. Y. Zhu, S. Xu, and D. Yi, *React. Funct. Polym.*, **70**: 282 (2010); doi:10.1016/j.reactfunctpolym.2010.01.007
13. T. Khalyavka, M. Bondarenko, N. Shcherban, I. Petrik, and A. Melnyk, *Appl. Nanosc.*, **5**: 695 (2018); doi:10.1007/s13204-018-0838-1
14. T. A. Khalyavka, N. D. Shcherban, V. V. Shymanovska, E. V. Manuilov, V. V. Permyakov, and S. N. Shcherbakov, *Res. on Chem. Intermed.*, **45**: 4029 (2019); doi:10.1007/s11164-019-03888-z
15. G. Sokolsky, M. Zahornyi, T. Lobunets, N. Tyschenko, A. Shyrokov, A. Ragulya, S. Ivanov, N. Gayuk, and V. Sokol'skii, **27**: 130 (2019); doi:10.15421/081914
16. A. Zaleska-Medynska, *Metal Oxide-Based Photocatalysis. Fundamentals and*

Prospects for Application (Elsevier: 2018).
17. F. Heshmatpour and S. Zarrin, *J. Photochem. Photobiol. A: Chem.*, **346**: 431 (2017); doi:10.1016/j.jphotochem.2017.06.017
18. M. Saraswati, R. L. Permadani, and A. Slamet, *IOP Conf. Series: Mater. Sci. and Engineer.*, **509**: 012091 (2019); doi:10.1088/1757-899x/509/1/012091
19. A. Gnanaprakasam, V. M. Sivakumar, and M. Thirumarimurugan, *Indian J. Mater. Sci.*, **2015**: 1 (2015); doi:10.1155/2015/601827
20. H. Moradi, A. Eshaghi, S. R. Hosseini, and K. Ghani, *Ultrason. Sonochem.*, **32**: 314 (2016); doi:10.1016/j.ultsonch.2016.03.025
21. Z. Xiong, J. Ma, W. J. Ng, T. D. Waite, and X. S. Zhao, *Water Research.*, **45**: 2095 (2011); doi:10.1016/j.watres.2010.12.019
22. J. Ma, Z. Xiong, T. David Waite, W. J. Ng, and X. S. Zhao, *Micropor. Mesopor. Mater.*, **144**: 97 (2011); doi:10.1016/j.micromeso.2011.03.040
23. H. N. Thi-Tuyet, T. A. Thi-Kim, S. N. Van, and N. The-Vinh, *AIMS Mater. Sci.*, **3**: 339 (2016); doi:10.3934/matersci.2016.2.339
24. D.-S. Lee and Y.-W. Chen, *J. of the Taiwan Inst. of Chem. Engin.*, **45**: 705 (2014); doi:10.1016/j.jtice.2013.07.007
25. W. Ammara, S. Quanquan, M. Nobutaka, M. Daniel, Q. Zhaoxian, Li Gao, and B. Alfons, *Catalysts*, **10**: 933 (2020); doi:10.3390/catal10080933
26. Y. Wang, D. Zhang, L. Shi, L. Li, and J. Zhang, *Mat. Chem. Phys.*, **110**: 463 (2008); doi:10.1016/j.matchemphys.2008.03.006
27. H. Ren, P. Koshy, W.-F. Chen, S. Qi, and C. C. Sorrell, *J. Hazard. Mater.*, **325**: 340 (2017); doi:10.1016/j.jhazmat.2016.08.072
28. M. Choquette-Labbé, W. Shewa, J. Lalman, and S. Shanmugam, *Water*, **6**: 1785 (2014); doi:10.3390/w6061785
29. H. Harada, A. Onoda, T. Uematsu, S. Kuwabata, and T. Hayashi, *Langmuir*, **32**: 6459 (2016); doi:10.1021/acs.langmuir.6b01073
30. T. K. Indira and P. K. Lakshmi, *Int. J. Pharm. Sci. Nanotech.*, **3**: 1035 (2010); doi:10.37285/ijpsn
31. M. Smith, M. McKeague, and M. C. DeRosa, *Methods X*, **6**: 333 (2019); doi:10.1016/j.mex.2019.02.006
32. E. Nassireslami and M. Ajdarzade, *Adv. Pharm. Bull.*, **2**: 201 (2018); doi:10.15171/apb.2018.024
33. D. K. Kim, M. Mikhailova, M. Toprak, Y. Zhang, B. Bjelke, J. Kehr, and M. Muhammed, *MRS Online Proceedings Library*, **704**: 6281 (2001); doi:10.1557/proc-704-w6.28.1
34. D. Caruntu, B. L. Cushing, G. O. Caruntu, and C. J. Connor, *Chem Mater.*, **17**: 3398 (2005); doi:10.1021/cm050280n
35. T. Kinoshita, S. Seino, Y. Mizukoshi, Y. Otome, T. Nakagawa, K. Okitsu, and T. A. Yamamoto, *J. Magnet. Magnet. Mater.*, **293**, Iss. 1: 106 (2005); doi:10.1016/j.jmmm.2005.01.050
36. K. Kawaguchi, J. Jaworski, Y. Ishikawa, T. Sasaki, and N. Koshizaki, *J. Magnet. Magnet. Mater.*, **310**: 2369 (2007); doi:10.1016/j.jmmm.2006.11.109
37. Q. G. He, Z. H. Wu, and R. Hu, *Adv. Mater. Res.*, **183**: 1989 (2011); doi:10.4028/www.scientific.net/amr.183-185.1989
38. C. K. Lo, D. Xiao, and M. M. F. Choi, *J. Mater. Chem.*, **23**: 2418 (2007); doi:10.1039/b617500g
39. B. L. Oliva, A. Pradhan, D. Caruntu, C. J. O'Connor, and M. A. Tarr,

J. Mater Res., **21**: 1312 (2006); doi:10.1557/JMR.2006.0163

40. L. Wang, J. Luo, M. M. Maye, Q. Fan, Q. Rendeng, M. H. Engelhard, and C.-J. Zhong, *J. Mater. Chem.*, **15**: 1821 (2005); doi:10.1039/b501375e
41. O. M. Lavrynenko, O. Yu. Pavlenko, Yu. S. Shchukin, N. O. Dudchenko, A. B. Brik, and T. S. Antonenko, *Springer Proceedings in Physics. Microstructure and Properties of Micro- and Nanoscale Materials, Films, and Coatings (NAP 2019)* (Eds. A. D. Pogrebnjak and O. Bondar) (Springer: 2020), Ch. 28, p. 297.
42. U. Tamer, Yu. Gündogdu, I. H. Boyaci, and. K. Pekmez, *J. Nanopart. Res.*, **12**: 1187 (2010).
43. V. A. J. Silva, P. L. Andrade, M. P. C. Silva, D. Bustamante, A. De Los Santos Valladares, and J. Albino Aguiar, *J. Magnet. Magnet. Mater.*, **343**: 138 (2013); doi:10.1016/j.jmmm.2013.04.062
44. T. T. Hien Pham, C. Cao, and S. J. Sim, *J. Magnet. Magnet. Mater.*, **320**: 2049 (2008); doi:10.1016/j.jmmm.2008.03.015
45. A. K. Gupta and M. Gupta, *Biomater.*, **26**: 3995 (2005); doi:10.1016/j.biomaterials.2004.10.012
46. J. Lin, W. Zhou, A. Kumbhar, J. Wiemann, J. Fang, E. E. Carpenter, and C. J. O'Connor, *J. Sol. State Chem.*, **159**: 26 (2001); doi:10.1006/jssc.2001.9117
47. S. Klein, J. Hüber, C. Menter, L. V. R. Distel, W. Neuhuber, and C. Kryschi, *Appl. Sci.*, **9**: 1 (2019); doi:10.3390/app9010015
48. P. Nguyen-Tri, V. Th. Nguyen, and T. A. Nguyen, *J. Compos. Sci.*, **3**, Iss. 2: 34 (2019); doi:10.3390/jcs3020034
49. E. Katz, *Magnetochem.*, **5**: 1 (2019); doi:10.3390/magnetochemistry5040061
50. G. V. Lashkarev, I. I. Shtepliuk, A. I. Ievtushenko, O. Y. Khyzhun, V. V. Kartuzov, L. I. Ovsiannikova, V. A. Karpyna, and D. V. Myroniuk, *Low Temperature Physics*, **41**: 129 (2015); doi:10.1063/1.4908204
51. S. H. Khan and B. Pathak, *Environmen. Nanotechnol., Monitor. Managem.* (2020); doi:10.1016/j.enmm.2020.1002
52. Q. Kezhen, B. Cheng, J. Yu, and W. Ho, *J. Alloys Comp.*, **727**: 792 (2017); doi:10.1016/j.jallcom.2017.08.142
53. A. Ievtushenko, N. Karpyna, J. Eriksson, I. Tsiaoussis, I. Shtepliuk, G. Lashkarev, R. Yakimova, and V. Khranovskyy, *Superlattices and Microstructures*, **117**: 121 (2018); doi:10.1016/j.spmi.2018.03.029
54. C. Belver, J. Bedia, A. Gymez-Avilés, M. Pecas-Garzyn, and Juan J. Rodriguez, *Nanoscale Materials in Water Purification* (Eds. S. Thomas, D. Pasquini et al.) (2019); doi:10.1016/B978-0-12-813926-4.00028-8

Наносистеми, наноматеріали, нанотехнології
Nanosistemi, Nanomateriali, Nanotehnologii
2021, т. 19, № 4, сс. 981–996

PACS numbers: 61.05.cp, 61.72.Hh, 68.37.Hk, 78.40.Fy, 78.67.Bf, 87.19.xb, 87.19.xg

Structural, Morphological and Optical Properties of Manganese (Mn) and Gadolinium (Gd) Ions-Doped ZnO Nanoparticles and Their Antimicrobial Activity

Abebe Belay Gemta and Diriba Tsegaye

Department of Applied Physics,
Adama Science and Technology University,
P.O. Box, 1888 Adama, Ethiopia

In this research, ZnO nanoparticles are doped with the manganese (Mn) and gadolinium (Gd) ions using chemical co-precipitation method. The effects of dopants on the structural, morphological and optical properties of ZnO are investigated. In addition, the antimicrobial activity of ZnO nanoparticles doped with the Mn and Gd metallic ions are revealed. The structural, morphological and optical properties are characterized using x-ray diffraction (XRD), scanning electron microscopy (SEM) and ultraviolet-visible (UV-Vis) spectroscopy. The XRD results reveal the synthesized nanoparticles possessed hexagonal phase of wurtzite structure and average crystallite size of 31–38 nm. The decreases in crystallite size, lattice parameters, unit volume and bond length are observed after incorporation of the Mn and Gd ions into the ZnO matrix. On the other hand, increments in strain and concentration of defects are observed after the Mn and Gd doping. Scanning electron-microscopy images show spherical shape with well-defined distributions observed. The energy band gaps estimated from ultraviolet-visible absorption spectra are found to be 3.35, 3.28 and 3.07 eV for undoped ZnO, Gd-doped and Mn-doped ones, respectively. The antimicrobial activity of undoped, Mn- and Gd-doped ZnO nanoparticles are tested against gram-negative bacteria (*E. coli* and *P. aeruginosa*), gram-positive bacteria (*S. aureus* and *B. subtilis*) and fungus (*C. albicans*) using agar-well diffusion method. The results indicate that the antimicrobial activity of doped ZnO nanoparticles is higher as compared to undoped ZnO nanoparticles. As also found, the gram-positive bacteria are more susceptible to ZnO nanoparticle than gram-negative bacteria and fungus.

У цьому дослідженні наночастинки ZnO леґуються йонами Манґану (Mn) та Ґадолінію (Gd) за допомогою хемічного методу співосадження. Досліджено вплив леґування на структурні, морфологічні й оптичні властивості ZnO. Крім того, виявлено антимікробну активність наночастинок ZnO, леґованих металічними йонами Mn і Gd. Структурні, морфологічні й оптичні властивості характеризуються за допомогою рентґенівської дифракції (РД), сканувальної електронної мікроскопії і спектроскопії у видимій та ультрафіолетовій областях світла. Результати РД показують, що синтезовані наночастинки мали гексагональну фазу структури вюрциту та середній розмір кристаліту у 31–38 нм. Зменшення розміру кристаліту, параметрів ґратниці, об'єму елементарної комірки та довжини зв'язку спостерігаються після втілення йонів Mn та Gd до матриці ZnO. З іншого боку, збільшення деформації та концентрації дефектів спостерігаються після леґування Mn і Gd. Сканувальні електронно-мікроскопічні зображення показують сферичну форму з чітко визначеними розподілами, що спостерігаються. Енергетичні зонні щілини, оцінені з ультрафіолетово-видимих спектрів поглинання, виявилися у 3,35, 3,28 і 3,07 еВ для нелеґованого ZnO та леґованого Gd і Mn відповідно. Антимікробна активність нелеґованих та леґованих Mn і Gd наночастинок ZnO перевіряється проти грамнеґативних бактерій (*E. coli* і *P. aeruginosa*), грампозитивних бактерій (*S. aureus* і *B. subtilis*) і грибка (*C. albicans*) за допомогою імунодифузійного методу в агаровому ґелі. Результати показують, що антимікробна активність леґованих наночастинок ZnO вище в порівнянні з нелеґованими наночастинками ZnO. Як також з'ясувалося, грампозитивні бактерії більш сприйнятливі до наночастинок ZnO, ніж грамнеґативні бактерії та грибок.

Key words: $Zn_{0.98}Mn_{0.02}O$, $Zn_{0.98}Gd_{0.02}O$, co-precipitation method, structure, antimicrobial activity.

Ключові слова: $Zn_{0.98}Mn_{0.02}O$, $Zn_{0.98}Gd_{0.02}O$, метод співосадження, структура, протимікробна активність.

(Received 11 December, 2020; in revised form, 31 December, 2021)

1. INTRODUCTION

Nanoparticles (NPs) are special classes of organic or inorganic materials having size in the range of 1 to 100 nm in at least one dimension. They have unique and enhanced functional properties such as high surface area to volume ratio and more atoms on their surface than their micro- or macro-scale counterparts owing to their nanoscale feature [1]. Metal oxide nanoparticles are important materials, finding applications in a diverse range of activities. Among them, ZnO NPs have many significant features such as chemical and physical stability, large exciton binding energy (60 meV), wide band gap, intensive ultraviolet (UV) and infrared (IR) adsorption [2–5]. ZnO NPs also have several advantages due to low toxicity, biosafe biocompatibility and biodegradability, which make the material important for antibacterial, antifungal, and wound healing applications [6–9].

Several studies have been conducted on various factors affecting the shape, size, optical properties and applications of ZnO NPs. The factors are precursor concentrations [10], temperature [11, 12], surfactant concentrations [13, 14], dopant concentrations [15], solvent medium and pH of the reaction mixture [16, 17]. Doping is one of the strategies to modify the structural, morphological and optical properties of ZnO nanoparticles and enhance its applications such as antimicrobial activity.

In addition, several available reports deal with the particle size-dependent antimicrobial activity of ZnO nanoparticles (NPs), where antimicrobial activity is inversely related to the particle size. Hence, the crystal size of ZnO nanoparticles needs to be reduced for better antimicrobial activity [18]. The antimicrobial activity of undoped and doped zinc oxide nanoparticles has also been studied against gram-negative and gram-positive bacteria using chemically synthesizing method [19]. The main mechanism of antimicrobial activities of ZnO NPs is the electrostatic interaction between ZnO NPs and cell membrane of the bacteria, penetration of ZnO NPs into the inside of bacterial cell wall, and the formation of reactive oxygen species (ROS) inside the cell of bacteria, which destroys the cytoplasm of the bacteria [20]. It is reported that gram-negative bacteria are more resistant against ZnO NPs than gram-positive bacteria due to that it has double cell membrane structure (outside and cytoplasmic membrane) and the difference in intracellular antioxidant content [21].

Many researchers reported the synthesis and characterization of zinc oxide nanoparticle doped metals in separate studies for different precursors at different conditions using different synthesis methods. But, to date results there is a controversy and debate on the influence of these dopants on the structural, morphological and optical properties as well as on the antimicrobial activity of ZnO nanoparticles. Therefore, in this research, it is intended to investigate the effects of Mn and Gd dopant ions on the structural, morphological and optical properties of ZnO nanoparticle and on its antimicrobial activity.

2. MATERIALS AND METHODS

2.1. Materials

The precursor chemicals for the synthesis of pure and doped ZnO NPs are zinc acetate dihydrate (Unichem, India), sodium hydroxide (Alpha Chemika, India), Manganese acetate dihydrate (Unimag. media, India) and Gadolinium chloride hexahydrate (uni. Himedia, India). Culture media such as Müller–Hinton agar (M173-500G HiMedia, India), tryptone soya agar (T131-500G HiMedia, India), and nutrient broth (N173-500G HiMedia, India) for cultivation of the test organisms and used for the determination of antimicrobial activity of ZnO nanoparticles. Dimethyl sulfoxide (Unichem, India), ethanol and double distilled water were used as the solvent. Antibiotic gentamicin was used as positive control. All chemicals are analytical grades and do not undergo further purification.

2.2. Synthesis Methods

For synthesis of pure ZnO, 21.95 g of zinc acetate dihydrate was completely dissolved in 100 ml of deionized water and 0.2 M of aqueous NaOH solution was added drop wise to the mixture. Later, the solution was stirred for 30 minutes and placed at room temperature for 5 hrs for precipitation to occur. This one resulted in the formation of white coloured precipitates in the reaction mixture. In order to separate the precipitates, the reaction mixture was filtered and washed several times using double distilled water and ethanol to remove impurities. Finally, it was oven-dried at 60°C for 17 hrs. The calcination of the white powder was performed at 200°C for 2 hrs in a muffle furnace (model No. MC2-5/5/10-12, Biobase, Chine).

Similarly, to prepare Mn and Gd ion doped ZnO NPs we followed the already developed procedures by [22]. In order to synthesis of $Zn_{0.98}Mn_{0.02}O$ nanoparticle, 0.54 g of manganese acetate dehydrate was dissolved in 100 ml of deionized water and it was mixed with an aqueous zinc acetate dihydrate solution (21.95 g of zinc acetate dissolved in 100 ml of deionized water). 0.2 M of NaOH solution was added drop by drop to the above homogenous mixture to get a white precipitate with pale green colour. For drying and calcination, similar procedures mentioned above were repeated. Similarly, for the synthesis of $Zn_{0.98}Gd_{0.02}O$ nanoparticle, 0.5478 g of gadolinium chloride hexahydrate was dissolved in ethanol: double distilled water (50%:50%) and it was mixed with zinc acetate dihydrate solution (21.95 g of zinc acetate in 100 ml of deionized water).

2.3. Characterizations

X-ray diffractometer (XRD-7000, Shimadzu Co., Japan) to investigate the x-ray diffraction pattern of NPs by generating CuK_α radiation, $\lambda = 1.54056$ operating at a voltage of 40 kV and applied current of 30 mA. It is used to determine the crystalline phase of the undoped, Mn and Gd-doped ZnO nanoparticles. Intensities were measured at room temperature at an angle range of $2\theta = 10° \leq 2\theta \leq 80°$. All the diffraction peaks are well indexed to the hexagonal ZnO wurtzite structure (JCPDS 36-1451). The average crystallite size estimated from the Debye–Scherrer formula [23]:

$$D = \frac{k\lambda}{\beta\cos\theta}, \tag{1}$$

where λ, θ, β and D are x-ray wavelength, Bragg's diffraction angle, full width at half maximum of the peak and average grain size of the crystallite, respectively. The lattice parameters a and c and the spacing distance d_{hkl} for the wurtzite structure of ZnO were calculated using Eqs. (2) and (3):

$$a = \frac{1}{\sqrt{3}}\frac{\lambda}{\sin\theta}, \tag{2}$$

$$c = \frac{\lambda}{\sin\theta}. \tag{3}$$

The dislocation densities (δ), the micro-strain (ε), the volume (V) of the unit cell for hexagonal system, the bond lengths (L), and the positional parameter (u) of undoped and doped ZnO nanoparticles were calculated by using Eqs. (4)–(8) [24]:

$$\delta = \frac{1}{D^2}, \tag{4}$$

$$e = \frac{\beta\cos\theta}{4}, \tag{5}$$

$$V = 0.88a^2c, \tag{6}$$

$$L = \sqrt{\left(\frac{a^2}{3} + \left(\frac{1}{2} - u\right)^2 c^2\right)}, \tag{7}$$

$$u = \frac{a^2}{3c^2} + 0.25. \tag{8}$$

The morphology of undoped and doped ZnO NPs was studied using a scanning electron microscope (Hitachi, H 7600). In SEM characterization, powder was mounted on a sample holder coating with a conductive metal. The samples were scanned with focused fine beams of electrons. The surface characteristics of the sample were obtained from the secondary electrons emitted from the sample surface [25].

The optical characterization of ZnO NPs was carried out using UV-Vis spectroscopy. The band gap energies are calculated using Eq. (9) [26]:

$$E_g = \frac{hc}{\lambda} = \frac{1240}{\lambda_{\max}} eV, \qquad (9)$$

where h is the Planck's constant ($6.626 \cdot 10^{-34}$ J·s), c is the light velocity ($3 \cdot 10^8$ m/s), and λ is the wavelength.

2.4. Determination of Antimicrobial Activity of ZnO NPs

The antimicrobial properties of undoped, Mn-doped and Gd-doped ZnO nanoparticles were determined against gram-negative bacteria (*E. coli and P. aeruginosa*), gram-positive bacteria (*S. aureus and B. subtilis*) and fungus (*C. albicans*) using agar-well diffusion method. Dimethyl sulfoxide and standard antibiotic gentamicin were used as negative and positive control for the bacterial strains respectively. The strains were transferred to nutrient broth and incubated to grow aerobically at 37°C for 24 h until it achieved the turbidity of 0.5 McFarland standards. 0.01 mL of each sub-cultured bacteria were spread using sterilized cotton swab on 20 mL of sterilized molten and cooled MHA and TSA media, respectively. Subsequently, agar wells of 5 mm diameter were prepared on different plates with sterilized stainless steel cork borer and labelled properly. Different concentrations of (100, 150 and 200 μg/ml) of solutions were added into well using micropipette. The plates containing the microbes and nanoparticles were incubated at 37°C for 24 hrs in case of bacteria and 28°C for 48 hrs in case of yeast. The plates were examined for evidence of zones of inhibition, which appear as a clear area around the wells. The diameter of zones' inhibition measured and means value expressed in millimetres and compared with the standard drug gentamicin. All experiments were performed three times and the results were averaged.

3. RESULTS AND DISCUSSION

3.1. X-Ray Diffraction (XRD) Analysis

The structural analyses of pure ZnO and doped ($Zn_{0.98}Mn_{0.02}O$ and $Zn_{0.98}Gd_{0.02}O$) nanoparticles are depicted in Fig. 1, *a–c*. The diffraction peaks observed at $2\theta = 31.7480°$, 34.4191°, 36.2366°, 36.6165°, 47.5244°, 56.5660°, 56.8454°, 62.8533°, 66.3569°, 67.9250°, 69.0605° and 76.9425° correspond to (100), (002), (101), (102), (110), (103), (200), (112), (201), (004) and (202) planes, respectively. All the diffraction peaks are attributed to wurtzite structure of ZnO as compared to JCPDS file for ZnO (JCPDS card No. 36-1451) with space group *P63mc* and lattice parameters $a = b = 3.25$ Å and

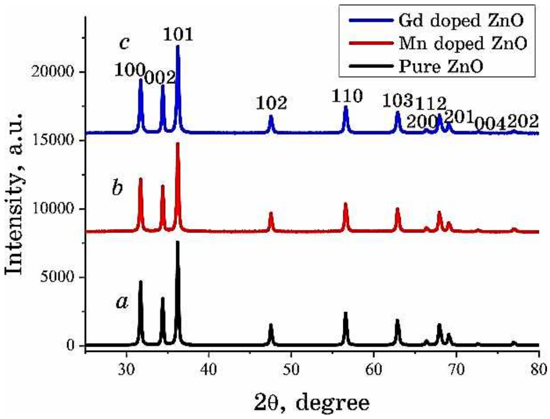

Fig. 1. X-ray diffraction patterns of (*a*) pure ZnO, (*b*) $Zn_{0.98}Mn_{0.02}O$- and (*c*) $Zn_{0.98}Gd_{0.02}O$-doped NPs.

$c = 5.206$ Å, which is in good agreement with previous reported in the literature [27, 28]. The sharp peaks and high diffracted intensity clearly indicated the crystalline nature of the particles. Similar patterns were also observed for Mn and Gd-doped ZnO NPs. The XRD results have no peaks correspond to Mn and Gd as well as MnO and Gd_2O_3 confirmed that Mn^{+2} and Gd^{+3} ions have clearly replaced the Zn^{2+} without introducing any impurities into the ZnO host lattice. On the other hand, the incorporation of Mn and Gd ions into ZnO host lattice or the replacement of Zn ions by Mn and Gd ions results in decrease the intensity of (101) peak which depicts that the decrease in the degree of crystallinity of samples as concentration of the defects in the sample increases [29].

The peak shift of (100), (002) and (101) are analysed using XRD. It is clearly seen that the FWHM slightly increases after adding the Mn and Gd dopants, indicating the growth of constrain of the crystalline or changes in the crystal strains according to the theory stated Eq. (5). In addition, peaks of (100), (002) and (101) slightly shift towards higher angles compared to undoped. The peak (100) is shifted from 31.7480° to 31.7506°, 31.7604° for $Zn_{0.98}Mn_{0.02}O$ and $Zn_{0.98}Gd_{0.02}O$, respectively. Similarly, the peak of (002) is shifted from 34.4191° to 34.4304°, 34.4359° for $Zn_{0.98}Mn_{0.02}O$ and $Zn_{0.98}Gd_{0.02}$, respectively. In the case of (101), it is shifted from 36.2366° to 36.2419° and 36.2532° for $Zn_{0.98}Mn_{0.02}O$ and $Zn_{0.98}Gd_{0.02}O$, respectively. Such a shifting of the XRD peaks depicts a lattice contraction and is attributed to the strain of the compound and mismatch of the ionic radii of Gd^{3+} (1.95°), Mn^{2+} (0.66°) and Zn^{2+} (0.74°) or replacement of some Zn cations with Mn and Gd ions in each compound [30].

On the other hand, the shift in the diffraction peaks is ascribed to the decrease in the crystallite size after the doping of Gd and Mn into the ZnO host lattice which results in the replacement of Zn ion with Gd and Mn ions and the formation of compression stresses in the ZnO that cause the positive shift of the ZnO peak. The positive shift indicates that when Gd and Mn are introduced into the ZnO matrix, the lattice contracts and the lattice parameter decreases. Thus, the positive peak shift is an indicator of incorporation of Mn and Gd dopants into the Zn sites [31].

The average crystallite size was estimated using Debye–Scherrer formula (1) and found to be 38, 36 and 31 nm for pure ZnO and Mn-, Gd-doped ZnO, respectively. The average crystallite size of Mn- and Gd-doped ZnO NPs is smaller as compared to pure ZnO NPs. FWHM of diffraction peak of ZnO (101) increases for Mn and Gd dopants; consequently, the size of nanoparticles decreases which is in agreement with results reported in literature [32]. The decrease in the crystallite size is attributed to the decrease in nucleation and growth of ZnO nanoparticles with the doping.

The values of lattice parameters (a, c), unit cell volume, bond length and positional parameter are calculated using Eqs. (2)–(8) shown in Table 1. It is observed that the unit cell volume, lattice parameters and the bond length slightly decreased after Mn and Gd doping, which might result from the difference in the ionic radii of Zn^{2+}, Mn^{2+} and Gd^{3+}, respectively. The smaller ionic radius of Mn^{2+} than Zn^{2+} results in the decrement of lattice parameter values of a and c whereas for larger ionic radius of Gd^{3+} than Zn^{2+} the increment of lattice parameter values of a and c would be expected but decreased due to strain as shown in Table 2. This slight variation in the lattice parameters of $Zn_{0.98}Mn_{0.02}O$ and $Zn_{0.98}Gd_{0.02}O$ is due to the substitution of Gd and Mn ions with different ionic radii. The slight variation in the aspect ratio (c/a) suggests that the Mn and Gd dopant ions are well substituted into the ZnO crystal lattice and indicated that the hexagonal wurtzite structure of ZnO is not altered due to Mn and Gd dopant ions [31]. The volume of the unit cell of doped ZnO NPs is decreased due to decrement of the lattice parameters after doping. The calculated values are 47.61, 47.50 and 47.01 Å^3 for ZnO, $Zn_{0.98}Mn_{0.02}O$ and $Zn_{0.980}Gd_{0.02}O$ respectively. This indicates that the addition of dopant ions into host lattice occupy partially in tetrahedral Zn positions. There is a strong correlation between c/a ratio and u. In this study, the c/a ratio reveals small perturbation for Mn and Gd doped ZnO NPs. The values of c/a and u parameters are given in Table 2. Moreover, the substitution of Mn and Gd ions results in significant changes in Zn–O bond length. From the Table 1, it is observed that the Zn–O bond length of pure ZnO NP is 1.979 Å. The bond length values decreased with Mn and

TABLE 1. Lattice parameters, cell volume and bond length of pure ZnO, $Zn_{0.98}Mn_{0.02}O$ and $Zn_{0.980}Gd_{0.02}O$ nanoparticles.

No.	Samples	Lattice parameters		Volume (*V*), Å^3	Positional parameters (*u*)	Zn–O-bond length (*L*), Å
		a, Å	*c*, Å			
1	undoped ZnO	3.250	5.206	1.601	0.379	1.979
2	Mn/ZnO	3.240	5.204	1.606	0.379	1.973
3	Gd/ZnO	3.230	5.202	1.600	0.379	1.968

TABLE 2. Dislocation densities and microstrain of undoped ZnO, $Zn_{0.98}Mn_{0.02}O$ and $Zn_{0.98}Gd_{0.02}O$ nanoparticles.

Samples	Dislocation density, lines/m^2	Microstrain, $\times 10^{-4}$
pure ZnO	$6.9252 \cdot 10^{+14}$	7.72
$Zn_{0.98}Mn_{0.02}O$	$7.7160 \cdot 10^{+14}$	7.98
$Zn_{0.98}Gd_{0.02}O$	$1.0405 \cdot 10^{+15}$	9.37

Gd-doped ZnO samples due to the replacement of Zn^{2+} ions in ZnO lattice [33].

The reduction in the crystallite size is due to the distortion in a host ZnO lattice by the incorporation of foreign impurities and the presence of Mn^{2+} and Gd^{3+} into host lattice sites hinders the nucleation and subsequent growth rate of ZnO NPs. The substitution of Mn^{2+} and Gd^{3+} ions in the interstitial positions of host ZnO lattice influences the concentration of the interstitial Zn, O and Zn vacancies. The detection of small changes in 2θ values and peak broadening of diffraction peaks are due to the increase of microstrain and line broadening effect caused by size and microstrain of NPs.

The dislocation densities and microstrain of ZnO NPs were calculated from Eqs. (4), (5) [33], and given in Table 2. Comparably, the microstrain values increase for Mn^{2+} and Gd^{3+} doped ZnO NPs due to the relaxation of strain in the respective unit cells, which alters the size and shape of the particles [34].

3.2. Scanning Electron Microscopy (SEM) Analysis

The morphologies of undoped, Mn- and Gd-doped ZnO nanoparticles were studied using SEM images. Figures 2, *a*–*c* show the morphologies of ZnO, $Zn_{0.98}Mn_{0.02}O$ and $Zn_{0.98}Gd_{0.02}O$ NPs respectively. The particle agglomeration as well as narrow particle size distribution is observed in all of the samples. Scanning Electron Microscopy (SEM) images showed spherical shape with well-defined distributions were observed [34].

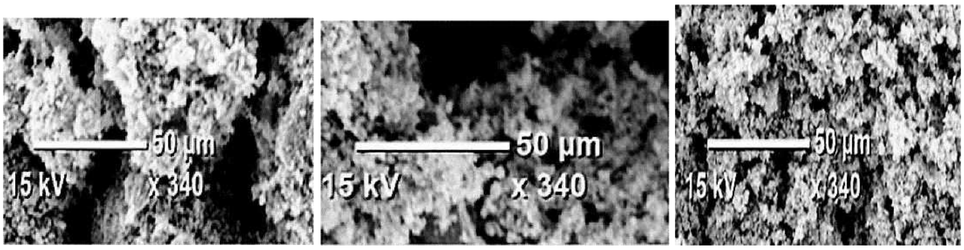

a *b* *c*

Fig. 2. SEM images of (*a*) undoped ZnO, (*b*) $Zn_{0.98}Mn_{0.02}O$ NPs, and (*c*) $Zn_{0.98}Gd_{0.02}O$ NPs. The particle agglomeration as well as narrow particle size distribution is observed in all of the samples.

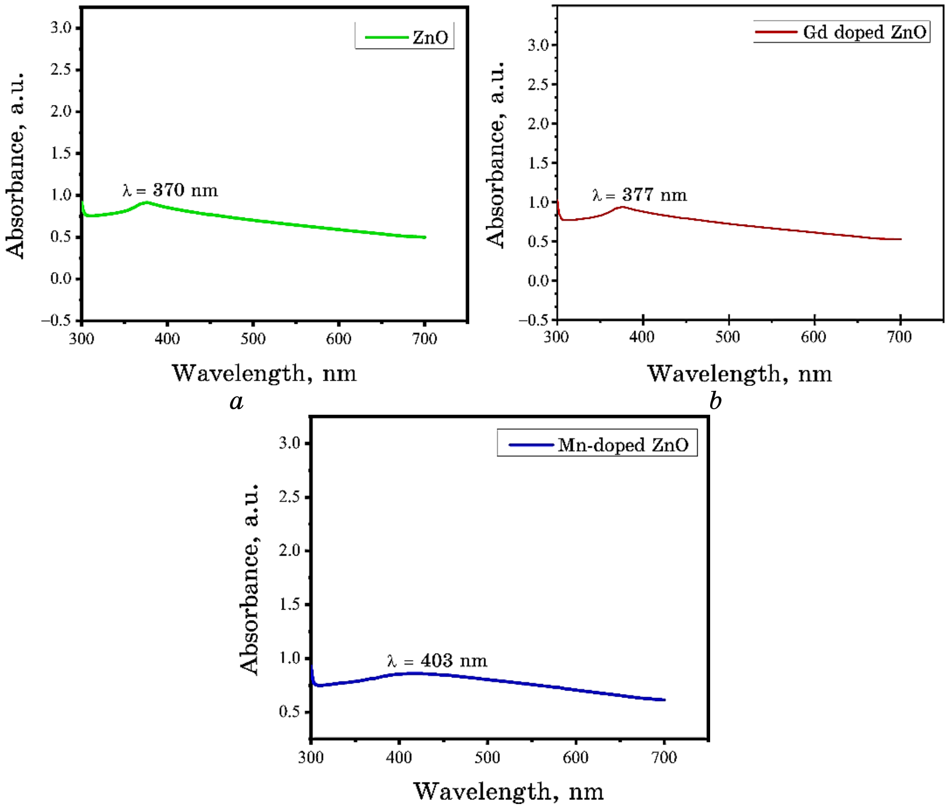

a *b* *c*

Fig. 3. The ultraviolet-visible absorption spectra of (*a*) pure ZnO, (*b*) $Zn_{0.98}Gd_{0.02}O$ NPs, and (*c*) $Zn_{0.98}Mn_{0.02}O$ NPs.

3.2. UV-Vis Spectroscopy Analysis

The effect of Mn and Gd doping on the optical properties NPs are shown in Fig. 3, *a–c*. The absorption peaks are observed at the wavelength of 370, 377 and 403 nm for undoped ZnO, $Zn_{0.98}Gd_{0.02}O$ and $Zn_{0.98}Mn_{0.02}O$, respectively. The corresponding optical band gap energy calculated using Eq. (9) was found to be 3.35, 3.28 and 3.07 eV, respectively. The ultraviolet absorption peaks regions are due to transition of electrons from valence band (VB) to conduction band (CB) [35]. It is observed that ZnO NP exhibited blue shifted absorbance peak as compared to its bulk counterpart having absorbance peak at 386 nm (3.2 eV) at room temperature. On another hand, decrease in the energy band gap of ZnO NPs with the doping of Mn and Gd ions, and this shift is ascribed to the influence of dopant ions. The interaction of d electron of Mn ion and f electron of Gd ion with *sp*-electron of ZnO may cause the dopant-induced states within the energy gap of ZnO NPs. These states correspond to the dopant additional pathways for electronic transition, thus, giving rise to the red shift of absorption due to incorporation of Mn^{2+} and Gd^{3+} ions into ZnO matrix [36].

3.3. Antimicrobial Studies

Figures 4, *a–e* demonstrate antimicrobial activity of pure ZnO, $Zn_{0.98}Mn_{0.02}O$ and $Zn_{0.98}Gd_{0.02}O$ nanoparticles against different pathogens (*P. aeruginosa*, *E. coli*, *S. aureus*, *B. subtilis*, and *C. albicans*) at the concentrations of 100, 150 and 200 μg/ml. The mechanism of antimicrobial activity are attributed to the release of Zn^{2+}, Mn^{2+} and Gd^{3+} ions in dissolution as well as the electrostatic attraction between negatively charged bacterial cells and positively charged nanoparticles, internalization into the bacterial cell wall and formation the reactive oxygen species (ROS) such as H_2O_2, hydroxyl radical OH^-, superoxide anion radical O_2^-, which cause damage to intracellular components such as DNA and cellular proteins, and may even lead to cell death [18–20]. The effects of concentrations on the antimicrobial activity of ZnO NPs are illustrated in Tables 3–5. It is observed that the zone of inhibition increases as the concentrations of NPs increases for both pure and doped NPs.

The interaction between the NPs and the cell wall of bacteria has been changed due to doping of Mn and Gd. Doping Mn and Gd with ZnO may lead to the variation in grain size, optical, morphology, and solubility of Zn^{2+} ions. All these factors have a significant effect on the antibacterial activity of ZnO [18–20]. In this study, the antimicrobial activity of ZnO NPs is increased with decreasing size of the crystal and energy band gap. It is observed that $Zn_{0.98}Gd_{0.02}O$

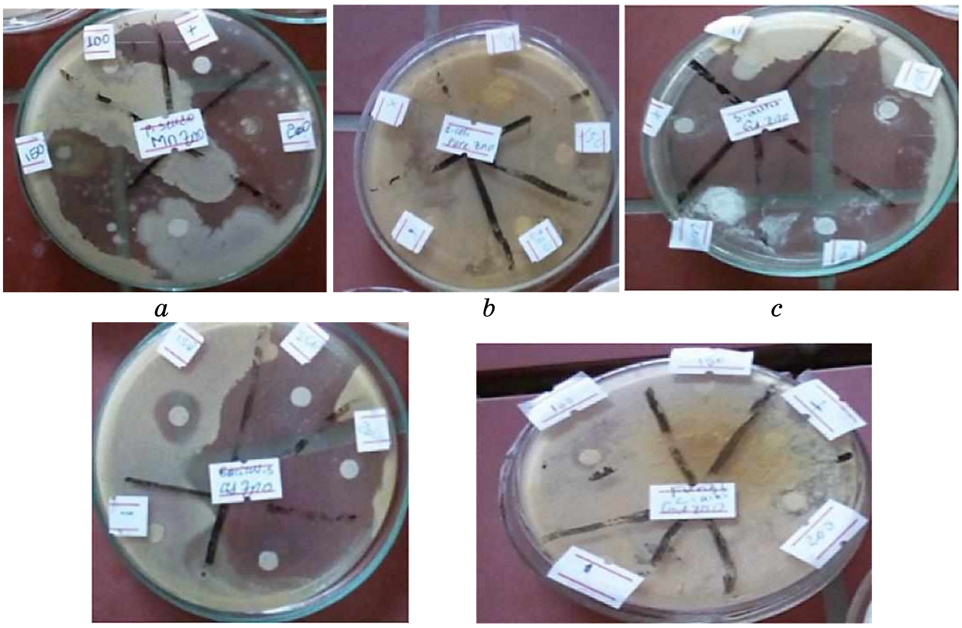

a *b* *c*

d *e*

Fig. 4. The antimicrobial activities of (*a*) $Zn_{0.98}Mn_{0.02}O$ NPs applied on *P. aeruginosa*, (*b*) pure ZnO NPs applied on *E. coli*, (*c*) $Zn_{0.98}Gd_{0.02}O$ NPs applied on *S. aureus*, (*d*) $Zn_{0.98}Gd_{0.02}O$ NPs applied on *B. subtilis*, and (*e*) $Zn_{0.98}Gd_{0.02}O$ NPs applied on *C. albicans* with different concentrations (100, 150 and 200 μg/mL).

showed better antimicrobial activity than $Zn_{0.98}Mn_{0.02}O$ and undoped ZnO due to its small size as shown in Tables 3–5. A large number of studies investigated on the considerable impact of particle size on the antibacterial activity, and the researchers found that controlling ZnO-NPs' size was crucial to achieve best bactericidal response, and ZnO NPs with smaller size (higher specific surface areas) showed highest antibacterial activity [20].

The growth of all bacteria and fungus are more affected by Gd^{3+}- and Mn^{2+}-doped ZnO nanostructures as compared with pure ZnO NPs. The other reason for the increment of antimicrobial activity of Gd doped ZnO NPs is ascribed to large generation of ROS species as doping creates a large number of defects which increases ROS species and consequently it increases antimicrobial activity. In general, nanoparticles with better photocatalytic activity have larger specific surface areas and smaller crystallite sizes, which increase oxygen vacancies, resulting in more ROS. Furthermore, due to the various surface–interface characteristics may have different chemical–physical, adsorption–desorption abilities in the direction towards

TABLE 3. Zones of inhibition of ZnO, $Zn_{0.98}Mn_{0.02}O$ and $Zn_{0.98}Gd_{0.02}O$ on different types of pathogens with concentration of 100 μg/mL.

Types of pathogens	Zones of inhibition [mm] at the concentration of 100 μg/ml of NPs			
	undoped ZnO	$Zn_{0.98}Mn_{0.02}O$	$Zn_{0.98}Gd_{0.02}O$	gentamicin (+control)
E. coli	5	8	18	19
P. aeruginosa	6	5	15	17
B. subtilis	7	10	20	28
S. aureus	7	15	19	29
C. albicans	4	10	15	21

TABLE 4. Zones of inhibition of ZnO, $Zn_{0.98}Mn_{0.02}O$ and $Zn_{0.98}Gd_{0.02}O$ on different types of pathogens with concentration 150 μg/mL.

Types of pathogens	Zones of inhibition [mm] at the concentration of 150 μg/mL of NPs			
	undoped ZnO	$Zn_{0.98}Mn_{0.02}O$	$Zn_{0.98}Gd_{0.02}O$	gentamicin (+control)
E. coli	8	10	20	19
P. aeruginosa	7	10	15	17
B. subtilis	8	17	25	28
S. aureus	9	20	25	29
C. albicans	6	10	20	21

bacteria, make sure in different antibacterial performances. The results have revealed that Gd- and Mn-doped ZnO nanostructures will be a promising candidate to be used for potential drug delivery systems to cure some significant infections [37, 38].

In the present study, we also found that gram-positive bacteria were more sensitive than gram-negative bacterial strains and fungus against the NPs tested as shown in Tables 3–5 for different concentrations. All NPs that means pure ZnO, Mn- and Gd-doped ZnO NPs were more sensitive to *S. aureus* and *E. coli* as indicated in tables. The more activity of NPs towards gram-positive bacteria is ascribed to the difference in their structure and chemical composition. The cell wall of gram-positive bacteria has single membrane whereas the gram-negative bacteria cell wall has outside and inside cytoplasmic membrane as well as lipopolysaccharide, which covers peptidoglycan. Therefore, in this case gram-positive bacteria cell surface results in more destruction and cell death than gram-negative bacteria. It was also reported earlier that various bacterial strains had considerably different infectivity and tolerance levels

TABLE 5. Zones of inhibition of ZnO, $Zn_{0.98}Mn_{0.02}O$ and $Zn_{0.98}Gd_{0.02}O$ on different types of pathogens with concentration 200 μg/mL.

Types of pathogens	Zones of inhibition [mm] at the concentration of 200 μg/mL of NPs			
	undoped ZnO	$Zn_{0.98}Mn_{0.02}O$	$Zn_{0.98}Gd_{0.02}O$	gentamicin (+control)
E. coli	9	10	20	19
P. aeruginosa	8	10	15	17
B. subtilis	10	18	30	28
S. aureus	11	22	29	29
C. albicans	6	18	21	21

towards the different agents including antibiotics [39].

4. CONCLUSIONS

The structural, morphological and optical properties of ZnO nanoparticle doped with manganese (Mn) and gadolinium (Gd) ions, and their antimicrobial activity were investigated.

The nanoparticles were characterized by XRD, SEM and UV-vis spectroscopy. The XRD result revealed that the synthesized ZnO NPs were in nanometre range with average crystallite size of about 31–38 nm from the Scherrer's formula. The lattice parameters, unit cell volume and bond lengths were decreased with the doping with Gd and Mn. On the other hand, physical defects and dislocations were increased. It was also perceived that XRD peaks shifted to higher diffraction angles due to the difference of the ionic radii of Mn^{2+}, Zn^{2+} and Gd^{3+}. Morphological studies obtained from SEM have revealed the formation of spherical nanoparticles for all samples. Optical band gap energy was found to be decreased with doping due to the introduction of new energy levels in the energy band gap.

The zone of inhibition was observed against pathogenic bacteria and fungus strains and suggests that $Zn_{0.98}Gd_{0.02}O$ and $Zn_{0.98}Mn_{0.02}O$ showed good antimicrobial activity on gram-positive bacteria (*S. aureus* and *B. subtilis*), gram-negative bacteria (*E. coli* and *P. aeruginosa*) and fungus (*C. albicans*) than the undoped ZnO nanoparticles.

In addition, the results of this study depicted that the antimicrobial activities of synthesized NPs were increased with the concentration and size decrement of the crystal. Furthermore, the results indicated that the gram-positive bacteria were more sensitive to all undoped, Mn- and Gd-doped ZnO NPs than gram-negative bacteria and fungus.

ACKNOWLEDGMENTS

The authors would like to acknowledge Adama Science and Technology University and the Ministry of Innovation and Technology of Ethiopia for financial support. We also like to appreciate the Biology Department of Adama Science and Technology University for allowing us to use UV-Vis spectroscopy and SEM facilities.

REFERENCES

1. M. Kasahun, A. Yadate, A. Belay, Z. Belay, and M. Ramalingam, *Nano Biomed. Eng.*, **12**, No. 1: 47 (2020); doi:10.5101/nbe.v12i1.p47-56
2. S. K. Mihra, R. K. Srivastava, and S. G. Prakash, *Journal of Alloys and Compounds*, **539**: 1 (2012); doi:10.1016/j.jallcom.2012.06.024
3. J. Wang, J. Cao, B. Fang et al., *Mater Lett.*, **59**: 1405 (2005); https://doi.org/10.1016/j.matlet.2004.11.062
4. Z. L. Wang, *ACS Nano*, **2**: 1987 (2008); https://doi.org/10.1021/nn800631r
5. M. Chaari and A. Matoussi, *Phys. B: Condensed Matter*, **407**: 3441 (2012); doi:10.1016/j.physb.2012.04.05
6. J. Ma, J. Liu, Y. Bao et al., *Ceram. Int.*, **39**, No. 3: 2803 (2013); https://doi.org/10.1016/j.ceramint.2012.09.049
7. P. Jamdagni, P. Khatri, and I. S. Rana, *Journal of King Saud University Science*, **2018**: 168 (2018); https://doi.org/10.1016/j.jksus.2016.10.002
8. R. Jalal, M. Abareshi, E. K. Goharshadi et al., *Materials Chemistry and Physics*, **121**, Nos. 1–2: 198 (2010); doi:10.1016/j.matchemphys.2010.01.020
9. J. Podporska-Carroll, A. Myles, B. Quilty et al., *J. Hazard Mater.*, **324**: 39 (2017); doi.org/10.1016/j.jhazmat.2015.12.038
10. P. Chand, A. Gaur, A. Kumar et al., *Appl. Surf. Sci.*, **356**: 438 (2015); https://doi.org/10.1016/j.apsusc.2015.08.107
11. M. Jyoti, D. Vijay, and S. Radha, *IJSRP*, **3**: 1 (2013).
12. G. N. Narayanan, R. S. Ganesh, and A. Karthigeyan, *Thin Solid Films*, **598**: 39 (2016); https://doi.org/10.1016/j.tsf.2015.11.071
13. Y. L. Zhang, Y. Yang, J. H. Zhao et al., *J. Sol–Gel Sci. Technol.*, **51**: 198 (2009); https://doi.org/10.1007/s10971-009-1959-5
14. A. Bera and D. Basak, *ACS Appl. Mat. Interfaces*, **1**: 2066 (2009); https://doi.org/10.1021/am900422y
15. A. Naskar, S. Lee, and K. Kim, *RSC Adv.*, **10**: 1232 (2020); doi:10.1039/C9RA09512H
16. A. Bagabas, A. Alshammari, M. F. A. Aboud et al., *Nanoscale Res. Lett.*, **8**: 516 (2013); https://doi.org/10.1186/1556-276X-8-516
17. R. Wahab, S. G. Ansari, Y. S. Kim et al., *Appl. Surf. Sci.*, **255**: 4891 (2009); https://doi.org/10.1016/j.solmat.2008.06.019
18. A. Sirelkhatim et al., *Nanomicro Lett.*, **7**, No. 3: 219 (2015); https://doi.org/10.1007/s40820-015-0040-x
19. A. J. Ahmed, *Int. Res. J. Pharm.*, **9**, No. 9: 16 (2018), doi:10.7897/2230-8407.099181
20. P. Narayanan, W. S. Wilson, A. T. Abraham, and M. Sevanan, *BioNanoSci-*

ence, **2**, No. 4: 329 (2012); doi:10.1007/s12668-012-0061-6

21. S. Getie, A. Belay, A. R. Chandra Reddy, and Z. Belay, *Journal of Nanomedicine & Nanotechnology*, **S8**: 1 (2017); doi:10.4172/2157-7439.S8-004
22. Sh. Jeetendra, H. Nagabhushana, K. Mrudula, C. S. Naveen, P. Raghu, and H. M. Mahesh, *Int. J. Electrochem. Sci.*, **9**: 2944 (2014).
23. R. Jenkins and R. L. Synyder, *Introduction to X-Ray Power Diffractometry* (New York: John Wiley and Sons: 1996)
24. O. Bilgili, *Acta Physica Polonica A*, **136**: 79 (2019); doi:10.1109/SMELEC.2010.5549430
25. W. Zhou, R. Apkarian, Z. L. Wang, and D. Joy, *Fundamentals of Scanning Electron Microscopy (SEM), Scanning Microscopy for Nanotechnology: Techniques and Applications* (New York: Springer: 2007), p. 1.
26. A. Khorsand Zak, M. Ebrahimizadeh Abrishami, W. H. Abd. Majid, Ramin Yousefi, S. M. Hosseini, *Ceramic International*, **37**: 393 (2011); https://doi.org/10.1016/j.ceramint.2010.08.017
27. A. B. Gemta, B. Bekele, and A. R. C. Reddy, *Digest Journal of Nanomaterials and Biostructure*, **214**: 51 (2019).
28. P. Ghosh and A. K. Sharma, *Journal of Nanomaterials*, **2013**: ID 480164 (2013); https://doi.org/10.1155/2013/480164
29. Y. Abdollahi, A. H. Abdullah, Z. Zainal, and N. A. Yusof, *International Journal of Basic & Applied Sciences IJBAS-IJENS*, **11**, No. 4: 62 (2015).
30. R. K. Sharma, S. Patel, and K. C. Pargaien, *Adv. Nat. Sci.: Nanosci. Nanotechnol.*, **3**: 035005 (2012); https://iopscience.iop.org/article/10.1088/2043-6262/3/3/035005
31. M. Sarfraz, N. Ahmed, K. U. Haq, S. H. SHahida, and M. A. Khana, *Materials Science-Poland*, **37**, No. 2: 280 (2019); https://doi.org/10.2478/msp-2019-0029
32. M. Aparecida, R. Bonifácio, H. d. L. Lira, L. S. Neiva, and L. Gama, *Materials Research*, **20**, No. 4: 1044 (2017); https://doi.org/10.1590/1980-5373-mr-2015-0765
33. G. Vijayaprasath, G. Ravi, A. S. Haja Hameed, and T. Mahalingam, *J. Phys. Chem. C*, **118**: 9715 (2014); https://doi.org/10.1021/jp411848t
34. S. D. Senol, B. Yalcin, E. Ozugurlu, and L. Arda, *Mater. Res. Express*, **7**: 015079 (2020).
35. J. H. Zheng, J. L. Song, Z. Zhao, Q. Jiang, and J. S. Lian, **47**, No. 7: 713 (2012); https://doi.org/10.1002/crat.201200026
36. S. S. Sartiman, N. F. Djaja, and R. Saleh, **4**: 528 (2013); doi:10.4236/msa.2013.49065
37. Sh. A. Khan, S. Shahid, W. Bashir, S. Kanwal, and A. Iqbal, *Tropical Journal of Pharmaceutical Research*, **16**, No. 10: 2331 (2017); http://dx.doi.org/10.4314/tjpr.v16i10.4
38. A. F. Fathima, R. J. Mani, K. Sakthipandi, K. Manimala, and A. Hossain, *Journal of Inorganic and Organometallic Polymers and Materials*, **30**, Iss. 7: 2397 (2019); https://doi.org/10.1007/s10904-019-01400-z
39. Z. E. Karvani and P. Chehrazi, *African Journal of Microbiology Research*, **5**, No. 2: 1368 (2011); doi:10.5897/AJMR10.159

Наукове видання

НАНОСИСТЕМИ, НАНОМАТЕРІАЛИ, НАНОТЕХНОЛОГІЇ

ЗБІРНИК НАУКОВИХ ПРАЦЬ

ТОМ 19

випуск 4

(2021)

Підписано до друку 31.12.2021. Формат 70×100/16.
Папір офсетний. Друк різографічний.
Ум. друк. арк. 19,18. Обл.-вид. арк. 17,64.
Наклад 80 прим. Зам. № 4

Поліграфічно-розмножувальна дільниця РВВ ІМФ ім. Г. В. Курдюмова НАН України
бульв. Акад. Вернадського, 36; 03142 Київ, Україна

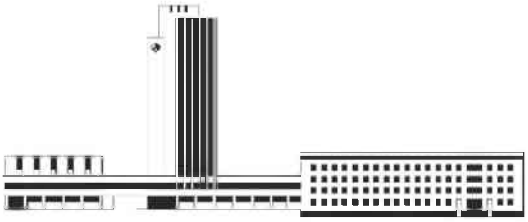

НАЦІОНАЛЬНА АКАДЕМІЯ НАУК УКРАЇНИ

НАНОСИСТЕМИ
НАНОМАТЕРІАЛИ
НАНОТЕХНОЛОГІЇ

NANOSYSTEMS
NANOMATERIALS
NANOTECHNOLOGIES

Засновник: Інститут металофізики ім. Г. В. Курдюмова НАН України
Видавець: Інститут металофізики ім. Г. В. Курдюмова НАН України

Подписной индекс 94919 ISSN 1816-5230

Информация о подписке на сборник научных трудов «НАНОСИСТЕМЫ, НАНОМАТЕРИАЛЫ, НАНОТЕХНОЛОГИИ»

Редакция ежеквартального сборника научных трудов
«НАНОСИСТЕМИ, НАНОМАТЕРІАЛИ, НАНОТЕХНОЛОГІЇ»
(CODEN: NNNAAT; ISSN (Print): 1816-5230, ISSN (Online): 2617-3794;
в «Каталоге изданий Украины» подписной индекс: **94919**)
извещает о подписке (начиная с текущего квартала выпуска).
Рекомендуем оформить подписку непосредственным перечислением оплаты

в гривнах:
«Получателю»: Институт металлофизики им. Г. В. Курдюмова НАН Украины
на расчётный счёт № UA058201720313291001201001901 в банке ГУГКСУ в г. Киеве
код банка 820172
код ЗКПО: 05417331
для «Поставщика» — Института металлофизики им. Г. В. Курдюмова НАН Украины
Свидетельство плательщика налога № 36283185
ИНН 054173326066
Код назначения платежа: 25010100
Назначение платежа: за сборник «Наносистеми, наноматеріали, нанотехнології» для РИО ИМФ НАНУ
Основание: предоплата 100%

в иностранной валюте (долларах США, евро) через соответствующие банки-корреспонденты АО «Государственный экспортно-импортный банк Украины»:
«Получателю»: Филиал АО «Государственный экспортно-импортный банк Украины»
в г. Киеве (Украина, 04053 Киев, ул. Бульварно-Кудрявская, 11$^{\text{б}}$)
на расчётный счёт № UA603223130000025308000000067
МФО 322313
для «Поставщика» — Института металлофизики им. Г. В. Курдюмова НАН Украины
Назначение платежа: за сборник «Наносистеми, наноматеріали, нанотехнології» для РИО ИМФ НАНУ
Основание: предоплата 100%

При этом способе подписки необходимо сообщить редакции сборника по почтовому адресу:
РИО (№ 83) ИМФ НАНУ,
бульв. Акад. Вернадского, 36,
03142 Киев, Украина

e-mail: tatar@imp.kiev.ua; факс: +380 44 4242561; телефон: +380 44 4229551, +380 44 4249042

дату оплаты, название учреждения или имя подписчика, адрес для почтовой доставки, а при необходимости — свои реквизиты для налоговой накладной.

Периодичность — том из 4 выпусков в год.

С учётом почтовой пересылки
для подписчиков в Украину подписная стоимость: одного экземпляра выпуска — 312 грн., тома — 1248 грн.;
для подписчиков в страны СНГ подписная стоимость: одного экземпляра выпуска — 36 US$, тома — 144 US$;
для иностранных подписчиков вовне СНГ подписная стоимость: одного экземпляра выпуска — 40 US$ (36 EUR), тома — 160 US$ (144 EUR).

✂ *Образец для оплаты годовой подписки*

Счёт-фактура

«Поставщик»: Институт металлофизики им. Г. В. Курдюмова НАН Украины
«Получатель»: Филиал АО «Государственный экспортно-импортный банк Украины» в г. Киеве (Украина, 04053 Киев, ул. Бульварно-Кудрявская, 11$^{\text{б}}$)
на расчётный счёт № UA603223130000025308000000067, МФО 322313
Назначение платежа: за сборник «Наносистеми, наноматеріали, нанотехнології» для ИМФ НАНУ
«Плательщик»: ____
____
Основание: предоплата 100%

№	Наименование	Ед. изм.	Кол-во	Цена	Сумма
1	сборник «Наносистеми, наноматеріали, нанотехнології» (включая доставку почтой)	экз.	4	36 US$	144 US$
	Сумма к оплате				144 US$

Індекс 94919